DOCTORAL THESIS

Novel Probes for Multimodal Imaging at the Nanoscale

Author:
David Atkins

First Supervisor:
Prof. Jonathan Weaver
Second Supervisor:
Dr. Phillip Dobson

A report submitted in fulfillment of the requirements for the degree of Doctor of Philosophy

in the

University of Glasgow
School of Engineering
September 17, 2025

Declaration of Authorship

I, David Atkins, declare that this thesis titled, "Novel Probes for Multimodal Imaging at the Nanoscale" and the work presented in it are my own. I confirm that:

- This work was done wholly or mainly while in candidature for a research degree at this University.
- Where any part of this thesis has previously been submitted for a degree or any other qualification at this University or any other institution, this has been clearly stated.
- Where I have consulted the published work of others, this is always clearly attributed.
- Where I have quoted from the work of others, the source is always given. With the exception of such quotations, this thesis is entirely my own work.
- I have acknowledged all main sources of help.
- Where the thesis is based on work done by myself jointly with others, I have made clear exactly what was done by others and what I have contributed myself.

Signed:
Date:

"Thanks to my solid academic training, today I can write hundreds of words on virtually any topic without possessing a shred of information, which is how I got a good job in journalism."

Dave Barry

Abstract

David Atkins

Novel Probes for Multimodal Imaging at the Nanoscale

Tip enhanced Raman spectroscopy is a technique which allows the user to retrieve topographic, morphological and chemical information of a sample with single molecule resolution, far beyond the Raman spatial resolution of conventional techniques. Its usefulness extends into many scientific fields, such as medicine, electronics and material science. Conventional probes used to conduct TERS , where metal is deposited onto commercial AFM tips, tend to be made of silver. This is due to silver having strong plasmon resonances in the visible and near-infrared regime, alongside low optical losses and there are well established processes for making them. The issue with these probes is that they are commonly deposited one at a time and silver is known to grow a sulphide layer. This sulphide film inhibits the electric field, shifting the plasmon resonance and limits the lifetime of these probes to 24-48hrs. The use of a conventional AFM tip as a substrate for the plasmonic film is also problematic since the coupling of the far field radiation to the tip plasmon occurs close to the tip and is facilitated by local roughness, leading to critical and irreproducible alignment requirements for the illuminating beam. The issue of tip contamination and lifetime may be eliminated by the use of gold instead of silver, at the expense of plasmonic performance. The use of a long-lived metal allows the use of more elaborate coupling methods based on plasmonic gratings or slot couplers fabricated by focused ion beam milling or self-aligned plasma processing. Both techniques of silver growth and gold coupler tip fabrication are irreproducible however, they do not have nm resolution placement or techniques to ensure the same tip is made over again using plasma or chemical etches. The work-around for this is to use a focused ion beam with the benefit of very high resolution (nm), but each probe has to be milled one at a time. A lot of effort goes into making these tips, where if one fails due to over/under etch or

other reasons, another metal deposition or plasma processing has to occur as the tip is scrapped.

A method for the wafer scale fabrication of novel TERS-AFM probes is presented. The probes are based on the use of a grating to couple light from free space into the dielectric of the tip at some distance from its apex, the grating allowing for the use of fixed – angle illumination at a known position far from the tip. Waveguide to surface plasmon coupling occurs near the tip and plasmons are then concentrated to the tip by a triangular metal structure. The fabrication was successfully completed, although operation at useful wavelengths was precluded by poor reproducibility of the probe dielectric thickness. Development work on the fabrication of scanning electro-chemical microscopy probes, where insulator adhesion to the metal electrode is a key issue, has also been been conducted.

To test the TERS probes, novel calibration samples were made. These samples employed statistical and correlation alignment strategies with an e-beam lithography tool to produce 70nm thick gold dots and dimers with separation distances of 1nm and above (1nm increments) in the x and y direction. Once coated with Raman Active molecules this sample will be useful for testing of TERS probes, allowing the study of separation distance vs. enhancement for different probe archetypes. A topography free sample with interdigitated electrode active areas has also been developed for the test of Scanning Electrochemical Microscope probes. This sample removes the introduction of topographic artefacts from a SECM scan, whilst retrieving useful information on the electro-chemical nature of the probes.

After extensive and rigorous testing, probes failed to exhibit local plasmonic enhancement at the available wavelength of the TERS systems. The lack of enhancement was confirmed by extensive processing of the acquired data using baseline correction and adaptive smoothness penalised least squares (asPLS) methods. For comparison of the SERS and TERS spectra the data was also intensity normalised and cosmic rays removed. This is attributed to poor control of dielectric deposition thickness preventing phase matching of the guided light to the surface plasmon polariton: Possible solutions are presented and their practicality discussed.

Acknowledgements

Well, where do i start. This project was really testing, being both mentally and physically draining. However, i've met some of the most amazing people in the world and wouldn't change it for the world.

I would firstly like to thank my support unit, my family. If it wasn't for the constant love and support of my adoring mum and dad, i wouldn't have even got close to getting a MEng degree, never mind tackling a doctorate project. All those nights spent going over homework as a young child, providing and caring for me, it means the world to me.

Prof Jonathan Weaver. What a fantastic supervisor, human being and all around legend. I owe a huge amount of gratitude to him, he has molded me into becoming a great engineer. He had patience, imparted wisdom, and had a great few laughs, even during a worldwide plague.

Phil Dobson. One of the hardest working men I have had the pleasure of knowing. Thank you for all the laughs, mostly at my expense, the fun times and exploring this field together.

Affar Karamullah. My saviour, you really stepped up when we needed someone to help get this projected finished towards the end. I wish we had worked together sooner as it was one of the most enjoyable times of my journey.

The AFM group. Rory, Lukas, Chris, Hao, James, Sixuan, thank you to all. We got through this journey together, and every one of you played your part in making this an incredible experience. From Lukas swallowing the coins and becoming "puggy", to being a bad influence on Hao by teaching her some naughty phrases. It experiences i'll never forget. Chris, that pandemic was hard, there is no way this would've been possible without yourself and our slot rotation. Major thanks. James, the laughs and all the experience i could give doesn't make up for the help you gave me also.

Last but not least, my new wonderful family. Lynsey, you have been here through it all, my rock, my shoulder to cry on, my absolute world. This book would have not been written without you. Alexander, my beautiful baby boy, you really put everything into

perspective. This is for all of you, all my friends and family and even you, the person reading this, thank you from the bottom of my heart.

As i finish my final draft of this work, i have lost a lot. This work is dedicated to you mum. I hope you rest in peace knowing everyone adored you and you meant the world to me. My Papa Alex and Grandma Jo, i love you and i hope you're looking after my mum for a change. Losing all 3 of you in 7 months has been very difficult, but i rest easy knowing you'll be watching over me and the rest of the family.

Contents

List of Figures

List of Tables

List of Abbreviations

AFM	**A**tomic **F**orce **M**icroscopy
SPM	**S**canning **P**robe **M**icroscopy
SECM	**S**canning **E**lectrochemical **M**icroscopy
TERS	**T**ip **E**nhanced **R**aman **S**pectroscopy
SEM	**S**canning **E**lectron **M**icroscopy
EBL	**E**lectron **B**eam **L**ithography
FIB	**F**ocused **I**on **B**eam
JWNC	**J**ames **W**att **N**anofabrication **C**entre
SPP	**S**urface **P**lasmon **P**olariton
SERS	**S**urface **E**nhanced **R**aman **S**pectroscopy
SP	**S**urface **P**lasmon
NA	**N**umerical **A**peture
CAD	**C**omputer-**a**ided **D**esign

List of Chemical Names and Compounds

IPA	**I**so**p**ropa**n**ol
RO Water	**W**ater with **18MΩ-cm R**esistivity
TMAH	**T**etra**m**ethyl**a**mmonium **H**ydroxide
KOH	**P**ottasium **H**ydroxide
Au	**G**old
Pt	**P**latinum
Si	**S**ilicon
NiCr	**N**ickel **C**hromium
Ti	**T**itanium
He	**H**elium
SiH_4	**S**ilane
NH_3	**A**mmonia
N_2	**N**itrogen

1 Review

1.1 Instrumentation

1.1.1 Introduction

This section gives a general overview of microscopy and its development to incorporate different sample types and extraction of various data types. A more in-depth investigation into the microscopy utilised within this project is then outlined, with a focus on the development of the field.

1.1.2 Microscopy

Microscopy is a technical field whereby users can examine areas of interest outwith the practical resolution range of a normal eye. Microscopy has proved its use within biological applications, from Hooke and van Leeuwenhoek [1] depicting the first image of microscopic organisms (Mucor) in 1665-83, or Ruska and colleagues becoming the first to visualize viruses (tobacco mosaic virus) with electron microscopy in 1939 [2], [3]. It also extends it's far reach into the semiconductor industry, where defects and impurities on the surface can be seen, therefore optimising fabrication processes [4], the control over which can affect the properties of the system it belongs to.

Control over a sample's dimensioning can also be used to save materials, such as in combustion processes where catalysts are used to reduce pollutants [5]. Only the outside atoms in these catalytic materials are used, with a lot of atoms remaining inaccessible, therefore control of dimensioning allows single noble metal layers for catalysis to be developed [6] and reduce material wastage.

Many natural occurring systems are also determined by their organisation and composition on the micro and nanoscale, like viruses and their ability to infect the human

population [7] by altering its structure. Although vaccines were created long before people even knew what caused disease, microscopy allowed us to determine what the infectious agent was. It is now standard practise in determining the 3-d positions of atoms in protein structures [8]. By understanding the structure of the infectious agent, drugs can be designed to target them more effectively, from giving insight into their binding modes [9] and interaction with the target protein, to understanding drug resistance from mutations or structural changes of the target protein. This is a massive step up in medicine where x-ray crystallography has commonly been used [10], however, this does not give an image of the protein and you must grow a crystal first, which is a difficult task [11]. Viruses can also be imaged using transmission electron microscopy [12], which helps identify unknown infectious agents in differing outbreaks, like the bovine papilloma virus in cows [13] and monkeypox in 2004 [14]. It is clear to see the benefits of microscopy within various fields, impacting the daily lives of humans, we therefore build microscopes to suit various applications, which in turn drives what microscope/technique we use.

1.1.3 Optical Microscopy

Optical microscopy is a technique which typically uses visible light and lenses, or a singular lens, to magnify an image of a sample with a resolution not available to the naked eye. In order for an image to be retrieved, the incoming light must interact with the sample. The emitted light propagates in space follows relation 1.1 [15].

$$\omega = \mathrm{c}\cdot\mathrm{k} = \mathrm{c}\sqrt{k_x^2 + k_y^2 + k_z^2} = \mathrm{c}\frac{2\pi n}{\lambda} \tag{1.1}$$

Where c is the speed of light in vacuum and k is the wavevector. The refractive index n, determines the speed at which light travels through a medium other than a vacuum and follows relation 1.2 [16].

$$\mathrm{n} = \frac{c}{v} \tag{1.2}$$

Where c is still the speed of light in vacuum and v is the speed of light in a material.

When modelling the propagation an electromagnetic wave, the angular spectrum method may be used (Figure 1.1).

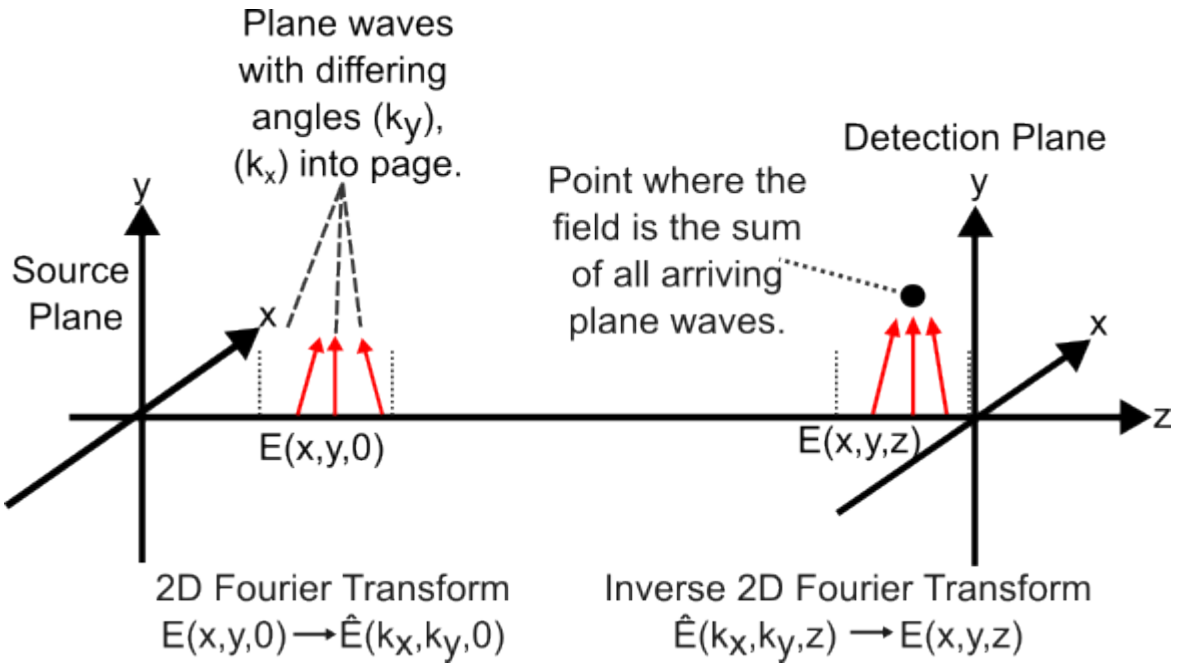

FIGURE 1.1: The schematic diagram depicts the angular spectrum method for wave propagation. This method decomposes a wave into plane waves, propagates each plane wave and reconstructs the field.

The angular spectrum method describes how the electric field evolves along the z-axis, from a source plane (z=0), to a detection point (z=(z)). The electric field at any point (x,y,z) is given by relation 1.3.

$$\bar{E}(x,y,z) = \iint_{-\inf}^{+\inf} \tilde{E}(k_x,k_y,0)\exp^{i(k_x x+k_y y+k_z z)}\,dk_x dk_y \tag{1.3}$$

Where $\tilde{E}(k_x,k_y,0)$ is the 2D Fourier transform of the field at plane z=0, and k_z is the longitudinal wavevector. The value of k_z is given by relation 1.4

$$k_z = \sqrt{\left(\frac{2\pi n}{\lambda}\right)^2 - k_x^2 - k_y^2} \tag{1.4}$$

Where n is the refractive index, λ is the wavelength of light, k_x and k_y are the spatial frequencies of the plane waves in the respective x and y direction. This relation shows that the value of k_z is the longitudinal wavevector component for each plane wave in the superposition, however not all spatial frequencies contribute equally to the electric field along z.

For a wave to propagate, k_z must be real and the following condition must be met:

$$\mathrm{k}_x^2 + k_y^2 \leq \frac{2\pi n}{\lambda}^2 \tag{1.5}$$

Reducing this to the x-z (k_y=0) plane:

$$k_x < \frac{2\pi n}{\lambda} \tag{1.6}$$

Spatial frequencies above this limit result in an imaginary k_z. This corresponds to an evanescent wave, which decays exponentially along z and does not reach the far-field. Therefore, only spatial frequencies below this limit (features larger than approximately$\lambda/2$n) reach the far-field and limit the spatial resolution.

The spatial resolution of the system can be described as the minimum distance between two objects whereby they can be distinguished as two objects, rather than amalgamated into one. The spatial resolution of an imaging optical microscope follows the Abbe criterion (1.7) [17]:

$$d = \frac{0.61\lambda}{NA} \tag{1.7}$$

Where NA is the numerical aperture of the optical system, λ is wavelength of the light and d is the minimum resolvable distance between the two objects. With optical microscopies using light sources within the visible optical wavelength, the lateral spatial resolution is limited to around 0.2 μm [18], [19]. Therefore objects closer than this distance cannot be distinguished from each other, unless they possess a difference in another optical property such as colour.

Although resolution is dictated by the Abbe criterion there are techniques which can surpass the imposed diffraction limit. We can increase the resolving power of a microscope by using an immersion medium and appropriate objective. Utilising a lens with a small focal length and high magnification, the objective is coated in an immersion oil, like 1-bromonaphthalene used in 1889 by Sigfried Czapski, leaving no air gap between that and the specimen [20]. As the refractive index of oil is greater than 1, it can achieve a NA value greater than 1, meaning an increase in the spatial resolution compared to air.

$$NA = nsin\alpha_0 \tag{1.8}$$

Where α_0 is one half of the angular aperture of the objective lens. Whilst using relation 1.7, it can be understood that for a larger NA, the resolving distance between 2 objects decreases, therefore an increase in the resolution is observed.

1.1.4 Super Resolution

Although the Abbe criterion dictates what the resolution of conventional optical microscopy is, there are multiple techniques which can increase the resolution of the system beyond the imposed limit known as super-resolution [21]. The development of super resolution was such a grand feat, it won the Nobel Prize in chemistry in 2014 through Eric Betzig, W.E. Moerner and Stefan Hell's efforts. The three men developed super-resolved fluorescent microscopy, which allowed optical microscopy to resolve features in the nanoscale [22].

Super-resolution relies on optimising conditions at either the near-field or the far-field. Whilst in the far-field regime, two major techniques, known as deterministic and stochastic super resolution, can extend the resolution far beyond the Abbe criterion. These are fluorescence microscopy techniques, which allows fluorescent samples to be imaged. Fluorescent microscopy is an essential imaging technique in cell biology to visualize any tissue, cells, organelles and even macromolecular assemblies within cells [23].

1.1.4.1 Far-Field

One far-field technique to obtain super resolution is known as Stochastic Optical Reconstruction Microscopy (STORM). STORM's operation relies on the stochastic activation of synthetic fluorophores containing photoactive properties [24], and routinely delivers spatial resolution of around 20-30 nm with standard optics and organic dyes [25]. STORM makes use of single fluorophores "blinking" from a dark to a weakly emissive state, before then quickly going back to a dark state or becomes deactivated by photobleaching [26]. To generate successful images, these fluorophores must be distributed far away from each other so that only single molecules are activated when exposed to the light. The technique then activates/deactivates each fluorophore until each molecule on the samples number of photons is detected. The centroid positioning of each molecule is then statistically fitted, with the precision of this value being greater with the more photons it detects. Taking multiple images within a diffraction limited area, a reconstruction of each individual emissive molecule can therefore be constructed with mathematical models [25].

Although wonderful for microscopy and for biological applications, image quality can be compromised through photobleaching of molecules [26]. A diagram of a STORM system is shown in Fig 1.2.

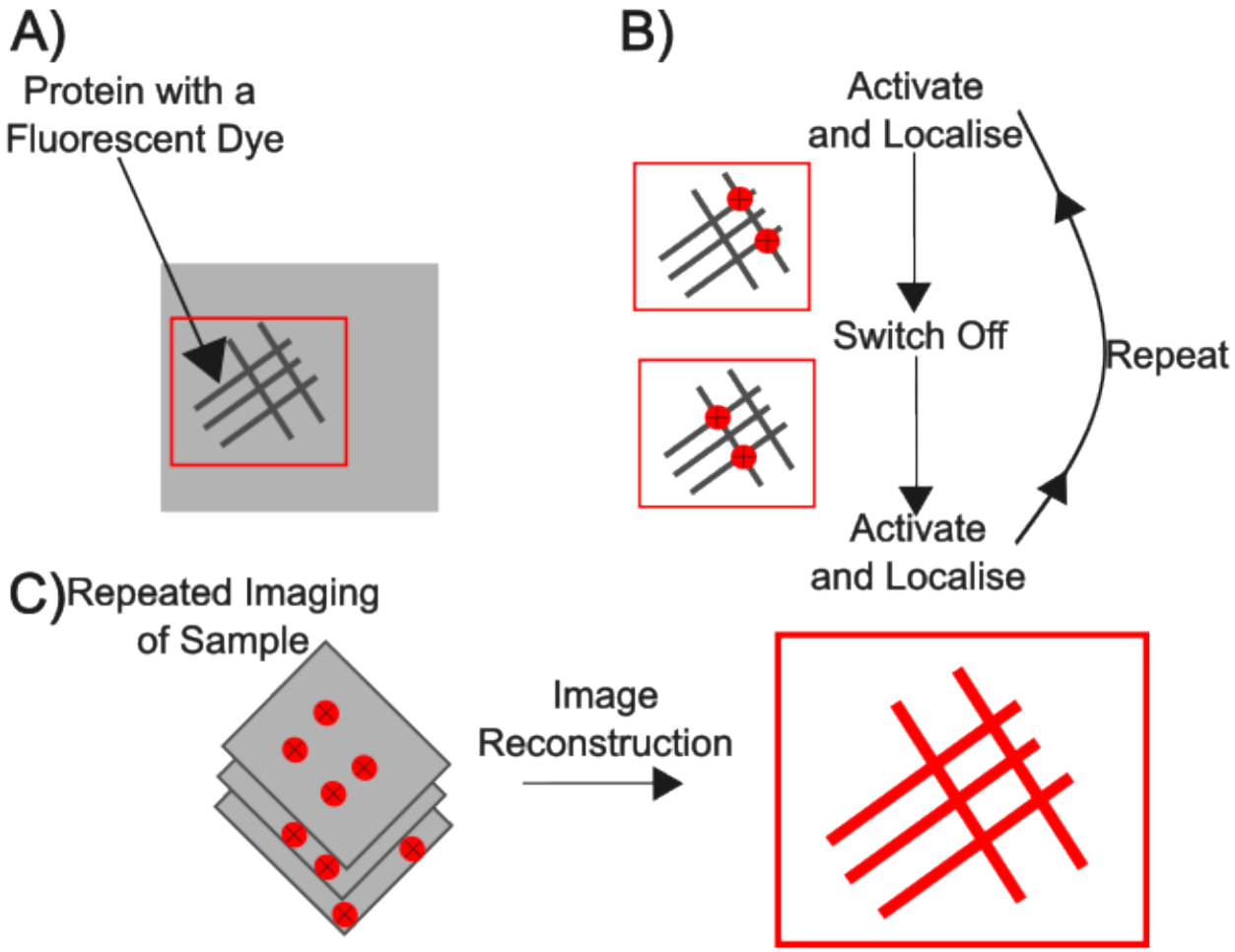

FIGURE 1.2: A) shows a protein labelled with a fluorescent dye. B) shows how a low intensity laser activates the fluorescence state of the dye, where fitting algorithms find the centre of the protein. The protein is then put back into a dark state typically with a high energy laser causing it to "blink". C) shows how the sample is then repeatedly imaged, activating and deactivating molecules with a wavelength specific to the fluorescent dye used. An image of the precise positionings of the fluorescence events is then reconstructed to form a super-resolution STORM picture. [27]

Another setup which makes use of fluorophores nonlinear response to excitation, is a deterministic super resolution technique known as Stimulated Emission Depletion microscopy (STED). STED differs from STORM, as STORM uses mathematical models of multiple diffraction limited images to create a reconstructed high-resolution image. It instead selectively deactivates fluorophores by minimising the exposure area at the

focal point, creating super high-resolution images [28]. In a conventional STED setup, a Gaussian excitation beam is aligned with a STED beam in a spatially targeted region. The STED beam de-excites fluorophores via stimulated emission and is in phase and/or polarized to generate a ring shaped focal intensity distribution, with the zero intensity value in the centre [29]. Although the intensity distribution is diffraction limited, the large intensities saturate the stimulated emission transition and keep most of the fluorophores at a ground state, apart from those located near the zero point. The region exposed, or kept at an excited state, is below the diffraction limit and gets smaller with a larger STED beam intensity, where the spatial resolution is determined by the fluorescent region around the zero point and the signal to noise ratio. These resolutions have been quoted as being down to 20 nm on cells [30], but is known to be prone to phototoxicity on live cells [31]. There was also development on 3-D STED imaging, with Osseforth et al. quoting a lateral and axial resolution of ($\approx$35 nm) and respectively whilst imaging colloids and single fluorescent molecules [32]. These are of course dependent on the fluorophore and its chemical environment [33]. A diagram showing the operation of a STED microscope is shown in Figure 1.3.

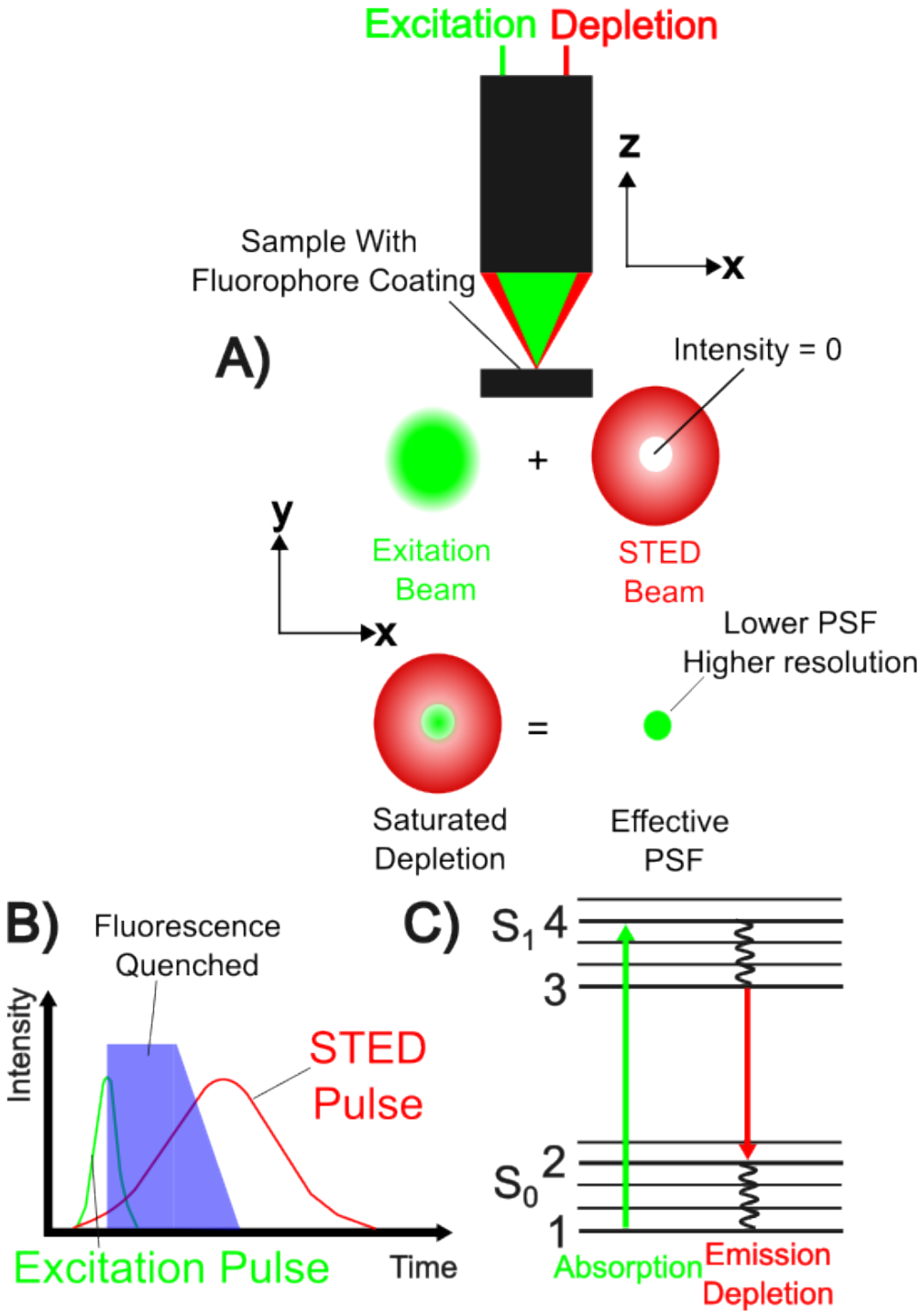

FIGURE 1.3: A) Shows excitation and depletion synchronized laser pulses focuses by an objective onto a sample plane. The focal points of the excitation and depletion lasers are shown, with the zero-intensity value of the STED laser highlighted. The depletion laser and excitation profiles are superimposed to reduce the effective point-spread function. B) depicts the short excitation pulse (green) which causes fluorescence. It is then quenched (blue region) due to the long STED laser pulse. C) shows a Jablonski diagram of the excitation states during STED operation. Molecules get excited to S1 (fluorescent state) where they normally return to S0 by spontaneous fluorescence emission. Stimulated emission of the excited state by the depletion layer brings all excited fluorophores within the red ring down to the ground state and prevents fluorescence emission. [34]

1.1.4.2 Near-Field

It is possible to produce super resolution images without the need for fluorescence, but such techniques require information from evanescent waves (near field) to do so. Evanescent waves differ from propagating waves in that they have an imaginary wave vector component. This causes an exponential decay of the electric and/or magnetic field amplitude as the distance from the source increases [35].

One method of achieving super resolution whilst making use of the near field was discussed by J.M. Guerra in 1990, publishing an article on a technique known as photon tunnelling microscopy (PTM) [36]. When light in a medium with a higher refractive index (n1) is incident, beyond the critical angle, on a material with a lower refractive index (n2) interface, total internal reflection generates an exponentially decaying evanescent field extending beyond the boundary[37]. While there is no net transfer of energy across the interface, by placing a material (n3) with a refractive index greater than or equal to n2 within the evanescent region, photon tunnelling is enabled by frustrated total internal reflection (FTIR) [36]. Tunnelling increases exponentially with the height of the sample with a homogenous refractive index, calibrated against a known geometry.

The original setup is discussed in more detail in a paper by Dyer [38]. The paper details the best operation on how Guerra used a reflective microscope with an objective lens (NA>1), this lens is in contact with oil which is in contact with a transducer (glass). As the angle of the incoming light is greater than the critical angle in this setup, TIR occurs at the bottom side of the transducer, with none of it extending to the region of air below the glass, only an evanescent wave. When no sample is present, a video camera captures all the reflected photons as a bright light as there is no obstacles in the reflection path. However, when a sample is brought near the transducer, the photons tunnel and no photons are detected at the point of contact whilst looking at the reflection microscope. These images are grey scale intensities, which can be plotted with an oscilloscope to get some 3D images, with x and y being lateral positions and the z being the reflection intensity. With real time imaging and green light, the sensitivity to height of this setup is 1 nm with a lateral resolution of 150 nm [38].

1.1.5 Further Resolution Improvements

Another method to increase the resolution of a microscope is to use an excitation source with shorter wavelengths, making it so that the Abbe limit is no longer a limiting factor.

One way of doing this is to use high energy photons, like X-rays [39] or UV [40], or to use heavier particles with a short de Broglie wavelength.

One common method is to use a scanning electron microscope (SEM), where the excitation source is a beam of electrons scanned over a samples surface. It makes use of the fact that an electron's wavelength is known as the de Broglie wavelength and is dependent on its momentum, with values typically being 0.0867-0.0388 Å at 20-100 kV acceleration voltages [41] (using CODATA values and neglecting relativity). In general, the range of energies of an electron beam is low ($\leq$1 Volt in 100 kV to 300 kV), hence why cold field emission is used for less thermal broadening. An electron microscope can resolve features smaller than 1 nm [42], providing useful nanoscale interrogations of features.

Although the resolution of a SEM provides great interrogative detail of substrates, electron lenses suffer from chromatic and spherical aberrations so they operate at a low NA. Chromatic aberration is where the long wavelength electron's refraction by the magnetic and electrostatic lenses are different than the short wavelength electrons [43], and spherical aberrations, where the electrons passing through the periphery of a lens are refracted more than through the middle [44], causing it not to reach the same focal point decreasing the spatial resolution.

Electron microscopy is especially useful when imaging conducting features, where the electrons are free to move. On insulating materials, a build-up of excess negative charges accumulate on the sample surface. Imaging at low kV $\approx$1 kV can improve charging but still results in artefacts due to different charge state's of different material. and due to the lack of ability for electron flow, it exacerbates the accumulation of charge. Insulating samples can be imaged with limited artefacts with detectors such as operating under low vacuum with a Helix detector using a FEI NovaNano SEM [45]. Whilst using this detector, a small amount of water vapour is ionised by the beam which is then ionised from taking an electron. This negative charge is then discharged by H2O+ ions. Lower accelerating voltages can also be used during SEM operation to reduce charging by decreasing the kinetic energy, thereby preventing the electrons from being embedded within the sample whilst increasing the relative backscattered and secondary electron emission.

The ability of the focused electron beam to raster scan allows for features over a sample to be examined with high resolution. A SEM also offers another important advantage in providing rich contrast. Contrast is a microscope's ability to distinguish the interrogated feature from its adjacent background. A SEM has the ability to obtain topographic and compositional contrast of a specimen, originating respectively from the generated

secondary and backscattered electrons [46]. A SEM provides even more contrast mechanisms, alongside the usual secondary electron and backscattered electron detection, but can also perform auger electron spectroscopy (will be discussed in more detail in the next section), potential measurement's [47], cathodoluminescence [48] and electron beam induced conduction [49], aswell as channeling [50].

Although a SEM provides nanoscale resolution and rich contrast, development of a scanning transmission electron microscope (STEM) enhances these parameters further. A STEM makes use of electrons passing through a thin, damage free sample <50 nm [51]. If the sample is too thick then multiple scattering events take place, so the best resolution is for thin samples. Researchers have worked on the development of STEM and by correcting for the aberrations they have been able to resolve single gold atoms, with a lateral resolution of 50 pm [52].

1.1.6 Spectroscopic Microscopy

Although obtaining dimensional and optical images prove useful with the discussed microscopy techniques, sometimes additional information is required. Spectroscopy is a technical field which pertains to measurement of the electromagnetic spectra obtained from the interaction of electromagnetic radiation (often light) and a specimen, with respect to the frequency or wavelength of the incident radiation. One such technique is known as electron energy loss spectroscopy (EELS). EELS is a form of electron microscopy, whereby a material is exposed to an electron beam with a narrow range of kinetic energy. EELS analyses the inelastic scattering of the incident beam's electrons with the thin sample's electrons [53], producing detailed topographic and spectroscopic maps with high spatial resolution and sensitivity [54], [55]. The spectra obtained from the examination provide detailed information about the chemical and electronic structure of the sample's atoms, their bonding states, band gaps, dielectric constant and much more [56].

Due to the interaction between the interrogating beam and the sample, the beam's electrons lose energy in the region of 0 eV to 3 keV [53]. A homogeneous magnetic field perpendicular to the charged electrons has a dispersive nature, due to Lorentz forces. Their deflection is monitored within an EEL spectrometer, counting the beam's electrons with respect to their energy. The two main regimes involved are core loss, where the loss is greater than 50 eV, this technique obtains information from the beams interaction with deep core states. A low loss regime (<50 eV) provides information on the optical properties of the sample through the excitation of low-lying states above the Fermi energy. The

0 -100 eV region is dominated by Plasmon peaks [57]. Combining this technique alongside TEM or STEM, we can retrieve high spatial and energy resolution images, dependent on the diameter of the probe and spectrometer entrance aperture, with rich contrast, and electronic and elemental analysis of a specimen. If the STEM – EELS system is spherical aberration corrected, then the probe diameter no longer plays a significant part and the spatial resolution is limited the delocalisation of the inelastic electron's scattering [58], with more delocalisation occurring for heavier atoms.

Another technique employed whilst combining microscopy with spectroscopy is Auger Electron Spectroscopy (AES). The first principles defining the technique were discovered by Lise Meitner in 1922-1923 [59], before further discovered again in 1925 by Pierre Auger [60]. Auger witnessed the radiationless decay by electron emission within a cloud chamber, when a monochromatic X-Ray source was incident on noble gas atoms. It should be noted an inner-shell ionised atom can decay radiatively by the emission of X-Ray's [61].

Using an electron gun source, AES provides amazing surface sensitivity as emitted electrons have a short inelastic mean free path within a solid (dozens of Å) or less than 10 Å) in the 20-200 eV energy interval [62]. Therefore, whilst analysing a sample, the escape depth is extremely small and the AES system is extremely surface sensitive with depth resolution of the composition of around 10 Å [63]. One drawback of having such low energy Auger electrons is that if the surface is contaminated by a single atom thick layer of oxide, or another contaminant, that is what will be detected. In order to prevent this happening, the systems are set up with a ultra-high vacuum system (UHV), with pressures lower than 10^{-7} Pa to reduce monolayer adsorption [64]. When the focused electron beam is raster scanned over a sample, the system becomes a Scanning Auger Microscope (SAM) technique where the intensity of the Auger peak is measured against the background scattered electrons and mapped. Within SAM the lateral resolution and shallow depth at which elemental composition is superior to that of other non-destructive methods. With new generation Auger probes providing high lateral resolution ($\approx$10 nm), depth ($\approx$2 nm) and $\approx$0.1% energy resolutions[65].

Although EELS provides information on the optical properties of a sample, the sample must be thin making it difficult to handle or fabricate. AES must use a UHV chamber and provides only surface information. If we want to use a thicker material and examine more than the surface chemistry without the need for a UHV, another technique known as photoluminescence (PL) spectroscopy can be used to determine the band gap of a material [66].

PL is the phenomena seen whereby the spontaneous emission of a photon occurs

through an electron relaxing from a higher energy state. PL is a two-step process in direct band semiconductors, whereby enough energy from the incoming photon promotes the samples electron to an excited state. If the excitation photons have energies larger than the band gap of the interrogated substrate, an electron is excited to the higher state which leaves behind a hole in the valence band [67]. Due to the molecular vibrations with the environment, a large thermal loss is seen, where the electron and hole lose both energy and momentum until they reach the conduction band or the valence band, respectively.

In materials which have a large binding energy, an exciton (bound state of an electron and hole pair) is formed, with the electron relaxing into a lower state through spontaneous emission. PL spectra can provide details on the optical band gap of a material, which differs from the electronic band gap by the exciton binding energy. With standard PL spectroscopy, the fluorescence signal emitted from the sample is dispersed with the use of a grating monochromator with the spectrum imaged onto a CCD camera. The typical setup can give a spectral resolution of around 100 GHz, or 0.1 meV, within the visible spectrum [68].

A similar arrangement is used to acquire Raman spectra. The main difference with Raman is that the Raman signals are collected very close to the pump, so a spectrometer with a very good rejection of nearby light is needed e.g. using multiple gratings and apertures in series or using a holographic notch or Raman edge filter.

Raman spectroscopy is a non-destructive metrological technique, whereby a signal containing information on the chemical identity and structure of a material is obtained [69]. This signal takes the form of a spectrum of the vibrational states of the chemical bonds of a sample. The spectrum also provides insight into the phase and polymorphism [70], intrinsic stress/strain [71] and the contamination/impurities of the sample. The data is then compared against a library of known materials to determine which analyte/analytes are within the sample. This information is extracted from the spectral peaks showing the intensity and wavelength position of the Raman scattered light. However, in order to obtain a Raman spectrum, an inelastic scattering of incident photons, known as Raman scattering, is required [72]. An energy diagram depicting Raman and PL spectroscopy is shown in Figure 1.4.

1.1.7 Scanning Microscopy

As the contrast, magnification and resolution on differing microscope techniques improve, point-by-point measurements can become practical. A scanning technique is now

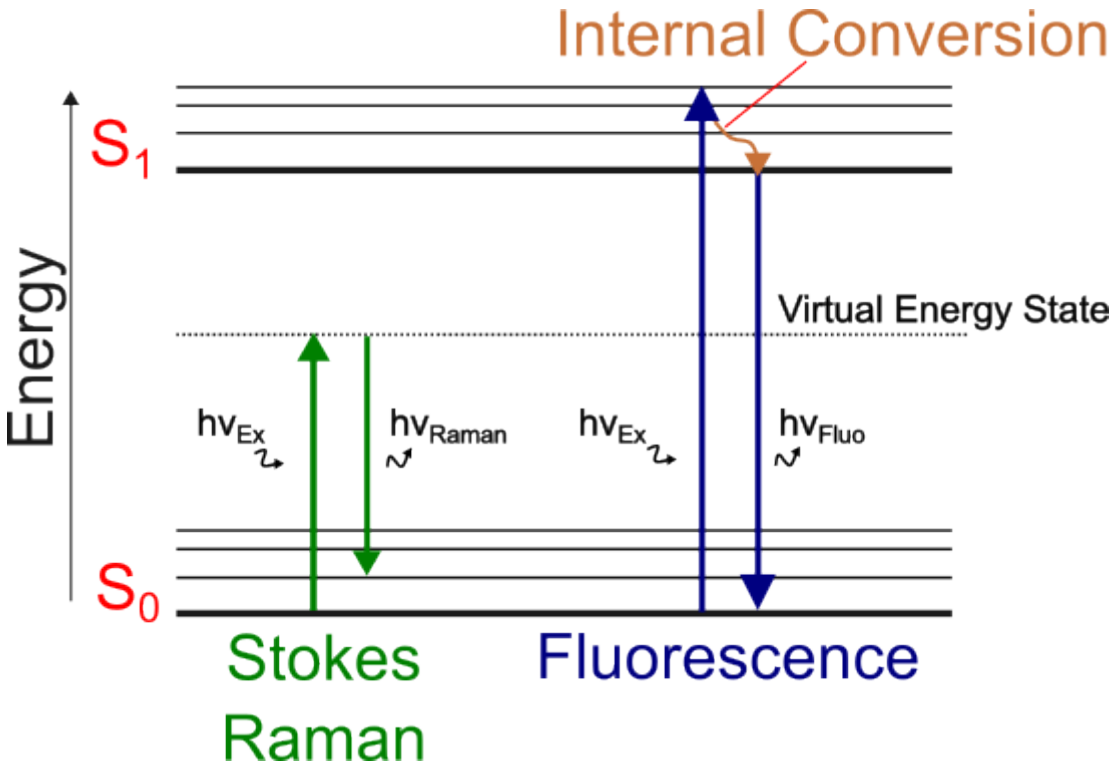

FIGURE 1.4: Jablonski diagram showing the difference between the energy levels of Stokes Raman Scattering and Fluorescence. The fluorescence shows the spin state of an electron which relaxes back into the ground state and emits a photon.

often used, whereby beam scanning or object scanning can paint a larger picture of a sample surface, like that discussed with a SEM and STEM.

One such technique is to take the optical microscopy system and either beam scan or object scan relative to the objective lens. The beam can be scanned with the use of rotating mirrors, or using acousto-optic devices [73]. More common devices utilise a mechanical stage which moves to generate the full image, producing a spatially invariant image over the entire scanned area, leading to images with better contrast enhancement with digital processing [74].

One such technique to employ the developed scanning optical technique is confocal microscopy. This technique was invented by Marvin Minsky in 1955 [75], with the primary aim of generating a point source of light and rejecting out-of-focus light by using a spatial pinhole. The diameter of the pinhole is inversely proportional to the NA of the objective and proportional to the magnification between the pinhole plane and sample, as well as the excitation wavelength [76]. The confocal microscope makes use of the illumination and detection optics being focused onto the same diffraction limited point,

where the different sections of the sample are interrogated at this region and build its image onto a photomultiplier detector or camera. During operation there is a broad beam of light constantly flooding the sample, but as it is not within the focal plane, it is spatially filtered and does not contribute much (if anything) to the resulting image [77].

The type of confocal microscopy can be further classified by how it scans. A common method is laser scanning confocal microscopy (CLSM), whereby a laser is scanned across the sample. The laser is targeted onto a pair of scanning mirrors whereby the beam is swept incrementally in the x and y direction of a single field of view to produce an optical section though the fixed pinhole and detector. A 3-D image can be reconstructed with this method by changing the focal point and scanning, then repeating this over until all optical sections of the sample are imaged [78]. When the optimal parameters and setup is used, confocal laser scanning microscopy may reach 180 nm of lateral resolution and 500 nm of axial resolution [79]. However, spherical aberration caused by refractive index mismatches causes the axial resolution to be impaired. A diagram of a confocal microscopy setup is shown in Figure 1.5.

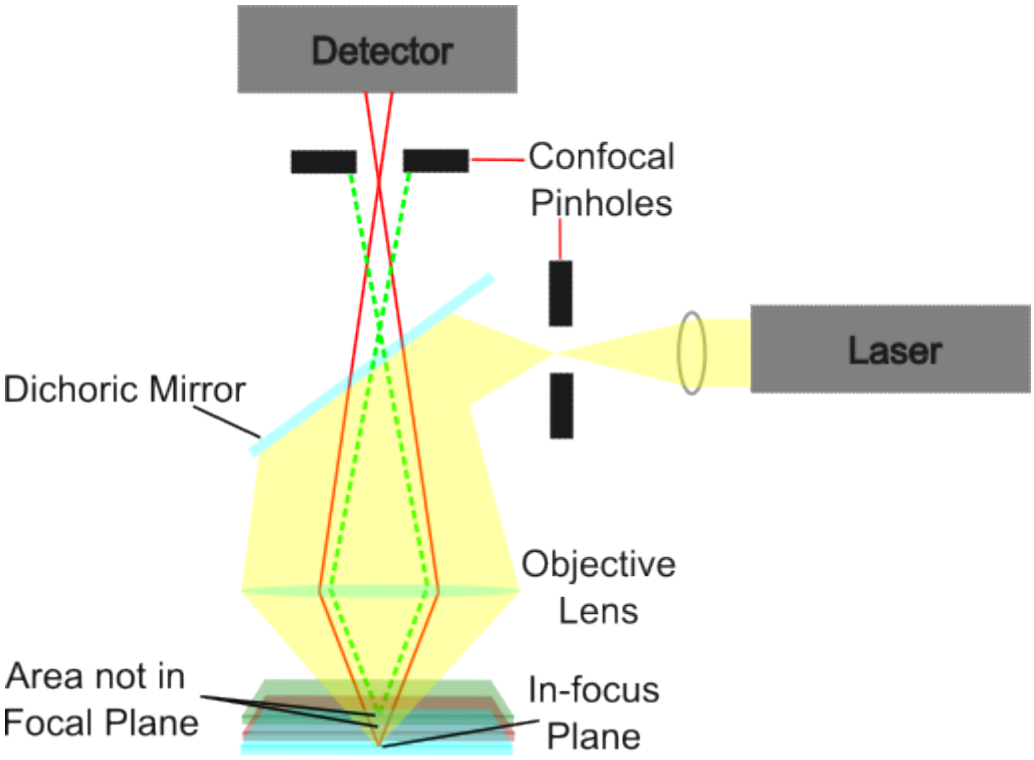

FIGURE 1.5: Schematic diagram of an confocal microscopy setup with the red line showing the in-plane focus on the blue sample, with the dashed green line depicting where the spatial filtering occurs due to out-of plane focusing on the sample.

Confocal microscopy can be utilised for its resolution and provide more contrast and

insight into cellular dynamics. The microscopy technique is also used in another technique known as Fluorescence recovery after photobleaching (FRAP). FRAP is a method developed in the 1970's for determining the kinetics of molecular diffusion through tissues or cells with a reasonably easy setup [80]. The apparatus comprises of fluorescent molecules and a confocal optical microscope. In this setup, fluorescent molecules are irreversibly photobleached by focusing a high intensity laser onto the region of interest. If this is successful and the molecules are mobile, the targeted area will lose all fluorescence and be exchanged with fluorescently tagged molecules surrounding this region [81]. This process is monitored, plotting the recovery of fluorescent intensity in the targeted area, whether it is diffusive (passive) or active, with the fraction of molecules that are mobile and the half time of recovery. The half time of recovery is a measure of the speed of the molecule within the cell which can be useful in the study of proteins in whether they are bound or free [82]. Within this system the resolution is limited as multiple channels must be imaged within the recovery time.

Confocal microscopy can also be combined with spectroscopic techniques such as Raman. A confocal Raman setup takes the benefits of a confocal microscope, in that optical information from light collected out of the focal plane is rejected and optical and spectroscopic information through a confocal pinhole is collected, whilst revealing spectroscopic information of the substrate with a Raman spectrometer. In a confocal Raman setup, after the excitation light crosses through the confocal pinhole and a concave mirror, it will reach the spectrometer where the incident light is separated by a grating. The grating within the spectrometer contains a periodic array of grooves on a reflective surface, where when the incident light constructively or destructively interferes with it, depending on the wavelength of the light. This means that the collected light is reflected off the spectrometer surface at varying angles. This wavelength-dispersed light is then projected onto a photodetector, typically a CCD device, which contains a pixel array. This array is divided into a sub array of pixels, where at each pixel a range of incident photon frequencies is converted into one or more electrons which are proportional to the number of absorbed photons. The spectral resolution of a confocal Raman setup is determined by the width and density of the grating, spectrometer focal length, entrance slit width, wavelength of incident light and the size of the pixels on the detector. 1 cm^{-1} is generally acceptable for most Raman spectroscopy applications [83]. A diagram of a confocal Raman setup is shown in Figure 1.6.

As with traditional optical (light) microscopy and scanning electron microscopy, we can also use different wavelength or frequency sources to interrogate materials. Scanning acoustic microscopy (SAM) is one such technique in which a transducer, mounted on

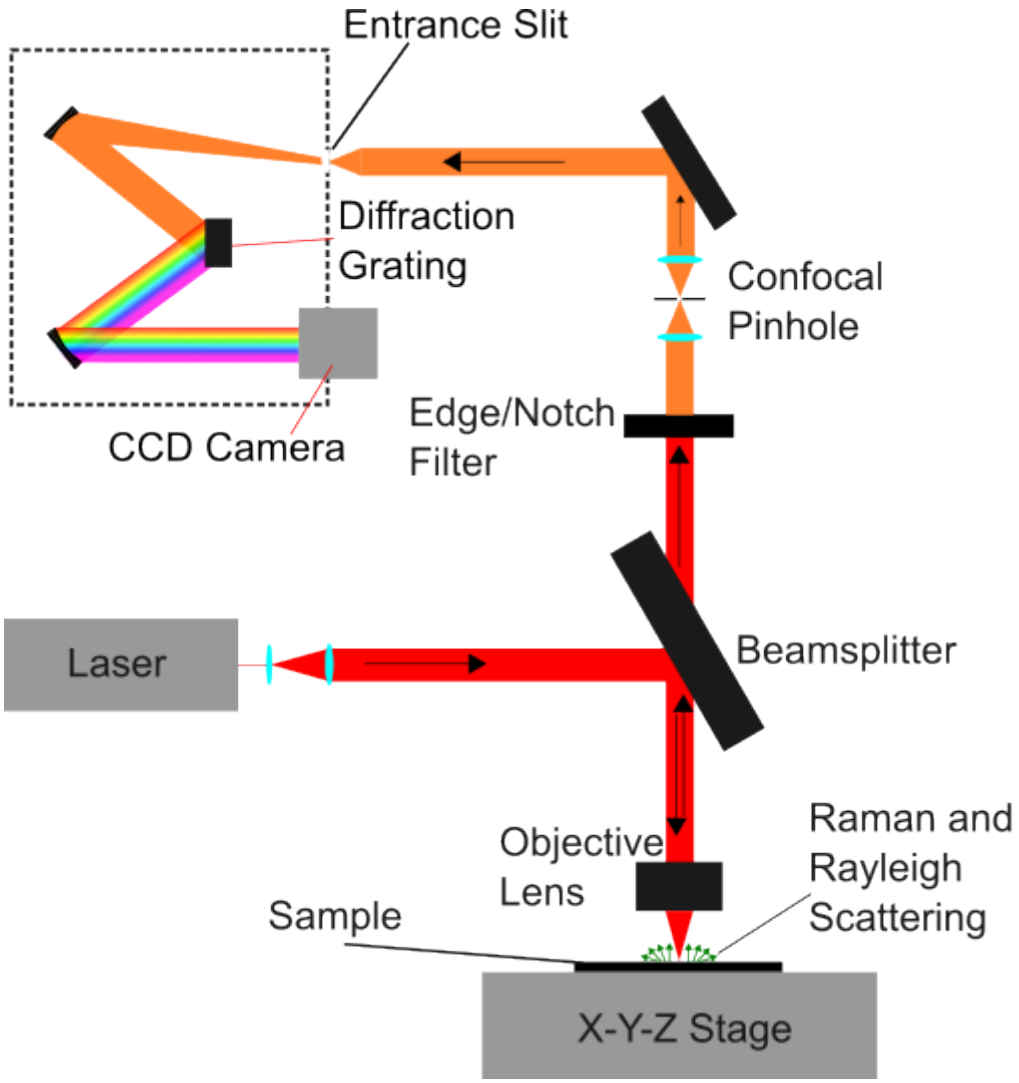

FIGURE 1.6: Schematic diagram of an confocal Raman microscopy setup.

an acoustic lens, emits ultrasonic waves (>10MHz) to detect defects in a wide variety of materials. It does so by monitoring the internal features layer by layer due to the waves high penetrative power [84]. As the wave propagates through the interrogated sample, it can be scattered, absorbed, reflected, or transmitted depending on the acoustic impedance, where the echo is detected by the transducer.

The transducer in the SAM technique is raster scanned over the sample surface, collecting the echo at each spatial coordinate with the depth information retrieved from the signals time-of-flight. The main limitation of this technique is the frequency used, as it reduces the ultrasonic pulses get longer, however the absorption and scattering decreases. The typical spatial resolution of this system is around 10 μm [85], [86], with the acoustic images describing the elastic properties of the material through its acoustic impedance

[87].

Scanning X-ray microscopy (SXRM), like optical microscopy relies on the wavelength of the interrogating beam to resolve sample surfaces. The resolution of SXRM is roughly five times better than visible light microscopy, with the top of the line being around 20-30 nm (wavelength limited) [39]. An X-rays photon energy can be classified into two regimes, with hard-X-ray photons having an energy greater than 4 keV [39], or the more typical soft X-ray photon energies being around 100-1000 eV [88]. Both hard and soft x-rays give amplitude/phase and X-ray absorption near edge structure contrast. Whilst scanning, the SXRM typically uses focusing optics to form a focused spot, or microprobe, onto a raster scanned specimen. The consequent image contrast comes from the different absorption of X-rays of the different examined materials and recorded onto photographic film, or a sensor such as a CCD camera [89].

When the focusing optics consist of Fresnel zone plates (circular gratings with radially increasing line densities), the light will diffract around the opaque zones. The spacing between the diffracted zones allow the diffracted light to interfere constructively at the desired focus zone. The Fresnel zone plates have been shown to work with hard X-rays, producing fine focal spots of 7.8 nm FWHM for 9 keV photons [90]. Compared to other techniques such as TEM, X-ray microscopy can use thicker samples with hard X-rays transmitting through tissue areas up to 40-60 μm thick [91], and does not need any sample preparation or a high-vacuum chamber.

1.1.8 Scanning Probe Microscopy

Much like other microscopic techniques, such as the FEM or FIM, a further increase in resolution can be achieved whilst using a tip. To gain a large overview of a sample surface and gain better contrast to the material, we can mechanically scan with a tip. One of the first such tools that mechanically scans a tip to map the microtopography of metallic surfaces was the topografiner [92]. Young et al. published their paper on the use of the topografiner in 1972, where it uses a field emission current to compute the distance between the instruments tip and the sample. The topografiner is advantageous as due to its non-contact technique of topographic mapping, reducing the mechanical damage to the sample surface during a scan to nil, unless accidental contact is made. The topografiner also has a long tip and a wide scan range, but is noise limited due to field emission currents being very noisy due to surface contamination, making it almost impossible to operate in atmospheric conditions [93]. The topografiner setup has been documented in a

2013 conference proceeding to retrieve almost a nanometre lateral spatial resolution [94]. The technique required the use of a polycrystalline tungsten tip, with a tip-sample distance of 5-40 nm within a UHV chamber. The tip was biased with a voltage of -20 and -110V with respect to the anode, allowing primary electrons to be emitted from the tip. It was then scanned parallel to the surface of the sample, with the scattered primary electrons generating secondary electrons. Through monitoring the secondary electrons, the electron current is measured to give details on what the sample topography is like and provide rich contrast mapping of it.

The topografiner never broke through as a common tool, with very few papers on it's use, due to the success of scanning tunnelling microscopy (STM). Scanning tunnelling microscopy also makes use of the mechanical scanning of a sharp tip and has no need for the use of light or electron beams, it is basically the topografiner at low voltage. It was first brought to the attention of the world in 1981 by two IBM scientists named Gerd Binnig and Heinrich Rohrer, with the success of that and Ernst Ruska for the invention of the SEM, winning them the Nobel Prize in Physics in 1986 [95]. STM was developed after the first scanning probe microscopy imaging mode (the topografiner), but as stated earlier, the use of which isn't well documented due to the ultra-high-resolution capability of STM (0.1 nm lateral and 0.01 nm depth resolution) [96]. STM works by scanning a sharp conductive probe close to the surface (around 4-7 Å) [97] of a conductive sample, with a voltage applied between them to cause a tunnelling current to flow. As the tunnelling current varies exponentially with the separation distance(d) as $I \propto e^{-2kd}$ [95] and k is the decay constant, the atoms closest to the tip produce most of the overall tunnelling current. Within vacuum tunnelling at a typical work function of 4 eV, the decay constant k takes a value of roughly 1Å^{-1} for the majority of metals. This means that as the tip sample distance increases by 1 Å, the current decreases by an order of magnitude [98].

An STM typically works in two modes, constant height and constant current mode. During constant height mode, the tip scans at a constant height above the sample surface with the sample roughness causing the tunnelling current to change. This mode is only possible for smooth samples [95]. Constant current mode utilises a feedback loop, continuously manipulating the height of either the tip or the sample to ensure that the current stays constant. This mode can be used on samples with a less planar topography, but the input from the feedback system can be slow making for longer scans. STM provided a method of obtaining novel contrast to the scanning probe microscopy family whilst offering high resolution. The STM is highly sensitive to the the density of states of a sample, hence imaging semiconductors and superconductors are possible. This technique is however limited to imaging conductors as it has a high density of electronic states at the

Fermi level, facilitating a tunneling current. only A schematic diagram of a STM system is shown in Figure 1.7.

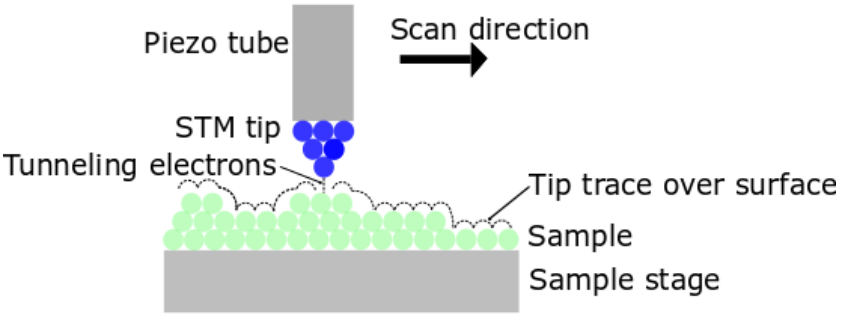

FIGURE 1.7: Schematic diagram of a STM system.

1.1.9 Tips

In the microscopic techniques described, we have seen better spatial resolution obtained by changing the optics and wavelength. Utilising different spectroscopic techniques to obtain more detailed information contrast on a specimen. Instead of relying on the varying the wavelength or lenses, the sample's sharpness can be utilised to also retrieve high resolution microscopy images. One of the first ways of achieving near atomic resolution was invented by Erwin Muller in 1936 [99] known as Field Emission Microscopy (FEM). FEM typically employs a screen within a UHV chamber and a sharp metallic tip. The tips are made with a high melting point and strong metal such as tungsten [100]. The reason the metals must be strong and have a high melting point is the high electric field seen during FEM causes an exertion of mechanical stress on the tip, with large temperatures also seen. Such measurements can image local variations in work function.

In a paper published in 2022, Yanagisawa et al. [100] induced field emission by holding a metallic mesh (covering a phosphor screen) at ground, with a 250-350 nm radius tungsten tip negatively biased. A high voltage was applied between the tip and mesh, with large electric fields concentrated at the tip apex. These electric fields cause radial electron emission from the solid to the vacuum, with a 2-D detector mapping the electrons onto a macroscopic screen. The spatial resolution of this setup is said to be around 1-2 nm [100] with relatively low vibration, however only molecules that can withstand a high electric field can be imaged.

Erwin Muller continued on with his progresses within microscopy and by 1951 had invented the field ion microscope (FIM) [101], with the first recorded observations of individual atoms published using this technique in 1955 [102]. FIM has similarities to the FEM in that a sharp tip is used alongside a fluorescent screen, however with FIM the potential held at the tip is positive and a gas is pumped into the chamber. The high electric field at the tip due to its small radius causes the outer electrons of the gas to be stripped away, forming ions. Any positive ions are repelled from the tip and accelerated towards the fluorescent screen where the images of the surface are magnified by the curvature of the electric field around the tip. As tightly packed atoms, as opposed to single atoms on a surface, have a weaker field for ionisation, the surface of the tip can be mapped as a function of the electric field. For instance, single atoms poking through the arranged surface would generate a larger field signal due to ionising the chambers gas more frequently [63]. The results of the ionisation of the gas and tip atomic arrangement give us information about the atomic structure of the tips, however producing black and white images only on refractory metals which can withstand high electric fields without desorption. A schematic diagram depicting the operation of a FIM is shown in Figure 1.8.

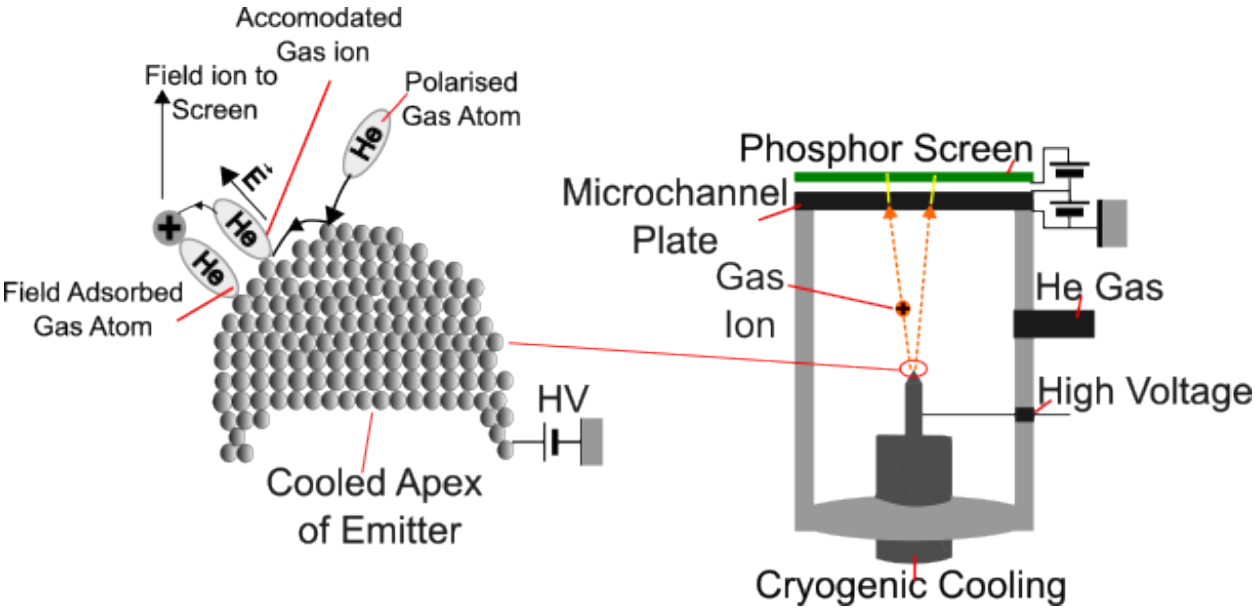

FIGURE 1.8: Schematic diagram of the electron emitter tip and working principle of the field ion microscope. The surface of the apex is projected onto the phosphor screen by gas ions. The imaging gas ions are created over the surface atoms covered by field-adsorbed gas atoms, the field-ionized atoms are replaced by accommodating gas atoms.

The FIM provides useful information in determining the atomic structure of dislocation and grain boundaries, and more recently some highly accurate 3D crystal lattice reconstructions of Tungsten [103]. The downfall of this technique are the images provide

little to no chemical information of the interrogated materials. Erwin Muller saw this as an opportunity and introduced the world to the atom probe in 1967. The atom probe consisted of a FIM with a single particle detection capability time-of-flight mass spectrometer [104].

The atom probe functions by make use of the field-induced removal of an atom from it's own lattice (field evaporation), as an effect of the induced polarisation of surface atoms due to the intense electric field. As the field grows sufficiently large, an atom is pulled away from the samples surface leaving behind an electron which is drained into it (ionisation). The ion is then accelerated away from the surface by the electric field towards a detector (electron multiplier tube in Muller's case), lowering the ionic potential [105]. In this case the tube was placed behind a small hole in the FIM screen, where the atomic site to be interrogated is selected through the hole and ions fed into the spectrometer, where their mass-to-charge ratio is computed. The spectrometer feeds back the information of what species is being imaged as well as a reconstruction of the imaging sites geometry.

Whilst Muller predicted the atom probe would be useful in the study of alloys and the chemical nature of precipitates [104], pulsed laser applications have been introduced (as opposed to high voltage pulses) to induce field evaporation [106]. This improves on the mass resolution compared to the energy spread caused by voltage pulsing, and no longer requires a conductor (metal), opening up the species in which can be imaged [106], importantly to include semiconductors [107] and superconductors [108].

1.1.9.1 Tip Fabrication

As the tip radius of these materials get smaller to gain atomic resolution (less than 15 nm for some atom probes [109]), it becomes necessary to use nano and microfabrication techniques to build these geometrically small parts. One such technique to fabricate atom tips is using an electropolishing technique. Electropolishing has been developed for sharpening non-porous metallic samples, where a small blank (small diameter wire) [110] is started with to reduce potential polishing times. The first step is to take these blanks and to them grind the surface to smoothen it out, compensating for non-uniformities whilst ensuring little heat and stress is applied onto the material surface. It is also important there is no polishing inhibitors like oxide films or contamination, so removal of these films is necessary [111].

A common electropolishing technique is known as the double-layer technique. This technique makes use of an electrolyte floated onto a dense, chemically inert, immiscible liquid [111] with a counter electrode, made of a noble metal, nearby. A DC power supply provides a voltage between the blank sample and the counter electrode, with the specimen acting as an anode. As the current flows from cathode to anode, an electrochemical reaction occurs whereby the metallic sample (anode) dissolves into the electrolyte. A reduction reaction is formed in response at the cathode, where hydrogen generation is usually seen [105]. When the appropriate temperature and voltage are used, the lumped and protruding parts should dissolve faster, with the reaction products above the receded areas forming a viscous resistive layer allowing for the gradual smoothing of the surface. In samples like tungsten [111], where a layer of the reaction products is formed, an AC current is applied whereby the frequency, with respect to applied voltage, can adjust the polishing conditions.

As the analyte gradually etches away material from the centre of the specimen, it starts to form a necked geometry. As the necked geometry at the air/electrolyte interface gets gradually thinner, the mass of the bottom half becomes too large and the tensile force causes the blank to fracture, leaving behind a needle like shape [111].

Direct chemical etching of a metal blank can also be used in a process known as chemical etching. This relies on the material being placed directly into a chemical bath and allowing the chemicals to etch away the material. This is however less common with less control over the etch rates and hence finish, but more useful on gaining a better finish on already needled semiconductor atom probe tips [112].

A well-used and documented technique of making tips suitable for the techniques Muller pioneered is annular focused ion beam (FIB) milling. FIB milling is a destructive technique, which uses a FIB to bombard a chosen surface with ions (often Gallium [113]–[115]) to cause atom sputtering of the targeted surface. It is very useful to directly pattern substrates, however, to make more conical features, like that of atom probe tips, annular milling can be performed. This technique utilises an annular (ring shaped) scan with a diameter larger than the specimen. The ion beam is orientated directly is above sub-10 μm diameter wires, fibres and electropolished needles [116], [117], which are mounted in a copper tube [116]. Whilst concentrically exposing the material, the focused beam's current is gradually decreased with decreasing inner and outer diameters to reveal the final sharp tip with a radius of around 50-150 nm. It becomes particularly useful when milling down wedge-shape electropolished or blunt specimens [116], [118], [119], where electropolishing rates change with different phases.

The tips of the probes can be simply grown on as well. In 2006, Perea et al. patterned a GaAs(111) wafer with EBL and a Au lift off procedure, creating Au catalyst discs. InAs nanowires were then grown, using the Au as a seed in a quartz metal-organic vapor-phase epitaxy (MOVPE) chamber. These long nanowires were then used within a local electrode atom probe microscope, mapping the individual Au atoms within the InAs wire and to map the interface between the catalyst and the nanowire with 0.3 nm resolution in 3 dimensions [120].

1.1.10 Atomic Force Microscopy

Considering the drawbacks of STM, Binnig, Quate, Gerber and Weibel went on to introduce the Atomic Force Microscope (AFM) in 1986 [121]. An AFM system can operate on various types of samples such as conductors, non-conductors and within various mediums such as air, vacuum and water, with atomic scale resolution being achieved [122]. This flexibility is regarded as a major advantage compared to the STM system.

In an AFM system, a micron-scale cantilever with a micro-or nano-fabricated tip is scanned in close proximity to the sample surface. The deflections of the cantilever are measured and the z-axis positional information sent to a feedback controller. The controller then adjusts the z-position of the cantilever to prevent tip damage through abrasion on the sample surface. The x and y positions of the sample are scanned until interrogation of the region of interest is finished. In commercial AFM systems the common method for measuring the deflection is the optical lever method. The optical lever method first published results with atomic scale resolution in 1990 by Rugar and Hansma [123], testing it out on both conductors and insulators. A schematic diagram of an AFM with the optical lever method is shown in Figure 1.9.

The optical lever method is relatively inexpensive to set up and requires a small mirror fabricated onto the probe cantilever. In this configuration, a laser beam is directed onto the cantilever's mirror and is reflected onto a position sensitive photodetector (PSD) where voltage is a function of displacement. Referring to the PSD in Figure 1.9, the following signals may be developed:

$$\frac{(A+B)-(C+D)}{ABCD} = Vertical\ deflection \tag{1.9}$$

$$\frac{(A+C)-(B+D)}{ABCD} = Horizontal\ deflection \tag{1.10}$$

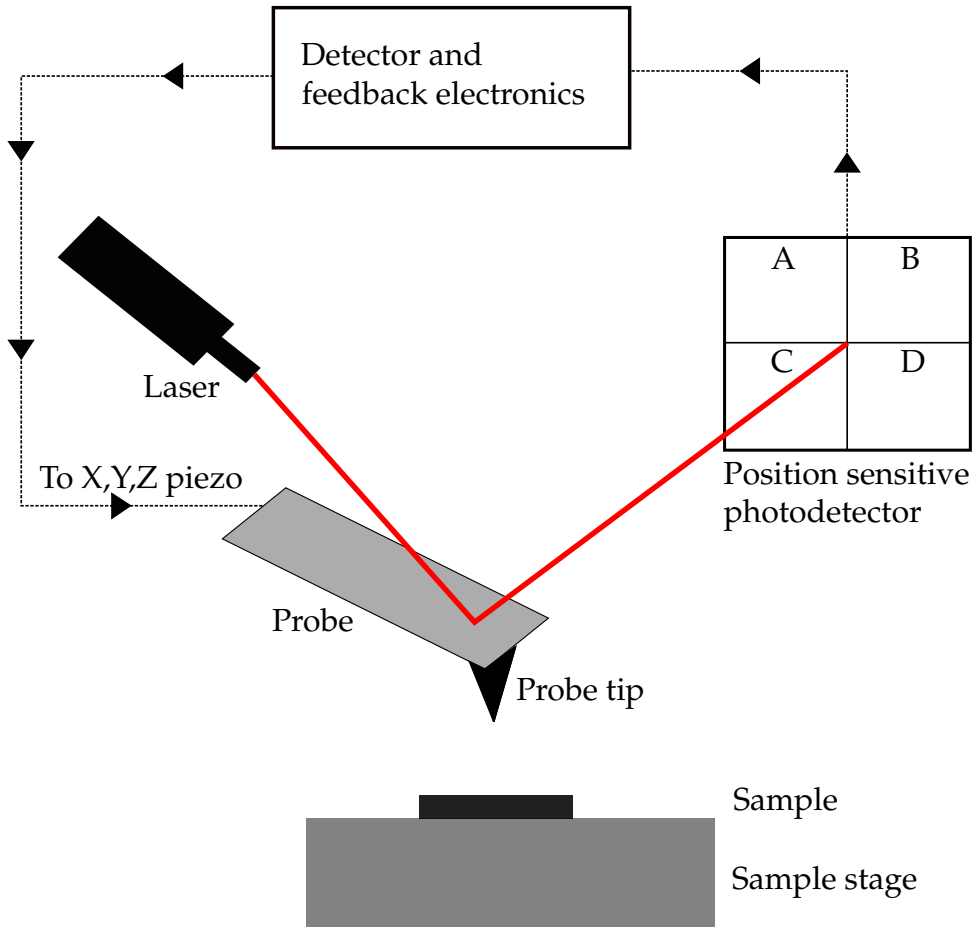

FIGURE 1.9: Schematic diagram of an optical lever AFM system.

As the cantilever deflects, the reflection of the laser beam changes and so the position on the PSD changes. Therefore, the cantilever's deflection is proportional to the measured voltage and can be calibrated from a measured sensitivity value [124], the inverse optical lever sensitivity [125], or by using a small mechanical lever as developed by Xie in 2008 [126]. Using these methods of calibration can be time consuming. The simplest way of determining the interactive forces is if the spring constant of the cantilever is known, the measured forces then follow Hooke's law.

$$F = k\Delta X \tag{1.11}$$

Where F is the applied force (N), k is the spring constant(N/m) and ΔX is the change in deflection of the cantilever from its original position(m). In order to achieve maximum force sensitivity the cantilever must be as soft as possible. However, within most AFM systems vibration noise is a limiting factor i.e. thermal noise, the Brownian motion of the

cantilver [127]. In order to reduce the noise, the spring must be stiff with a resonant frequency between 10-100kHz, all dependent on cantilever dimensions [128]. A compromise must be made during probe fabrication to ensure good force sensitivity and low noise.

AFM is used within many scientific fields as a means of quantification. Although many of the experiments in those fields do not require atomic resolution, it's ability to do so has aided advancements in research. In 2009, Gross *et al.* used an AFM to retrieve images of single atoms within an adsorbed molecule with atomic resolution [122]. Guedes *et al.* used an AFM in 2016 to evaluate the risk of cardiovascular diseases within humans, monitoring the binding force of erythrocytes and fibrinogen. They found that patients with a larger binding force were more likely to be admitted into hospital with cardiovascular complications [129].

1.1.10.1 Modes of Operation

As well as being able to operate within different media an AFM has 3 main modes of operation, each useful for different purposes. In contact mode, the tip of the probe is in direct contact with the samples surface at all times. Contact is maintained through either monitoring the beam deflection, or more commonly, a control system whereby a feedback loop corrects the z-position of the cantilever. Damage to the sample and tip is expected through constant contact, which is known produce one of the many topographic artifacts [130] on an image. When the sample is left in ambient conditions, a liquid meniscus layer may form between the tip and sample. The capillary force gives rise to an attractive force which pulls the tip into the sample, making it hard for the tip to be retracted.

As contact mode may damage the sample and the tip, it is often not the mode of operation for a delicate sample. An alternative to contact mode is tapping mode. Within tapping mode the cantilever oscillates at its resonant frequency, or often, just off resonance if amplitude of oscillation is the measurand, near resonance if by phase. The tip then repeatedly comes in and out of contact with the sample during a scan. During the tip-sample interaction the resonant frequency, amplitude and phase of the cantilever changes with respect to the cantilever-sample distance. Using a feedback controller, the cantilever's sample distance is controlled by either keeping the amplitude or phase of the oscillating cantilever constant. As an example, as the tip touches the sample, the cantilever's oscillation amplitude decreases due to a restricted range of motion. Taking into account a set point, where the amplitude is known, the feedback loop adjusts the tip-sample distance to ensure a constant amplitude. The position of the tip is recorded as a function of the tip's lateral position with respect to the sample, where the scanned height represents the

sample's surface topography. Tapping mode has been shown to reduce damaging lateral forces and was pioneered by Zhong *et al.* in 1993 [131]. A schematic diagram of an AFM probe in tapping mode is shown in Figure 1.10 , whereby the "free" amplitude and the reduced amplitude are shown.

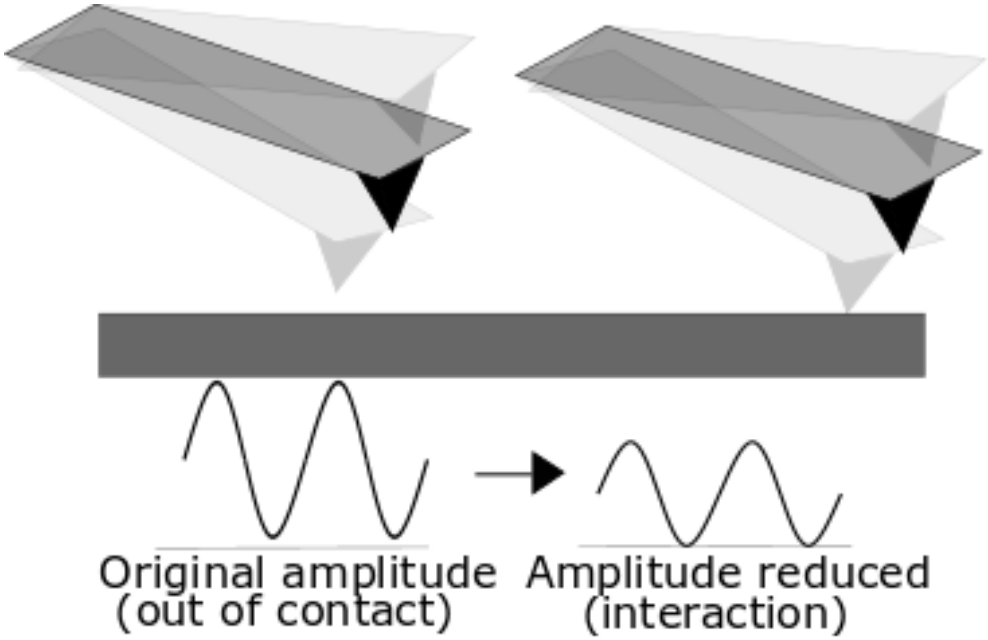

FIGURE 1.10: Schematic diagram of the amplitude response to a tapping mode experiment.

The final mode of operation is non-contact mode. Non-contact mode can be used when the sample is delicate and the tip would cause irreparable damage. Within this mode the tip is kept at a distance of roughly 5-15 nm from the sample [132]. A small oscillation is applied to the cantilever, monitoring a change in amplitude, frequency or phase of the cantilever in response to the force gradients on the sample. There are two main forces whilst scanning, the attractive Van der Waals force and a static electric repulsive force, both between atoms a short distance apart. There are also capillary, electrostatic and magnetic forces within the attractive regime. The force between the tip and sample in the repulsive regime is due to reduced screening of the nuclei from the displacement of electrons. As the distance of the atoms on the probe tip and atoms on the surface is reduced, the repulsive force becomes more dominant and force changes with growing distance [133]. A schematic diagram of a typical force-distance curve of an AFM tip landing on a surface is shown in Figure 1.11. The probe is raster scanned over the substrate, recording the force as a function of position. A feedback loop is used to maintain a fixed separation distance.

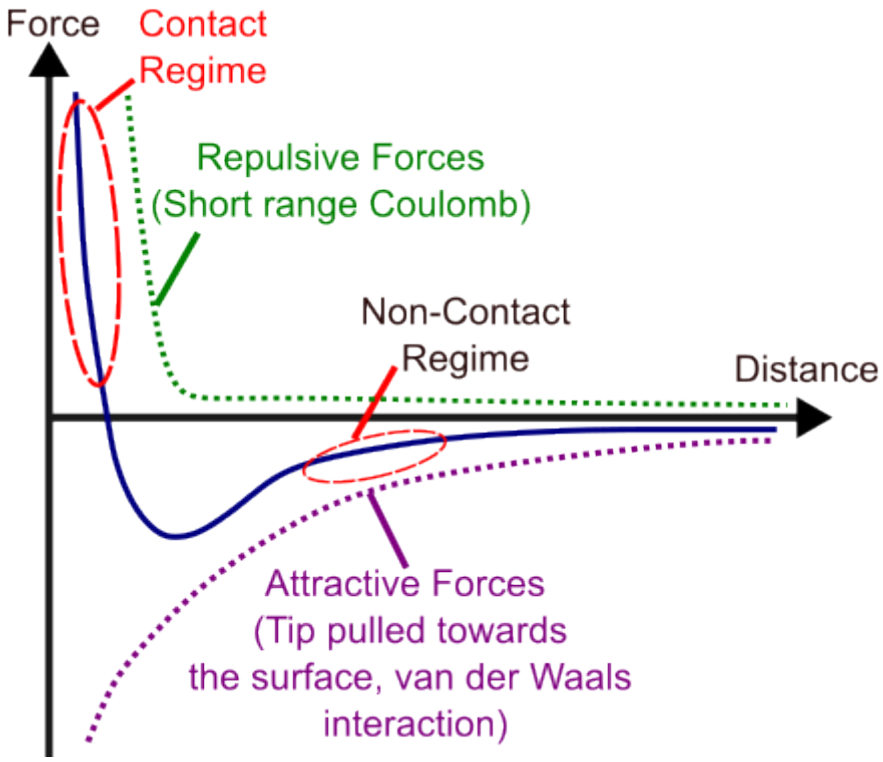

FIGURE 1.11: Force distance curve of the interactions between the tip and surface during an AFM scan.

1.1.10.2 Sensor Integration

Just like in scanning electron or optical microscopy, we can also integrate more sensors onto the measuring device as well as change the physics of the measurement to retrieve more physical characteristics of a sample in SPM. One method is known as scanning capacitance microscopy (SCM). SCM is used to measure the spatial capacitance variations on semiconductors, whilst using a conductive coated tip, with Pt/Ir coatings being widely used [134]–[136]. The tip is scanned and can generate a map of the local carrier concentration [137] and doping-profiles of non-uniformly doped insulation coated samples [138]. The capacitance/voltage data retrieved from the scans must be converted into the concentration of the dopants via a model [139]. This is important because how the dopants are concentrated and localised, influences the electrical characteristics of a semiconductor sample, which becomes increasingly difficult to measure as the dimensions shrink. Commercial SCM probes are known to observe capacitance changes of 10^{-21} F, with a resolution of 10-20 nm [139].

Another scanning probe technique, with leading nano-characterisation probes developed with the University of Glasgow's AFM group, is Scanning Thermal Microscopy

(SThM). SThM makes use of thermocouples or resistance temperature detectors (RTD) fabricated onto AFM probes. The probes allow for the spatial mapping of a substrate's temperature or thermal conductivity. This is determined through monitoring the voltage changes of the probe as it conducts heat in active mode, or monitoring the tips resistance changes as the tip contacts a heated substrate in passive mode [140]. As the tips are scanned, topographic and thermal maps of the sample surface are resolved with a resolution of roughly 50 nm [141]. As different materials and thicknesses have different thermal conduction properties, the output of the scans provide a unique thermal contrast at high resolution.

Scanning probe's resolution don't have to be limited to solid films, the substrates can be immersed in fluid as in the case of scanning electrochemical microscopy (SECM). Scanning electrochemical microscopy (SECM) is an electroanalytical scanning probe technique used to measure the electrochemical behaviour of liquid/liquid [142], liquid/gas and liquid/solid interfaces. When the sensor is combined with AFM, simultaneous imaging of a substrate's topography and surface reactivity can be mapped. During an SECM scan, current flows through an ultramicroelectrode (UME) fabricated onto the probe's apex. The UME is fabricated to a nm or μm scale and of various geometries such as a disk, ring or sphere. The probe's tip is placed in close proximity to a conductive, semiconductive or insulating substrate which is immersed in a solution. The tip and substrate are part of a four-electrode electrochemical cell, with a bipotentiostat to control the potential and current at both the tip and the substrate. Spatially resolved electrochemical signals are retrieved by measuring the current at the SECM probe's tip, resolved as a function of tip position. The SECM signal is analysed based on the diffusion-limited current phenomena [143]. After the scan, the information is compiled to make images of surface reactivity, chemical kinetics and topography. A schematic diagram of a SECM system is shown in Figure A.1.

As scanning probe microscopy develops, just like traditional microscopic techniques, researchers build the microscopes and develop techniques to resolve the chemical and physical characteristics of interest. It is clear to see as components get smaller for better efficiency, the development of these techniques is critical in offering an insight into what is going on. As the technology for Raman Spectroscopy is of great interest, and the scanning probe technique offers great resolution and contrast over widespread areas, the focus of this work is the development of scanning probes which can enhance a Raman spectroscopy signal. The benefit of this archetype is that it can generate rich contrast, whilst retrieving topographic maps of a sample's surface, plotting the chemical species alongside its surface profile.

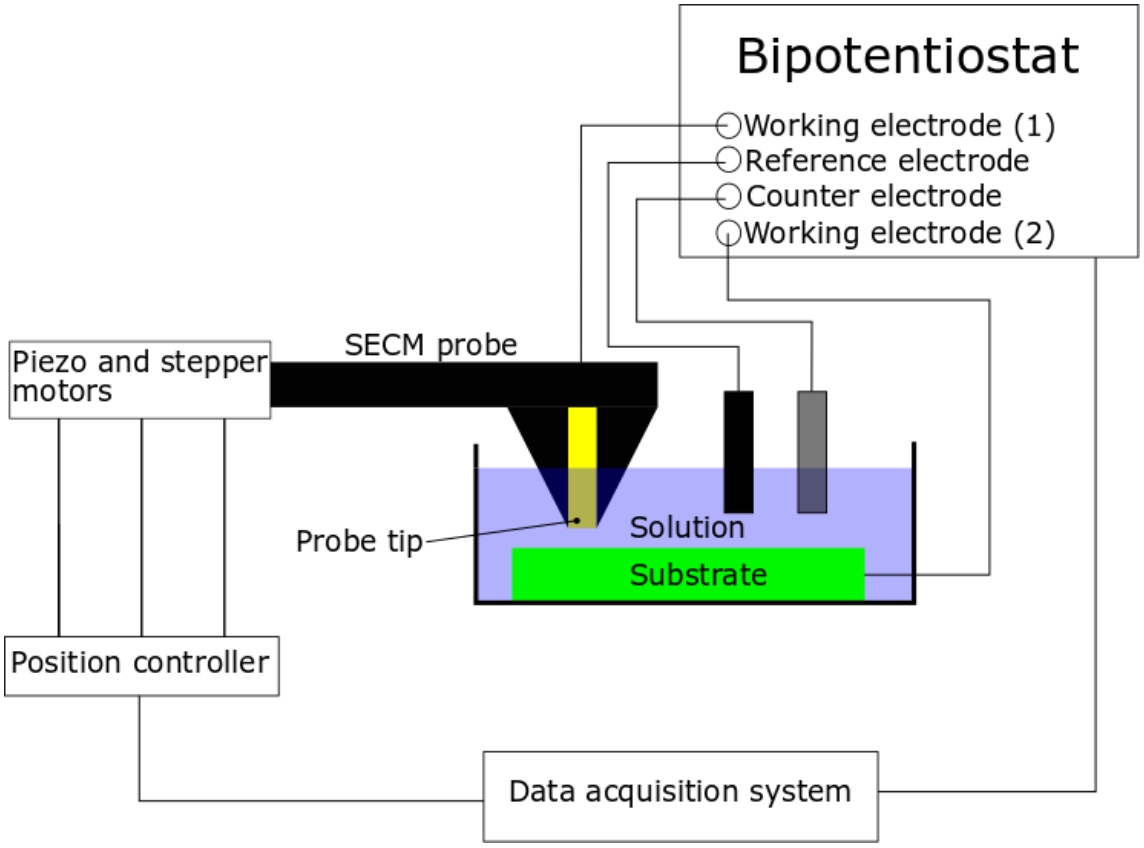

FIGURE 1.12: Schematic diagram of an SECM system.

1.2 Optical Spectroscopy

1.2.1 Introduction

Optical spectroscopy is a technique used to study how electromagnetic radiation within the UV, Visible or infrared wavelength interacts with matter. The linear absorption of the electromagnetic radiation's energy onto the interrogated area of a non scattering medium, where the number of photons absorbed is directly proportional to the number of incident photons, can be described by the Beer-Lambert Law [144].

$$I(x) = I(0)exp^{-\mu_a x} \tag{1.12}$$

Where -μ_a is the materials absorption coefficient (a function of the wavelength of the light), *I(0)* is the incoming lights intensity, x is the thickness of the sample and *I(x)* is the intensity of the transmitted radiation.

1.2.2 Raman Spectroscopy

As mentioned earlier, Raman spectroscopy is a non-destructive metrological technique used to identify an interrogated material. In order to obtain a Raman spectrum, Raman scattering is needed. Raman scattering requires the use of a light source, usually a laser, which is directed onto the sample. However, the wavelength or frequency of the laser directly affects the resolution of the spectrum. At short wavelengths (<400 nm) the laser will produce strong Raman scattering, however, this can induce problems such as fluorescence which will obscure the weaker Raman signal. As the wavelength increases, the scattering gets weaker, and as such the optimal wavelengths for Raman spectroscopy occur within the visible and Near-Infrared (NIR) regime. Within the visible regime, there is a trade-off between high Raman efficiency for a reduction in fluorescence. X-ray sources can also be used [145], however for the purpose of this project, only light based sources will be explored.

When the light source impinges on the sample, its photons interact with a sample's molecular vibrations. Each molecule's vibrational modes depend on the orientation of the atoms and their bonds, as well as the atomic mass and bond order of the atoms. The excitation from the source's photons will put the molecule into a virtual energy state. Once the molecule comes out the virtual energy state, a photon is emitted. The emission causes

an energy gain or loss from the source photons [146] to, or from, the sample's molecular bonds. This change in energy provides information on the vibrational modes of the system, as the molecules are in a different vibrational state. Stokes and anti-Stokes scattering are the two forms of Raman scattering. These forms of scattering have a gain and loss in vibrational energy, respectively, upon exiting the material. Raman spectroscopy offers benefits compared to Infrared (IR) spectroscopy, although both give information from the vibrational modes of the molecule, in that the vibrational modes have low energy, hence, long wavelength. A disadvantage of IR spectroscopy is that the spectra's wavelength falls within the mid-long range Infrared regime. The large wavelength range means that the diffraction limit for focusing is poor. In contrast, Raman gives a spectrum that is close in wavelength to that of the monochromatic source, allowing the light to be focused easily.

Raman scattering is usually very weak and the main form of scattering is Rayleigh scattering. The Rayleigh scattered photons have the same energy as the incident photons but exhibit a change in direction; they are "elastically scattered". The intensity of the Raman signal is explained through relation 1.13 [147]:

$$p(t) = \alpha \mathrm{E}_{inc}(t) \tag{1.13}$$

Where E_{inc}(t)=E_0cos(ω_mt). From relation 1.13, the induced dipole moment of an atom is proportional to the enhancement of the polarizability, α, and the enhancement of the electric field, E_inc. The greater the polarizability change the more intense the Raman scattering. If the exposed atoms are vibrating at the frequency ω_m, the nuclear displacement *(q)* can be described by the following relation:

$$q = q_0 cos(\omega_m t) \tag{1.14}$$

Where cos(ω_mt) has its usual meaning and q_0 is the amplitude of the nuclear displacements vibration. When q_0 is small, the polarizability follows the relation:

$$\alpha = \alpha_0 + (\frac{\partial \alpha}{\partial q})_0 q + ... \tag{1.15}$$

Where $(\frac{\partial \alpha}{\partial q})_0$ is the derivative of the polarizability against the motion of the molecular vibrations at its equilibrium position and α_0 is the polarizability at equilibrium. Introducing all our relations together, assuming there's an already vibrating molecule and all amplitudes are equal, we arrive at the expression:

$$p(t) = \alpha \mathrm{E}_0 cos(\omega_0 t) + \mathrm{q}_0 E_0 \tfrac{1}{2} (\tfrac{\partial \alpha}{\partial q})_0 \, (\cos[(\omega_0 + \omega_m)t] + cos[(\omega_0 - \omega_m)t]) \tag{1.16}$$

From equation 1.16 we can extract three separate terms with differing frequencies. We extract of those with oscillations in them, $\cos(\omega_0 + \omega_m)t$ describes Anti-stokes and $\cos(\omega_0 - \omega_m)t$ depicts Stokes scattering. Mathematically all three scattering phenomena can be further simplified, following the Planck relation, integral to quantum mechanics. Taking $\widetilde{\nu}_0$ as the wavenumber of the laser and $\widetilde{\nu}_v$ as the wavenumber for the vibrational transition; the relation governing Rayleigh, Stokes and anti-Stokes scattering respectively are described:

$$\Delta E_R = -h(\widetilde{\nu}_0) \tag{1.17a}$$

$$\Delta E_S = \text{-h}(\widetilde{\nu}_0 \text{-} \widetilde{\nu}_v) \tag{1.17b}$$

$$t\ \Delta E_{AS} = \text{-h}(\widetilde{\nu}_0 + \widetilde{\nu}_v) \tag{1.17c}$$

From the first relation (1.17a), it can be determined that the energy of an incident photon has an equal and opposite value, upon exiting the sample, during Rayleigh scattering. The energy of the exiting photons for Stokes is higher (1.17b) and anti-Stokes lower (1.17c) with their relations. The energy difference between the incident and inelastically scattered photons is typically known as the Raman shift, with units of cm^{-1}, where 1 cm^{-1} is approximately 0.124 meV, Δf is 29.93 GHz and $\Delta\lambda$ at 633 nm is 633.04 nm [148]. The energy changes are depicted in Figure 1.13.

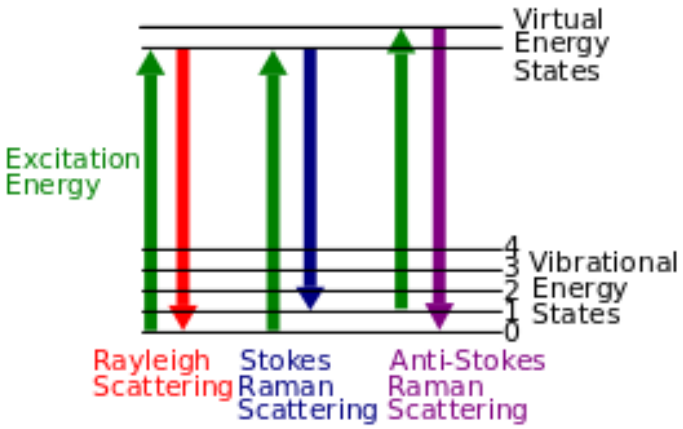

FIGURE 1.13: Schematic diagram showing the energy levels of the three different scattering possibilities.

1.2.3 Selection Rules

The selection rules in Raman spectroscopy determine which vibrational modes are Raman-active and give rise to Raman scattering. For a Raman transition to occur, the molecular polarizability must change as a molecule vibrates. The polarizability of a molecule describes how easily an electron cloud within an atom or molecule can be changed or distorted in response to an electric field. An atom where the electron cloud is further away from its nucleus has a larger polarizability than one where the cloud is close to the nucleus.

These vibrations relate to symmetrical species which have a product of two translations. Symmetric vibrations lead to strong Raman signals and no IR signals. Asymmetric and bending vibrational modes are possible but lead to weaker Ramans signals and quite strong IR signals. If a molecule has both IR and Raman signals at the same frequency, if one signal is strong, the other will be weak. An example of a triatomic linear molecule with stretching vibrations is shown in Figure 1.14.

Although symmetrical and asymmetrical stretches show how atoms in a molecule move relative to each other, whilst analysing crystals, it is important to understand both the symmetry of the vibrational mode and the lattice vibration to interpret the Raman Spectra. These lattice vibrations can be broken down into transverse and longitudinal optical modes, where the modes refer to the direction of the lattice vibrations relative to the propagation of the phonon, or electromagnetic wave. Within transverse optical modes, the atomic displacements are perpendicular to the direction of propagation and in longitudinal, the displacements are parallel. These distinctions become important when analysing Raman spectra of crystals, where the intensities rely on both the symmetry of the vibrational mode, the orientation of the crystal, polarization of the laser and the direction where the scattered light is detected.

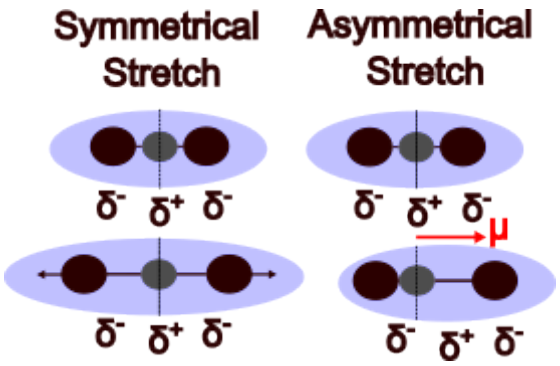

FIGURE 1.14: Schematic diagram depicting the basis of Raman selection rules. The symmetric stretch leads to a polarizability gradient as shown by the blue area getting larger, but the dipole moment (μ) is unchanged, which means it is Raman active but IR inactive. The assymetric stretch has a changed dipole moment, but polarizability is unchanged leading to it being Raman Inactive but IR active.

1.3 Plasmonics

Plasmonics is a field of study of interest in nanophotonics and nano-optical systems. Plasmons are a collective oscillation of free conduction electrons in materials, and nearby conductive particles, with fixed positive ion cores. When an electromagnetic source, in the case of this work the source is light (optical oscillation), irradiates the free electrons in a sample various phenomena can be observed depending on the photon's frequency [149].

1.3.1 Dielectric Function of Metals

The dielectric function of metals and how they interact with the electromagnetic spectrum can be described by Maxwell's equations of macroscopic electromagnetism [150]. Maxwell's equations are:

$$\nabla \cdot \mathbf{D} = \rho_{free}, \tag{1.18}$$

$$\nabla \times \mathbf{H} = \mathbf{J}_{free} + \frac{\partial \mathbf{D}}{\partial t}, \tag{1.19}$$

$$\nabla \times \mathbf{E} = -\frac{\partial \mathbf{B}}{\partial t}, \tag{1.20}$$

$$\nabla \times \mathbf{B} = 0. \tag{1.21}$$

Where **D** is the electric displacement, **B** is the magnetic induction, ρ_{free} and **J** are the densities of free charge and free current, **E** is the electric field and **H** is the magnetic field. If the material is non-magnetic, linear and isotropic we arrive at the following:

$$\mathbf{D} = \epsilon_0 \mathbf{E} + \mathrm{P} = \epsilon_m \epsilon_0 \mathbf{E} \tag{1.22}$$

$$\mathbf{B} = \mu_m \mu_0 \mathbf{H} = \mu_0 \mathbf{H} \tag{1.23}$$

$$\mathbf{J} = \sigma \mathbf{E} \tag{1.24}$$

Where the relative permeability of the medium (μ_m) is 1 for non magnetic materials, **P** is the polarization, σ is conductivity, ϵ_0 is the permittivity of free space, ϵ_m is the dielectric value of the material and μ_0 is the magnetic permeability in vacuum.

As Maxwell's equations have been described, when an external harmonic field is applied to a metal, consisting of a plasma of n freely moving electrons, this will give rise to a characteristic known as the plasma frequency (ω_p). The plasma frequency describes a limit in which the electrons no longer move in response to the external oscillating field, where their frequencies are typically in the UV regime for natural metals [151].

The oscillation motion of an electron *(x)* when an external electric field **E** is applied is shown by the Drude model [152], starting with relation 1.25:

$$m \frac{\partial^2 x}{\partial t^2} + \mathrm{m} \frac{\partial x}{\partial t} \gamma = \text{-}e \, \mathrm{E}_{inc} \tag{1.25}$$

Where γ is the damping factor to the free motion, or the collision frequency, e is the electron charge and m is the mass of each electron. Assuming the same conditions as equation 1.13, where the external field's frequency will oscillate an electron with the same frequency and x is the displacement, the following relation of electron oscillation with relation to the E_{inc} is as follows:

$$\mathrm{x(t)}=\frac{e}{m(\omega^2+i\gamma\omega)}\mathrm{E}_{inc}(t) \tag{1.26}$$

Re-arranging equation 1.26, and introducing Maxwell's equations we can determine the polararization *(P=-nex)* induced by an electric field.

$$P = -\frac{ne^2}{m(\omega^2 + i\gamma\omega)}E \tag{1.27}$$

In the non-magnetic, linear and isotropic medium we use then introduce this relation into equation 1.22 to get the electric displacement.

$$\mathbf{D} = \epsilon_0(1 - \frac{ne^2}{\epsilon_0 m(\omega^2 + i\gamma\omega)}\mathbf{E}) \tag{1.28}$$

Whereby if you compare 1.22 to equation 1.28, the dielectric function of a metal can be determined to be :

$$\epsilon_m(\omega) = 1 - \frac{ne^2}{\epsilon_0 m(\omega^2 + i\gamma\omega)}\mathbf{E} \tag{1.29}$$

The plasma frequency within a metal can be related with:

$$\omega_p = \sqrt{\frac{ne^2}{\epsilon_0 m}} \tag{1.30}$$

This relation further simplifies equation 1.28 to:

$$\mathbf{D} = \epsilon_0(1 - \frac{\omega_p^2}{(\omega^2 + i\gamma\omega)}\mathbf{E}) \tag{1.31}$$

and further simplifies equation 1.29:

$$\epsilon_m(\omega) = 1 - \frac{\omega_p^2}{\epsilon_0 m(\omega^2 + i\gamma\omega)} \tag{1.32}$$

Whereby the real and imaginary parts of the equation can be split up into equation 1.33, the magnitude of polarization, and equation 1.34, the phase-shift delay in dielectric response, respectively.

$$\epsilon_1 = 1 - \frac{\omega_p^2}{(\omega^2 + \gamma^2)} \tag{1.33}$$

$$\epsilon_2 = \frac{\omega_p^2\gamma}{\omega(\omega^2 + \gamma^2)} \tag{1.34}$$

As stated earlier, when the radiation frequency is below that of the plasma frequency the radiation is reflected and when it is above the radiation is transmitted.

At the plasma frequency the imaginary part of the dielectric function becomes positive with the real part becoming zero. We can calculate the plasma frequency using the relation already described in 1.30, but is rewritten below:

$$\omega_p = \sqrt{\frac{ne^2}{\epsilon_0 m*}} \tag{1.35}$$

Where ω_p is the plasma frequency (rad/s), n is the free electron density (electrons per unit volume), e is the elementary charge, ϵ_0 is the vacuum permittivity and m* is the effective mass of electrons in the gold (kg). Within a thin gold film, the free electron density of gold is 5.9×10^{28} electrons/m^3, the effective mass is taken as the electron mass which is 9.109×10^{28} kg and the thickness is 70nm. The elementary charge can be taken as 1.602×10^{-19} C and ϵ_0 can be approximated as 8.854×10^{-12} F/m = 8.98 eV.

As can be seen from equation 1.35 these plasma oscillations depend on the electron density of a conductive medium. These plasma oscillations are also known as Langmuir waves, after Langmuir termed the phrase "plasma" when noting something of interest in 1916 [153], before then coining it in 1929 [154] whilst describing the collective electrical properties in an ionized gas. After further research into the electron "gas" of metals and semiconductors, it can be concluded that within these media a plasma oscillation is the collective longitudinal excitation of the conductive electron gas [155]. These oscillations are caused through the Coulomb interaction of their respective electrons. A plasmon is the quanta representing these charge density oscillations.

1.3.2 Plasmon resonance

Plasmon resonance can be split into two phenomena of surface plasmon resonance (SPR) and localised surface plasmon resonance. The terms are purely based on dimensions, whereby when the resonance propagates along a dielectric interface of the metal, it is known as surface plasmon resonance. A diagram depicting SPR is shown in Figure 1.15.

When the wavelength of the excitation field is greater than the geometric dimensions of the sample, it is then referred to as localised surface plasmon resonance. Surface plasmons occur when a plasmon is constrained to a material's surface.

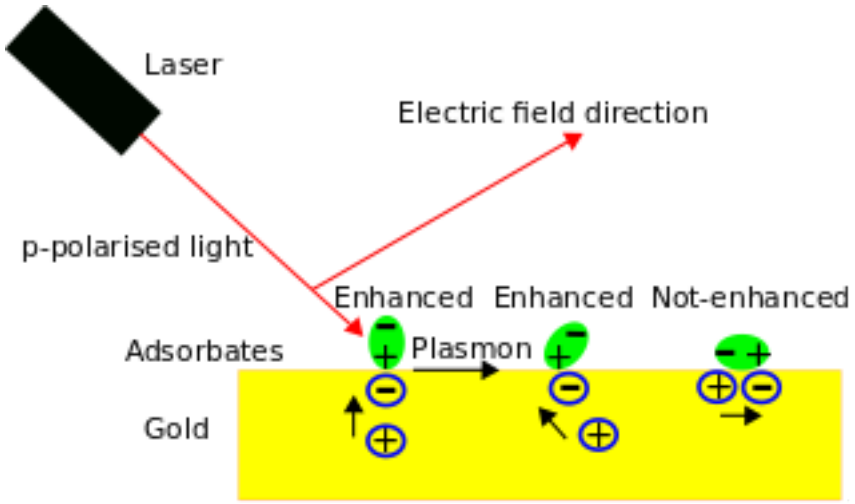

FIGURE 1.15: Schematic diagram of SPR.

1.3.2.1 Localised surface plasmon resonance

Localised surface plasmon resonance (LSPR) occurs due to electron charge oscillations within metallic nanoparticles that are excited by light. The shape and size of the metal nanoparticles play an important role on the strength of the enhancement. If the particles are too large and thick, an excitation of multipoles is created which will decrease the enhancement efficiency [156]. If the particles approach the size of an atom, they cannot enhance the electric field as there is no plasmon. A plasmon requires a collective oscillation of the free electron gas i.e. more than one [157]. As such the substrate should contain high uniformity between particles, have a high field enhancement and allow only a dipole transition. A typical thickness of metal for optimal LSPR is between 10-100 nm [158]–[160], this is strongly dependent on the metal, geometry and the target resonance wavelength. It is these de-localisation and restoration of the free electrons around the ion core that effectively makes a nanoparticle a dipole. A near field enhancement is exhibited at the resonance wavelength [161]. A diagram depicting LSPR is shown in Figure 1.16 below :

When the nanoparticle size is much smaller than wavelength of light in the surrounding medium and typically of sizes less than 100 nm with visible light [162], it can be assumed that the phase of the electromagnetic wave is constant over it. This is the regime where LSPR occurs, and it is more pronounced for nanoparticles with effective diameters between 2-20 nm [163] or up to about 30 nm [164], dependent on how they are made and experimental conditions. For nanoparticles this small, the resonance is sharp due to the entire nanoparticle responding coherently to the incident field, making it easy to detect

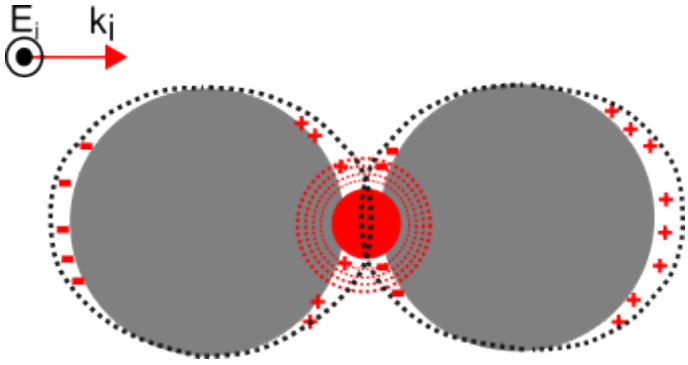

FIGURE 1.16: Schematic diagram of LSPR in effect.

within spectroscopy and quantum/surface effects are not dominant. As the particles get even smaller (<10 nm), quantum and surface effects become important. This can lead to a shift in the plasmon resonance, or cause it to weaken or broaden, due to increased surface scattering, a reduction in the free electron density and quantum confinement, making it less useful within spectroscopic applications.

However, as the size of the particle increases even more from 30 nm (remaining smaller than the wavelength of light), the particle's polarizability also increases. The larger particles have more free electrons and a larger region where collective oscillations brought on by the electric field can occur, leading to a stronger LSPR response. However, due to the larger size, radiative damping and surface scattering also increases, leading to the resonance peak becoming broader and more sensitive to the surrounding environment.

1.3.3 Surface Plasmon Polariton

Generating surface plasmons can allow for great electric field enhancement and sub-wavelength confinement, paving the way in biosensing [165] and nano-photonics [166]. Ritchie's work on plasma losses in 1957 allowed us to determine that SP's are in fact EM waves, which can propagate along a metal/dielectric interface [167]. These SP's oscillate at the surface of the metal and then couple with incident photons, given the materials can support the waves, to form something known as surface plasmon polaritons (SPP).

The polaritons occur at highly localised at an interface of a positive real relative permittivity material (like a dielectric material) and a negative real relative permittivity material (usually a noble metal like silver or gold) at the given frequency of light. If the size of the negative real relative permittivity is not greater than the positive region, the light

will not bind with the surface and hence won't propagate along it. This is because the EM waves consist of light waves, where its photons resonate with the free electrons of metal, oscillating at the interface. It is this resonance between the incident photons and oscillation of the plasmons which generate a SPP, where the negative real permittivity (dielectric function) must be sufficiently negative to support SPP generation. The permittivity of the metal typically follows dispersion models known as Drude or Drude-Lorenz when operating within the visible regime. The metallic permittivity can be defined as:

$$\epsilon_m(\omega) = 1 - \frac{\omega_p^2}{\omega(\omega + i\gamma)} \tag{1.36}$$

Where ω_p is the plasma frequency and γ is the scattering rate of the electrons.

As the SPP's are highly localised, an enhanced electric field intensity can be seen where it propagates, meaning its effects are susceptible to the conditions of the metal/dielectric interface. These can be put to use in fields such as surface enhanced Raman spectroscopy (SERS), where SPP generation has been seen to enhance a Raman signal by 4 orders of magnitude than what it is without SPP's [168], gaining a stronger signal and more comprehensive chemical fingerprint of lower concentration analytes [169]. This is all dependent on the structure of the host and analysed material, like the period of a grating, roughness of the surface and thickness of the metal. A diagram showing the excitation of a SPP is shown in Figure 1.17:

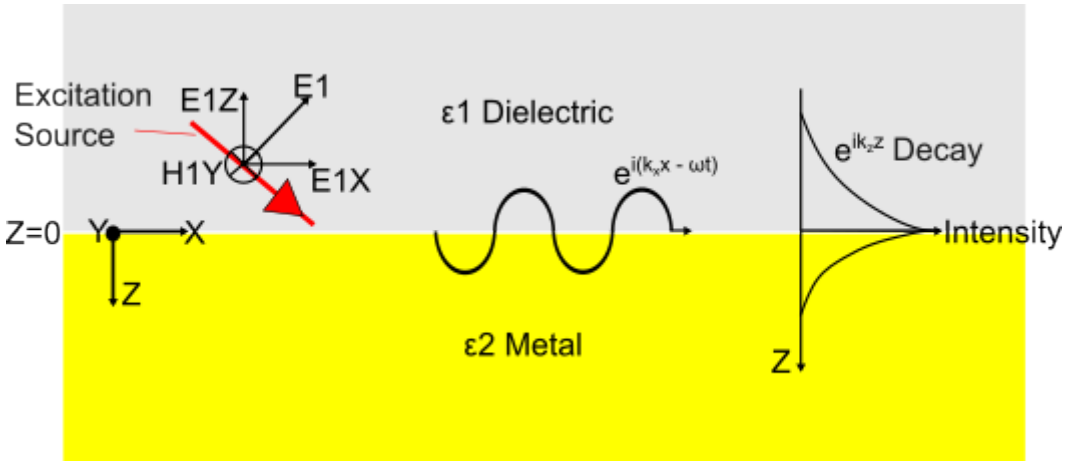

FIGURE 1.17: Schematic diagram of the excitation of a SPP.

1.3.4 Surface Plasmon Polariton Excitation

To excite a SPP, a photon must match the frequency and momentum of the SPP. However, when operating in air, a photon has less momentum and doesn't match that of the SPP as they have differing dispersion relations [170]. This is the reason why you cannot directly couple a photon from air to a SPP. A dispersion relation details how light interacts at a dielectric/metal interface, relating the incident photons wavenumber (momentum) to a SPP mode's frequency using Maxwell's equations. It should be noted that there is no normal solution for a TE mode, this is because it only has an electric field component in the y and therefore can't create SPP's at an interface. These relations are detailed below for a TM mode at a dielectric/metal interface [171]:

First, we derive the electric and magnetic fields from Maxwell's equations:

$$H_y^m(z) = A_1 e^{i\beta x} e^{k_1 z} \tag{1.37}$$

$$H_y^d(z) = A_2 e^{i\beta x} e^{-k_2 z} \tag{1.38}$$

$$E_x^d(z) = iA_2 \frac{1}{\omega\epsilon_0\epsilon_2} k_2 e^{i\beta x} e^{-k_2 z} \tag{1.39}$$

$$E_z^d(z) = -A_1 \frac{\beta}{\omega\epsilon_0\epsilon_2} e^{i\beta x} e^{-k_2 z} \tag{1.40}$$

$$E_x^m(z) = -iA_1 \frac{1}{\omega\epsilon_0\epsilon_1} k_1 e^{i\beta x} e^{-k_1 z} \tag{1.41}$$

$$E_z^m(z) = -A_1 \frac{\beta}{\omega\epsilon_0\epsilon_1} e^{i\beta x} e^{-k_1 z} \tag{1.42}$$

Where β is the wave vector of the SPP, ϵ_1 and ϵ_2 are the relative permittivity of the metal and dielectric respectively. Considering the wavevectors normal components and the dielectric constants of the mediums, we can solve for the dispersion relation of SPP's (β):

$$\beta = k_0 \sqrt{\frac{\epsilon_1 \epsilon_2}{\epsilon_1 + \epsilon_2}} \tag{1.43}$$

Where the boundary conditions take the form of:

$$\frac{k_2}{k_1} = -\frac{\epsilon_2}{\epsilon_1} \tag{1.44}$$

$$k_1^2 = \beta^2 - k_0^2 \epsilon 1 \tag{1.45}$$

$$k_2^2 = \beta^2 - k_0^2 \epsilon 2 \tag{1.46}$$

Figure 1.18 is a plot of $k_{(x)}$ (wave vector of the propagating wave in x) vs the angular frequency of the wave. The gradient of this plot is known as the group velocity, this represents the speed where energy or information carried by a SPP propogates along a metal-dielectric interface. When the wave vector has a low value, the SPP behaves like a photon before reaching an asymptotic limit known as the surface plasma frequency with increasing k. If $k_{(x)}$ is plotted against ω as in Figure 1.18, a light line where the angular frequency is $\omega = ck$, and with the low k value of the SPP, you can see how it nearly touches the light line before bending away due to an SPP having a shorter wavelength due to evanescent decay [172]. A diagram of a SPP dispersion relation is shown in Figure1.18.

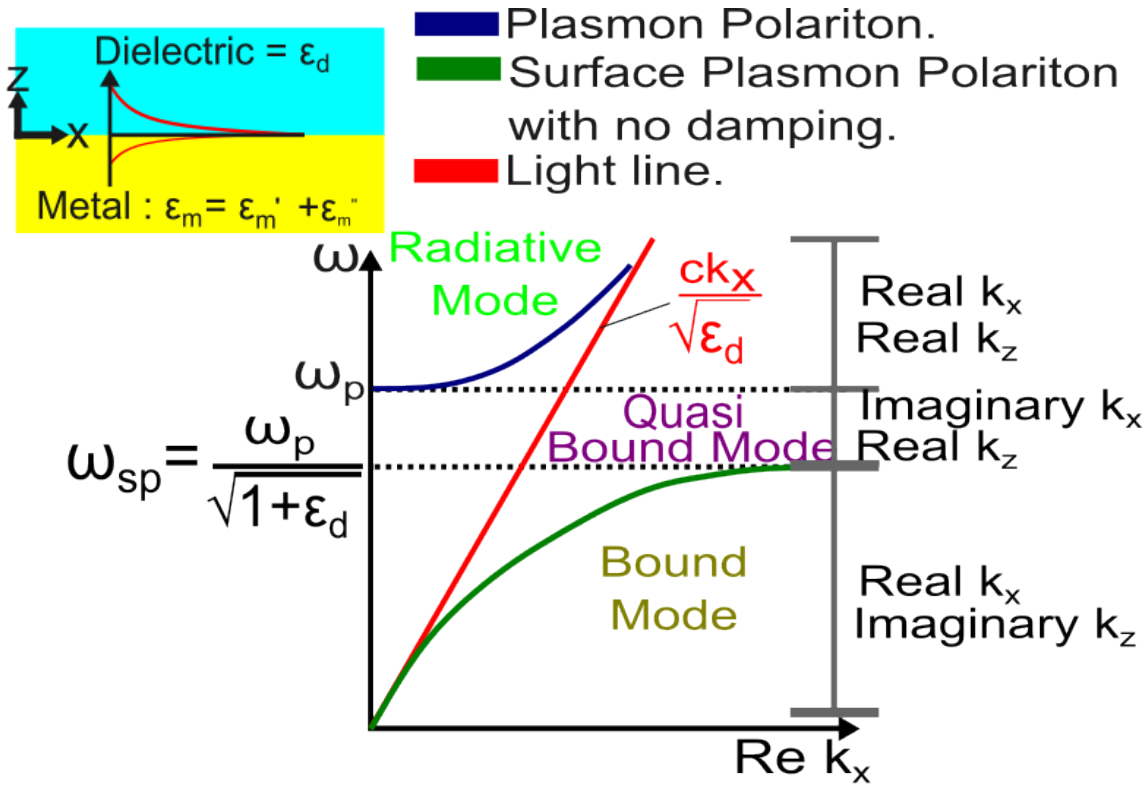

FIGURE 1.18: Schematic diagram of a SPP dispersion plot.

1.3.4.1 Gap Plasmon

When the wavelength starts to get longer within the visible wavelength regime, a surface plasmon polariton vs light dispersion curve shows the SPP curve trends closer to the light line. This in turn means any SPP is less likely to achieve a large, enhanced

field. To generate large fields within these longer wavelength regimes and at any other wavelength [173], two metal-dielectric interfaces can be placed very close to each other to induce near-field coupling of SPP's at each interface. These small regions contain guided electromagnetic waves known as gap surface plasmons, which propagate with micrometre lengths [174] through transparent mediums between two very close metallic regions [175]. The guided modes only exist with p-polarisation and lead to large field enhancements within the dielectric which strongly enhance plasmon-enhancement interactions like SERS [176] and TERS [177], confining light to within a subwavelength region [178].

Utilising metal-insulator-metal interfaces allows for strong mode confinement of the near-field coupling. At these interfaces, we can determine the effective index which best describes how strong the plasmonic mode is confined within the dielectric gap and the phase velocity and attentuation of the gap plasmon, where a higher effective index means a lower phase velocity a gap plasmon. The effective index is a measure of the ratio of the velocity of light in a vacuum to the velocity of a plasmon mode, for a given polarization, in the direction it is propagating within the system [179].

1.3.4.2 Integration of SPP's

Surface-plasmon polaritons can confine and concentrate light, as well as localising a plasmon mode. Combining the localisation and concentration of optical energy, an enhancement of the optical fields in nanometre scale regions can be seen. In the case of the TERS probe design in this thesis, the concentration of the energy in these regions can be achieved through plasmon nano-focusing and optical antennas.

An optical antenna, in this work, is a metallic nanostructure which allows for localised plasmon modes. When the nanostructures are exposed at their resonant frequency, a resonant enhancement of the localised near field of the plasmonic mode can be seen. Exploiting this phenomenon, light can be coupled into the local and enhanced field of the plasmonic mode.

Plasmon nano-focusing gradually concentrates the SPP mode as it propagates along a tapered waveguide, dependent on the polarization and symmetry. This is regarded as a transport phenomenon, it does not have a direct relation between the interaction of the incident light and the gold structures, but describes the SPP's increasing energy concentration and amplitude, along with the changing field localisation along the propagation direction [180].

An increase in the wavelength causes the critical taper angle to decrease, this is due to the absolute value of the real part of the metal's permittivity increasing [181]. In the case of direct metal evaporation onto an AFM tip, it becomes possible to enhance the local fields with the non-resonant "lightning rod" effect. The lightning rod effect makes use of the sharp coated tips, where a high concentration of local charge densities enhances the near field. As the laser most readily available on the instruments available for use in this work is 633 nm, Au was chosen as it has a good enhancement effect within its range; whereas a green laser most suits silver. Gold is also good from a processing perspective as it does not get etched within any wet or dry processes used in the fabrication of probes and can be stored for use at a later date without risk of damage to it's optical properties. Gold has a positive dielectric function below 500 nm, making it unsuitable for any surface plasmon enhancement at these wavelengths. The drawback of using silver is that it tarnishes very quickly in air, meaning from the deposition of silver for use in TERS has to be performed with a very quick turnaround, usually for use within the next day. Aluminium becomes a better choice when operating in the ultraviolet and deep UV bands [182].

Pt is not used for SPP applications within the visible region (633 nm laser is used in this work) as it has a low quality factor (Q) due to it's high imaginary permittivity [183]. For any material, a high quality factor indicates that it has less loss and a stronger resonance property to induce a plasmonic response within the frequency range. Pd also has a higher imaginary permittivity compared to Au and Ag [184], indicating how much light is absorbed by the material, related to how it dissipates and stores energy, as the light passes through it. If the permittivity is high, a large portion of the light is also converted to heat. For SPP's to propagate effectively, the oscillating EM field needs to travel along the metal interface with minimal losses. The high permittivity value means that the wave is damped as it propagates as the energy is continuously absorbed by the material.

Fabricating the antenna and a grating coupler onto a substrate, a plasmonic waveguide is constructed. How a plasmonic waveguide performs depends on the mode confinement and the propagation distance of the excited mode. The mode confinement serves as a ratio of how much of the field penetrates the metal compared to the dielectric. If we penetrate more of the metal we have a better mode confinement, but we receive more losses. Hybrid waveguides offer a compromise between mode confinement and long propagation length [185].

1.3.5 Grating Coupler

Although near field coupling provides large and confined plasmon modes, metal gratings used within plasmonic materials have been extensively studied throughout the years, enabling coupling from far field sources, and inducing near-field localisation. The "anomalies" associated with the interaction of light and gratings were first reported on by Wood, who studied the reflectance spectra of a ruled metallic diffraction grating in 1902 [150]. Wood discovered dark and bright bands of TM light spectra, with the intensity changing over a very small spectral region but was unable to explain the physics behind it [186]. It wasn't until 1907, when Lord Rayleigh predicted the bright anomalies in the TM spectra when the electric field is polarized perpendicular to the grating grooves [187]. It was found that the scattered field is singular at a wavelength where one of the diffracted orders emerges from the grating at an angle, where a shift in the available energy is observed. We call this sharp dip in the reflectance a Rayleigh anomaly [186], [187].

In 1941 Fano [188] performed further research into these anomalies. It was theorized that when the momentum of the radiation parallel to the grating surface is larger than the incident beam's radiation, it will become evanescent and diffract into a pair of surface waves. These surface waves decay exponentially in the direction perpendicular to the propagation. The interface between the metal and dielectric continuously reflects the waves, exchanging energy and creating losses such as thermal loss. The electrons in the metal will only resonate if the momentum approaches the real part of the metal's permittivity. If the permittivity has a negative value, it indicates that the normal component of the electric field is in the opposite direction and allows for charge density variations. Rayleigh's anomaly is found to only occur with gratings with shallow trenches [188].

From then on, when the metal-dielectric interface has real and opposite signs, the corresponding guided mode is known as a Fano mode. The Fano mode correspond to the EM mode that propagates without loss along a metal-dielectric interface, where the exponential field decay to 0 is seen in the y direction. If the dielectric constants of both media are positive, Brewster modes are seen, these are not surface waves but radiative plasma waves where K_x and K_z are real. Fano resonance occurs when a discrete resonance interferes with a continuum of other states.

It is known that launching a SPP into a gold antenna is not possible through direct illumination. This is impossible due to a phase mismatch between the SPP and the incident photon, meaning it cannot decay back into light either.

There are two main solutions to ensure efficient coupling between the SPP's and propagating light. One solution utilises arrangements known as the Kretschmann and Otto configurations. These configurations rely on the evanescent field produced by Total Internal Reflection (TIR) at an interface between the smooth metal surface and substrate, in turn launching SPP's. The Otto and Kretschmann configurations utilise TIR to achieve propagation, a guided mode in silicon nitride/dioxide is a totally internally reflected mode aswell, and are widely used. The Kretschamnn configuration has been used for real time detection of SARS-CoV-2 in 2021 [189] and quantifying the influenza virus for seasonal vaccines in 2010 [190]. Silicon Many more recent uses of these setups are detailed in a book chapter by Shukla et. al [191]. A diagram depicting both the Otto and Kretschmann configurations is shown in Figure 1.19.

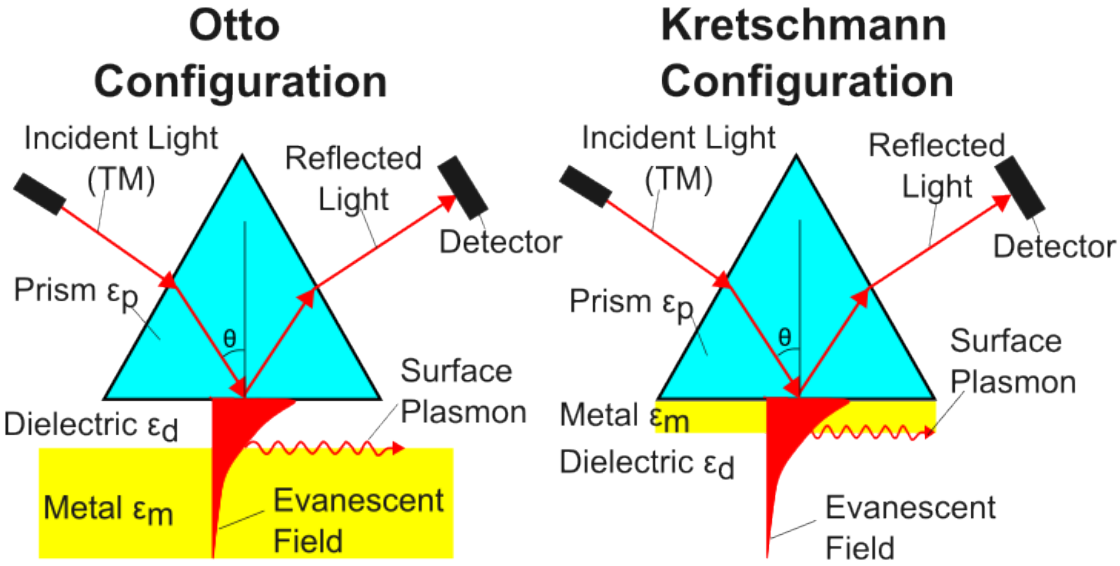

FIGURE 1.19: Diagram depicting the Otto and Kretshcmann configurations to ensure SPP generation.[192]

Although these provide great insight to the power of SPP's, they rely on smooth surfaces to get the required reflections, the setup is bulky and consist of larger feature sizes, especially in the case of binding sites for molecules to attach. To launch into smaller features, a scattering structure such as a grating, can be used to generate the required momentum onto the light and convert it from free space into SPP's.

To add to the required phase and to avoid mismatch, a grating adds to the K vector. The wavevector of a launched SPP by a grating is defined by equation 1.47, whereby a match ensures coupling:

$$K_{SPP,x} = K_{incident,x} + nK_{grating,x} = K_{incident,x} + n\frac{2\pi}{a_0} \tag{1.47}$$

Where $K_{incident,x}$ is the incident light wavevector, period of the grating is a_0, and the diffracted order n. As can be seen from equation 1.47, the grating adds a momentum which is the same as the Fourier component of the grating period, where the coupling bandwidth can be determined from the width of the first order spatial Fourier transform [193]. It shows that to conserve energy and match momentum, at a different angle and/or wavelength, the period of the grating must be altered. In order to determine the grating coupling condition, reflectance spectroscopy can be used, whereby the grating coupling condition appears as a resonance [194], [195]. Other methods such as patterning an input and output grating and measuring the input/output of incident radiation can be used [196], however it is much more time consuming.

At normal incidence, the grating period is equal to the plasmon wavelength to be excited. With a wavelength (λ_0) equal to 633 nm for our experiments and utilising the gold dielectric interface, we use relation 1.49:

$$Period = \frac{2\pi}{k_{spp}} = \lambda_{spp} \tag{1.48}$$

Which means that the period of the grating should match the excitation light wavelength for efficient SPP excitation. So, In the case of a 633 nm laser the relation to use is:

$$\lambda_{spp} = \lambda_0 \sqrt{\frac{\epsilon_d \epsilon'_m}{\epsilon_d + \epsilon'_m}} \tag{1.49}$$

Where the RI is n= 0.168 and k is 3.475, and ϵ'_m is the real part of the permittivity of the metal. Using Olmon's paper [197]., we arrive at a value of ϵ_m = -12.047 + 1.163i at 633 nm. Substituting the numbers into equation 1.49 we arrive at a value of 661.03 nm.

The coupling efficiency of the gratings can be low with SPP excitation efficiencies of 2.8% for longer wavelengths (10 μm) [198] or 50% at 600 nm with an optimal slit width [198], with it even quoted in the range of 25 –30% [180]. In order to address this issue, multiple researchers have looked into different defects to achieve a higher coupling efficiency using single slits [199], nanoantennas [200] and gratings [201].

1.3.5.1 SPP Taper Modes

Once the SPP is generated and the propagation direction is determined by the grating, a confinement of the mode is required to ensure a large electric field at the tip apex. As stated earlier, a gold taper as part of the antenna allows for a gradual concentration of the SPP mode, inducing a reduction in the transverse dimensions of the mode. These modes strongly dissipate as they go into the metal features. Whilst the gradually concentrate along the propagation length, increasing the localisation, the dissipation increases. These energy losses have been known to exceed even 90% [202]. Despite this, high localisation of SPP modes have been observed and utilising similar media to that of this project. The probe's antenna material is made of a stack consisting of a gold film surrounded by an asymmetric ($\epsilon_{air} \neq \epsilon_{nitride}$) dielectric environment (air/gold/silicon nitride), which can support local modes on different sides. As the taper is extended in the lateral direction the SPP modes which can be excited are an asymmetric and symmetric mode [203].

The symmetric mode allows the plasmon propagation at the low refractive index of the film. At either side of the metal the electric field has the same polarity, which in turn make the surface charges have the opposite polarity. The asymmetric mode is the opposite, where the mode is bound to a high refractive index side of the film. The surface charges have the same polarity due to the electric field having opposite polarity either side of the metal.

Looking into O. Lozan [204] and Verhagen et.al [205], we know it is possible to support asymmetric modes to focus the plasmon. Lozan used a glass substrate coated with SU-8 as a sticky layer and gold tapered antenna. As expected, the launched SPP-mode is dominant at the edges of the taper, with the profile broadening at the apex as the gold film adsorbs. They monitored the hot spot absorption at the taper apex by illuminating a gold slit coupler. The generated SPP's propagated through a lateral tapered waveguide and recorded a x30 enhancement of the local SPP adsorption at the apex [204]. Verhagen experimentally and computationally monitored a gold lateral tapered waveguide within a symmetric and asymmetric environment. Within the asymmetric dielectric environment, it was found to exhibit strong field confinement and concentration at the apex when the SPP mode is propagating at the substrate side of the metal. The authors also showed that the leaky mode (on the air/gold) side exhibited no concentrating behaviour. Their work demonstrated no cutoff waveguide width when the SPP mode is propagating within the substrate/gold medium, tightly bound to the gold with a large electric field build up at the apex air side [180], [205]. It is important to note that as the SPP approaches the last 10's of nm's at the apex, it gradually slows down with a velocity v_g. This parameter is

proportional to the distance from the apex $v_g \approx \omega x$ [204], [206] . As the electric field scales with v_g^{-1}, the apex sees a large absorption proportional to x^{-2}.

The final parameter which needs attention to ensure efficient mode concentration is the SPP propagation decay length. The optimal length describes the distance from the tip in which the SPP is formed to create the largest field enhancement. As we increase the distance from the optimal length, the dissipation in the metal becomes larger and the field enhancement decreases, we call this the decay length. Lozan et al. [204] realised their optimal length to be around 10 μm for an 800 nm laser, as such the taper length was decreased to account for the higher energy lower wavelength light.

1.4 Surface-enhanced Raman Spectroscopy

As Raman scattering is very weak, a technique was developed to amplify the signal with the use of a metal surface as an antenna. Surface-enhanced Raman Spectroscopy (SERS) is this technique and it is widely used to detect and characterise analytes adsorbed onto suitable metal surfaces. Amplification of the Raman signal occurs due to the rough nature of the metal surface. This surface can be fabricated from a change in metal depth following the plasmon's direction, using a cluster of colloids or electrochemical etching of the surface [207]. The choice of metal is chosen by its plasmon resonance frequency, where visible and near-infrared radiation wavelengths are generally used to excite Raman modes. Silver and Gold are often used within SERS due to their resonance frequencies falling within the visible and near-infrared wavelengths [208]. When the metal surface is coated with an analyte and is excited with a laser, a polarizability change of the analyte occurs due to its molecular motion acting in a direction perpendicular to the surface. This polarizability change leads to Raman scattering [209]. It should be noted that a SERS spectrum of a molecule may differ from a classical Raman spectrum as the majority of vibrational bands correspond to the vibrations of the closest bonds to the metal's surface and contact with the surface stops some vibrational modes. A Figure depicting SERS occurring on a nanoparticle coated substrate is shown in Figure 1.20.

Within SERS, the light strikes the surface which causes local surface plasmons to become excited. Whilst interrogating nanoparticles, the electric field is highly localised at them and dissipates quickly into the dielectric background from the dielectric/metal interface.

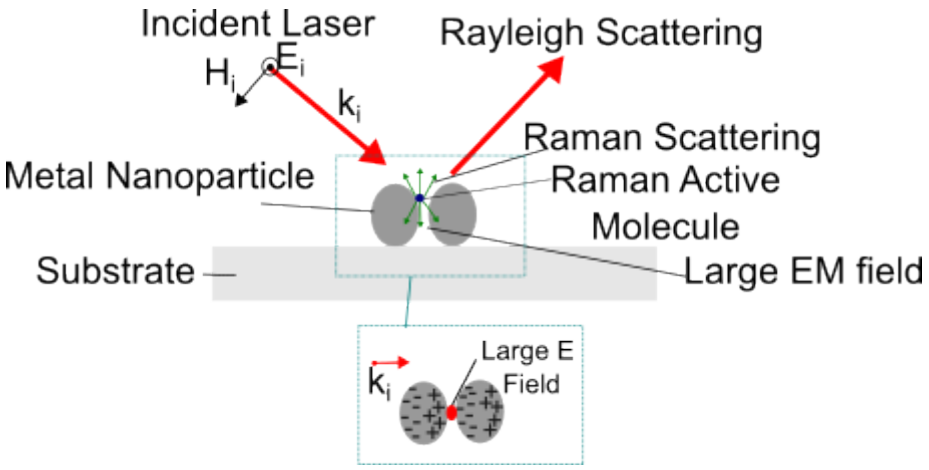

FIGURE 1.20: Diagram depicting SERS in operation with metal nanoparticles on a glass substrate, with an enhanced view of the particles.

The amplification of the Raman signal relies on an electromagnetic enhancement, where within SERS this is caused by plasmonic resonances on a rough or ordered structure metal surface [210]. The reasoning behind this is that metals contain free electrons travelling and transporting electric current. When the electrons are displaced within a metal, a positive charge is left in its place. This positive charge exerts a restorative force on the electrons and the interaction between them causes plasmons to oscillate when excited by light. The plasmons continue to oscillate at the plasma frequency until some form of resistance stops them. If the light source (excitation source) has a frequency below the plasma frequency without damping, it is reflected by the material as the electrons in the sample screen the electric field of the light [211]. However, if the frequency of the source is greater than the plasma frequency, the light is transmitted as the electrons cannot screen the electric field fast enough [212]. The photon energy at the plasma frequency is the plasmon energy, this can be approximated with the Planck-Einstein relation (1.50) [213]:

$$\mathrm{E}_p = \hbar\sqrt{\frac{ne^2}{m\epsilon_0}} \quad = \hbar\omega_P \tag{1.50}$$

Where e is the elementary electric charge, m is the mass of the electron, n is the conduction electron density, $\hbar$ is the reduced Planck constant, ϵ_0 is the permittivity of free space and ω_P is the plasmon frequency.

1.5 Tip-enhanced Raman Spectroscopy

Spectroscopic techniques such as Surface Enhanced Raman Spectroscopy are useful to determine chemical structure and properties, however the spatial resolution of this technique is limited and it can't be used to determine structures at the nanometre-scale. Tip-enhanced Raman spectroscopy (TERS) combines the merits of scanning probe microscopy (SPM) and Raman spectroscopy to give topographic, morphological and chemical information of a sample with single molecule resolution [214]. In a TERS setup, the SPM tip is coated with a metal in a similar way to that of SERS, mainly gold or silver, and is excited with a laser to excite local plasmons at the tip. The tip is then placed next to/in the analyte of detection whereby the excited plasmons have an enhanced electromagnetic field, leading to Raman scattering at the tip. A diagram of a basic TERS system and the its operation in shown in Figure 1.21 below.

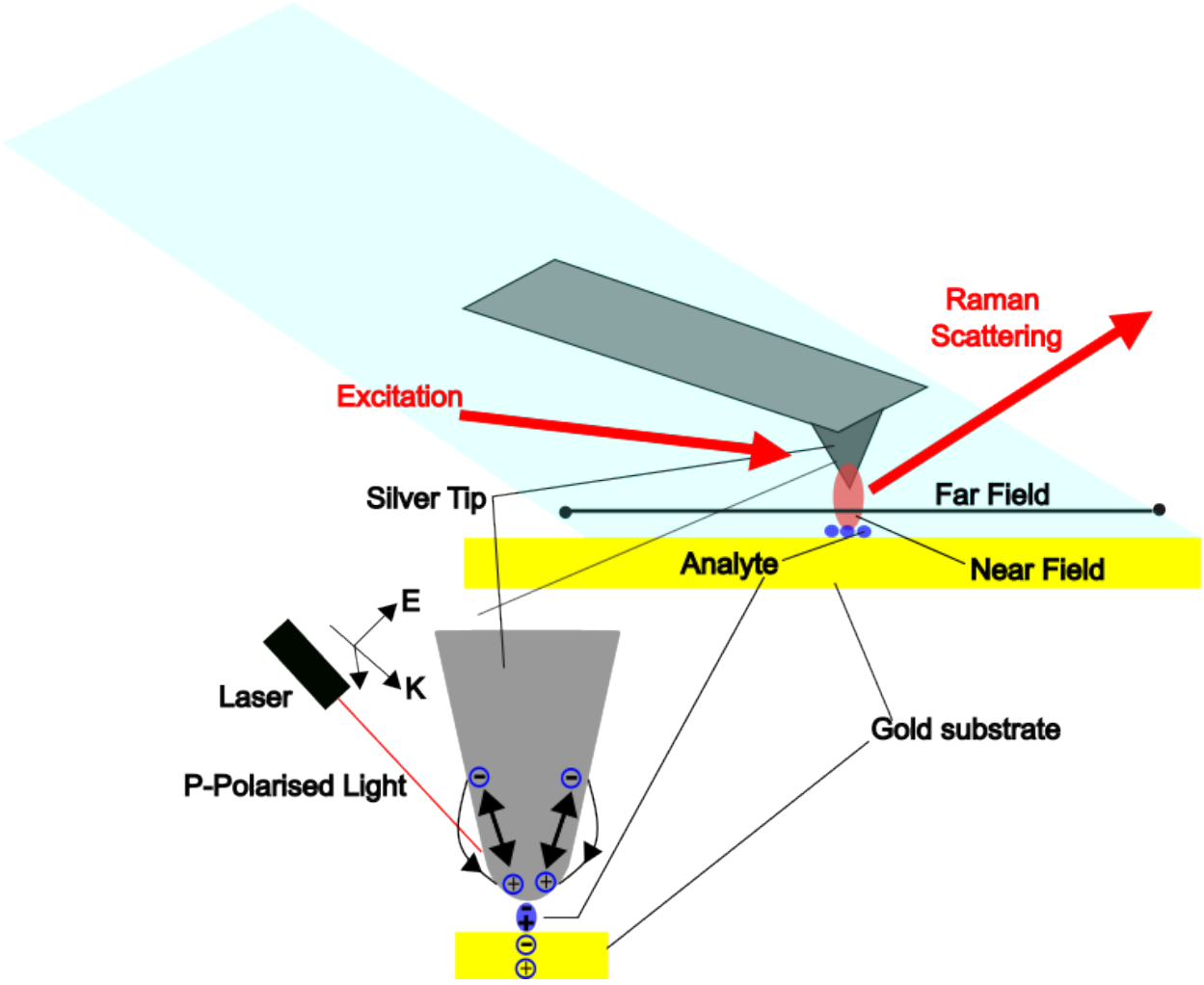

FIGURE 1.21: Schematic diagram of a TERS system.

A drawback of TERS is that it has a weaker enhancement compared to SERS as it cannot have multiple hotspots. The tip enhancement however follows similar principles to SERS, whereby the electromagnetic effect is the dominating enhancement factor [215]. The electromagnetic field enhancement is due to a combination of localised surface plasmon resonance and the lightning rod effect [216]. The lightning rod effect is a phenomenon arising from the sharp edges of the metal having a higher field strength, as explained by Gauss' law. As the tip apex for a TERS probe is sharp, conductive and plasmonically active, the surface charges are confined and concentrated, resulting in intense Raman signals of molecules underneath the tip. The effect is however dependent on the tip's material, geometry and conductivity [214]. In order to further increase the TERS enhancement, the tip could be brought within 1-2 nm of a plasmonically active metal substrate using the AFM's z-piezo. Controlling the gap between the tip and substrate is demanding of the AFM system. However, as the tip contacts the substrate within contact-mode, the feedback loop adjusts the tip height, so it maintains a constant deflection. At these distances the tip is in the repulsive force regime. These forces are sensitive to topographic changes, meaning a small change in the topography will cause a cantilever deflection and correction by the feedback loop. However, if this small gap is achieved it allows for electromagnetic coupling of the tip and substrate to create a strong field intensity and confinement. This gap-mode however comes at a cost of imaging artifacts [217] such as light scattering from the tip, fluctuating enhancement factor over the interrogated surface and tip degradation [218].

1.5.1 Selection Rules

Within both SERS and TERS, a surface selection rule governs the enhancement of the surface electric field. The selection rule states that only the vibrational modes along the direction of the surface electric field can be given sufficient enhancement [134]. An image showing this in a SERS configuration is shown in Figure 1.22. The Raman intensity is dependant on the sample's adsorption configuration. The selection rule in Figure 1.22 only applies to the molecular vibrational modes with the relative direction of the electric field.

Within TERS, the symmetry of the molecule can be lowered upon absorption onto the surface and may activate some Raman silent modes [134]. As there is a large gradient in the intensity of the electric field within TERS, the intensity may change along the vibrational modes. The change in intensity, especially present near a metal surface, may increase/reduce the potential of the induced dipole asymmetrically, defeating the known

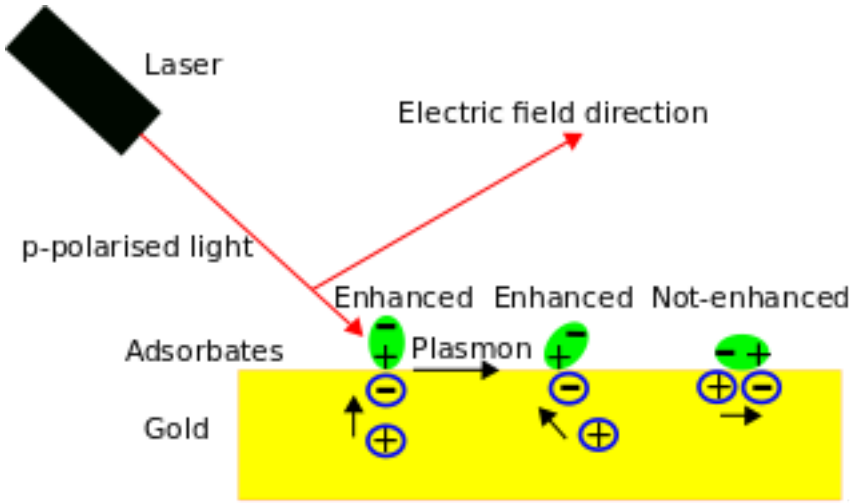

FIGURE 1.22: Schematic diagram showing the surface selection rule for SERS. As can be seen, there isn't sufficient enhancement with the horizontal particles as the vibrational mode is'nt along the direction of the electric field.

selection rule's terms [219]. The benefits of this is that previously undetectable molecules can be detected, however, as the field and conformation are both complex and dependent on shape, this makes reproducibility hard to achieve.

The plasma frequency of a gold thin film is 5.8 eV and silver is 3.735 eV [220]. This is the frequency in which the collective oscillations of the free electrons in the material are at a maximum. This is unfortunate as silver provides sharper and more intense resonance peaks, as well as inducing better scattering than gold [221]. However, gold does still provide sharp and intense peaks, be it not as strong as silver, and it is also less susceptible to corrosion making it viable for longer term experimentation [222] and within a batch fabrication technique.

1.5.2 TERS Tip

As with every SPM technique, a critical aspect of the system is the tip. Within TERS the electromagnetic field is amplified and confined to the apex of the tip close to the sample's surface. As the tip-sample distance is on the order of nanometres, the diffraction limit is not of any importance as the resolution of the Raman signals are dominated by the localisation of the field. As with other SPM techniques the material, morphology, radius and angle of the tips apex play a vital role on the spatial resolution of the images and with TERS, the enhancement factor is also affected.

1.5.3 Gap Plasmon in TERS

Whilst performing TERS, we can utilise a gap-mode enhancement (between a tip and metallic substrate) to resolve with higher spatial resolution (tip geometry dependent) and strong enhancement of Raman signals [223] in a small resonance volume.

If using an inverted microscope setup, two different enhancement mechanisms with gap plasmons can be expected. If the probe is close to contact and If the thickness of the Au on the substrate is lower than the skin depth (≈20 nm [224]), light can pass through the film and form a focus between the tip and the substrate to enhance the local electric field. Where a larger metal film is deposited, most of the light is reflected backwards and only some of the light will match the SPP excitation angle to focus and enhance the electric field in the gap. This has been demonstrated by Zhang et al., where a 45 nm metal film excites a sharp SPP focus (known as a SPP virtual probe) on the metal surface, whilst utilising an objective lens with a high NA to generate a very small optical focus [223]. The extent of the gap resonance frequency is a function of the separation distance of the tip and substrate, along with the geometry and metal of the tip. This approach allows both a SPP and optical focus to generate a more longitudinal electric field, leading to greater enhancement and resolution compared to a focused laser.

Using a side or top-down illumination configuration has the benefit that there is no substrate in the incident path. The drawback is it is also not possible to use a high-NA lens due to a typical short working distance which limits the orientation and positioning of the probe, which may cause damage to the tip [225]. Focusing with a linear polarised beam, normal to the surface, will enhance any Raman scattering close to the tip, radial polarisation has been recorded to increase this interaction as well, through generating a longitudinal mode at the laser focus [226], [227]. A schematic diagram of gap plasmon formation is shown in Figure 1.23.

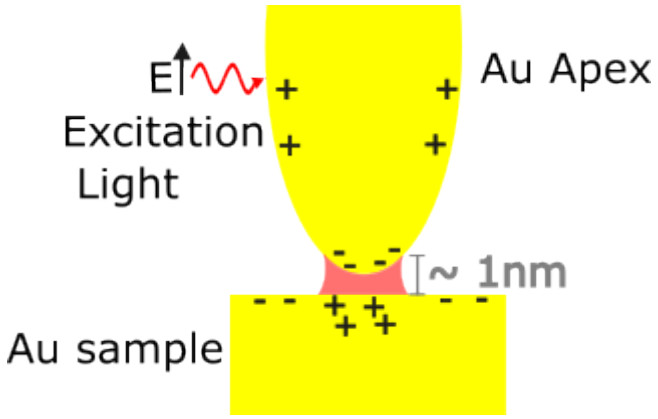

FIGURE 1.23: Schematic diagram showing the formation of gap plasmon when a Au TERS tip is irradiated with a top down/side illumination excitation, with a Au substrate beneath it.

1.6 TERS Tip Design In This Work

As discussed in section 1.5, the intensity of the Raman signal is affected by the tip's geometry, material and conductivity. Noble metals only meet the surface plasmon resonance condition within the visible to near-IR region, and as such the focus is on those. As the current process for the batch fabrication of SPM probes at the University of Glasgow relies on a release etch with a strong alkaline solution, the plasmonic antenna would have to be made of gold. The probes could be made out of silver if it was encapsulated with ICP-nitride within the facility, however, this would require a nitride dry etch of the tip, putting the probes through further processing and damage. This would also require the tips to be etched from both front side and back, with the tip facing down it is prone to fracture. An oxide layer could also be used, but the intrinsic stress of the oxide has been known to cause cracks within the release etch, this could cause the wet etch solution to seep in and etch the silver. The etchant used is 1.4L of 25% TMAH and 350ml of IPA, heated to 80 degrees for 2.5 hours. This etchant would react with silver and as such, cannot be used within the probe fabrication.

In general a rough surface is required for TERS applications, allowing a localised electromagnetic field to excite the nearby interrogated molecules. A number of techniques such as nano-particle deposition, electrochemical etching and focused ion beam milling have been used to fabricate such rough surfaces. Geometric shapes vary within TERS literature, however, the potential designs for use in this project have been narrowed down to three. The three geometric designs are known as a metal coated AFM probe, a campanile structure or the use of a surface plasmon polariton waveguide structure. These structures have been proven to be efficient in obtaining an enhanced Raman signal, although

each have their own set of drawbacks. Although the design's breadth is restricted, the geometry of each can be manipulated to provide an efficient enhancement.

1.6.1 Metal Coated AFM Probe

A TERS probe comprising a noble metal coated onto the tip is one of the more basic designs. It comprises of a standard AFM probe with a Si_3N_4 or SiO_x tip before having around 20-100 nm of the chosen noble metal deposited onto it. As stated before, a rough surface is preferred for localised enhancement and Atshushi Taguchi et. al. did so with his metal grained probe [228]. With a regular probe, smoothly coated with a metal film, the plasmon can propagate non-radiatively and decays over time [229]. Although the film behaves like a waveguide, its electromagnetic field is still localised at the tip with some enhancement due to the lightning rod effect.

In the literature, it is common to retrieve a value for the TERS enhancement as the fourth power of the field enhancement at the tip's apex [228], [230], neglecting the wavelength shift from excitation. It was found that 4 nanoparticles separated by 1 nm on the apex provide an enhancement factor of 8400, around 10 times larger than a single nanoparticle. A basic diagram of this design is shown in Figure 1.24. The report also shows that for both rods and spherical particles the optimum number is 4. When there are 4 particles, the scattering intensity is strong. The large scattering intensity, compared to a single particle, is due to the clustering of the particles behaving as an efficient coupler with the incident light from the far-field and coupling out the scattered light to the far-field. The particle that has the smallest tip-sample separation distance behaves as a near-field antenna, this efficiently excites the sample's interrogated molecules [228]. A larger number of particles saw a decrease in the scattering intensity and the resonance wavelength increases. The reduction in the scattering for the larger number of particles can be explained by the propagation loss of the plasmons through the particle chain over the larger distance [231]. Rods would be easier to replicate with the electron beam lithography tool available within the nanofabrication facilities at the University of Glasgow. As the enhancement decays through metal it is beneficial to reduce the thickness area of the metal. The rods had a gap size of 4 nm also, with a width of 30 nm, length of 40 nm and thickness of 40 nm to produce a near-field intensity enhancement of around 100 [228].

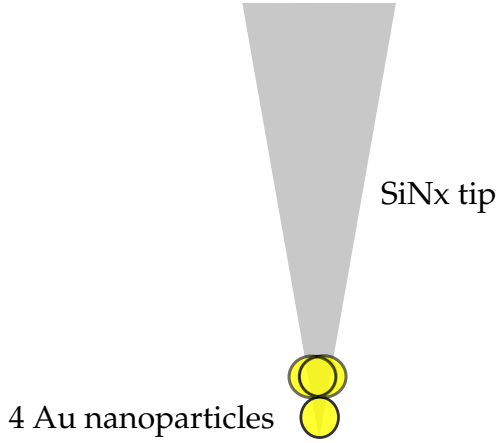

FIGURE 1.24: Schematic diagram of the metal AFM probe's tip with four gold nanoparticles at the end.

1.6.2 Campanile Probe

A campanile structured TERS probe comprises a metal-insulator-metal tip, with a nanoscale width gap within the metal and dielectric surface. A diagram of the structure is shown in Figure 1.25. When fabricated correctly, broadband field enhancement and confinement can be seen through the coupling of near and far-field electromagnetic energy [232]. In this structure the plasmons are confined to the gap region, dictating the spatial resolution and the electric field enhancement. The worry is that the edges on the taper may produce a large amount of background scattering, however, this is insignificant as the signal is collected through the gap into a collecting waveguide. These tips are usually attached to an optical fibre which provides both the laser excitation and collects the signal [233]. The small gap can be fabricated at the University of Glasgow with the use of a focused ion beam (FIB). With the aim of the project to batch fabricate the probes, FIB would not satisfy these conditions as it exposes one probe at a time.

1.6.3 Surface Plasmon Polariton Waveguide

Within a setup using direct illumination of the tip apex, a reduction of the enhancement can be seen [200]. This loss is due to a mode mismatch in the far-field excitation focus and the near-field localisation. As a consequence, direct illumination causes background signals from the far field which can account for imaging artefacts and poor contrast. Surface plasmon polariton (SPP) waveguides can be used within TERS tips as they are known for their extreme near field confinement.

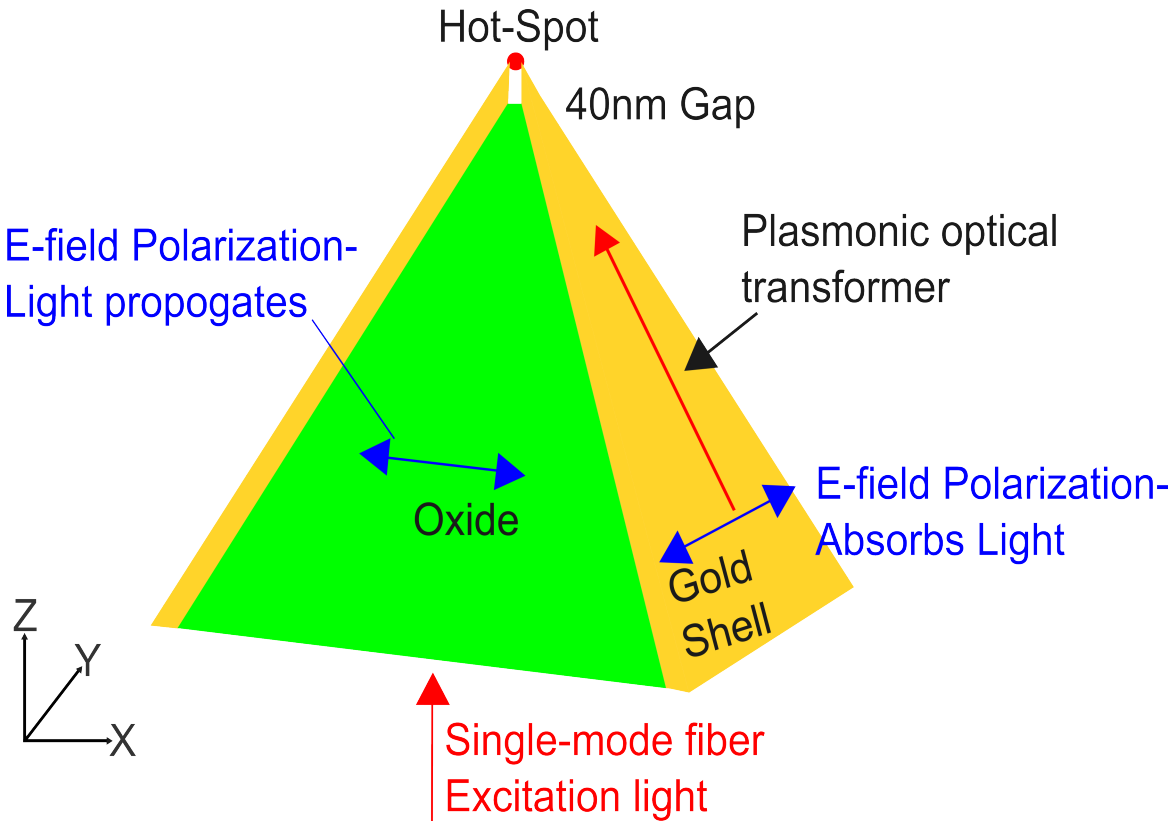

FIGURE 1.25: Schematic diagram of a campanile TERS probe's tip.

A SPP probe consists of regular trenches within the bulk of the tip, acting as a waveguide towards the apex. The side of the probe is illuminated and the continuous change in thickness of the grating allows the propagation of the SPP to focus into the tip's apex. The required period of the grating can be determined by the in-plane momentum conservation condition (2.1) and the SPP dispersion relation on the planar interface energy conservation (1.15) [234]:

$$\omega_L = \omega k_{SP} \tag{1.51}$$

$$\mathrm{k}_{SP} = \mathrm{k}_{||} + p\frac{2\pi}{a_0} \tag{1.52}$$

Within these relations, ω_L is the frequency of light with the in plane vector component $k_{||}$, p is the diffraction order and a_0 is the period of the grating. The need for these conditions shows that the resonance is an effect of the collective oscillation of the grating and not the resonance of the tip [234]. The grating used in Berweger et. al.'s paper was positioned 10 μm from the tip's apex and had a period of 750 nm, close to the wavelength

of the incident light. The constraint on the wavelength of the light can be extended by manipulating the tip angle and the grating parameters on the tip. It was found that angling the incident laser 25°, with respect to the flat of the grating, resulted in no far-field background signals as the SPP propagation focused down to the apex. A diagram of this setup is shown in Figure 1.26.

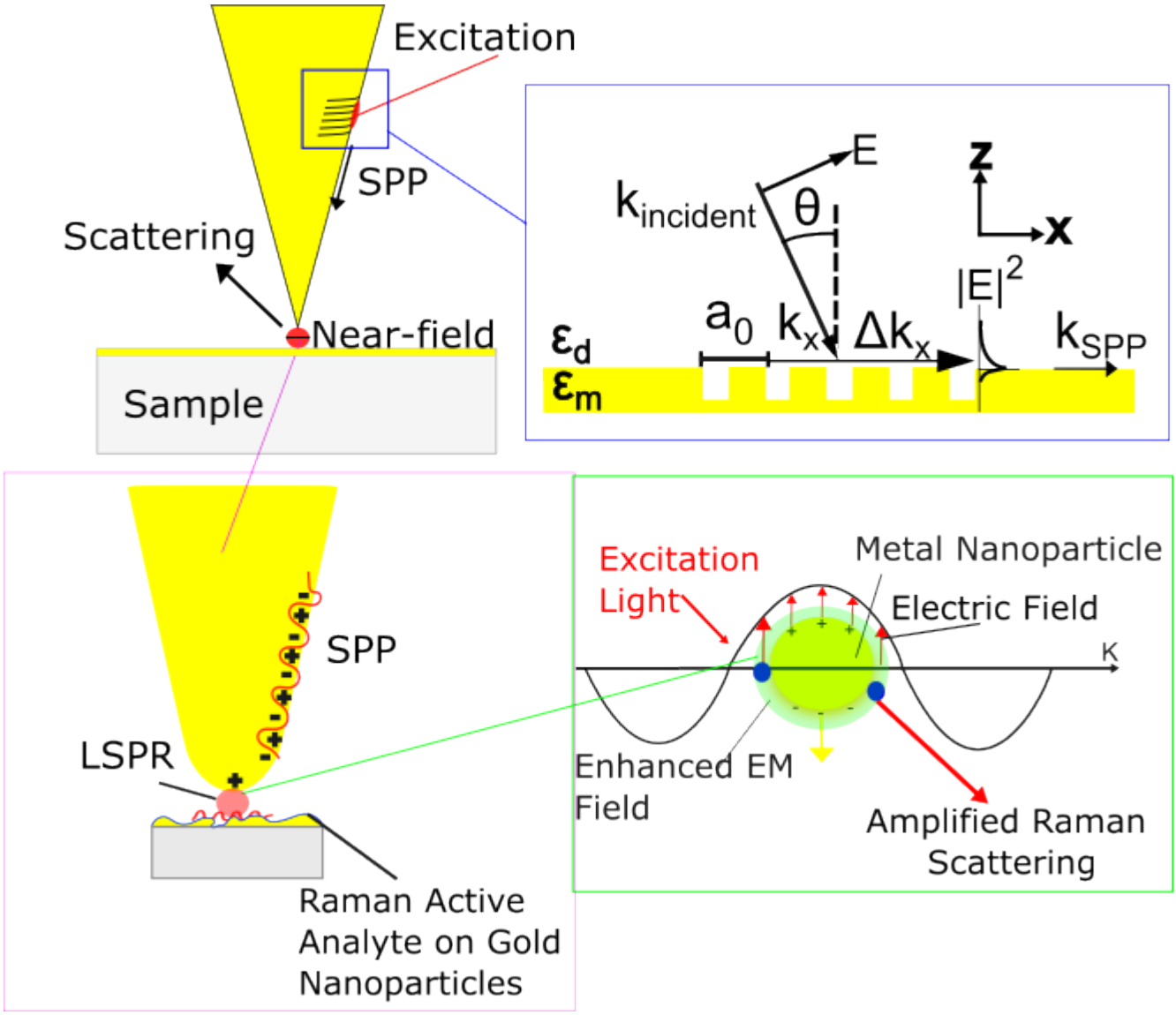

FIGURE 1.26: Schematic diagram of a surface plasmon polariton TERS probe tip, excited with an incident laser.

The simple geometric shape allows for gratings to be easily made, especially for batch fabrication purposes. These gratings can be put onto thin dielectric tips for TERS purposes, which will be discussed later. Large metal depositions and further etches would compromise the structural integrity of the tip, causing critical failure and compromise the

functionality of a dual-purpose probe, which is to scan as an AFM probe whilst operating as a TERS antenna. The mode excitation critically depends on the geometry of the grating, especially on the depth and width of the metal parts. Within a grooved grating, the required accuracy to create a controlled pattern is difficult to achieve, especially in terms of batch fabrication.

It is notably easier to fabricate a slit in a bulk metal film by FIB, or lithography than to fabricate well defined grooves. The addition of a metallic bottom on a grating can cause a waveguide mode to be reflected off the bottom, acquiring a 180deg phase shift on reflection [201]. These metallic backings allow for a large electric field at the edges, which in turn excite the SPP's. Despite having these options available, it is much simpler to launch an EM wave into a thin dielectric (nitride) to cause a phase match like that of a total internal reflection prism.

A table detailing the advantages and disadvantages of the three various probe archetypes are outlined in Table1.1.

	Resolution (Spatial)	E-Field Enhancement	Coupling Efficiency	Broadband/ Single Frequency	Topographic Control	Far field/ Pump Excitation
Campanile [233], [235]	60 nm	300 at 650 nm	50%	Single mode optical fibre	Shear-force feedback	Confined Pump
METAL [228]	14 nm (dependent on particle size)	Over 120 at 550 nm	Not known	Broadband	Constant tip-applied force	Far-field background
SPP [200], [234]	nm (dependent on tip radius)	20 at 633 nm	785 nm excitation, 9% at the apex	Both	Shear-force feedback	No far-field Raman with grating.
Dielectric Waveguide [236]	<10 nm	32 at 660 nm	Not known	Single frequency	Not known (contact mode)	Low background far-field.

TABLE 1.1: Table comparing the 3 main types of TERS probes

1.6.4 Aims and Objectives

The main aim and novelty of this work is to design a method for the batch fabrication of TERS probes, where the sensor is patterned by electron beam lithography. A large drawback of current TERS probes is the irreproducibility of data due to complex excitation and readout scattering [237], [238].

Direct illumination of a probe tip is a common method of generating TERS signals [239], this however can cause localised heating of the probe tip which leads to thermal drift [240], morphological changes to the metal [239] and overall reducing measurement stability. This method also generates a large amount of background light, making it harder to separate out Raman signals due to the amount of fluorescence and elastic scattering [239]. A novel approach to couple into the probe tip has also been designed, where a grating is illuminated through the silicon nitride cantilever to match the momentum and phase of a plasmon and generate an enhanced signal this way. This will couple the external light and reduce the large background collected, increasing the signal to noise ratio, as the Raman signals are weak compared to the background, and increase the spatial resolution, near-field TERS signals become more distinct from the far-field.

Patterning the sharp tip also uses methods like Focused Ion Beam Milling [241], where they are done one at a time or in low volume, costing operator time and differing tip shapes. Electron-beam lithography (EBL) allows for multiple design changes to the antenna, over wide areas with high resolution. This means that the tip and antenna geometry is reproducible and done so using uncontaminated materials in a resist based process. As the probe fabrication is also wafer scale, it means if they work they are more cost effective than commercial probes, generating hundreds of reproducible probes at the same time.

2 Probe Development

2.1 Introduction

This chapter outlines the techniques employed to fabricate the TERS probes. The same base technology used to fabricate commercial SThM probes was employed within this process. These fabrication methods are stable and a good basis to start a wafer fabrication, having been extensively studied and improved on within the AFM group. The process allows fabrication on a 3-inch wafer, with electron beam lithography to gain the much-required lithographic resolution on high aspect ratio features, as well as the planar parts of the probe chip. Electron beam lithography also gives excellent geometric control, which is important when designing a grating coupler. We know from the previously fabricated SThM probes that the cantilever supports the optical lever method, providing cantilever topographic feedback during scanning. The probe chips are of a conventional die size, so they fit in most conventional AFM probe mounts.

Employing the batch fabrication methods of the SThM probes, the key distinction made to the design is on the sensor lithography. All the processing issues arising from making conventional SThM probes still exist, as it's the same process, however methods were undertaken to resolve these whilst fabricating. One such issue is that the back side etch used to connect the back of the chip to the front is 320 μm deep, this removes most of the base Si material and makes the final "release etch" much quicker and cleaner. In doing so, this leaves behind a small amount of Si to hold the probes in place and makes the wafer very fragile and causes handling issues. Techniques to mitigate this and prevent wafer breakage are discussed further in this chapter.

2.2 Photolithography

Photolithography is a technique which is used to create detailed patterns on the probe wafer. The technique utilises a 360 W Hg lamp, with a constant light intensity of 7

mW/cm^2, emitting broadband UV (230-450 nm) onto a sample. The sample is usually coated with a photosensitive polymer dissolved in solvent known as photoresist, which depending on it's chemistry, can either be positive or negative. On exposure to light, negative photoresist is further polymerised or cross linked, which in turn hardens it to render it resistant to etching. The bonds in the positive photoresist do the opposite and break down on exposure to the irradiative source and are less resistant to an etchant [242]. The resists used in this project to fabricate the probes are positive-toned and are known as s1828 and AZ4562. In some exposures a "mask plate" is used, these allow the transfer of a pattern onto the sample. A mask plate consists of plate with opaque features and transparent surroundings, which (respectively) restricts and allows the radiation to go through onto the photoresist coated sample. The mask plate's features used within this projected are patterned using EBL and wet etched, leaving the chromium design on a quartz plate. The mask plate designs for these probes are shown in Figure 2.1.

2.2.1 Photolithography Alignment

Alignment markers play a vital role in the lithographic definition of features within this work. These feature's positions are known and any further definition, be it through EBL or photolithography, is performed in relation to these feature's coordinates. All of the patterned features within this work were aligned in relation to etched silicon markers, defined during the first photolithographic stages of the probe fabrication.

The importance of having good alignment before bulk micro-machining is paramount as this allows the probes to be released from the wafer without much damage, rather than eating into the probe body and for EBL and sensor alignment. The most important part is that it ensures that the cantilever is centred and still attached to the probe tip. If there is misalignment of the tip, it may not be attached to the probe body, making it a non-functional SPM probe

The photolithographic tool used (SUSS MA6) utilises a microscope to view the markers defined on the mask plate and on the sample. The focus of which can be manipulated by moving the z of the microscope. The sample is housed on a chuck which is able to move in the x and y direction with sub-micron accuracy, with a rotational accuracy of half a degree. The photolithographic exposure mode used whilst fabricating the probes is contact mode. This technique brings the sample into contact with the mask plate above before exposure. The sample is thereby manipulated rotationally and in the x and y direction until the alignment markers on the sample correlate with the alignment markers

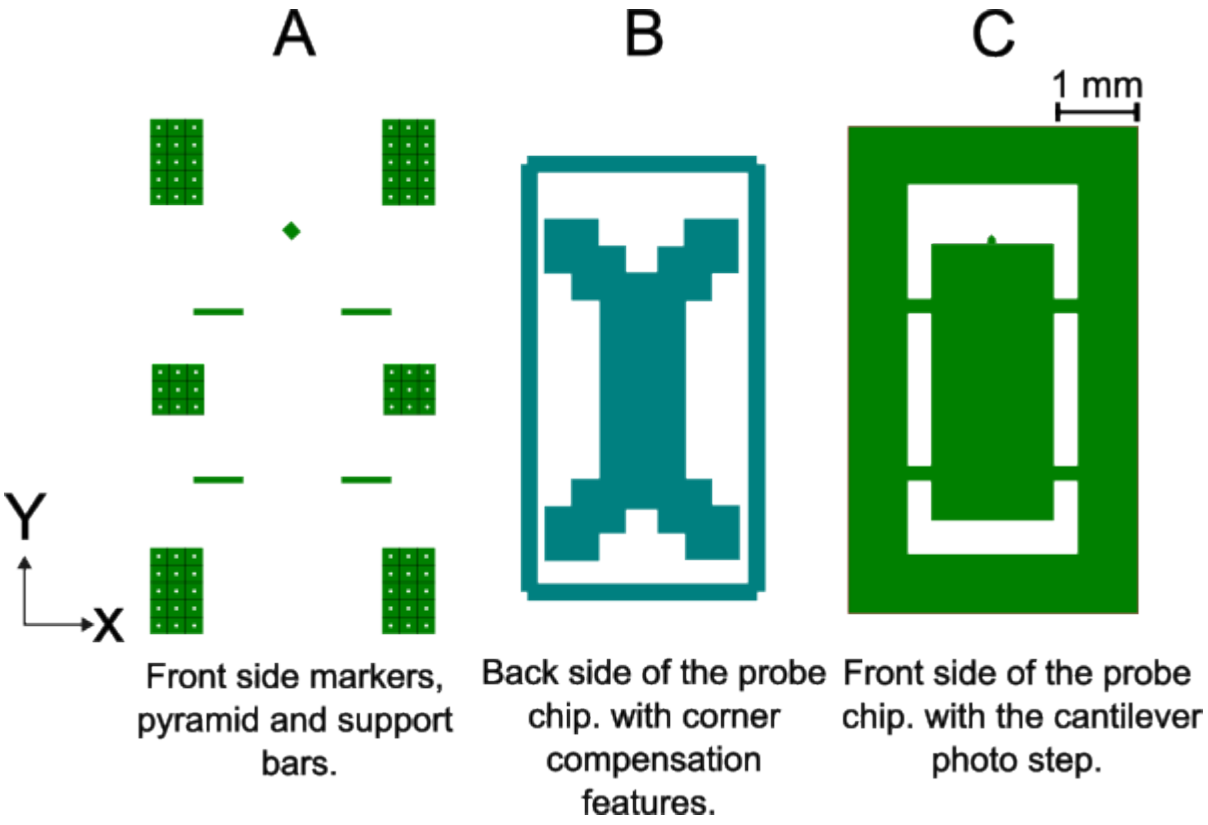

FIGURE 2.1: Diagram of the three mask plates used to define the features on the wafer. The first level (A) defines the rotated square for the pyramids aswell as the alignment markers for subsequent photolithography and e-beam steps. The second mask (B) defines the etch mask of the backside of the wafer. This lithography step leads to the bulk of the etching done on this wafer. The final step (C) defines the front side of the probes chip, defining the cantilever and the support bars. These support bars hold the probe onto the wafer until the can easily be removed in the final wet etch.

on the mask plate. This allows the newly defined features to be in the position it was supposed to be, relative to the first level's markers.

The accuracy of the alignment will vary between machines, processes and operators. One such phenomenon which also influences the alignment accuracy is known as chromatic abberation. Chromatic abberation will occur as the lens of the camera or microscope is a prism. The light rays passing through will disperse, bending and the colour wavelengths seperate. This can lead to a dissolution of the image intensity profile and thereby a reduction on the image resolution. The degree to which this effect takes hold depends many factors such as the optical path and field size [243]. In order to prevent this, contact mode photolithography is used during the photolithography stages in this work.

In general, we can see an alignment accuracy of around 5 μm for a skilled operator

with well-defined alignment markers. This accuracy degrades with the thicker resist coverage used on the cantilever definition level. This is due to the light from the microscope refracting more and the topographic features having a different focal point than the flat, giving various focal points between the mask plate and sample with a tolerance of around 10 μm observed. As photolithography is also used to define the etched markers, we need to have the same coordinate system on the mask plate as the EBL level, meaning that the EBL field is distorted to conform to the photomask.

The probe process also requires the use of backside to frontside alignment, allowing features to be defined on both sides of the wafer. The probe chip is defined on the back side as well as the front side, with deep trenches formed by the side of the chip on the backside side of wafer through an aggressive etch. The alignment of the front to the back must be good enough to allow the chip location to match up and etched region to go through the whole wafer at the end of the fabrication. The backside alignment technique uses a camera to broadcast a live image through the chuck area where the mask plate is first loaded. The camera position is moved in x and y until the marker region on the mask plate is found and the image captured. The wafer is then loaded onto the chuck with the front side face down, the camera can then locate the marker region defined on this side from the initial etch. The image of the markers on the mask plate is looped in with the live feed of the cameras observations on the front side. Manual alignment using the micrometers is utilised so that the region of markers on the front side (live feed) matches that of the still image of the mask plate. An image depicting photolithography alignment with an etched marker substrate is shown in Figure **fig:photoaln**.

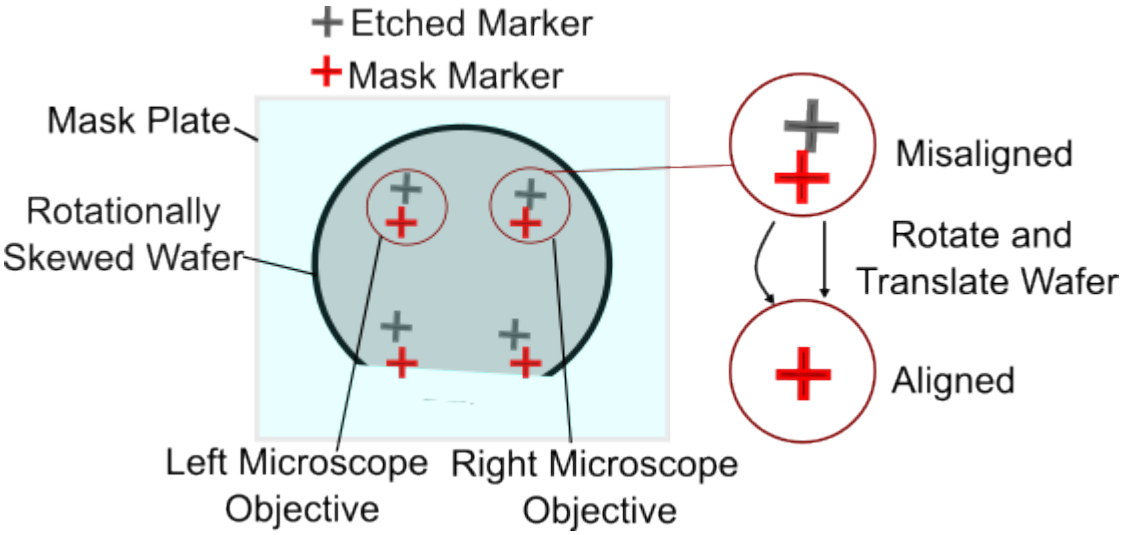

FIGURE 2.2: Diagram showing how the photolithography mask has to align with the etched markers on the substrate to align pattern layers.

2.3 Electron Beam Lithography

2.3.1 Overview

Electron beam lithography is the lithographic defining process for all the high resolution features of the probe manufacture, as well as the calibration samples. In this project, the lithographic tool utilises a high accelerating voltage (100kV) anode to directly pattern features onto electron beam resist, compared to photolithography whereby UV and photoresist is used.

2.3.2 Pattern Design

In order to define features onto the resist, the pattern's dimensions are designed using CAD. The designs of the photolithography layers and EBL patterns are written within the same CAD file, which is helpful in assessing how the full patterned substrate will look and determining placement of alignment markers. This means that the photolithography masks can be written within the same tool as the direct exposure levels. The CAD file can be taken and generated into commands understood by the machine, be it exposing a mask plate design, which will be subsequently wet etched into a metal film, or directly writing an e-beam layer.

The "resolution" is the address grid and sets the accuracy of the design placement of the EBL tool, this is not the resolution of shapes patterned by the tool, but the granularity of the beam position. The BSS is the size of the distance where the beam is moved to fill a shape. The BSS is an integer multiple of the resolution known as the VRU. These statements follow the relation in equation 2.1 below:

$$BeamStepSize(BSS) = VRU \cdot Resolutiongrid \tag{2.1}$$

2.3.2.1 Fracturing

The GDSII files outputted from the CAD software (L-edit) used to design the patterns are input into a tool known as Layout BEAMER. The software transforms polygons (of any shape designed using L-edit) into trapezoids in which the EBPG can recognise. As well as doing this, BEAMER can also be used to define the field ordering, whereby the order of structure writing can be specified within the writing field. BEAMER allows the user

to "Follow Geometry" as opposed to the standard "Array Compaction" when designating the writing path. The electron beam path of both orders are depicted in Figure2.3, where a penrose pattern is being exposed.

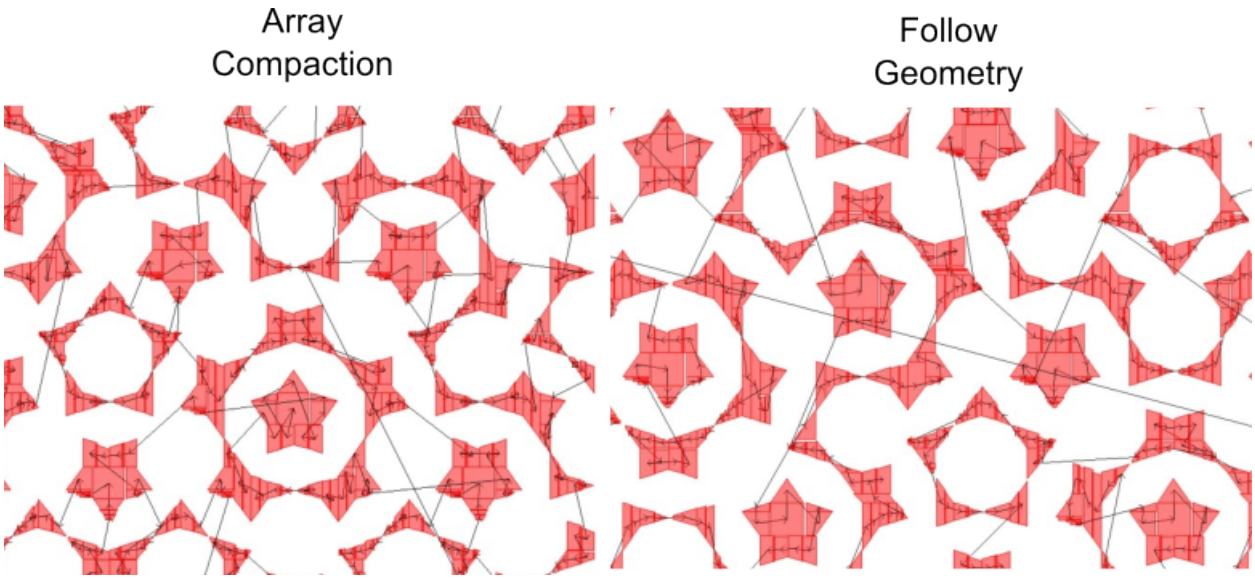

FIGURE 2.3: The image depicts the path the EBL path will take to expose a penrose pattern. As can be seen in the Follow Geometry method, the beam finishes what it is writing in the pattern and will then move off. The Array Compaction beam path moves all across the pattern, half-finishing some and then coming back.

Follow geometry groups features that belong together and exposes them successively even when they cross field boundaries. This reduces the risk of overexposure due to drift, i.e. the beam exposes some of the same pattern file, moves and returns to complete the job. It also ensures any long structures where stitching may be an issue, like a waveguide, are completed in one go even if they cross a field/subfield boundary. In this case the Penrose patterns are written one at a time and there will be less error in pattern shape due to drifting of the e-beam. The Penrose patterns will be used within the fabrication of calibration samples where precise alignment is paramount.

The software used to set dose, spot size and pattern placement on the substrate is known as C-JOB. C-JOB turns BEAMER's outputted GPF file and turns it into a JOB file which can be read by the EBPG. A process flow of this drawing to lithographic pattern on substrate is shown in Figure 2.4 and a diagram of the EBPG column is shown in Figure 2.5.

FIGURE 2.4: Process flow depicting the path and the software used to turn a CAD file into a job which the EBPG can read and pattern. The software and servers used are indicated in Blue below the rectangles and the operation shown in the rectangles. The exported file from said operation is indicated in red writing above the rectangles.

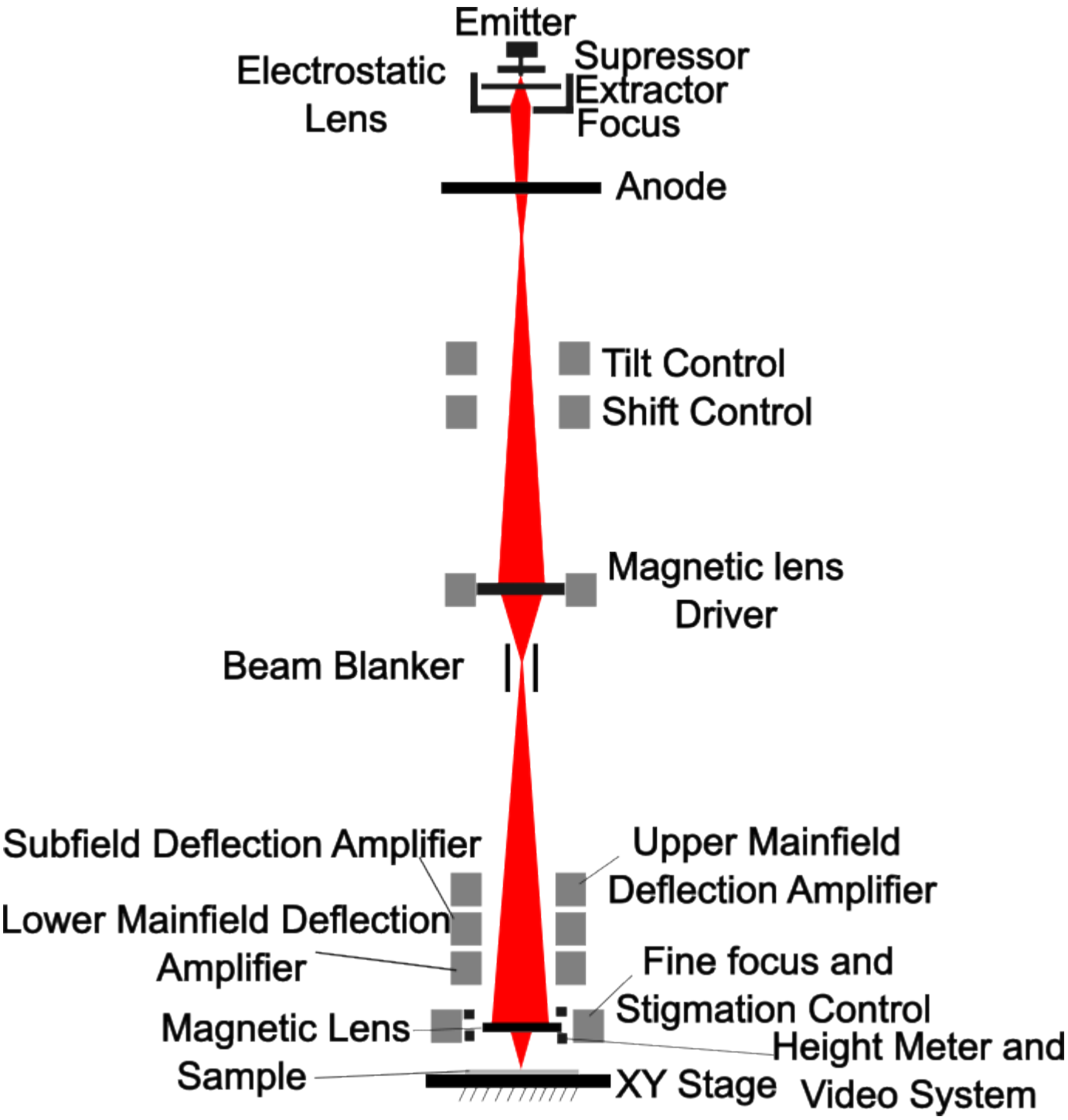

FIGURE 2.5: Diagram of the EBPG column used to expose the majority of the EBL patterns in this work.

2.4 E-beam Alignment

Many semiconductor devices require the use of multiple lithographic levels, be it to have different metal thicknesses after-lift off around the devices or to have better proximity control during exposures. These TERS probes require good alignment from the start, without it the probe cantilever could be misaligned from the chip, affecting the spring constant and the effectiveness of the cantilever to operate as an AFM probe. The grating also must be close to the apex of the tip as the surface plasmon polariton can only propagate for short distances before it decays. In a similar geometric design this is 10 μm for an 800 nm laser [204]. The taper apex of the nanoantenna must also cover the apex of the probe tip, this gives a large enhancement of the electric field whilst retrieving topographic data at the same location, allowing for a TERS measurement to be taken. If the taper is offset, the electric field would be localised elsewhere or not concentrate and leak out the sides with no useful TERS measurements.

The process of alignment requires a marker feature, usually a square or cross, to be put down with the first lithographic level. Any subsequent lithography will then use these markers as a starting point to find where to expose with another lithographic level with respect to this marker position. There can be misalignments on the patterns position due to poor marker correlation, i.e. not finding enough markers or any at all. A figure of these misalignments is shown in Figure2.6.

One such alignment error is translational misalignment. This is where the pattern that has been exposed is offset vertically, horizontally, or both from the original patterned feature. These can occur due to poor clamping of the substrate onto the sample holder, causing drift or a shift of the sample's positioning, or even surface charging from the electron gun, or column causing the beam to translationally shift with respect to the sample. These occur very often due to sample loading, and it is imperative corrections are put in place to find the true placement of the first pattern's marker set.

Another error that can arise is rotational misalignment. These are also frequent and occur during sample loading, where if the sample is clamped facing the wrong way, or the wafer/piece flat is not making contact against the holder pins, then subsequent exposures can cause a sheared exposure.

Scale errors are another kind of misalignment during e-beam lithography exposures. These can occur if the height meter isn't operating efficiently, or the sample thickness is larger/smaller than prescribed. As the laser spot for the EBPG height meter is around 1mm in diameter, the readings for the height may not be as accurate as necessary and

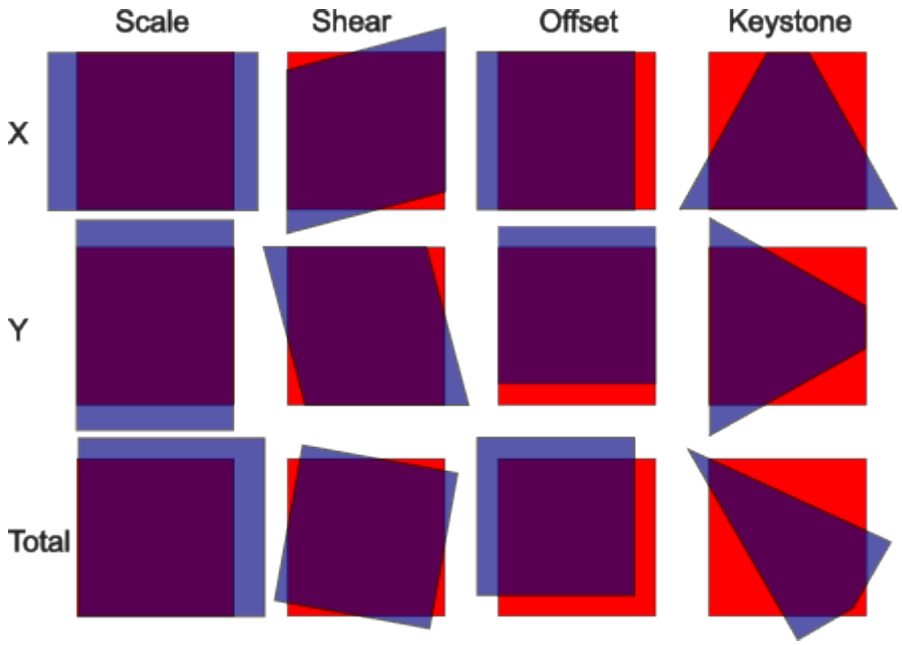

FIGURE 2.6: Diagram of the various misaligned patterns caused by poor marker correlation. The intended exposure is shown in red with the actual exposure due to the misalignment shown in green.

adjustments to the lens-sample distance may be off. This is due to the thickness of the sample significantly changing over smaller distances e.g. at the alignment marker blocks or the probes tip. This is why fine structures are written on axis by translating the stage before exposure. A schematic of the height meter in operation is shown in Figure 2.7.

Keystone errors occur when the sample to be exposed has a tilt offset from that of when the alignment markers were put down. These cause significant shift in the alignment and care must be taken to clean resist off the back of samples (ensuring it has no significant topographic difference from the first layer) and ensure the stage has no tilt.

When designing the layout of the lithographic features, there exists an ideal grid of what you wish to see on your wafer after exposure. However, because of the many errors discussed, distortions can induce errors on the coordinates of marker and feature placement. Projective transformation is then used to account for these errors and map the ideal, designated coordinates to the coordinates of what is already on the sample. These are linear transformations which map the two sets of coordinates as any misalignments are small enough to be regarded as linear, be it the tilt, positioning or even rotation. Any bowing or bending of the wafer that occurs can also be approximated as linear due to their small magnitude over a small sample area [244]. On the latest batch of 4" wafers, this bow is $\leq$40 μm, giving a 2 μm per mm slope at the wafer edge (worse case scenario).

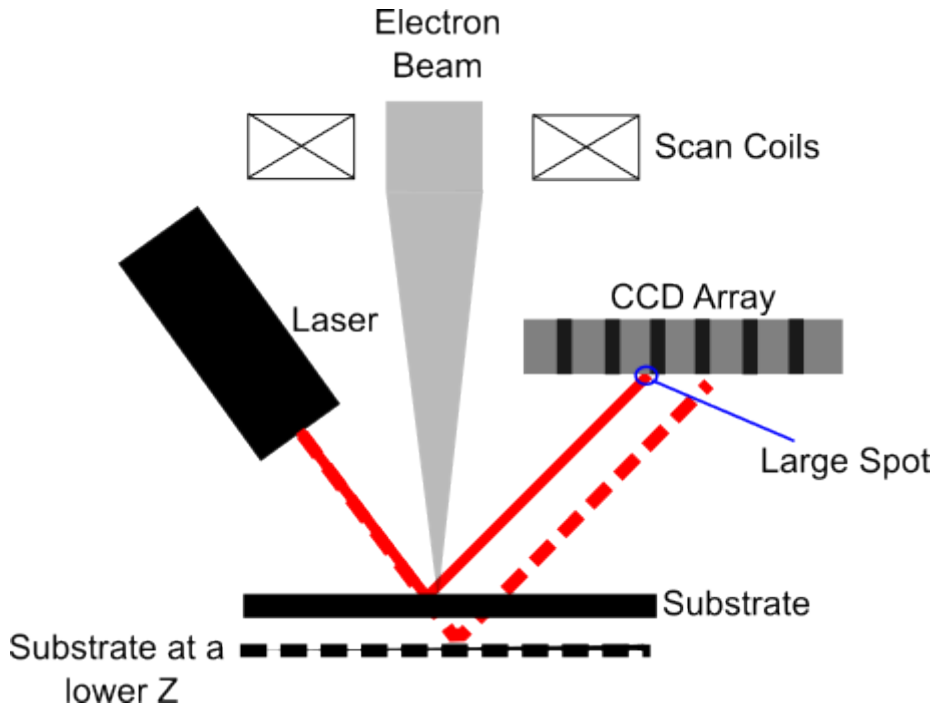

FIGURE 2.7: Diagram of the height meter of the e-beam tool in operation. It shows how the detection of the substrate surface is done so via the reflected laser onto the CCD array, where the lens-surface separation distance is calculated and dependent on the substrate height.

To convert between the displaced system and ideal system, the relationship between the $4x$ and $4y$ coordinates of the previously exposed pattern and the ideal design (8 points total) is determined as shown in Figure 2.6. This allows for a good alignment as it contains enough information for the tool to compute a projective transformation. This is usually taken from the corners of 4 markers as reference points, positioned on 4 corners of a sample, this is to give good sensitivity to keystone distortions. Further markers can be placed close to the exposure area, these are known as cell markers. These account for any local variations on the sample, accounting for them and maximising the sensitivity to all distortion classes. A problem with this scheme is that a single bad marker can lead to misalignments on the order of 100 nm [245]. An example is whilst using a topographic marker search, damage and anisotropic etching of a surface can give the appearance of a perfect marker, but be in the wrong place.

To combat this, Thoms et al. [245] came up with an algorithm for the detection and removal poor markers during a search in an EBL tool. Markers with a residual offset greater than 3 standard deviations were considered outliers, with a box and whisker approach also being used with an ordinary least squares method. This method was able to detect outliers well especially placed around the edge of the sample uniformly. A trimmed least

squares regression algorithm [246] consistently found outliers, from minimising the sum of squares of a subset of the markers. Thoms found he could get 20 nm alignment accuracy on a patterned substrate with 50% poor markers, with positional errors between 100 and 300 nm [245].

2.4.1 Marker Detection

As described above, we can correct for local (cell) and sample size (global) misalignment of a sample by mapping the relative positions of markers on a distorted sample from an idealised one. These markers are commonly shaped like squares which are etched into a sample or are composed of a noble metal. Noble metals are used as they have a high atomic number and stay the same during processing. Their interaction with an interrogating electron beam are governed by Rutherford's scattering formula, whereby the yield of backscattered electrons scales as the square of the atomic number [244], [247]. Note that backscattered electrons are elastically scattered by the substrate so have almost the same energy as the incident beam.

The markers are detected with a backscatter detector of the e-beam tool, where the beam scans over the marker and detects the backscattered electron signal as a function of beam position. For a positive metal marker, the beam will scatter a lot on the sample region, especially if it has a high atomic number. This means that when a large atomic number material is surrounded by a material with a lower atomic number, the magnitude of the total backscattered electron signal will be larger on the marker than around it. The beam is scanned multiple times along the x and y axis of the marker edge, whilst taking the average of the backscatter magnitude, or rate of change, to account for noise. This provides a level of contrast required to detect a marker is in that position, calculating where the marker centre is from the detected edges. An example magnitude trace of a backscattered signal is shown in Figure2.8.

Another contrast phenomena which occur during marker detection is edge contrast. This is where backscattered electrons have a high energy and probability of escaping on a topographic feature. As the backscattered electron path on the topography differs from that on the flat, the BSE detectors receive a signal differential from the BSE escape points allowing for edge detection [247]. This phenomenon is seen on the etched markers employed on probe wafers with a diagram depicting it shown in Figure2.9.

The drawbacks of using a marker, like a square, is the marker's positioning is only as useful as the edges that encompass it. This directly relates to how accurate the beam's

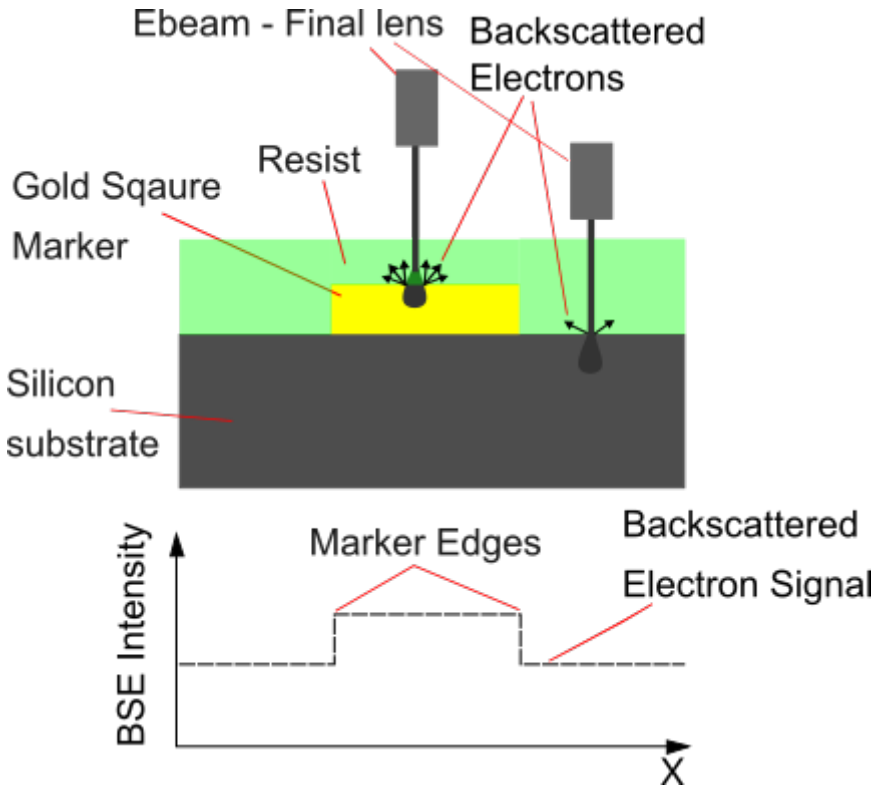

FIGURE 2.8: Diagram depicting how the magnitude of backscattered electrons varies with a metal and a semiconductor sample. The trace at the bottom shows how the magnitude of the backscattered electron signal increases as the beam scans across the metal on the sample.

alignment will be, with an increasing number of edges you get a larger signal to noise ratio but a longer interrogation time. This means the marker searches are slower which leads to the beam drifting over time, degrading the search accuracy. The marker interrogation also requires a large beam current to generate the larger signal to noise. This in turn also exposes the resist and leaves the marker exposed after development, meaning it is open to any further processing after the exposure and hence marker edge degradation. This is why multiple alignment markers are required around the substrate whilst doing multiple exposures, so a fresh marker can be used at each processing step.

As the machine's determination of what is a marker is the difference in contrast, it may pick up anything as a marker unless parameters are prescribed. One such parameter is location of where to search for marker and it's dimensions. Prescribing a search radius and rough location, the electron beam scans the area receiving the signal of the backscattered electrons. It determines, by the signal, if the measured contrast difference is equal to that of the dimensions prescribed in the job file. A SEM image of the tool's search of an etched marker is shown in Figure 2.10 with the video signal in Figure2.11 .

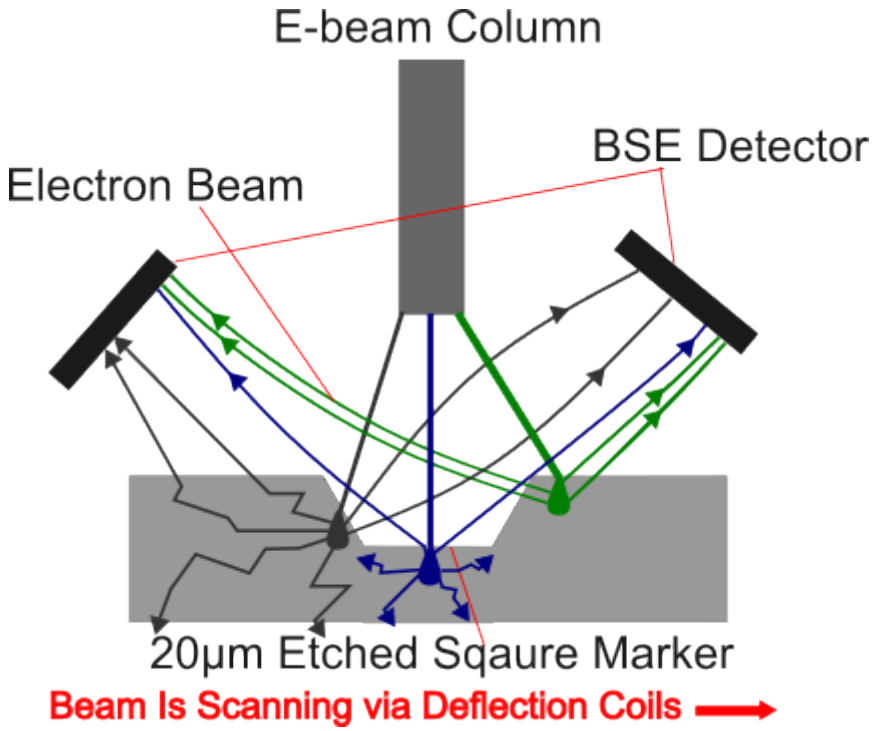

FIGURE 2.9: Diagram showing edge contrast in operation, illustrating how the detector can visualise the marker edges.

2.4.1.1 Marker Correlation

A method of reducing marker degradation and misalignment known as correlation is detailed within K. Docherty's PhD thesis [244]. Within e-beam, marker correlation is the measure of similarity of two functions, or a reference image file of the designated marker with the image of the marker which is on the sample (distortions included) [248], [249]. Correlation takes multiple points between the images and measures this similarity with the differing relative offset.

Marker correlation is not limited to the use of linear scans across edges which is traditionally the method used to perform alignment using square markers. Any shape with a well-defined centre may be used with preference given to shapes with many edges. In 2009, Docherty et al [244], [248] pioneered the way for using Penrose patterns as image correlation markers. The Penrose tiling is an infinite aperiodic pattern on a 2-D plane, with any patch translationally unique to that area over a distance on the order of 12 times the size of the patch. When used as alignment markers, patterns are made up rhombic and triangular elements with 5-fold rotational symmetry, which means that when the e-beam samples a region using a rectangular grid the pattern is incoherent with the sampling grid. This incoherence means that whilst sampling occurs, a small change in position

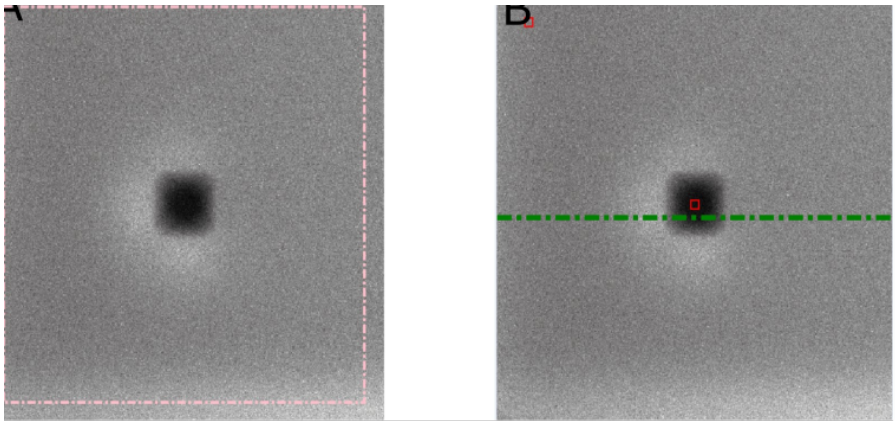

FIGURE 2.10: Captured SEM image of the ebeam tool's search of an etched marker.

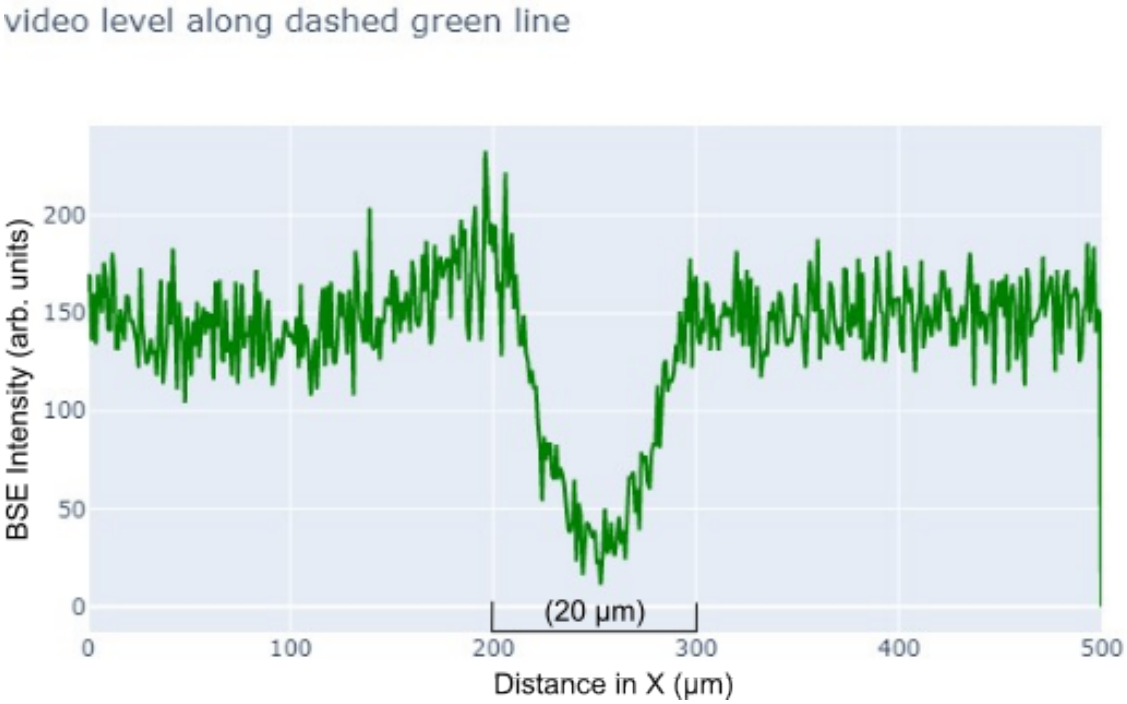

FIGURE 2.11: Captured plot of the e-beam video signal whilst scanning across the dashed green line in the marker depicted in Figure 2.10. This shows the contrast over the green area, and where the tool will determine where the edges of a marker is. Index is the length of scan and value is the intensity.

always makes a large change in the detected pattern, since some samples will always be on an edge. Another attractive aspect of these markers is that the correlation process is highly tolerant of damage to or defects in the marker and optimal in the presence of

Gaussian noise (shot noise in this case). Penrose patterns are featured in this work in section4.2, where it is paramount to achieve optimal alignment accuracy between gold dots and dimers written as two separate exposures.

2.5 Etching

2.5.1 Dry Etch

Dry etching is a commonly used procedure during the batch fabrication process. In this work, photolithography is used to define a feature and remove the resist, whilst selectively masking the remaining parts before exposure with a RF plasma etchant. Depending on the gas selection and other process parameters (e.g. temperature, pressure, power) a variety of side-wall profiles and chemical selectivity can be achieved [250].

The removal of material by dry etching can be done with a physical or a chemical approach [251]. The physical approach employs the use of energetic ions from the plasma source (usually a noble gas) to bombard the sample. The momentum transfer within this process physically removes the material from the sample, resulting in a slow, anisotropic etch.

The chemical approach occurs when non-noble gases are used, usually consisting of a Halogen, with some fluorine-based gas for silicon samples as SiF4 is very volatile [252]. When a plasma is struck with these gases, it induces the generation of free radicals. These free radicals are directed towards the sample, are absorbed onto the surface, and undergo localised chemical reactions. It should be noted that free radicals can also transfer momentum with the surface and as such cause a physical reaction before any chemical reaction. After the chemical reactions are finished, the by products of the reaction desorb from the surface before diffusing back into the plasma. These by-products are pumped out of the chamber if they are volatile, reducing the contamination within the chamber. These reactions are typically anisotropic, especially when using a resist, dielectric or metal hard mask. The processing parameters such as the process power and pressure will generate differing degrees of anisotropy. The tools used within this work are Oxford Instruments R.I.E. tools known as the BP80 and 80+, with staff at the JWNC facility operating them, however process parameters must be determined by the user.

Within this work, Fluorine-based gases are used to pattern into silicon nitride with photolithography masks. Oxygen based plasma has routinely been used to remove organic contaminants off the substrate surfaces in a process known as "ashing". These parameters are highlighted in Sections 2.7 and 2.8.1.

2.5.2 Wet Etch

All the bulk silicon etching within this project has been performed with anisotropic alkaline (hydroxide) etches. The chemical etches are used to "release" the final probes from the wafer use TMAH. Removal of dry etching contamination and fabrication of the pyramids, used to define the angle of the cantilever, were conducted with a 55 °C KOH and IPA solution. More details on the pyramid fabrication of the probes and etch solution are detailed within section 2.7. An image of the lithographic steps with a cross sectional view of the accompanying etches of the material are depicted in Figure 2.12.

The basic chemical reaction with Si in an alkaline medium is shown below [141]:

$$Si + 2OH^- + 2H_2O \rightarrow SiO_2(OH)_2{}^{2-} + 2H_2$$

These etches are considered anisotropic since different crystal planes in the Si lattice are etched at different rates. This arises from the Si atoms having differing bonding strengths at differing crystal planes [253] and because KOH/TMAH Si etching is etch rate limited and not diffusion limited. The choice of etchant chemistry delivers different plane selectivity and surface finish, and as such must be chosen carefully. As the fabrication of the released probes has been extensively studied by R. Lambert [141] and pyramidal etches by A. Midha [254], the only necessary changes required was an increase in etch time to account for the increase in silicon left over from the final dry etch and release the probes from the wafer. The reasoning behind this will be discussed further in section 3.3.1.

As these are chemical attacks of all exposed wafer material, a suitable masking material is also required to etch the correct region. PMMA or photoresist masks are not suitable as they are not durable within the etch, although short wet etches to hydrogen terminate an exposed silicon area with HF or to perform a quick clean is possible. This body of work utilises LPCVD silicon nitride as the masking material due to its good etch resistance to both the TMAH and KOH solutions used. The masking material is patterned with the use of photolithography and e-beam lithography (see Figure 2.12), where the cantilever lithography was designed by myself. The time of the wet etches used to free the cantilever

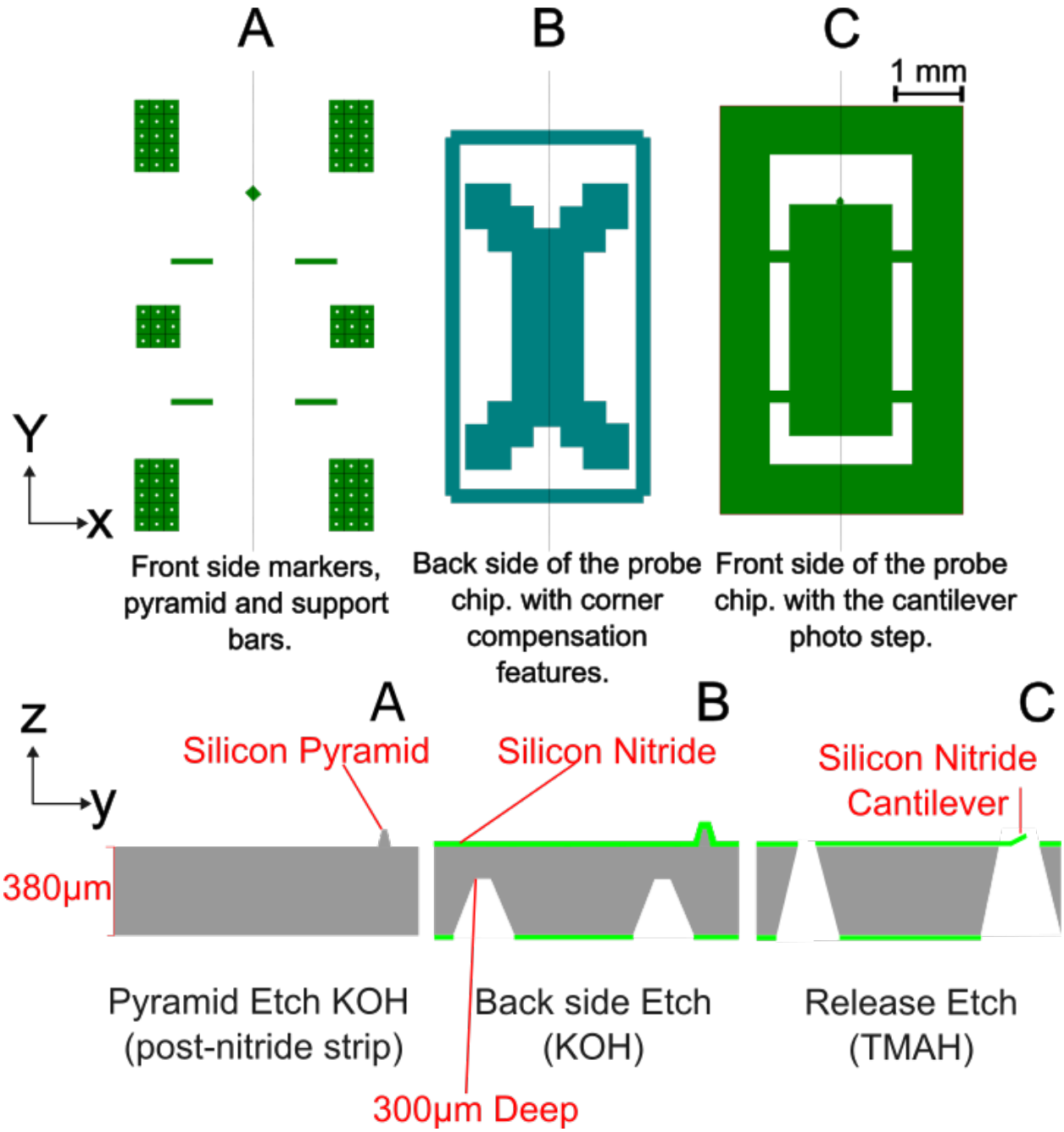

FIGURE 2.12: Diagram showing the photomask layers of the substrate with a cross sectional view of the wet etches it undergoes beneath it.

and etch the backside were also determined by myself. The anisotropic etch of the (100) silicon that is used in the project, with the LPCVD silicon nitride mask, results in sloped silicon sidewalls. This is due to the {111} planes etch much slower than the {100} planes. A slight undercut of the LPCVD nitride can also be seen in the {111} planes. A diagram of this is depicted in Figure 2.13.

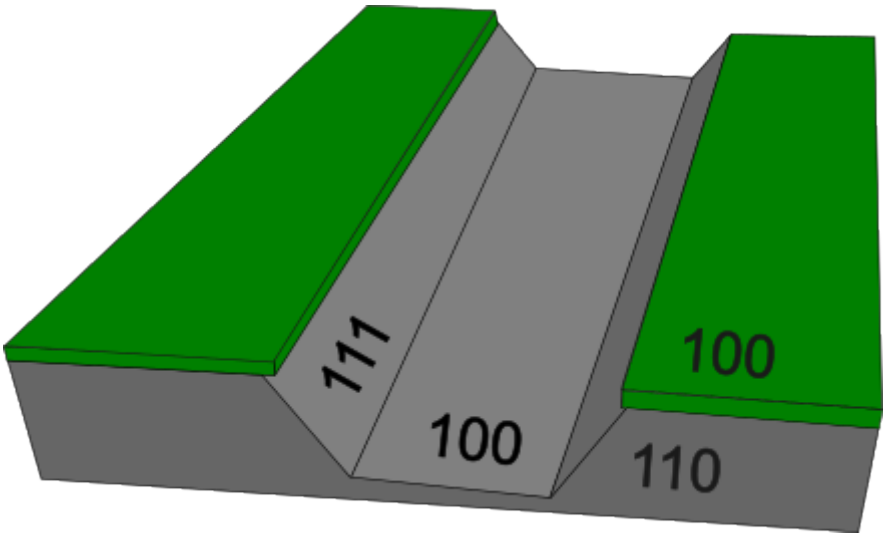

FIGURE 2.13: Diagram showing a wet etched silicon substrate with silicon nitride mask. The angle formed between the two planes is 54.7 °.

2.5.2.1 Wet Etch Kit

Two things are required for a stable wet etch. Firstly a constant temperature, or at least good regulation, since the rate of reaction increases by . Secondly it is necessary to keep the concentration of etchant constant, as if the solution is more concentrated than a previous etch, then it is expected that the etch rate will also increase. For the TMAH release etch, the stability of the etch has to be within 5 μm in 300 μm and for the KOH pyramid etch it has to be within 2 μm in 15 μm. A diagram of an example etch rate vs temperature of <100> silicon and how it behaves with concentrated KOH or mixed with IPA is shown in Figure 2.14. It shows as that with an increase in temperature, an exponential increase in the etch rate of <100> silicon is seen. Although the etch rates of the {100}, {110} and {111} planes etch rates increase exponentially with temperature, the {100} and {110} etch at a much faster rate than the {111} plane.

This work made use of a wet etch kit, which hosts the etch solution in a 2L Pyrex reaction flask. This flask then sits on top of a heated electro-mantle, where the temperature is regulated with an immersion thermometer connected to a temperature controller regulating the power of the heating mantle. An earth leakage circuit breaker disconnects power from the system in the event if a leak onto the heating element. At the etch temperature, water can evaporate and hence change the concentration of the etchant, this is corrected for with a Teflon cover with a steel clamp covering it to create a tight seal. Any water vapour is cooled down with a reflux condenser placed into an opening in the Teflon lid. Wafers are placed into a variety of Teflon holders dependent on sample size,

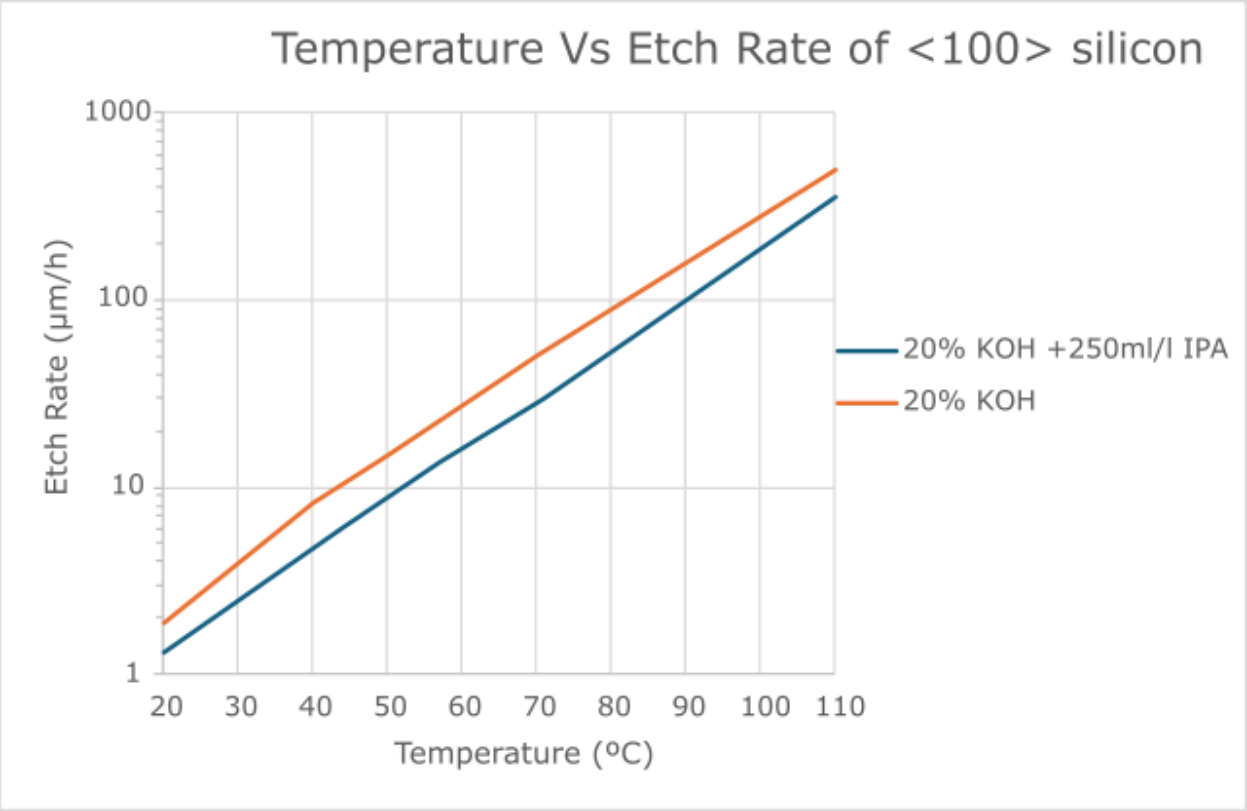

FIGURE 2.14: Graph showing the etch rate vs temperature of <100> silicon. All data was taken from a paper by Seidel et. al. [255]

held together with Teflon screws. The holder is hooked onto a corrosion resistant steel rod which passes through the lid. This all together seals in the etchant ready for the etch to begin. A diagram of the etch kit is shown below in Figure 2.15.

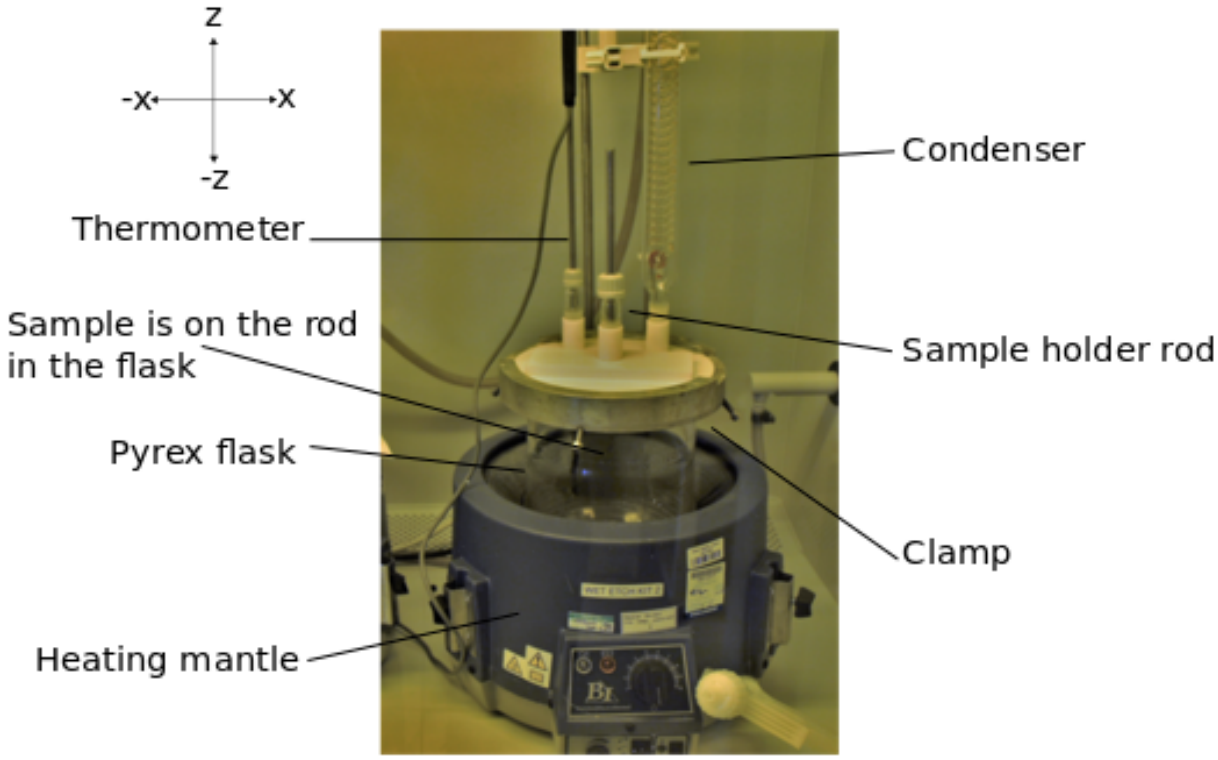

FIGURE 2.15: Annotated photo of the etch kit which is used for the majority of the wet etches within this work.

2.6 Base Level Fabrication

As the tip imparts the sensor functionality to the device, it's importance is key to device operation. The fabrication techniques and design choices made to ensure the tip is fabricated effectively will be discussed below.

With traditional AFM probes the most important factors to consider are spring constant, quality factor, resonant frequency and tip sharpness. Within the fabrication process, different materials and thicknesses can be used to suit the specific requirements of the end-user metrologist. The geometry of the tip directly affects resolution, if it is not small, it may produce a false reconstruction of the sample's topography. An example of this is shown in Figure 2.16. In order to produce accurate topographic mapping, the tip geometry should be tapered to a point and the tip radius should be small, typically less than 50 nm [256]. If the tip is not hard enough, the shape of the tip will change over time causing irreproducibility and artefacts in the images obtained [130].

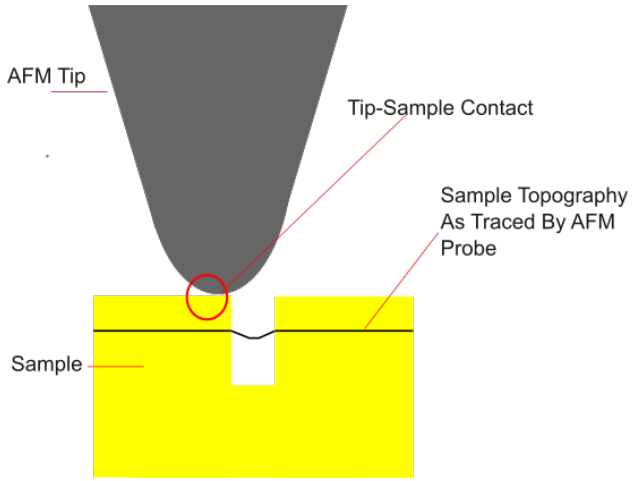

FIGURE 2.16: Schematic diagram showing a topography trace of a poorly resolved sample. It is apparent that the trace is not a true convolution as there is no way to de-convolve the trajectory to achieve the true dimensions of the sample.

Dealing with functionalised SPM, these factors are all still of great importance but with more focus on other properties. During the fabrication of the probes it is imperative to consider the compatibility of the chemicals and tools available to deposit or etch. Design limitations are introduced by the chemical etchants, dry etch gases, surface adhesion used within the fabrication process and the effectiveness when acting as an antenna. As an example, aluminium can't be used on the probes using the current process as in the release etch the primary etchant is TMAH (Tetramethylammonium hydroxide), which etches this material [257]. This could be prevented by doping the solution with silicon and ammonium persulfate [258], but this would involve changing the chemistry of the current high yield/robust process. Individual probes may have aluminium evaporated onto them when they are freed from the wafer, this is however less efficient than within a batch fabrication process.

2.7 Pyramid Fabrication

Design of the tip geometry for the probe wafers is based on KOH (Potassium hydroxide) etching of silicon to reveal pyramidal structures. The pyramids provide a slope and solid surface for patterning and defining the tip using EBL. The optimum etch parameters and crystallographic orientations are given in the thesis by A.Midha [254]. A process flow for the fabrication is tabulated below in Table 2.1 with Figure 2.17 to match.

Process flow for pyramid fabrication	
Step number	Stage details
1	A 380 μm thick double side polished 3" silicon wafer, with 40 nm silicon dioxide and 60 nm silicon nitride on top is cleaned with acetone, methanol, IPA (all within an ultrasonic bath) and an RO water rinse, respectively for 5 minutes each.
2	MCC 80:20 primer is applied before S1828 photoresist at 3 krpm for 30 s on top of the back side.
3	Sample is baked at 90 °C for 30 minutes.
4	Front side of the sample is oxygen barrel ashed at 100 W for 5 minutes.
5	MCC 80:20 primer is applied before S1818 photoresist at 4 k rpm for 30 s on top of the front side.
6	Sample is baked at 90 °C for 30 minutes.
7	Sample is exposed with a photolithography tool for 5 seconds with a 35 μm alignment gap at hard contact.
8	Sample is developed in a 1:1 microposit:RO water solution for 75 seconds before a 5 minute RO water rinse and nitrogen gun dry.
9	The sample is placed into the BP80 RIE. Using C_2F_6 as the inlet gas with a flow rate of 20 sccm, 23 mT pressure, 100 W power for 5 minutes.
10	The remaining resist is then removed using acetone, finishing off with an IPA rinse and nitrogen gun dry.
11	The sample is placed into the RIE 80+ for an O_2 ash. The flow rate is 50 sccm with a pressure of 50 mT, 100 W power and a time of 5 minutes to remove surface contaminants.
12	The sample is added to a 20:1, RO water:48% hydrofluoric acid solution and finished with an IPA rinse.
13	618.9 g of KOH pellets is dissolved in 1.5 L of RO water. 1.6 L of the final solution is added to the kit, along with 400 mL of IPA where the mixture is kept at a constant temperature of 55 °C. The sample is added for 69 minutes.
14	The sample is transported into a 5:1 RO:98% sulphuric acid solution. The sample is then rinsed in RO water for 10 minutes before optical microscope inspection.

TABLE 2.1: Table detailing the process flow for the fabrication of the silicon pyramids.

The next step is to remove all the silicon nitride and oxide in the areas without resist, using it as a mask. The wafer is placed into a reactive ion etching tool known as the BP80. The etchant in the tool is C_2F_6, with a flow rate of 20 sccm, 23 mT pressure, 100 W power for 5 minutes. The remaining resist is then removed by solvent cleaning, before being O_2 plasma ashed. As this process is sensitive to resist residues, as to not mask or inhibit the subsequent wet etch, both a wet procedure to dissolve the resist and plasma to remove the remaining resist and any remaining solvent residues is required.

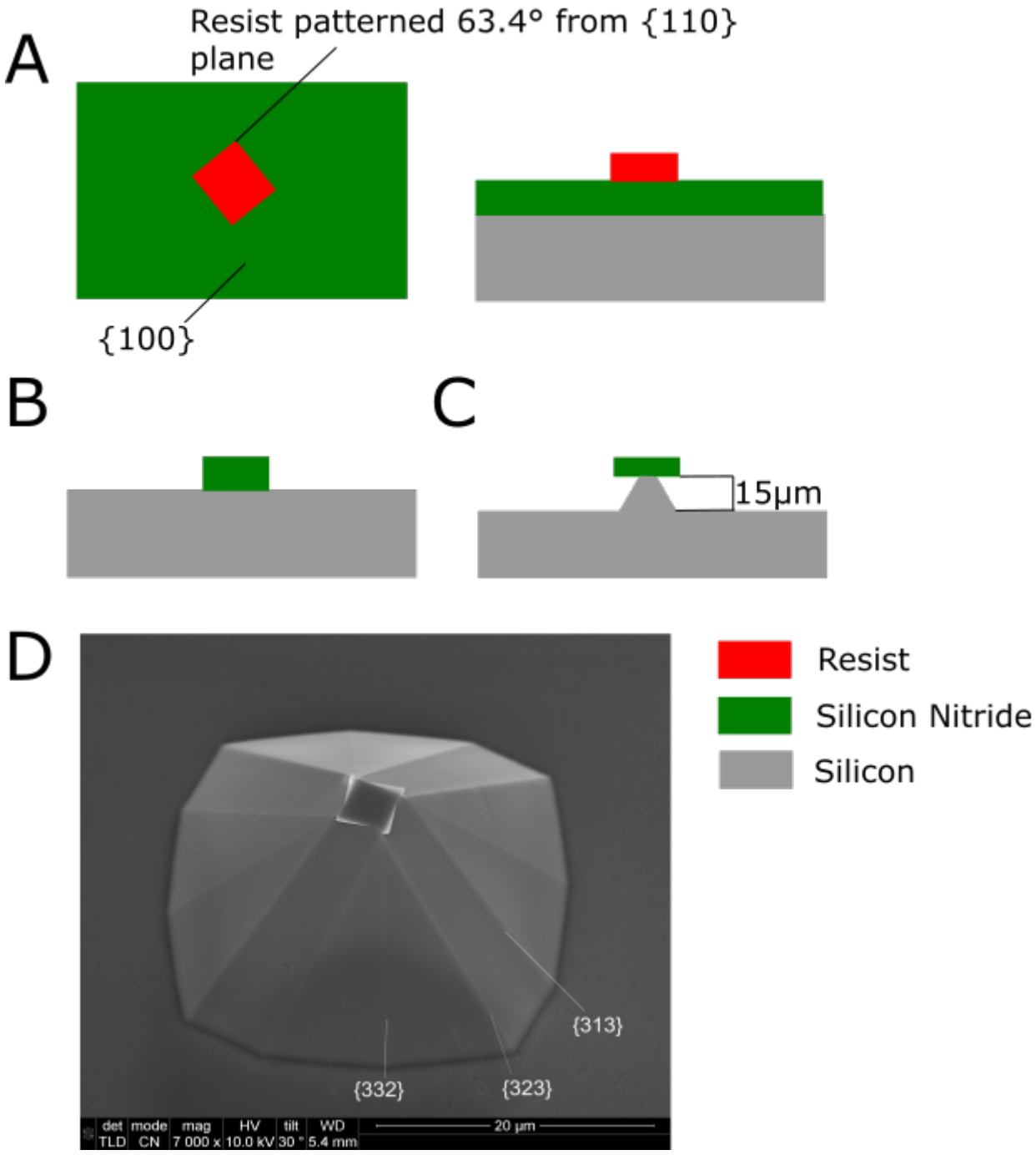

FIGURE 2.17: Schematic diagram of the pyramid stages. A shows the patterned resist square on the silicon nitride i.e left unexposed, with a side profile of the diagram beside it. B shows that after the dry etch the non-masked areas have been removed of silicon nitride and all that is left is a silicon nitride rotated square. C is the result of the KOH wet etch with the silicon con-caving towards the nitride cap. D is a SEM of the final result (the pyramid) after the HF etch removed the silicon nitride cap.

Before for the wet etch starts, the O_2 plasma removes the organic surface contamination. However, a native oxide grows on the surface of the silicon when exposed to air at room temperature and standard humidity [259]. Removal of this oxide layer is achieved through immersion in a 20:1, RO water : 48% hydrofluoric acid solution to produce a hydrogen-terminated silicon surface. The wafer is then rinsed in IPA before being dried with nitrogen to maintain the hydrogen terminated surface. The selectivity of the etching between the silicon and oxide is around 500:1 [260], this leads to an induction time if the oxide is not stripped, leading to a lack of reproducibility of the pyramid depth.

The sample is subsequentially placed into the wet etch kit where the constant temperature allows for better control of the etch depth. A magnetic stirrer is added to the kit to prevent bubble adhesion to the sample's surface. Adding IPA to the mixture reduces the etch rate in this direction and improves surface morphology [261] and smoothness. The etch rate of the KOH-IPA mixture is roughly 250 nm/min in the $\langle 100 \rangle$ direction. Furthermore, IPA is added to the etchant to prevent an "egg-timer" like geometry [254]. After the etch is complete, any remaining alkali is neutralised through submersion in 5:1 RO water:98% sulphuric acid. An etch depth of 15 ± 2 μm is acceptable because the angle does not change as this is dependent on plane selectivity. The plane selectivity of the etch causes the rotated square area to twist, resulting in pyramids with $\langle 313 \rangle$ plane sidewalls. The angle between the (100) surface and the sidewalls is 46.5 °. An angle greater than this would make the sample interrogation easier and produce a higher aspect ratio, however, with the directional nature of the metal evaporation tools, it is difficult to evenly coat high aspect ratio features. The pyramids are not etched to a sharp point, as the side walls are the only structures of interest, and a small silicon nitride cap (mask) still remains on the top. A SEM image of successfully patterned pyramids are shown in Figure 2.18.

Once the wet etching process is complete, the removal of the silicon nitride cap is performed. The nitride cap is removed by immersing the wafer in a 5:1 RO:48% hydrofluoric acid solution for 50 minutes and is inspected with an optical microscope. If it passes inspection it is packaged up to be sent to an external source for a 400 nm deposition of low pressure chemical vapour deposition (LPCVD) silicon nitride at Chalmers University of Technology. The deposition results in a conformal coating of the dielectric all across the sample, where the nitride on the walls of the pyramid will become the tip of the probe.

In the present work, the batch of silicon nitride deposited wafers came back with a quoted average thickness of 315 nm with a 3.12% uniformity. The reduced thickness decreases the spring constant, however this will make no difference to the TERS probes operation as the mechanical resonant frequency is found and used after each tip is loaded.

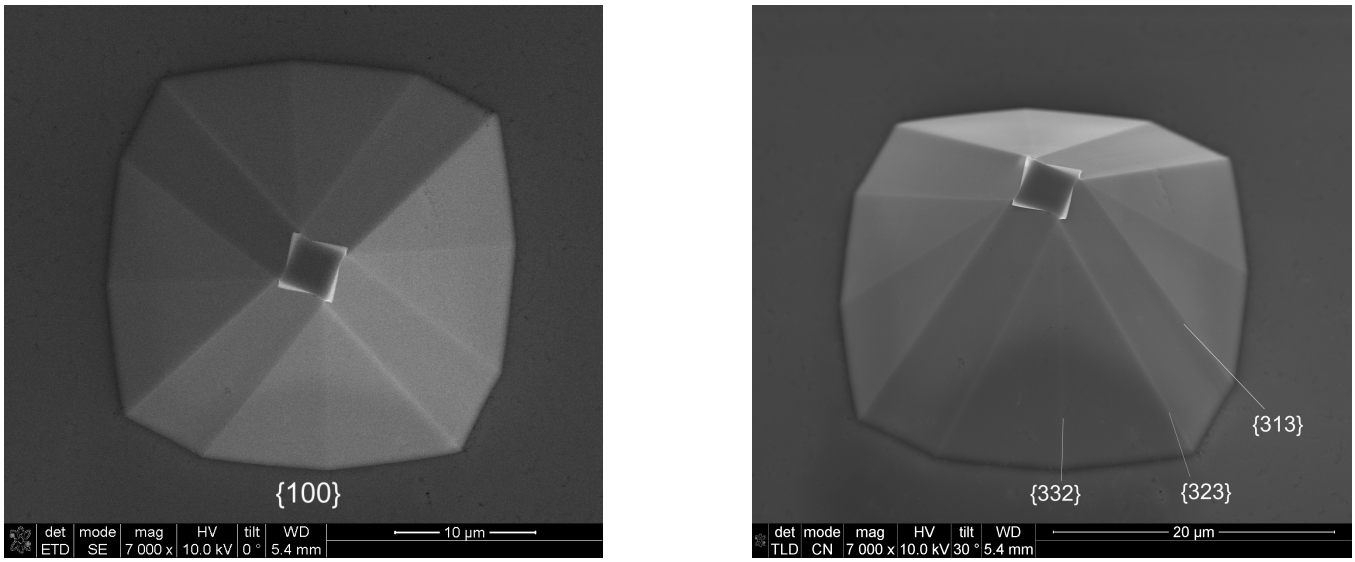

FIGURE 2.18: The image on the left shows an SEM image of the pyramids with 0 ° tilt and on the right is an SEM image of the same pyramid but with a 30 ° tilt.

The results of the deposition, which was sent by Chalmers, is indicated in Figure 2.19.

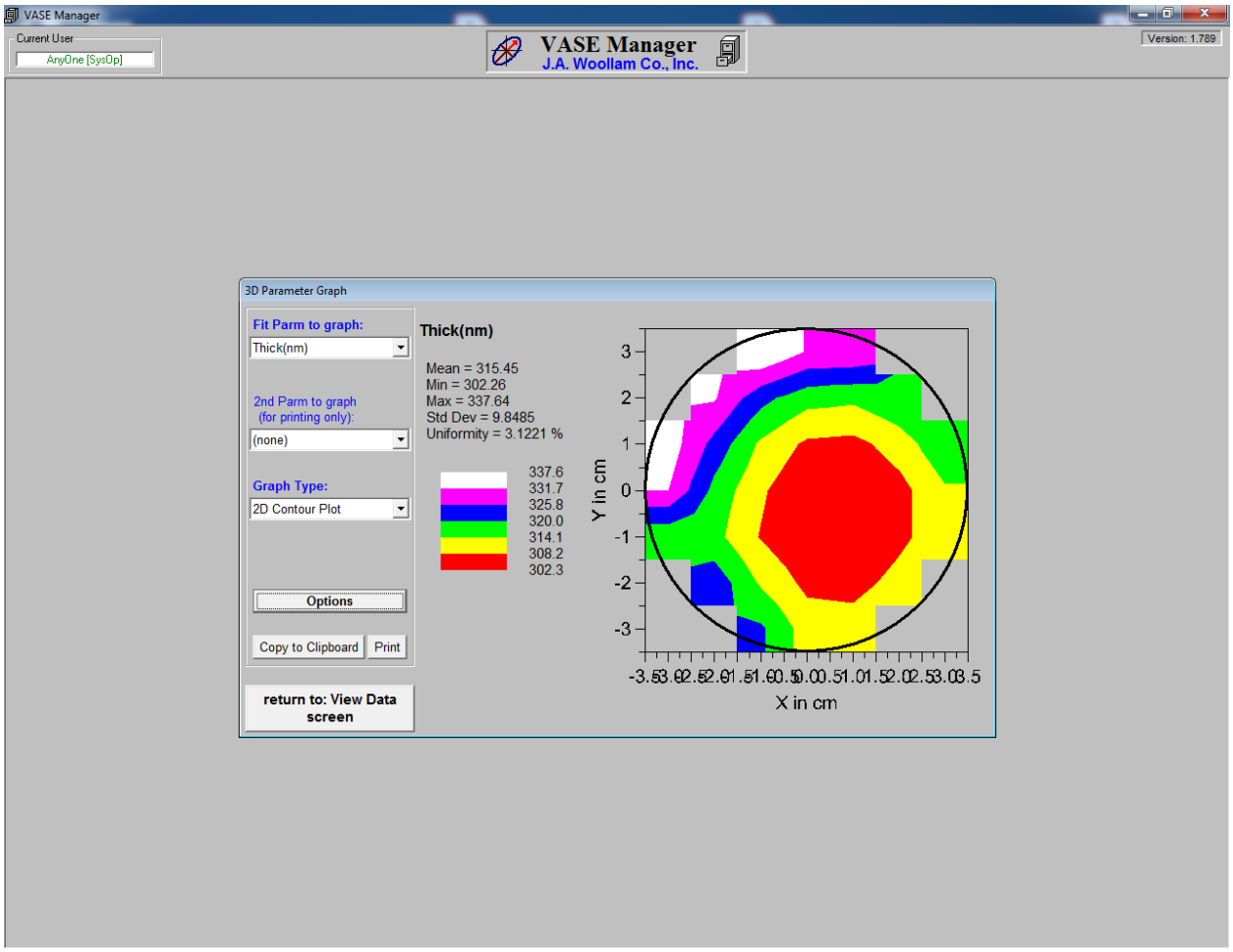

FIGURE 2.19: Image containing the deposition data recovered from the deposition of the LPCVD silicon nitride at Chalmers.

2.8 Cantilever and Chip Fabrication

2.8.1 Cantilever Defintion

The stages of fabrication of the probe cantilever and chip are well established in production of scanning thermal microscopy (SThM) probes. The SThM process utilises the exact same pyramid fabrication techniques and the same deposition process of the LPCVD nitride as detailed previously for the TERS probes. This section details how the cantilever shape and exposure parameters of both the photo and electron beam lithography are different and why it was needed. Experimentation on the subsequent *mow the grass* stages to release the tip from the cantilever were also conducted. Changes to times on the backside etch were also undertaken. The main overall differences to this compared to SThM are the sensor design and material for the production of the TERS probes.

With the pyramidal structures coated with the low stress silicon nitride, the cantilevers are ready to be fabricated onto the sloped sidewalls. The processing that occurs with the micromachined wafers, including the cantilever lift off and release is shown in Figure 2.20.

The cantilevers are formed using a two stage lithographic process. The first stage defines the outline of the cantilever using EBL, where a metal lift-off with 70 nm of evaporated NiCr is performed to allow the NiCr to act as a hard mask. The small spot size used within the EBL level allows for sharp, high resolution patterning to ensure the tip is sharp. The rest of the cantilever, as well as the probe chip is then defined using photolithography.

Although probes have been in development at the University of Glasgow since the early 1990's, defining the cantilever and sensor on AFM probes (Step 4 of Figure 2.20) is difficult due non-conformal coating of spun resist. Spin coating does not properly coat the pyramids, the topography causes the resist become non-uniform and thin across the top of the pyramids (see Figure 2.21).]

The non-conformal resist spread would lead to a variation in the dose in the resist, which in turn reduces the process latitude and gives different resolution in different areas. A thinner resist will also etch quicker in a plasma etch, meaning different selectivity at differing points and a bi-layer resist, where the bottom resist layer is at least twice the thickness of deposited metal, is required for a smooth subsequent metal lift-off (reduced flagging). These issues lead to the development of a technique known as float coating. The technique allows a solidified film of resist to coat the pyramids on the wafer. Through the combination of the processes spin coat and float coat, EBL can be used on the pyramids as the features are adequately coated [262]. The amount of float coats performed has increased to 6, as the previous 3 produced insufficient coverage over the pyramids. The technique of float coating is depicted in Figure 2.22.

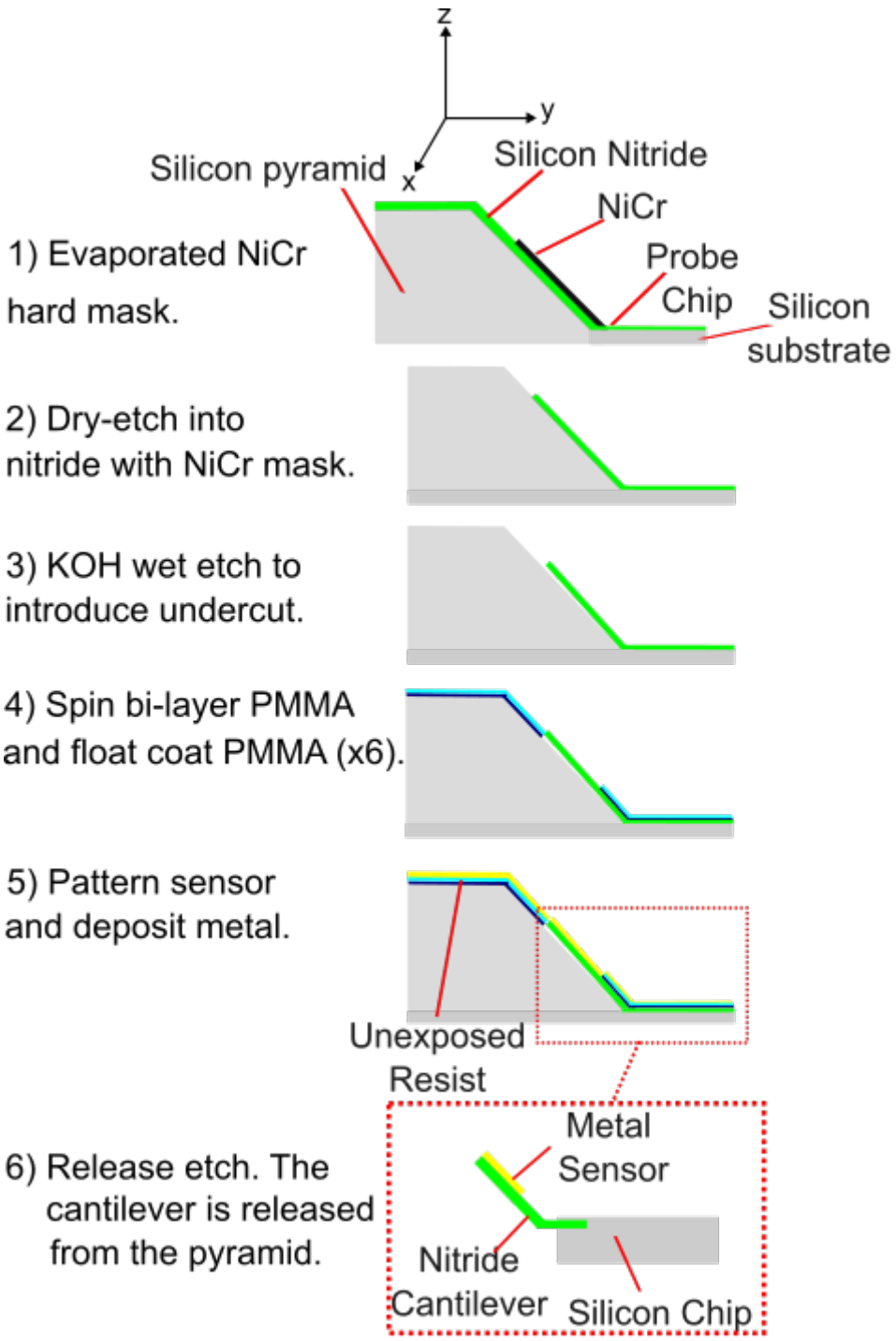

FIGURE 2.20: Diagram of the processing stages required in cantilever definition. Silicon is shown in grey, silicon nitride shown in green, NiCr is shown in black and gold in yellow.

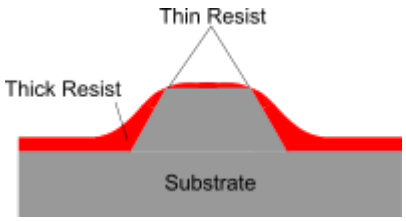

FIGURE 2.21: Schematic diagram showing the poor coating quality of spun resist over a pyramid.

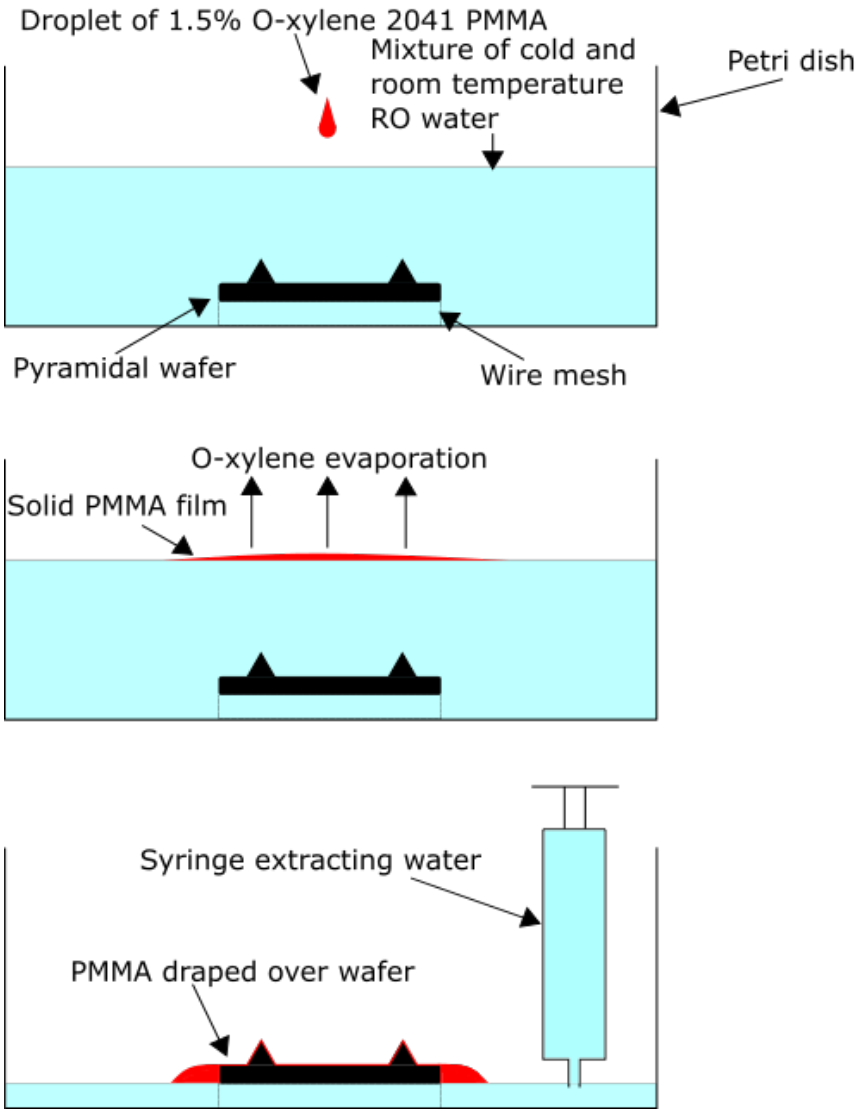

FIGURE 2.22: Schematic diagram showing the float coating procedure on the pyramid wafer. The wafer is placed on a wire mesh and submerged in a 50:50 mixture of RO water from the refrigerator and RO water at lab temperature. A droplet of resist is added and the solvent evaporates at room temperature. The water is then slowly extracted, revealing a thin film of resist covering the pyramids and wafer flat.[141]

The difference in molecular weights of PMMA is exploited throughout all the EBL definition processes where metal lift-off is undertaken. When the pattern is defined onto the resist and metal is deposited, it undergoes a process known as lift off [263]. After evaporation, the metal coats the resist, hot acetone peels back the remaining resist and metal remains on the sample only in the developed region. A schematic diagram of this process is shown in Figure 2.23

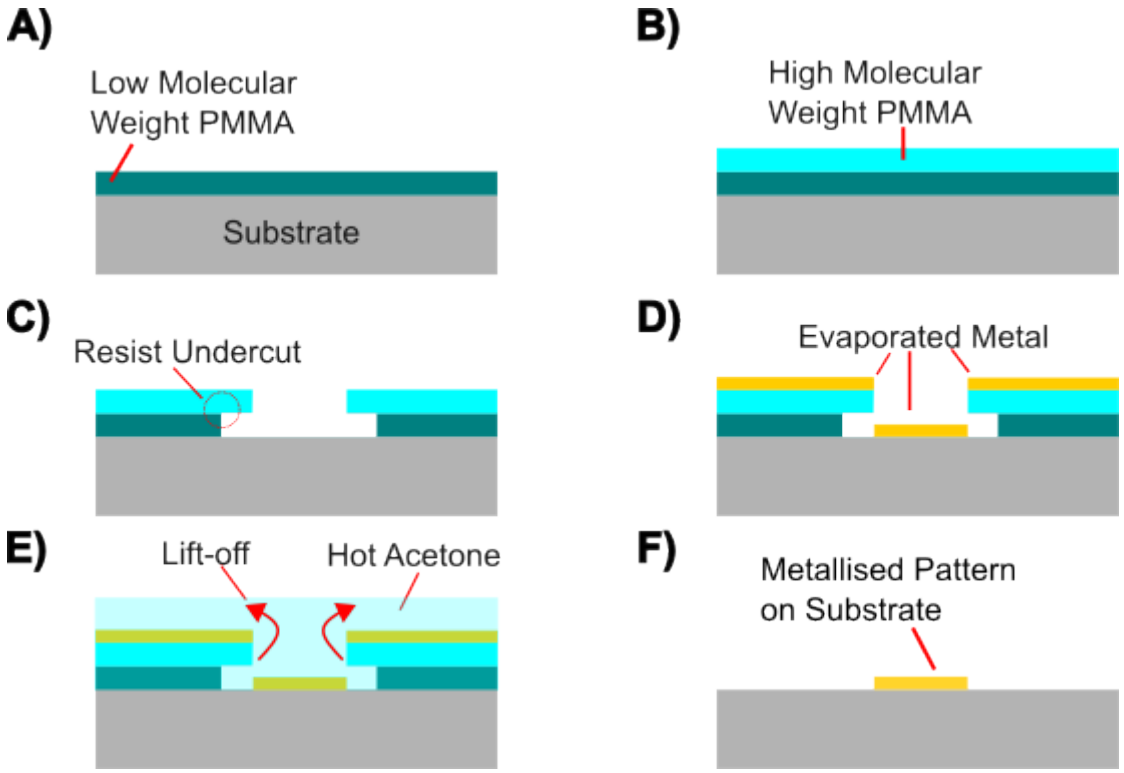

FIGURE 2.23: An illustration of how lift-off works. In step a) the metal is evaporated onto the sample surface, adhering to the resist and exposed sample surface. The sample is placed into 50 °C acetone for 4 hours whereby the resist is removed. The arrows indicate the the peeling back of the resist. Step b) shows the result of the lift off. Just the exposed area is left with metal remaining.

Once the cantilever is patterned with the hard mask, the a photolithography layer is put down to define the probe body and remainder of the cantilever. The mask design of the photolithography layer is shown in Figure 2.12 within section 2.5.2. An optical image of the cantilever once it has completed this stage is shown in Figure 2.24.

The wafers nitride is then subsequently dry etched with the RIE80+ tool with CHF3/02 as the etchant gases. The flow rate is 50/5 sccm respectively, with a 55 mT pressure and 150 W power which gives an etch rate of 24.99 nm/min. This stage requires a 150% over-etch to ensure the cantilever is fully defined as this creates the base structure of the

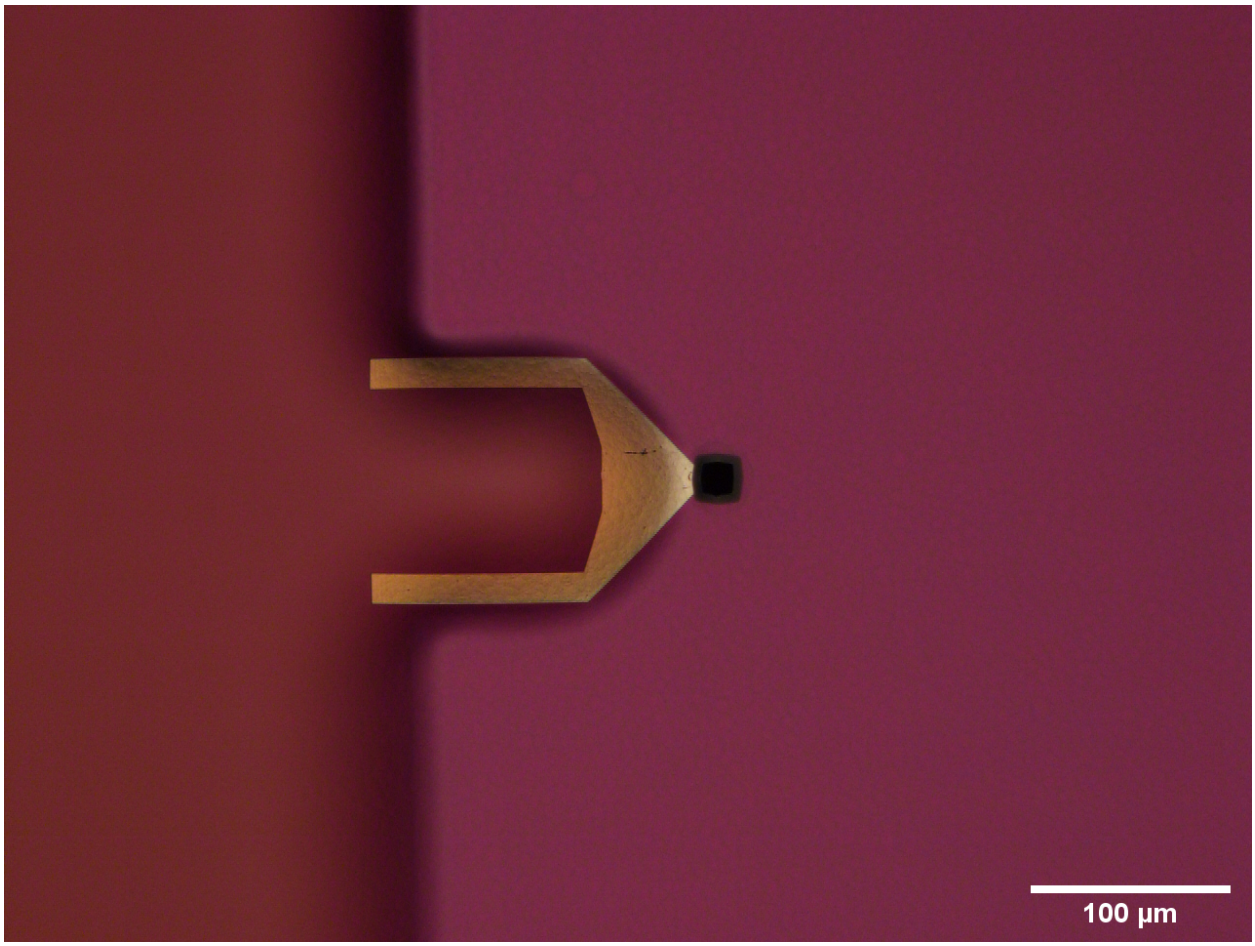

FIGURE 2.24: An optical image of the ebl defined NiCr cantilever on the pyramid with the exposed photolithography mask layer joining it.

TERS tip. As this etch time is usually 24 minutes long for 400 nm of nitride (including over-etch), the etch time would have to be reduced to 20 minutes and 13 seconds as the maximum nitride thickness received from the Chalmers deposition was 337 nm on these wafers. After the dry removal, the wafer undergoes a quick MF319 clean (2 mins) to clean up any debris left over from the dry etch before the resist is subsequently stripped. The NiCr is then cleared away with a 10 minute chrome etch to reveal a silicon nitride cantilever on top of a silicon pyramid with the supporting probe body defined.

A quick KOH wet etch is then performed within a beaker for 5 minutes, leaving an undercut under the cantilever to help lift-off of the sensor metal and remove any debris of the etch in a process known as *mow the grass* (Figure 2.25). The etch solution is comprised of 7m KOH (61.9g of KOH pellets and 150ml RO water), where it is completely mixed and the wafer is submerged. The wafer is placed into the beaker as soon as the As this stage requires a change from that of the standard SThM process flow due to perforation of resist

at the tip, experimentation has to be conducted. Details of this stage and experiments are discussed in section 3.3.4.

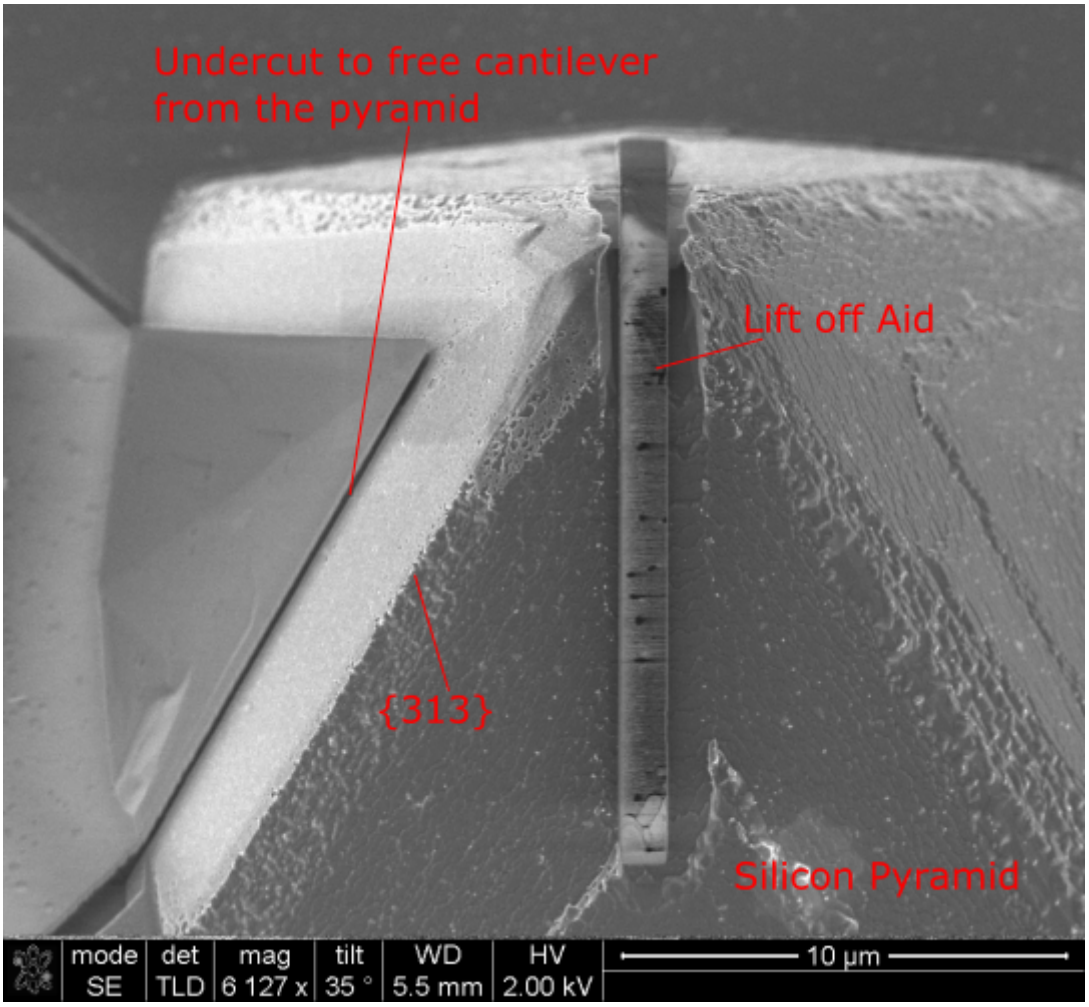

FIGURE 2.25: SEM image of a nitride cantilever post mow the grass, where the KOH frees the nitride cantilever from the silicon pyramid.

The next stage is for the sensor to be patterned onto the tip. As this requires a more in depth discussion pertaining to it's function as a TERS tip, the details of the design and fabrication can be found in Chapter 3.

After the sensor has been patterned, the last and final stage of this process for TERS probes is the release etch. The wafer is placed into the etch kit filled with 80 °C TMAH solution (1.4 L 25% TMAH: 350 ml IPA). Care has to be taken to ensure the wafer is orientated so that surface tension acts perpendicular to the bending axis of the cantilever beams. If this does not happen, the cantilevers will break off when getting removed from the solution. The wafer is then carefully rinsed in RO water to neutralise the alkaline TMAH before being transferred to methanol. The wafer is lastly blow dried from

methanol using nitrogen, which has a lower surface energy than water and IPA and evaporates more readily, ensuring the fragile wafer is safe. This then leaves a free-standing silicon nitride cantilever with the patterned sensor on top of it, ready for use in TERS probes.

3 TERS Design

3.1 Introduction

Tip enhanced Raman Spectroscopy provides a powerful means of determining phonon spectra with high sensitivity and sub-wavelength spatial resolution. Common probe designs utilise a commercial AFM probe, the tip of which is then coated in silver as this is known to generate a large enhancement of the electric field. These probes are effective at generating a large enhanced Raman signal, however it is known to grow a sulphide layer which inhibits the electric field and shifts its plasmon resonance, meaning the lifetime of these probes is usually 24-48hr after having the metal coated. Alumina can also be coated on the outside of these probes to preserve the lifetime, however the coating is susceptible to wear during scanning, especially at the apex of the tip which is where the field enhancement is required. Gold is a suitable alternative to silver in a batch fabrication process as it is resistant to oxidation and corrosion, crucial for maintaining the probes integrity and performance over time. It exhibits SPR in the visible and near-IR regimes, making it highly effective for enhancing Raman signals with common excitation sources, albeit it's enhancement is not as strong as silver.

A speculative advantage of gold over silver is that in biological applications, such as the detection of ultra low level SARS-COV-2 [264], silver can be cytotoxic [265]. Although prior art and the main fabrication processes for the design of probes is well understood within the University, TERS probes have not been fabricated here.

3.2 Fabrication

As discussed in the first chapter, there are many ways of being able to fabricate a TERS probe, with a notable way discussed by Huh et al. who electrochemically etched with a 20 nm radius Au probes with a yield rate of 85% [266]. These however are etched from gold wire, where the end of the tip is the probe, meaning this is also done one at a time.

There is also batch fabrication of ball bonding with force TERS probes with a 96% yield, where the active tips are attached by stamping onto them [267]. These also do not have great positional alignment, so the tip can be off centre from the probe, meaning any force sensing will be not reliable, compared to using EBL where the alignment between layers can be on the nm scale [268]. These tips also require side illumination coupling, meaning the tips are constantly exposed to a laser whilst scanning, generating heat and degrading the tip. A schematic of the ball bonding process is shown in Figure 3.1.

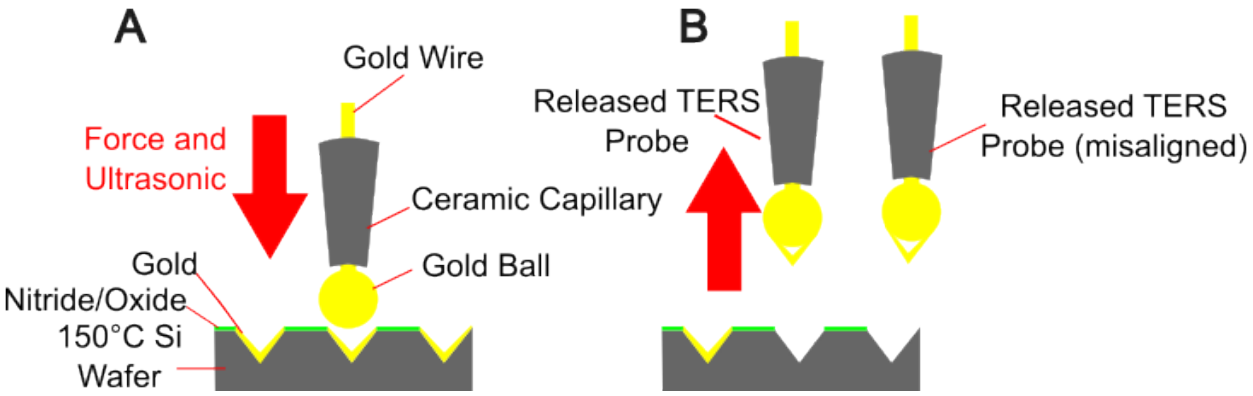

FIGURE 3.1: A - Schematic of the release process using a ball bonder with force. A gold ball is aligned over a cavity on the heated substrate. B - Force from the ball and ultrasonic is applied onto the substrate, where the tip attaches to the probe body before being released to form a free standing probe. The tip on the right had the alignment misjudged and the tip is not correctly centred relative to the ball [267].

A reliable method of batch fabricating gold tips, which are reproducible, have a longer lifetime (use SPP, isntead of direct illumination), have a reliable force sensing capability, and can be tunable to a specific wavelength (change period) is sought after within this work. As discussed in Chapter 1.6, the surface plasmon polariton waveguide probes were chosen to be fabricated. Following design discussions with the NPL and research from Lozan et al. [204] and Berweger et al. [200], a combination of their principles on waveguide-antenna on probes seemed a sensible design choice.

As the metallic antenna is remotely excited, the incident light background compared with the direct excitation of plasmon resonances, where the source is generated at the observed sample, is not really an issue. The wavelength range of the excitation source can also be broad with remote excitation as it is based on the propogation of SPPs, unlike resonance-based effects [269].

3.2.1 Design Criteria

The first part of the system sees incident light going into the nitride cantilever. If the light is incident on the tip along the axis perpendicular to the sample, then it enters the tip at an angle of 56.5 ° to the normal of the silicon nitride surface. This is due to the angle of the probes being 46.5 ° and the probe mounting on their holder adds an additional 46.5 ° to the normal. When the wave enters the silicon nitride it will bend towards the normal of the tip and as it leaves the silicon nitride it bends away from the normal. For an angle of incidence from the nitride to the air, total internal reflection occurs when the angle of refraction is greater than 90. Following Snell's law of refraction [270], the smallest angle of incidence which total internal reflection occurs is known as the critical angle. Taking the measured refractive index value of the silicon nitride ($n_{nitride}$ = 2.267) the critical angle can be calculated with the following relation:

$$\theta_{(Crit)} = Sin^{-1}(\frac{1}{n_{nitride}}) = 26.15^{\circ} \tag{3.1}$$

This means that for an illumination angle less than 26.15 °, some of the light is refracted and exits the silicon nitride. For any angle greater than this, all of the light will undergo total internal reflection. Total internal reflection will carry the light along the probe, however the angle of the wave in the nitride may not match what is needed to generate a SPR. The angle of incidence from the light in the nitride onto the gold sensor for surface plasmon resonance can calculated by the following relationships:

$$K_0 = \frac{2\pi}{\lambda_0} \tag{3.2}$$

$$\beta = K_0\sqrt{\frac{\varepsilon_m}{1+\varepsilon_m}} = 1.04 \times 10^7 m^{-1} \tag{3.3}$$

Where ε_m is the permittivity of gold (-12.047) and λ_0 is the wavelength of incident light (633 nm), K_0 is the wavenumber of incident light and β is the propagation constant of a plane wave. The wavelength of light in nitride is given by:

$$\lambda_{nitride} = \frac{\lambda_0}{n_{nitride}} = 279nm \tag{3.4}$$

Using these relationships, the angle at which the in-plane component of the incident light's wavevector matches the SPP propagation constant can be realised:

$$\theta_{inc} = sin^{-1}(\frac{\lambda_{nitride}}{\frac{2\pi}{\beta}}) = 27.40^{\circ} \tag{3.5}$$

As the light travels towards the grating, it scatters and adds a K value of :

$$K_{gr} = \frac{\lambda_{nitride}}{d} \tag{3.6}$$

Where d is the period of the grating (nm). In order to calculate the angle before scattering of the grating, where the intention is to match the light coming out the grating to the spr angle (27.407 °), the following relation can be used:

$$Sin\theta_{int} = Sin\theta_{inc} - K_{gr} \tag{3.7}$$

Where θ_{int} is the angle of the light as it propagates within the nitride, before it interacts with the grating. The light will enter the nitride from air at an angle, where the angle of the beam is decreased by Snell's law. This follows this relation:

$$Sin\theta_{ext} = Sin\theta_{inc} n_{nitride} \tag{3.8}$$

Where θ_{ext} is the external angle (air) which would refract into θ_{int} within the nitride. The path the laser will take throughout the TERS probe is shown in Figure 3.2. Where the incident angle is drawn as 56.50 ° (NPL side illumination angle). The light is unpolarised in the NPL setup, meaning only the TM component will couple and excite SPR.

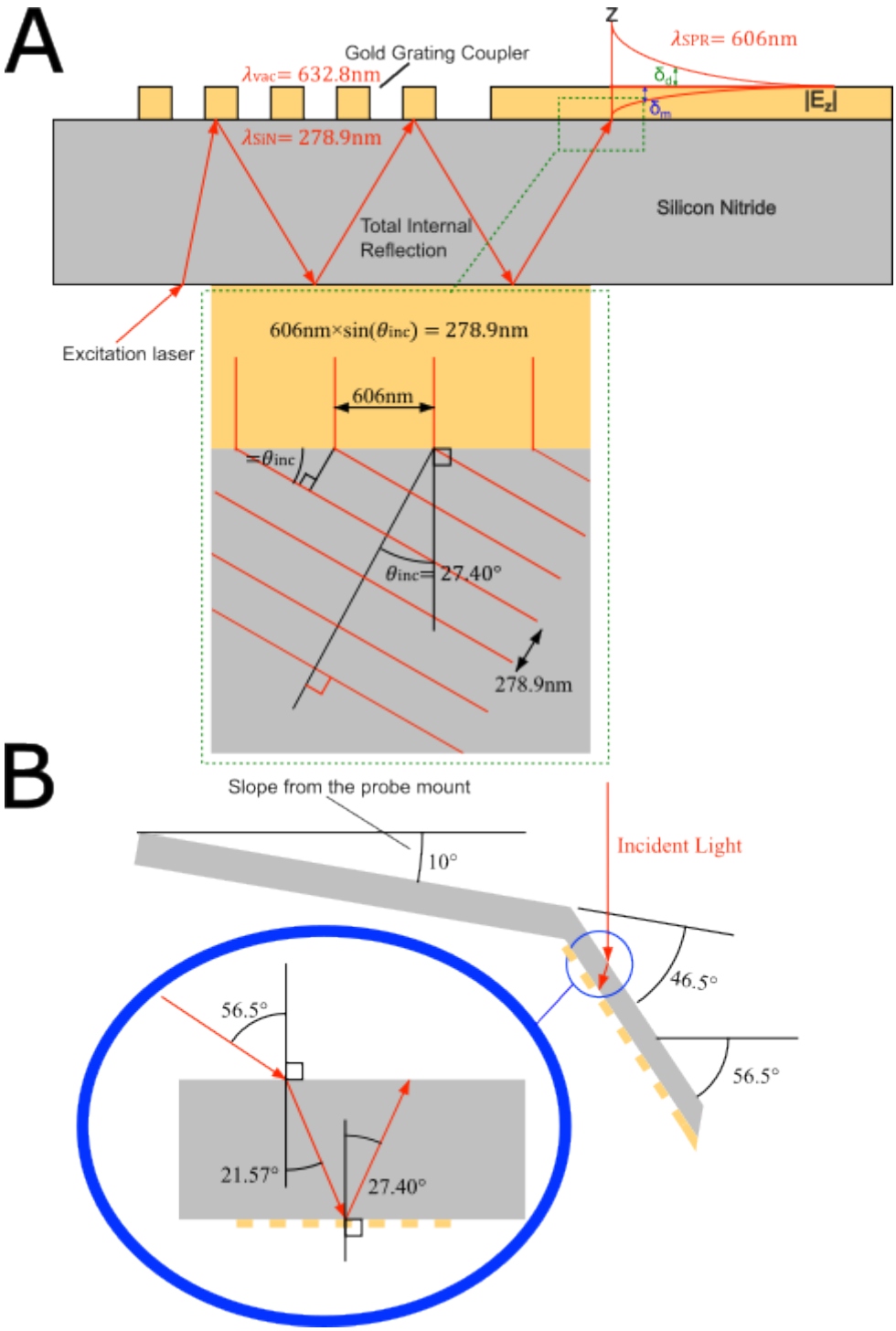

FIGURE 3.2: Diagram depicting the beam path of the laser with a 56.50 ° incident laser angle. The beam enters and is transmitted at 21.57 °. The grating scatters the light through diffraction and adds K_{gr}, where the diffraction angle is 27.40 °. The light then undergoes total internal reflection as the diffraction angle is greater than the critical angle ($\theta_{(Crit)}$)of 26.15 °. As the angle of diffraction matches the angle to generate a SPR in gold, a surface plasmon is generated at the apex.

In order to calculate the internal nitride angle, the grating equation is used[271]. These are described in Equations 3.9 - 3.11.

$$\sin(\theta_{\text{int}}) = \sin(\theta_{\text{inc}}) + m\frac{\lambda_{\text{nitride}}}{d} \tag{3.9}$$

For $m = +1$:

$$\sin(\theta_{\text{int}}) = \sin(\theta_{\text{inc}}) + \frac{\lambda_{\text{nitride}}}{d} \tag{3.10}$$

For $m = -1$:

$$\sin(\theta_{\text{int}}) = \sin(\theta_{\text{inc}}) - \frac{\lambda_{\text{nitride}}}{d} \tag{3.11}$$

Here, m denotes the diffracted order. The term m=0 (zero-order) refers to direct transmission or reflection of incident light. The term m = 1 corresponds to the first-order diffracted beam on one side of the zero-order beam, m=-1 is the first-order diffracted beam on the opposite side.

With these relations it becomes possible to calculate the angle of incidence required to match an SPR angle of (27.407 °), after it has undergone total internal reflection. Taking the grating period as d and the n of nitride is 2.269 at 633nm, the results are tabulated for a diffraction order of m=1:

Grating Period (nm)	$\sin(\theta_{int})$	θ_{ext} (deg)	Angle to Vertical Z-axis
250	-0.655	-	-
350	-0.337	-49.84	106.35
450	-0.159	-21.25	77.75
550	-0.047	-6.12	62.63
650	0.031	4.04	52.47

TABLE 3.1: Table of the Coupling Angles for the TERS Grating Coupler with m=1

As can be seen in Table 3.2, for a 650 nm period the incident light has to be 52.45 ° from the angle of the *z*-axis. The 550 nm grating period excitaion angle from the z at 62.61 ° has been drawn in Figure 3.3 for clarity.

The same calculations are done to find out the excitation angles for a diffracted order m=-1.

These tables will be used during experimentation at the NPL, for the differing geometries, so that a SPR match can be made and effective TERS can be achieved.

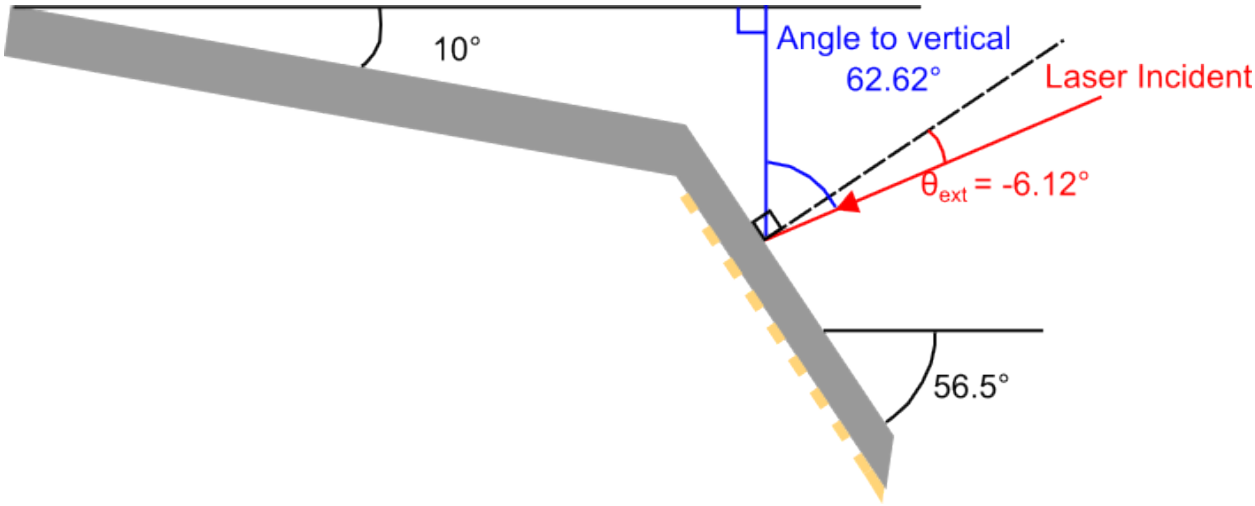

FIGURE 3.3: Diagram depicting the angles of illumination for the TERS probe with a 550 nm period.

Grating Period (nm)	$\sin(\theta_{int})$	θ_{ext} (deg)	Angle to Vertical Z-axis
250	-0.655	-	-
350	-0.337	49.84	6.67
450	-0.159	21.25	35.26
550	-0.047	6.12	50.39
650	0.031	-4.04	60.55

TABLE 3.2: Table of the Coupling Angles for the TERS Grating Coupler with m=-1

3.2.2 Design

With the surface plasmon polariton waveguide archetype of probe, nanofocusing to a sharp tip is of utmost importance. The sharp tip allows for the probe to take use of the lightning rod effect, efficiently enhancing and confining the electromagnetic field whilst allowing for high spatial resolution. With the tip in close contact or contact over the surface, a tightly coupled tip will emit light over a broad continuum [272].

With this the design parameters were set and are shown in Figure 3.4 and in Table 3.3 below.

The width of the grating was determined through trigonometry and the number of metallic bars remained constant at 7, as any more would take a lot of the gratings off the angled part of the cantilever (where they are needed) and onto the flat part of the cantilever where they are of no use.

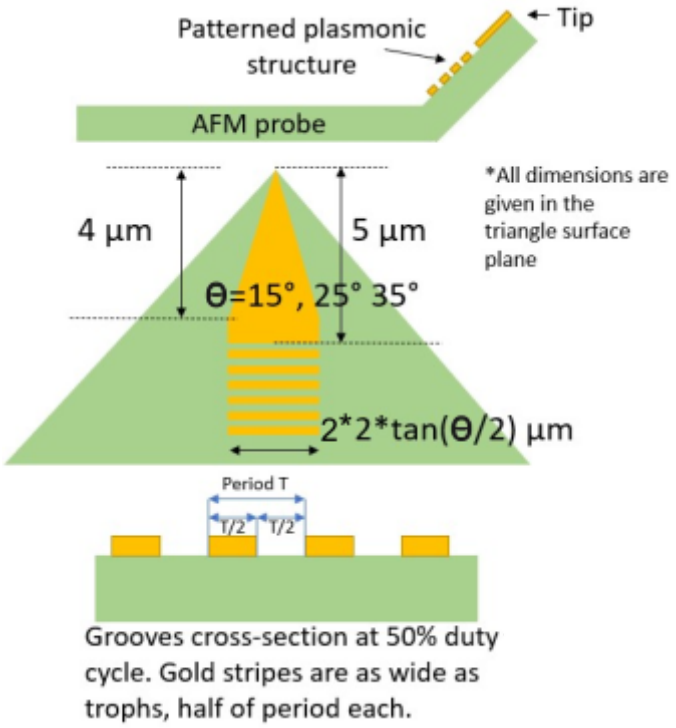

FIGURE 3.4: Schematic diagram of the TERS design paramaters.

A dose test was conducted to find out the best option for not only coverage of tip, to test the alignment of the EBPG on the etched markers and figure out the clearing dose of the resist. A metal lift off with 1 nm NiCr and 70 nm of gold was subsequently done as imaging in PMMA can be challenging due to charging.

SPR is typically strongest when the gold film is around 40-50 nm, giving high sensitivity and sharp resonance dip at a gold-dielectric interface [273]. Films thinner than 20 nm often show a lack of distinct resonances due to damping and incomplete film formation [273]. In this case, the metal isn't thick enough to absorb the energy of light and generate plasmon oscillations.

For TERS enhancement, the optimal thickness of the gold coating to achieve the highest enhancement is in the range of 60-80 nm [274], with Wang et al. using a 70 nm thick film [275]. As such, the coating for the probes was designed to be 70 nm thick.

The testing of 4 geometries was employed to ensure this with:

- 10 nm thick line with overexposure.
- 30 nm thick line with overexposure.
- 30 nm tip overlap.

Design specifications of the TERS tips	
Opening Angle (°)	Grating period (nm)
15	450 550 650 750
25	450 550 650 750
35	450 550 650 750

TABLE 3.3: Table detailing the TERS probe design parameters.

- 50 nm tip overlap.
- Normal alignment exposure.

A diagram of these design strategies is shown in Figure 3.5.

The results of the dose test, while looking at normal alignment (perfect placement), showed misalignments of the sensor metal on the silicon nitride tip of around 350 nm in the x. This was not adequate as the metal would not coat the apex of the probe and so another lithographic run was done where the pattern was shifted 350 nm in the x, within the cjob file, to compensate for the misalignment. The results are shown in Figure 3.6.

The results of this concluded that a normal alignment was not possible with these probes and so a patterned overlap of 30 nm would allow for sensor metal to cover the apex. The 50 nm overlap would still work, however it takes up a larger surface area, meaning the taper of the sensor material would be more compromised. The thick lines would also work, however it again compromises the taper geometry of the sensor, which would not concentrate the electric field as well as a shaper taper would. The results of a 350 nm shift in the job file with a 30 nm overlap at the apex, which will be used in the final design is shown in Figure 3.7.

Taking into consideration the result of the dose test and alignment strategy, using a 2nA beam with a dose of 2100 $\mu C/cm^2$ was the best option. The results of which produced Figure 3.8 below.

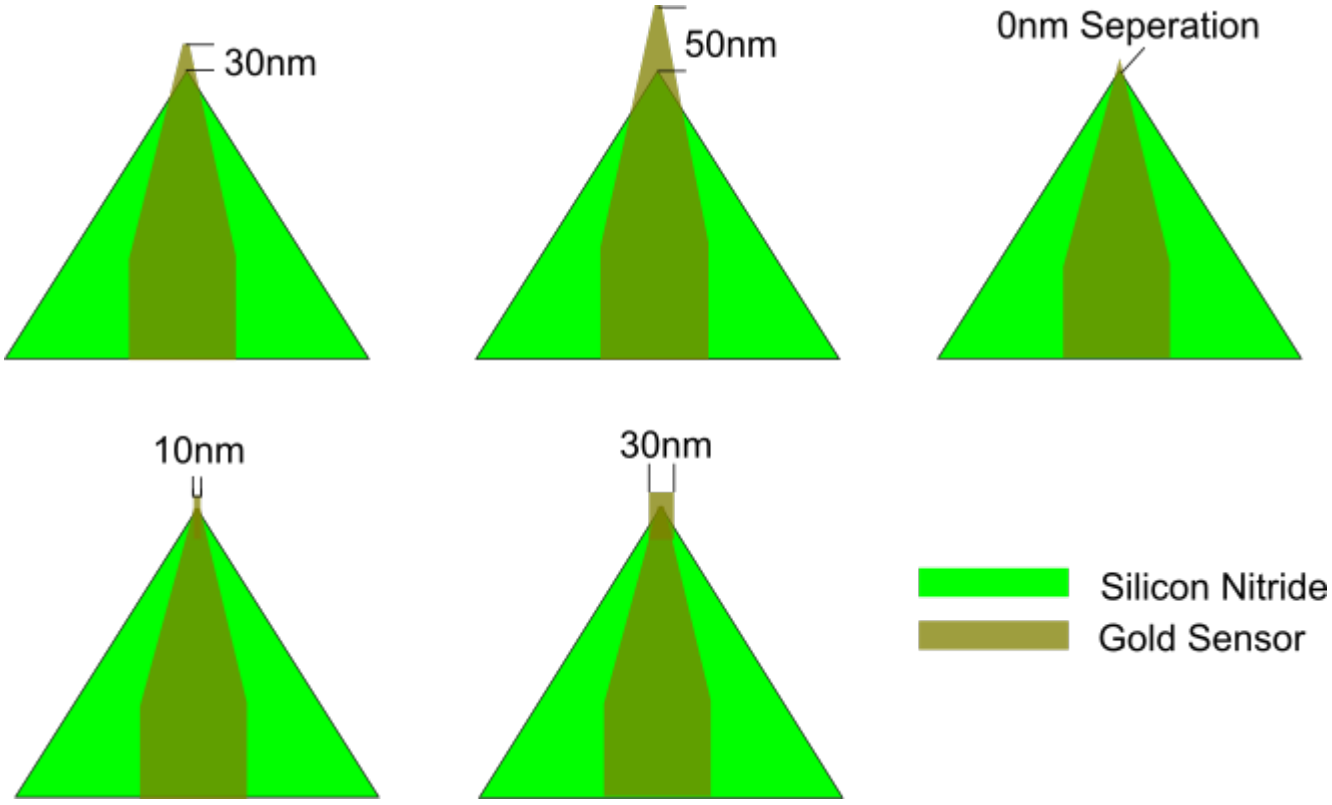

FIGURE 3.5: Schematic diagram of the alignment strategies which could be employed on the sensor lithography pattern files.

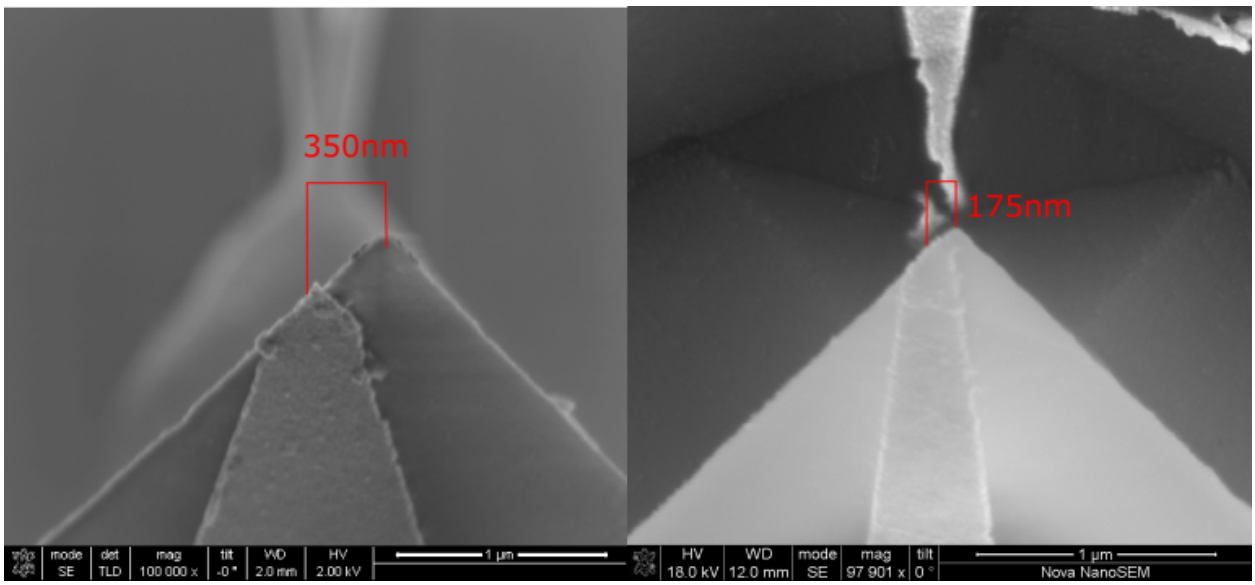

FIGURE 3.6: The SEM image on the left shows the patterned sensor metal on the apex of the probe with a misalignment of 350 nm. The SEM image on the right shows a misalignment of 175 nm where the pattern was shifted 350 nm within the job file.

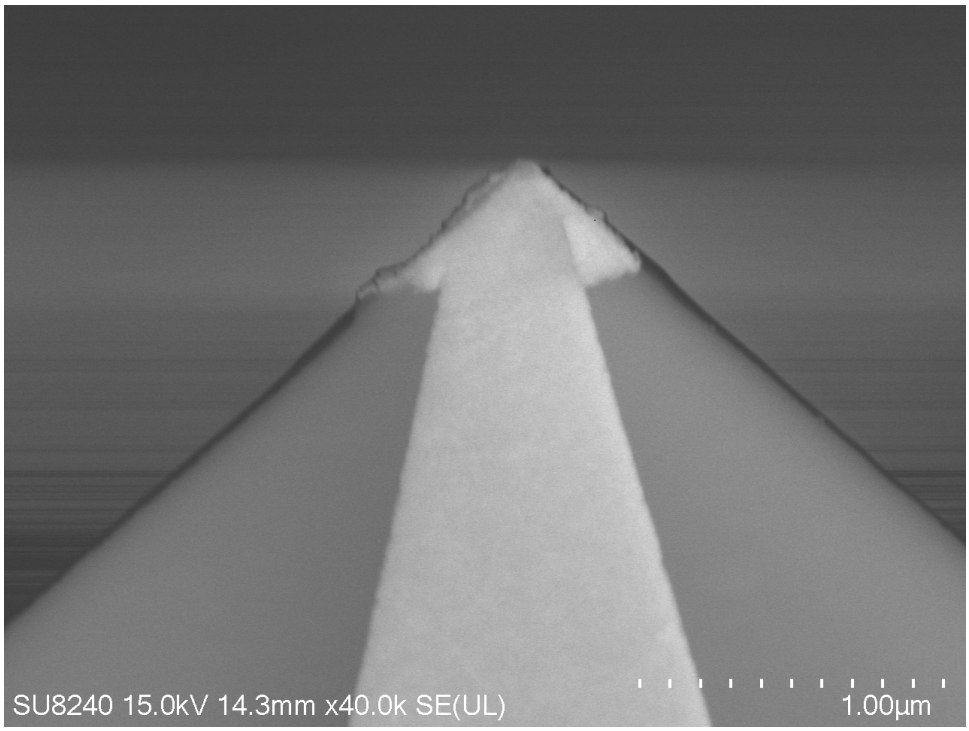

FIGURE 3.7: A SEM image of the finalised ebl job pattern. The job file was shifted 350 nm in the x and exposed a 30 nm overlap.

As can be seen in Figure 3.8, the overlap leaves the tip with a bit more metal than desired, however it does leave the full apex covered in metal. This is the most important aspect as when the tip comes into contact with a surface, the resulting sensor will be in contact with the surface, allowing for a high spatial resolution image.

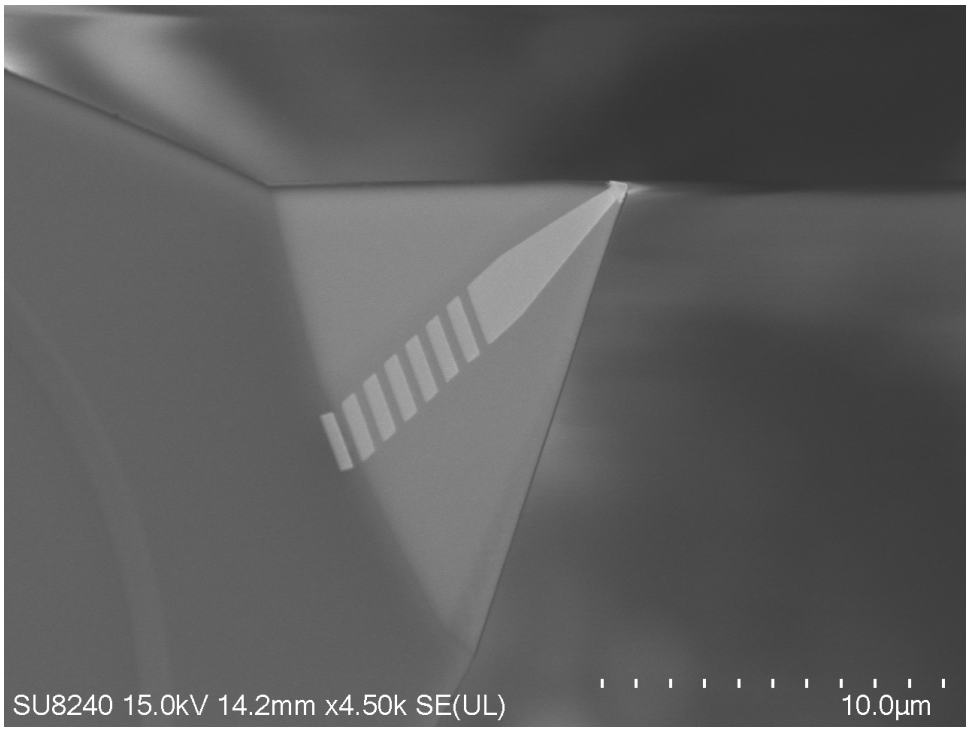

FIGURE 3.8: The image depicts an SEM image of a successfully fabricated TERS probe, post lift off.

3.3 Fabrication issues

This section provides details on the changes made to the traditional SThM fabrication process due to complications arising from the cantilever definition stages.

3.3.1 Back side etch

As discussed in Chapter 2.2.1 the backside etch is critical in reducing the time required in the slow release etch. The main issue with the original timing was the etch took 320 μm of silicon off the surroundings off the probe chip, leaving 60 μm. When the wafers were being clamped in the ebeam tool or metal evaporation tools, cracks would often nucleate. This would leave the structural integrity of the wafer compromised and result in unwanted pieces breaking from a full wafer. It is possible to further process these part pieces, and this has often been done, however it is not ideal for a batch fabrication process. An example of such cracks, which happened when clamping in the ebeam tool is shown in Figure 3.9. As a result the backside etch time was reduced to ensure only 300 μm of silicon was etched, providing an extra 20 μm of silicon at the price of a 30% increase in the release etch time.

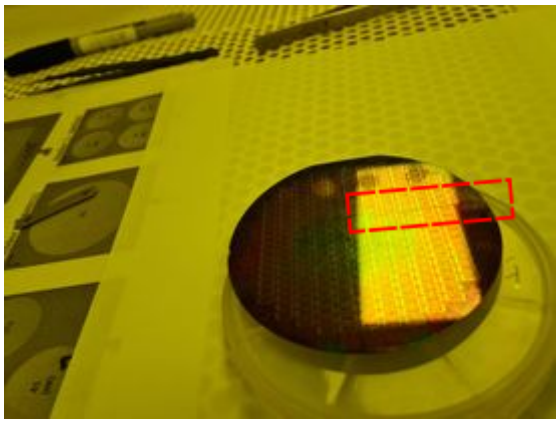

FIGURE 3.9: An image of the wafer with a crack over the surface caused by over-clamping. The area where the wafer is cracked is outlined in the red box.

3.3.2 Alignment

As this is a batch fabrication process of over 200 probes, FIB milling of individual probes is out of the question. This however means that the alignment of the e-beam process needs to be good enough to coat the tip apex, and this can be challenging with deep etched Si markers. One way to combat this would be to use traditional metal markers, put in place and used for the cantilever definition as well as the plasmonic structure so that their positions in relation to the same marker. The issue of this is that the adhesion layers present within the JWNC are Ti and NiCr, of which would be etched away with the chrome etch and the KOH *mow the grass* stages. The last option was to use Ni as an adhesion layer. These were tested on flat probes and put through the same chrome etch but were etched away. It was therefore decided to trust the tool's alignment capabilities and remain with the silicon markers.

3.3.3 Photolithography

During the cantilever photolithography stages, a bi-layer of AZ4562 photoresist with a thickness of around 14.25 μm is spun on the wafers to allow coverage of the pyramids. This resist is very viscous and requires a rehydration stage before exposure.

This resist undergoes reflow when subjected to a post development bake, leading to mechanical distortions of the pattern [276]. The extent of the distortion is dependent on factors such as the yield stress, coefficient of thermal expansion and surface tension of the resist. It is necessary to bring this resist above the glass transition state to improve its

thermal and physical resistance in the subsequent dry etch stages. The previous reflow parameters were problematic in that when examined optically, the alignment from the photolithography stage and e-beam stage could look perfectly fine. The resulting dry etch stage would etch through any misaligned area, rendering probes which require a fully intact cantilever useless. An example of said misalignment is shown in Figure 3.10.

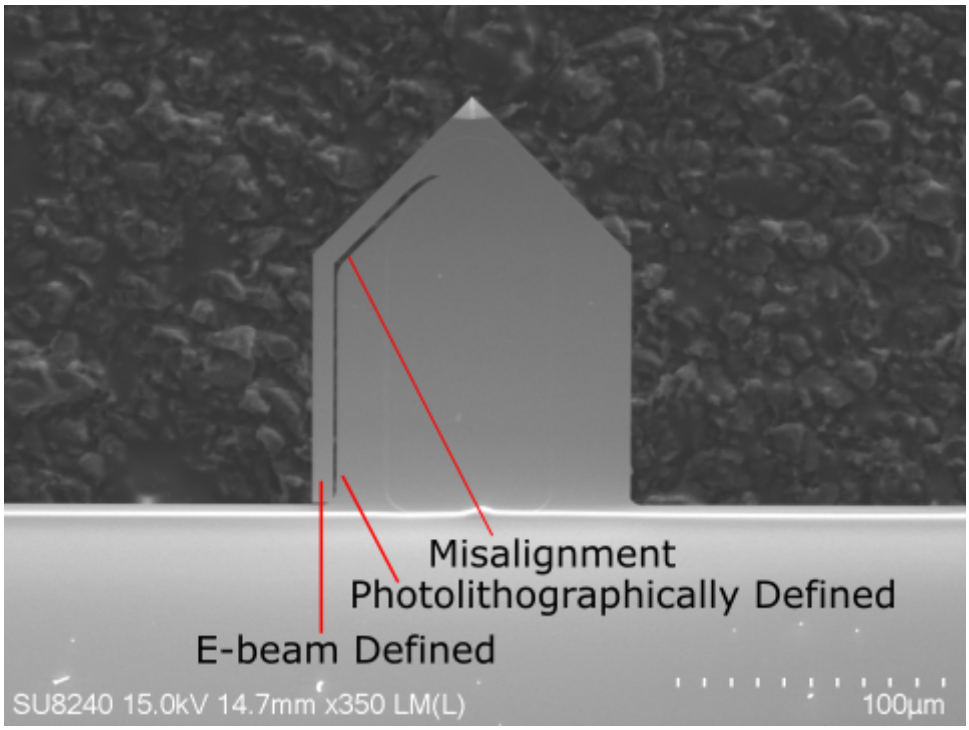

FIGURE 3.10: SEM image of probe which is misaligned between the photolithography and ebeam levels.

In order to combat this, the geometry of the cantilever was changed during the e-beam stage, where the pattern was made to have a larger overlap with the area of the resist. The consequence of this added time onto the job, however would aid the prevention of misalignment and provides a higher success rate of fully intact tips at this later fabrication stage. The cantilever differences in CAD are shown in Figure 3.11.

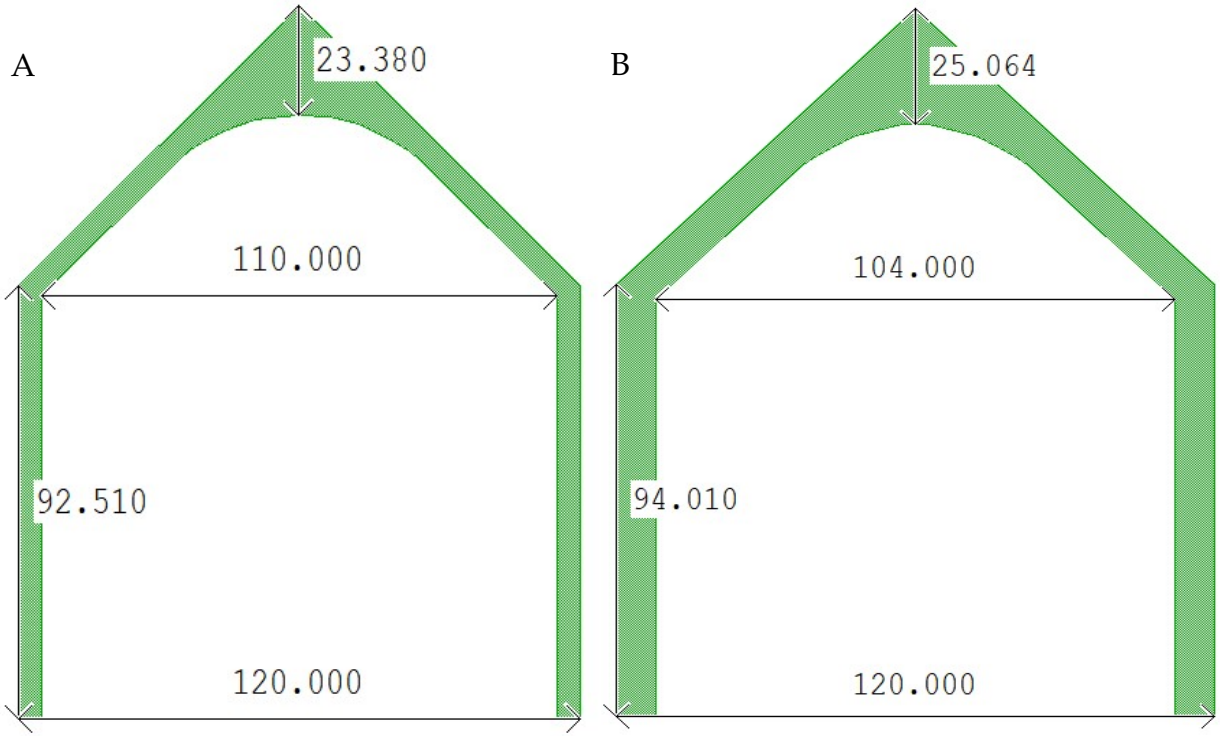

FIGURE 3.11: Screenshot of the CAD drawings of the old (A) and new (B) cantilever designs. The e-beam pattern is made larger to increase the overlap with the photolithography level but maintains the sharpness and extent of the cantilever, at the expense of increased exposure time. All dimensions are in microns.

3.3.3.1 Reflow temperature study

The next stage was a short study on how the temperature of the bake would effect the reflow. Resist reflow is a thermal treatment applied to a photoresist after patterning. The resist is baked above it's softening temperature (110°C) causing it flow and reshape due to surface tension. This phenomena leads to change in the resist profile and dimensions as shown in Figure 3.12.

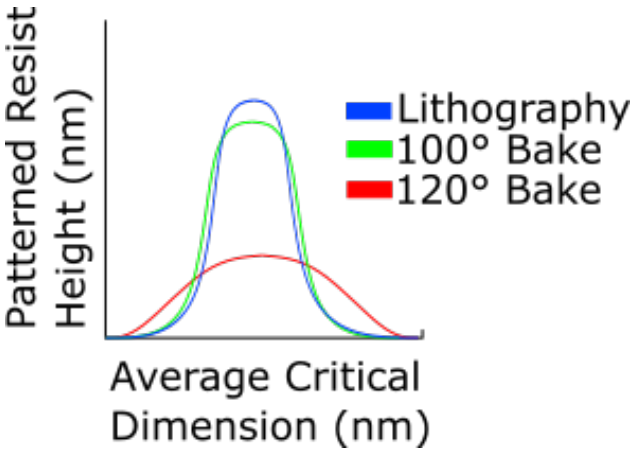

FIGURE 3.12: A schematic diagram depicting how the resist profile changes upon reflow. This is a positive resist, leaving the exposed pattern either side of the graph. It can be seen that for a higher temperature bake, the exposed region is no longer what was prescribed (lithography), as the reflowed resist flows into it.

The current process brings the resist above the softening temperature but in doing so, the corners at the exposed region become more round and change the dimensioning of the prescribed lithography. This means that the overlap between the metallic e-beam defined mask and photoresist mask may reduce or the resist may become so much smaller that a gap appears between the two.

In this stage of the process, the cantilever is defined with a NiCr hard mask, with the photolithography region aligning to it prior to nitride dry etching. So if the masked region becomes shorter due to reflow, this means that the subsequent etch will remove the nitride from the gap between the smaller photo defined area, and the NiCr mask, leading to a gap in the material like as shown in Figure 3.10 in the previous section. A study was conducted in order to correct for this, meaning the new resist edge profile is straighter, resilient to the subsequent etch and dimensioning is matching that of the lithography. The process would still be bringing the polymer above its softening temperature but reducing the reflow effect in 3 instances and one just below the softening temperature.

In order to achieve this, 4 wafer pieces taken from a fractured wafer were used during this study, instead of using a full wafer. The wafers were exposed, developed and the post exposure bake was taken at different points. There were three temperature points studied during the experiment which were 90, 100, 110°C, baking for 20 minutes in the oven. The last piece was baked with at the standard 120°C on top of the EBL cantilever stage to indicate where things align. Optical images of the cantilever post bake are shown in Figure 3.13.

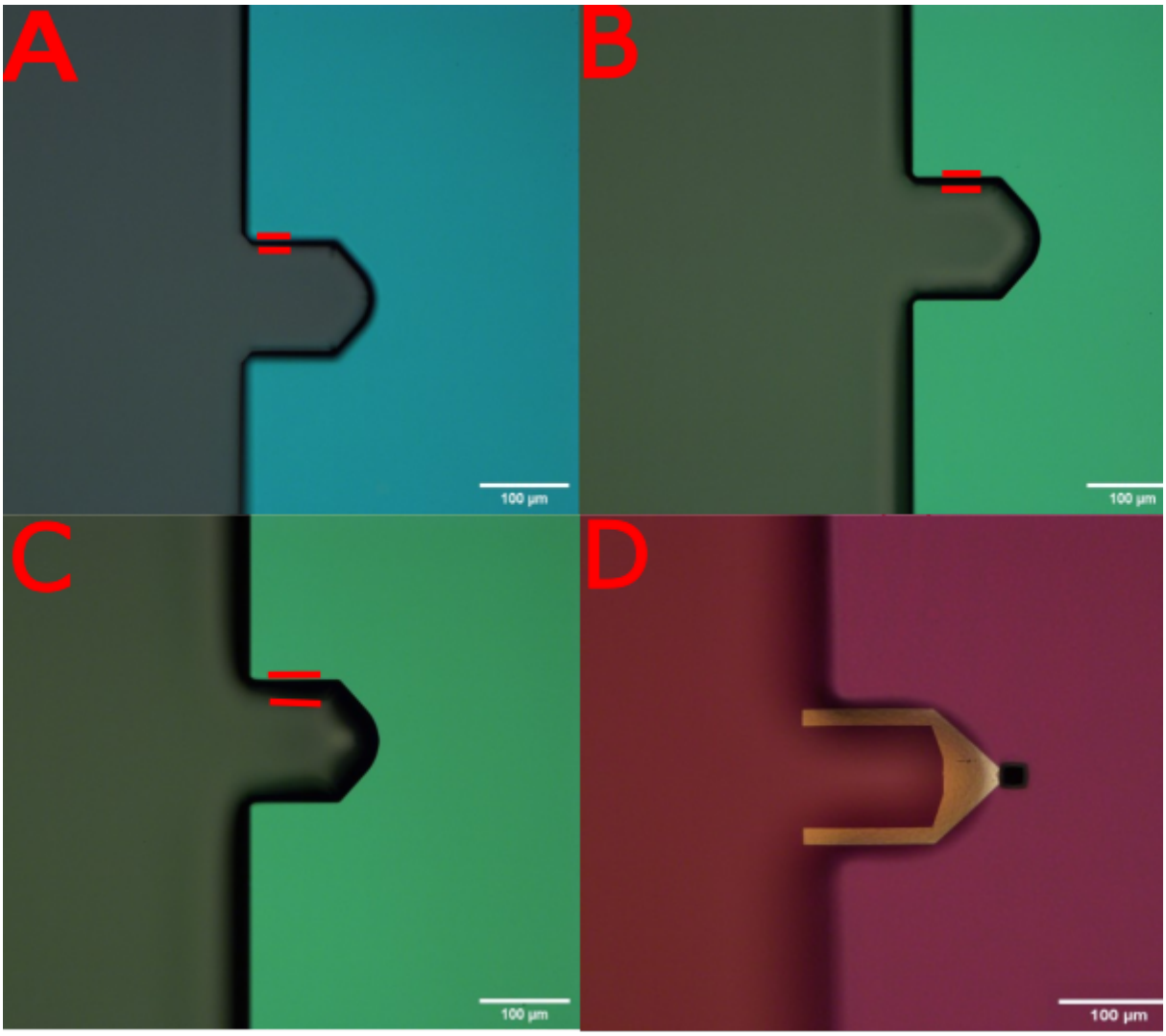

FIGURE 3.13: Optical images of the cantilevers post bake with the reflow areas highlighted. A-D, follows 90-120°C in 10°C increments respectively. The areas within the red lines show a shaded dark area where the resist has reflowed. All dimensions are in microns.

In Figure 3.13 the reflow of resist can be seen within the red lines, it appears as dark shadows. Figure (D) shows the 120°C bake on top of the EBL defined hard mask. As

the temperature increases the reflow area increases as the material becomes less viscous. Especially at 110°C, the resist profile does not resemble what the lithography prescribed, which could lead to a break in the resist as it is dry etched. This means that the metal hard mask to pattern the cantilever under the resist would also be insufficient as a gap would be formed between the metal and the resist as seen at 120°C, leading to a break in the etched cantilever. This means that the function of the probe would be hindered as it's structural integrity is compromised. However, it is apparent that even from the lower temperature at 110°C that the reflow is too much.

At at temperature of 100°C (Figure (B)), it was deemed more than sufficient in fabricating the cantilevers, as the profile resembles the lithography resulting in the images shown in Figure 3.14. These indicate that the modification to post bake temperature and design improvement were successful and in turn will reduce the error incurred by misalignment and large reflow.

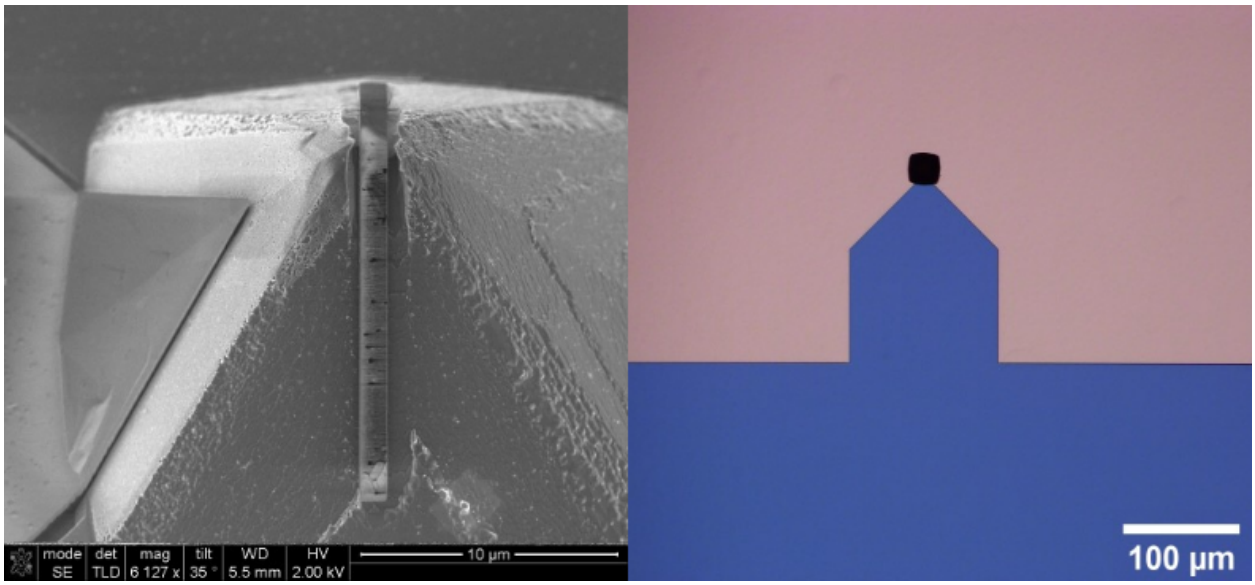

FIGURE 3.14: The image on the left shows a SEM of the tip area which has been etched through after the new 100°C bake. The image on the right shows an optical image of the cantilever region after the modified bake. The pyramid appears dark in the optical image as it is a bright field image.

3.3.4 Mow the Grass

As discussed in section 2.8.1, the *mow the grass* stage is required to release the cantilever from the pyramid. The consequence of this action is that when the resist has been float

coated on, the sharp tip sometimes breaks through the resist rendering it useless in the intended regions for exposure.

In order to combat this, an experiment was set up to determine the time in which the cantilever was released enough from the pyramid during the wet etch, but not so much so that it would perforate the resist.

3.3.4.1 Setup

In order to achieve results resembling that of a real sample, an old-design wafer with misaligned cantilevers was used. This wafer was no longer of use but the tip structures such as silicon nitride thickness and pyramids resembled a continuing live sample. The wafer was firstly cleaved into 8 seperate pieces. As it was believed the etch timing may be too long (9 minutes), the wet etch timings ranged from 1-8 minutes in 1 minute intervals. The next stage was to tell if the resist was compromised, so the basic spin coat and float coat procedure was performed. As the resist is electron sensitive, the resist would be exposed when checked using the SEM. This crosslinks the resist and makes it impossible to remove. In order to prevent this from happening a 20 nm Al contrast layer was deposited onto the resist. After optical inspection the samples then underwent a lift off. This would remove any of the remaining resist but the exposed area, or area that wasn't coated with resist would still have Al remaining. An image showing this process is depicted in Figure 3.15. A collection of SEM images of this stage are shown in Figure 3.18, with a table of the process flow shown in Table 3.4.

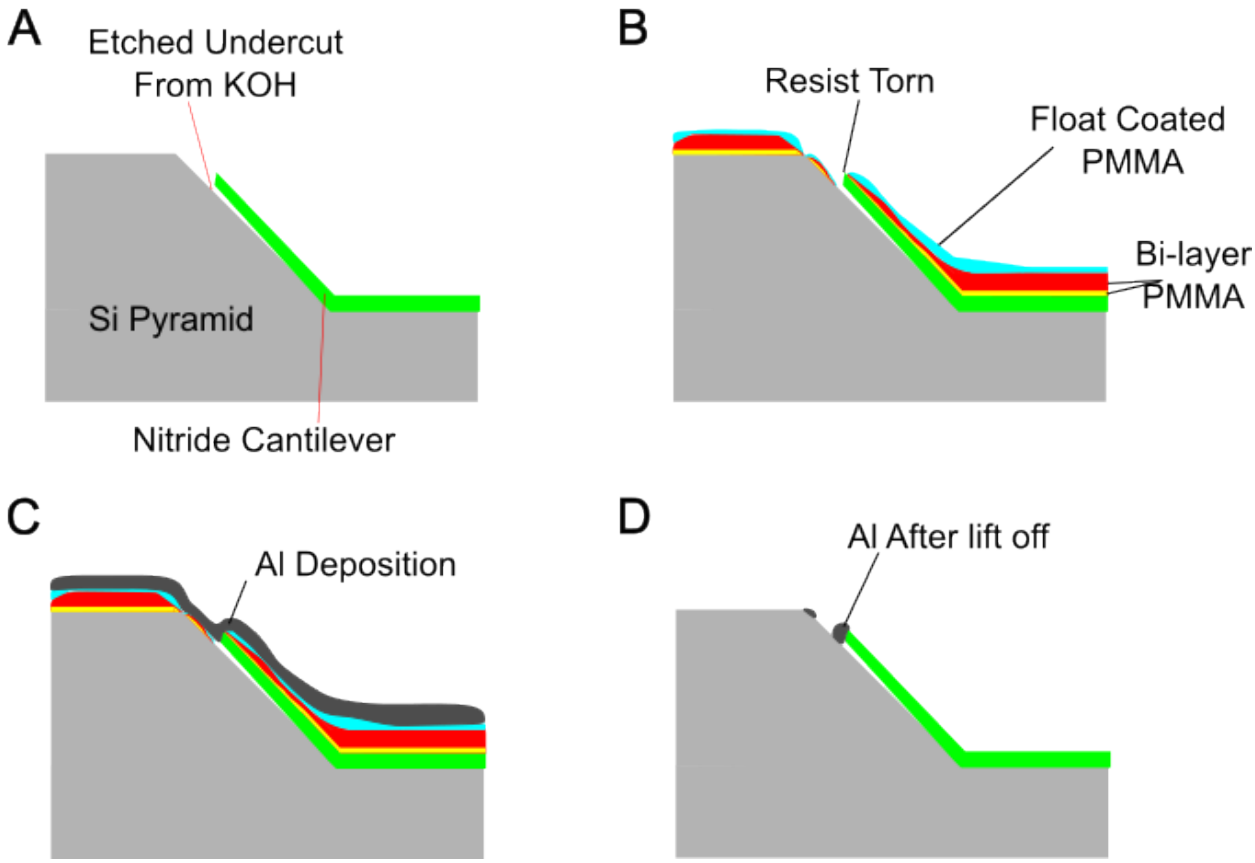

FIGURE 3.15: A - The silicon nitride cantilever is released by a timed KOH etch. B - A bi-layer of PMMA is spun before 4 float coats onto the sample, where a protruding tip perforates the resist. C - 20 nm Al is deposited onto the sample before SEM images are taken. D - The sample is then placed into 50 °C acetone to undergo a lift off, where any perforations of the resist around the tip are visible as there is now Al there.

3.3.4.2 Mow the grass results

It can be seen in Figures3.16-3.18 that we have perforated the resist in nearly all the etch cases, especially at the top of the pyramid. This in essence means that 3 float coats aren't enough, and more of it would be required to ensure adequate coverage of the pyramid. 6 float coats were used and resist status was monitored throughout the project. However, in terms of the wet etch, a significant undercut of the nitride cantilever can be seen even after 1 minute. To make sure the nitride is freed from the pyramid, a 4 or 5 minute KOH etch was conservatively chosen. As can be seen in Figure 3.16, the 5 minute etch has definitely freed the cantilever at the base and is suitable for further processing.

Process flow for the mow the grass study	
Step number	Stage details
1	A 380 μm DSP previously processed silicon probe wafer, with 400 nm silicon nitride on top is cleaved into 8 pieces. They are cleaned within 80 °C nanostrip solution for 20 minutes, before being neutralised in RO water.
2	Sample is oxygen barrel ashed at 150W for 5 minutes.
3	61.89g of KOH pellets is dissolved in 150mL of RO water in a petri dish. The samples are then added 1 at a time for a range of times from 1-8 minutes in 1 minute intervals.
4	The samples are then placed into a 5:1 RO:98% sulphuric acid solution. The sample is then rinsed in RO water for 10 minutes before optical microscope inspection to ensure a visible undercut.
5	Steps 1 and 2 are then repeated.
6	8% 2010 PMMA is spin coated on the samples at 2500rpm for 30s on the pyramid side.
7	Samples are baked in the oven at 180 °C for 15 minutes.
8	4% 2041 PMMA is spin coated on the samples at 2500rpm for 30s on the pyramid side.
9	Samples are baked in the oven at 180 °C for 15 minutes.
10	1.5% 2041 PMMA with a molecular weight of 410MDa is float coated onto the sample.
11	Samples are baked in the oven at 180 °C for 15 minutes.
12	Steps 10 and 11 are repeated 3 more times.
13	The samples are oxygen barrel ashed at 80W for 30 seconds.
14	20 nm of Al is evaporated onto the resist surface.
15	The samples are then inspected individually on the SEM.
16	Samples are then placed into 80 °C acetone for 2 hours, before being rinsed with IPA and dried.
17	The samples are then inspected individually on the SEM.

TABLE 3.4: Table detailing the process flow for mow the grass study.

3.3.5 Results and Discussion

Improvements to the existing process of fabricating probes allow for more efficient and reliable batch fabrication of the wafers. Although the cantilever dimensioning adjustments increase the write time of the e-beam tool, with using an optical microscope to align with a photolithography level after e-beam, a rework of the wafer is much more costly in terms of fabricator and facility time. This would also introduce more opportunities for contamination of the wafer and more time spent in tools than necessary. A shorter time in the wet etch in the *mow the grass* stage allows the necessary geometry to continue on, whilst reducing perforation of resist, as there is less detached surface area for it to break through.

It can be seen that even at the reduced etch times perforation does occur, but this is due to poor coverage of resist to begin with. As the number of float coats have been increased, this will be corrected for to ensure high contrast lithography followed by a smooth lift-off of the patterns defined by the resist and edge of the silicon nitride tip.

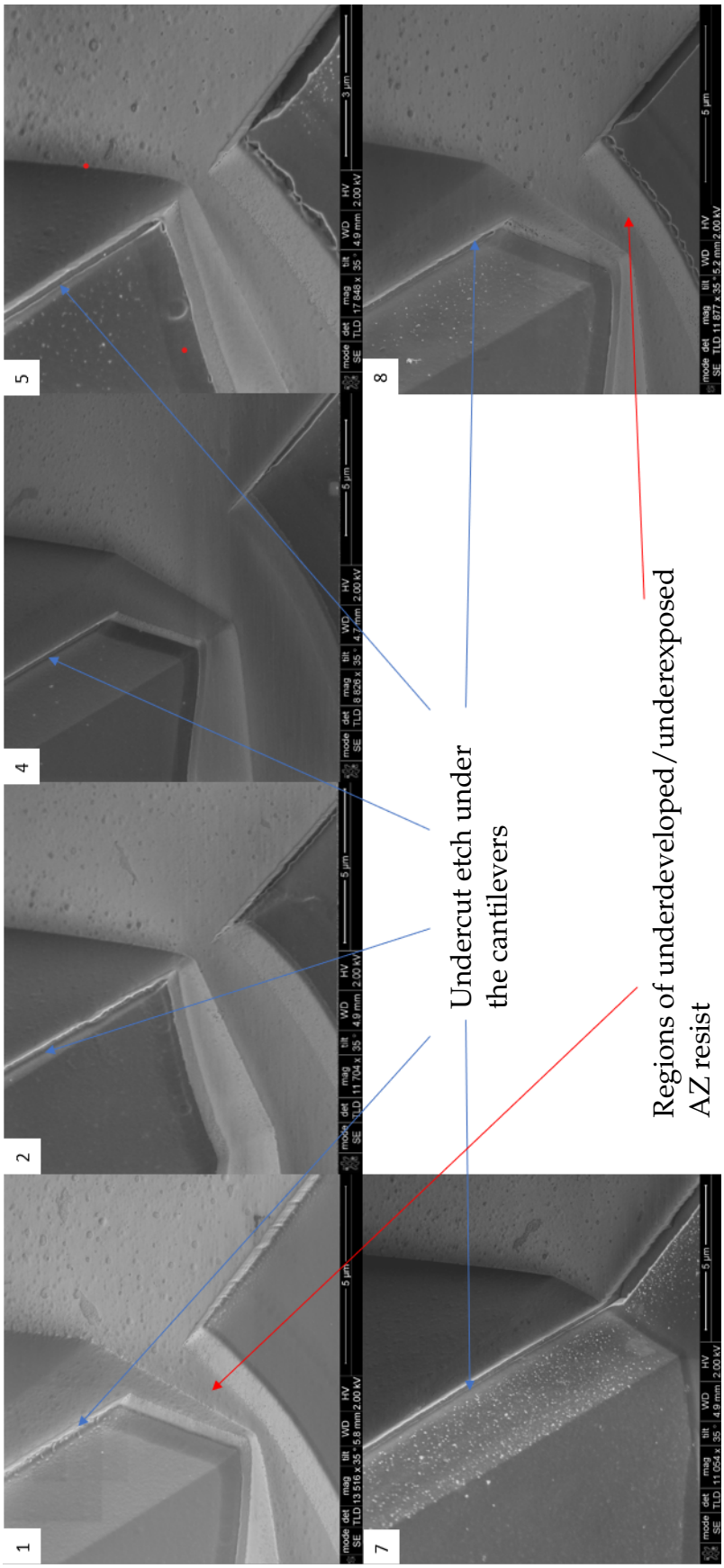

FIGURE 3.16: Collection of SEM images of the tips on the pyramid post mow the grass with no resist or Al. The numbers reference the wet etch time, i.e. 1 is 1 minute, 2 is 2 minutes.

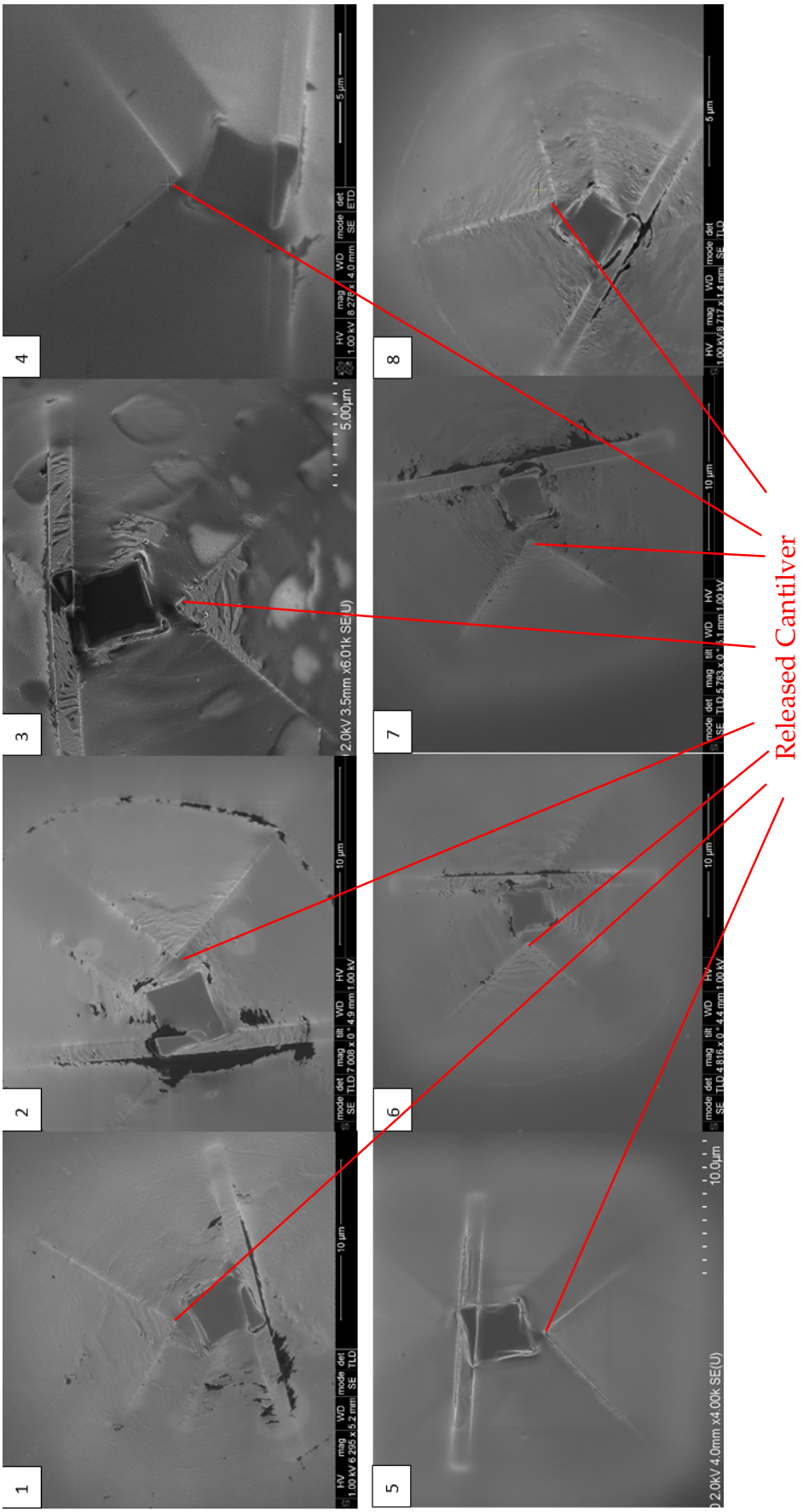

FIGURE 3.17: Collection of SEM images of the tips on the pyramid post mow the grass. The figures have the float coated resist on them with a layer of Al acting as a charge conduction layer. The numbers reference the wet etch time, i.e. 1 is 1 minute, 2 is 2 minutes.

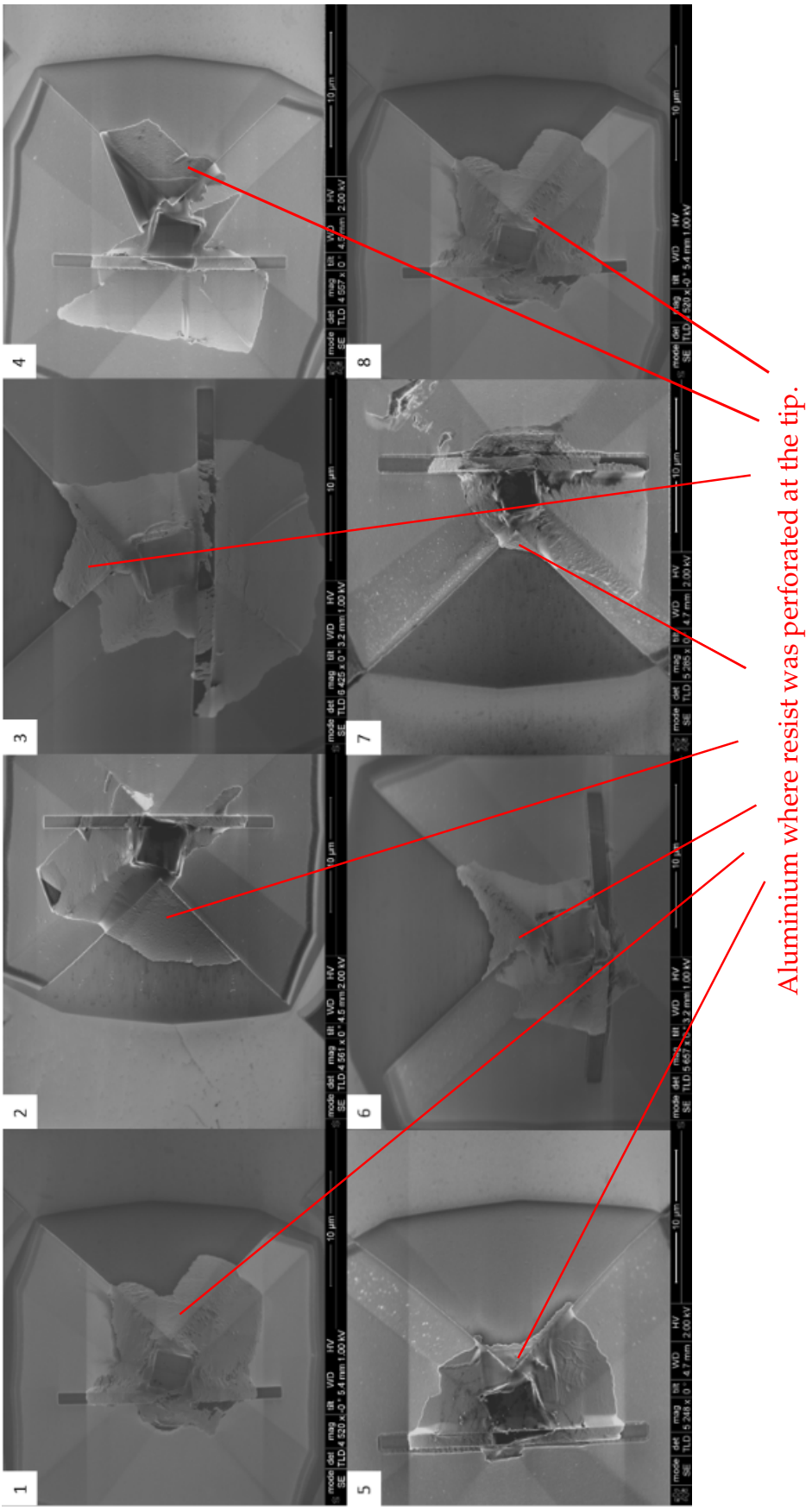

FIGURE 3.18: Collection of SEM images of the tips on the pyramid post resist lift off. If there is metal there on the image, it means the resist was perforated after the float coat to allow the Al to stick to the surface. The numbers reference the previous etch time, i.e. 1 is 1 minute, 2 is 2 minutes..

4 Calibration Samples

4.1 Topography Free Sample for Scanning Electrochemical Microscopy

4.1.1 Introduction

Scanning probe microscopy (SPM) scans can result in high resolution topographic images, however the combination of extremely short range force distance dependence and extended tip structure may lead to artefacts in that the measured topography is not a simple function of the sample shape [277]. Topographic artefacts in contact mode arise because the tip is not a sharp point, and so the point of contact on the tip between the tip and sample can vary. There is usually only one contact point at a time, unless its a double or fractured tip, so this can change discontinuously at the edge giving a jump in the image. Henceforth, the image is not a linear convolution and the image will not be topographically equivalent to the sample. An image of a topographic artefact is shown in Figure 4.1

Fabricating the tips for a scanning electrochemical microscopy (SECM) probe must take the artefact's influencing factors into consideration. If the probe's tip, with the working electrode, is too blunt then the resolved features will not be true to their actual geometries. This would mean the use of a small electrode on a spiked tip, which can get into the small gaps, and having the rest of the probe well insulated so the signal is just from the very end.

During a scanning electrochemical microscopy scan, the topographic changes on a sample restrict the resolution of electrochemical and topographic imaging due to the chemical complexity of the solid-electrolyte interphase. The probe-sample distance within the system affects the diffusion rate of the analyte surrounding the electrode, and as such, the SECM system has analytic difficulty in distinguishing the constituents of the solid-electrolyte interphase from topographic artefacts. The solution to the problem, which

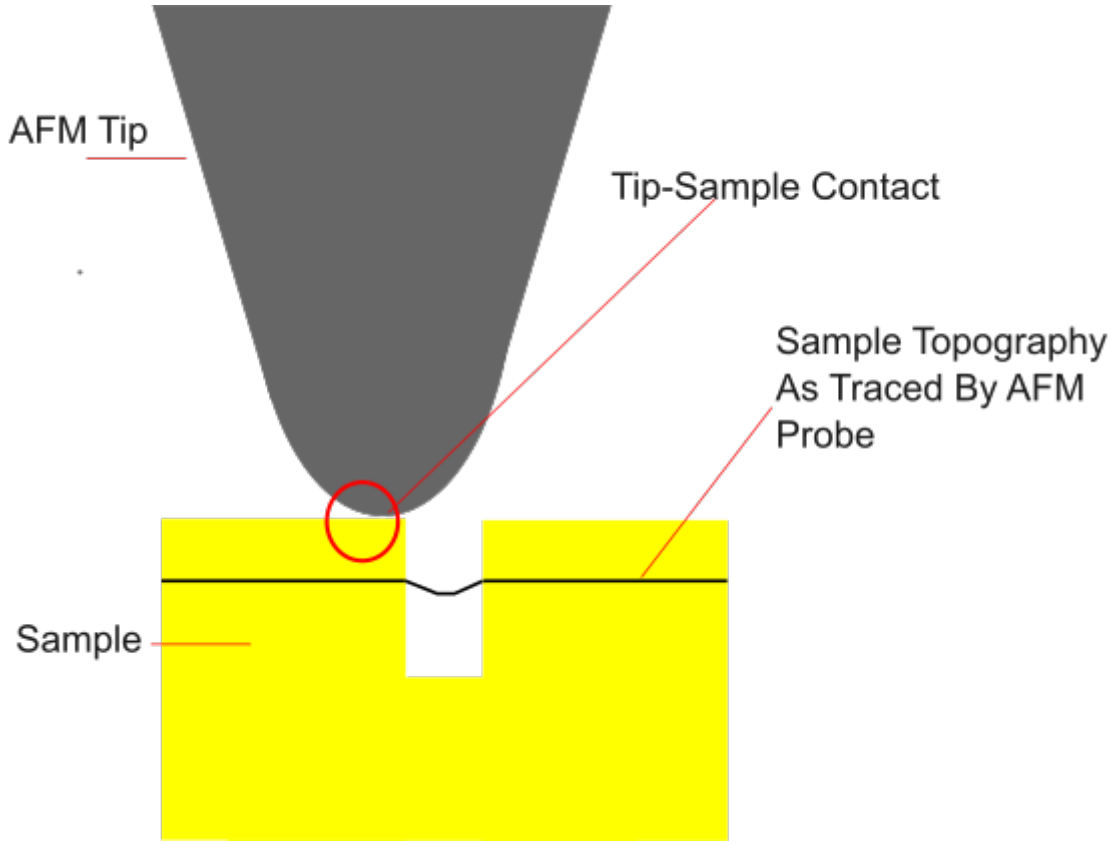

FIGURE 4.1: Schematic diagram showing an AFM scan of an etched sample. It can be seen (grey) that the resolved topographic dimensions is a lot larger than the real dimensions.

is to be explored in this part of the work, is based on the observation that if a sample has minimum topography i.e. "topography free", the electrochemical activity of a sample could be resolved, without the introduction of topographic artefacts. Hence such a sample enables robust separation of the intrinsic electrochemical spatial resolution from the spatial resolution of topographic artefacts coupling into electrochemical contrast.

4.1.2 Design

It is desirable to utilise a topography-free type sample to characterise any SECM device, eliminating any topographic artefacts in the electrochemical scan. As a fundamental part of the SECM sample design, contact pads able to pass nano-amps of current with the ability to make external connections to the sample were added. Contact pads with the dimensions of $500 \mu m^2$ were chosen, made square for simplicity and effectiveness and large enough to be analysed by the Probe-Station. The wires connected to the pads were designed to be 20 μm thick and 4 mm long, allowing for a permanent connection to be made.

A region of interdigitated nano-electrodes comprised the useful part of the sample as this is where the analyte's electrochemical activity is to be monitored using a nano-scale tip. As the electrodes are interdigitated, there is an increase in the effective area and a reduction in the overall surface area compared connected electrodes. The electrode's finger width and length were designed to be 30 nm and 400 nm respectively, with an increasing spacing between fingers of 50, 70 and 90 nm. The gap variance between the electrodes can be used to determine optimal spacing to retrieve accurate and precise electrochemical behaviour of analytes. The electrode pairs were arranged parallel to one another so that if one pair failed open circuit, it would still allow the other electrode pairs to still pass current. A CAD screenshot of the final design is shown in Figure 4.2 and a close-up of how the electrodes are patterned is shown in Figure 4.4 and 4.3, all numbers have the units of a micrometre.

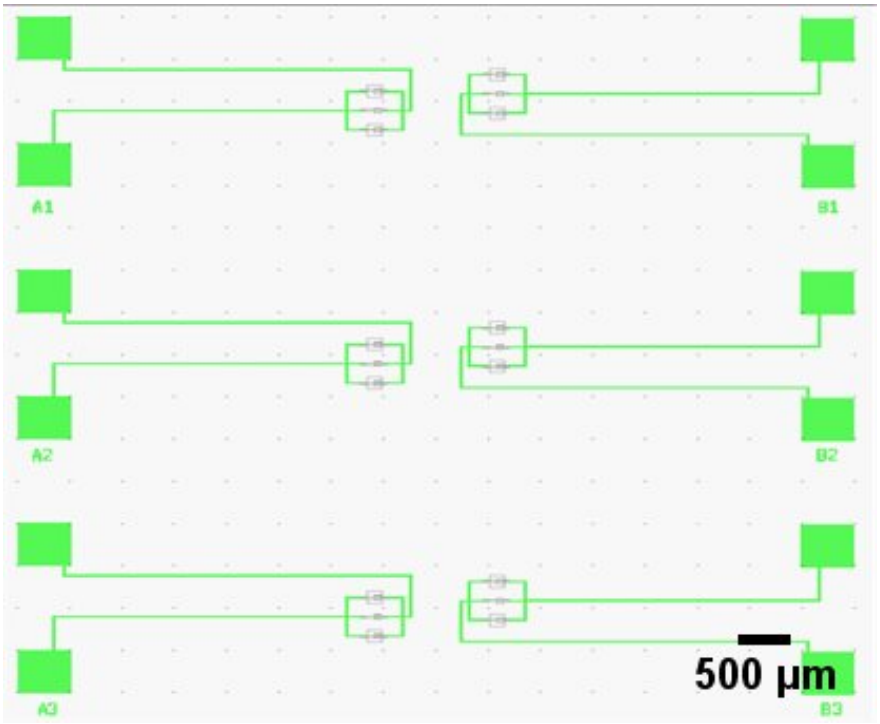

FIGURE 4.2: This image shows a CAD screenshot of the full topography free sample design.

The design was patterned using the Vistec VB6 electron beam lithography tool operating at 100 kV. The machine allows the electrodes to be patterned with high resolution and contrast. A disadvantage of electron beam lithography is that the backscattered electrons can expose more areas of the resist than originally prescribed, and as the electrodes are narrowly spaced, may cause them to merge. This phenomena is known as the proximity effect [278] and is depicted in Figure 4.5 below:

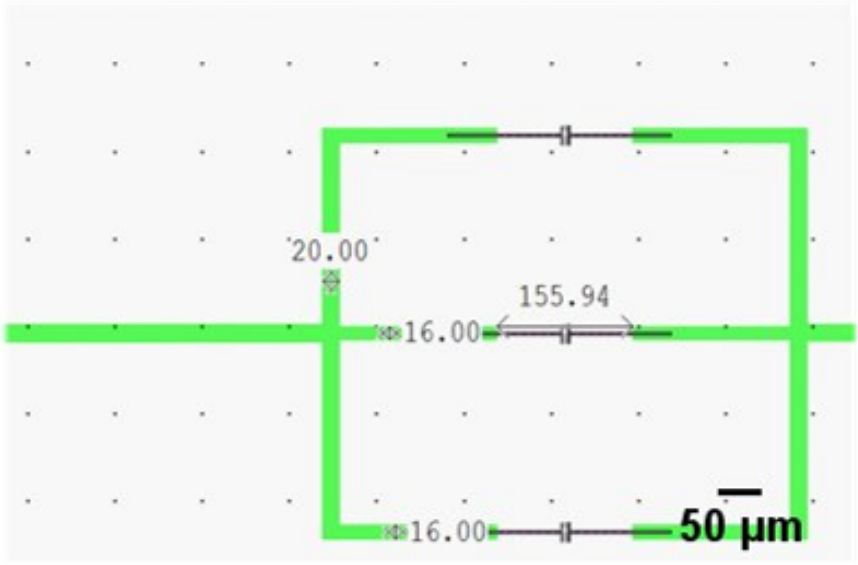

FIGURE 4.3: This image shows a CAD screenshot, zoomed in towards the connecting wires for the interdigitated electrodes.

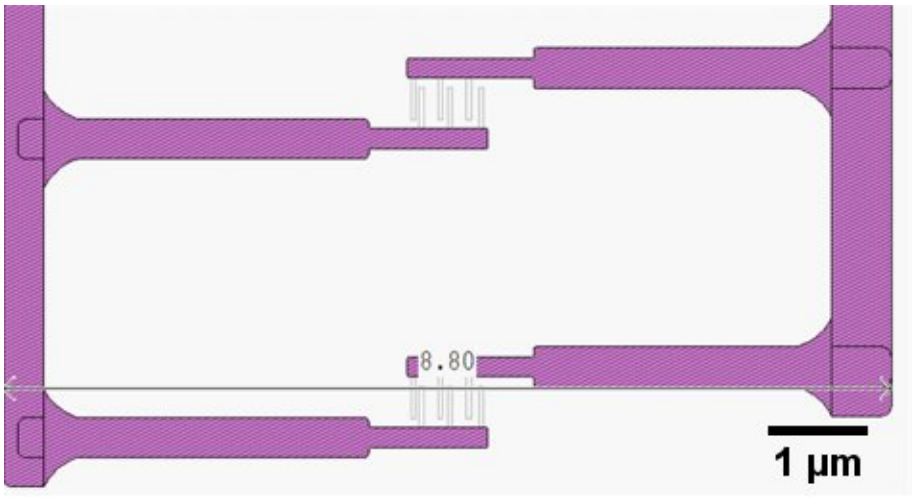

FIGURE 4.4: CAD screenshot of the final connecting wires going to the interdigitated electrodes.

Gallium Arsenide (GaAs) was the chosen substrate to be patterned on due to its ease of wet etching and availability. GaAs is easily etched with weak etchants which do not etch gold or nitride and will become a sacrificial layer in the final fabrication step. Gold was chosen to be the electrically active material on the substrate due to it's resistance to corrosion in electrochemical experiments as well as device processing, good electrical conductivity, availability, weak chemisorbing properties, low stress and high corrosion resistance. The insulating material (silicon nitride) was used as it had a resistance to the etchant and normal electrochemical reagents.

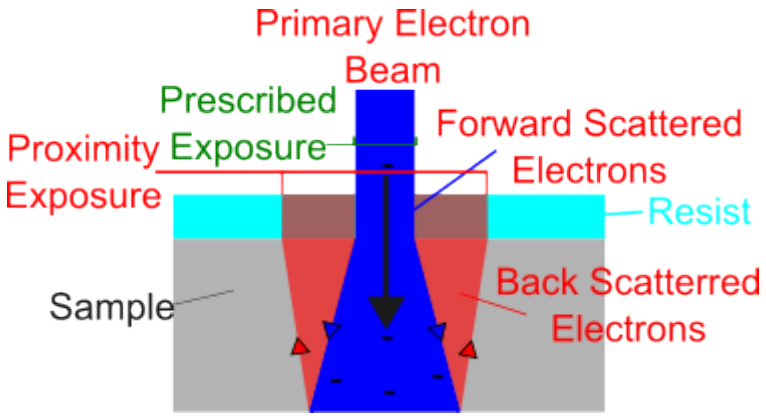

FIGURE 4.5: Schematic diagram depicting the proximity effect. The backscattered electrons cause a larger clearance region of the resist than prescribed on the sample.

4.1.2.1 Fabrication

Previous fabrication of a topography free sample was conducted by Yunfei Ge et al. [279]. The sample's use was to determine SThM's real tip-sample interactions and had boasted sub-2 nm topography. During his process, contamination of the surface after the release etch may have occurred, as well as incomplete wet etching. Therefore, care was taken to etch for longer than the previous process. The fabrication process conducted is shown in Table 4.1 and a visual aid shown in Figure 4.6

On top of the gold features, 400 nm of low stress silicon nitride was deposited. The nature of of the silicon nitride film used to insulate the electrodes is a key experimental variable and has a strong effect on device yield. The low stress nitride came from the ICP 380 tool located in the JWNC. From work done by [279] it was found that this tool's nitride was the only one to produce viable samples, the others showed signs of cracking and poor adhesion. SU8 is added at step (c). This provides a supporting layer to bond the quartz support to the device layer layer's. The quartz is then added to the sample so it can stick together, providing a rigid mechanical handle to the substrate. It should be noted that the quartz piece was solvent cleaned with opticlear, acetone, methanol, IPA and RO water, respectively in an ultrasonic bath for 5 minutes each. The sample was then flood exposed with a photolithography tool known as the MA6 for 150 seconds.

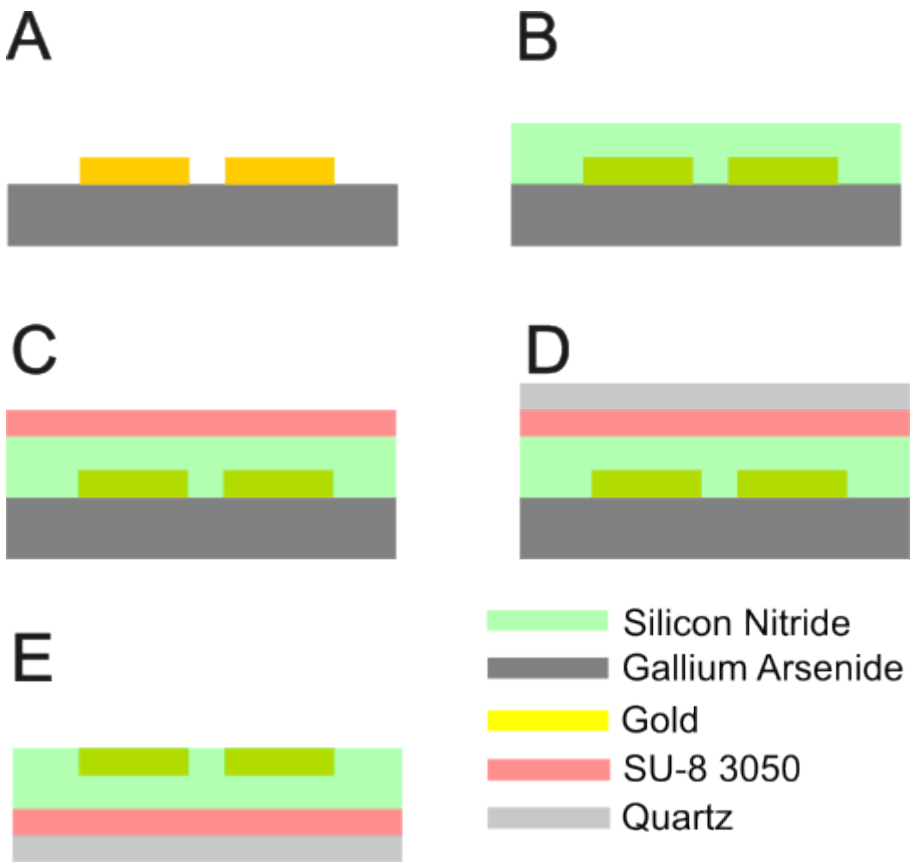

FIGURE 4.6: Fabrication stages of the topography free sample. Within the first stage (a), the GaAs had the patterned gold placed on top of it. Step (b) had ICP 380 silicon nitride deposited on it, whilst step (c) had a bi-layer of SU8-3050 spun on the silicon nitride face. In step (d) clean quartz was placed upon the SU8, acting as a rigid mechanical handle, before wet etching away the GaAs and leaving the topography free sample in step (e).

Process flow for the SECM calibration sample	
Step number	Stage details
1	A 400 μm SSP GaAs wafer was cleaved with a diamond scribe into 20x20 mm^2 pieces. The samples are then cleaned with acetone, methanol, IPA (all within an ultrasonic bath) and an RO water rinse, respectively for 5 minutes each
2	All resist (AR-P 632.06), with a molecular weight of 50 kDa, is spun on the front side at 4000 rpm for 60 seconds to give a thickness of 110 nm.
3	Sample is baked at 180 °C for 10 minutes.
4	All resist (AR-P 679.01), with a molecular weight of 950 kDa, is spun on the front side at 4000 rpm for 60 seconds to give a thickness of 30 nm. The total thickness is now 140 nm.
5	Sample is baked at 180 °C for 10 minutes.
6	Sample is exposed with the VB6 to give the desired pattern. The pads and electrodes had a dose of 650 μC/cm^2, however the beam size was 1nA and variable resolution unit (VRU) of 2 for the electrodes and the pads/connecting wires had a beam size of 64nA and a VRU of 32.
7	Sample is developed in a 23 °C 2.5:1 MIBK:IPA solution for 30 seconds before an IPA rinse and nitrogen gun dry.
8	Sample is oxygen barrel ashed at 80W for 30 seconds.
9	5 nm of Ti and 45 nm of Au is evaporated onto the substrate before being soaked in a 50 °C acetone solution for 2 hours.
10	The remaining resist is then removed using fresh acetone, finishing off with an IPA rinse and nitrogen gun dry.
11	400 nm of low stress silicon nitride was deposited on top with the use of the ICP380 tool in the JWNC.
12	SU8-3050 was spun onto the sample (nitride face) at 500 rpm (with 100 rpm/s ramp) for 5 seconds, succeeded by a speed of 2000 rpm for 30 seconds.
13	Sample is baked at 65 °C for 10 minutes before being baked at 95 °C for 2 hours.
14	A second layer of SU8-3050 was spun onto the sample (nitride face) at 500 rpm (with 100 rpm/s ramp) for 5 seconds, succeeded by a speed of 2000 rpm for 30 seconds. This allows for a more uniform coat and reduced edge bead effects than a single coat.
15	Sample is baked at 65 °C for 10 minutes before being baked at 95 °C for 4 hours.
16	Whilst the sample is still hot, a piece of quartz is placed onto the front face.
17	Sample is then flood exposed with a photolithography tool for 150 seconds (quartz side up).
18	Sample is hard baked at 65 °C for 2 minutes before being baked at 95 °C for 2 hours. This step is repeated a total of 3 time to evenly distribute the thermal load, ensure uniform curing and allowing good adhesion to the quartz, after which the sample should be allowed to cool until at room temperature.
19	Sample is wet etched in a citric acid : hydrogen peroxide (5:1) solution, sitting at 30 °C with the rotational speed of the holder at 80 rpm for at least 48 hours.
20	Sample is rinsed in RO water for 10 minutes before being dried with a nitrogen gun.

TABLE 4.1: Table detailing the process flow for the fabrication of the SECM

The SU8 is exposed so the SU8 molecules become cross linked, giving it a high stability to chemical damage. The sample is post baked to complete the polymerisation process. In step (e) the sample is wet etched in a 30 °C citric acid : hydrogen peroxide (5:1) solution, with agitation, for a minimum of 48 hours. This stage removes the sacrificial GaAs substrate and leaves the exposed gold and silicon nitride surfaces at the same height as the original polished surface of the GaAs wafer.

4.1.3 Results and Discussion

The resulting SEM image of the electrode fingers is shown in Figure 4.7 alongside an AFM scan of one of the finalised finger pairs.

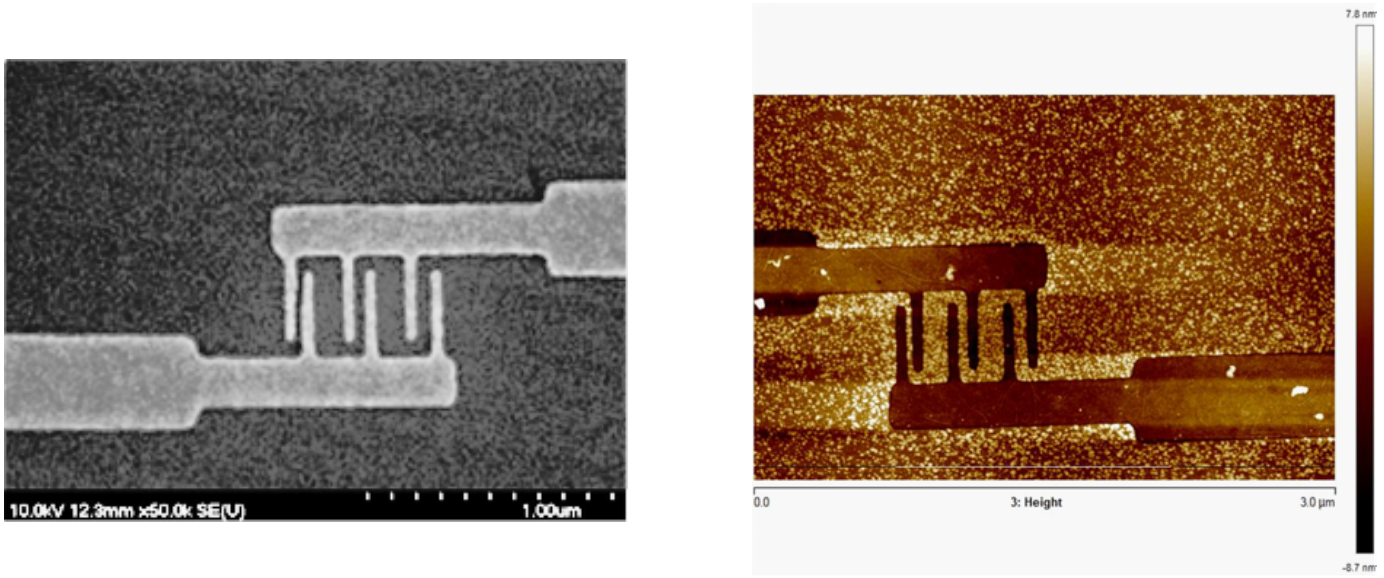

FIGURE 4.7: The image on the left shows an SEM image of the interdigitated electrodes fabricated with the VB6. The figure on the right is an image of an AFM scan conducted on the sample.

As can be seen from the AFM scan in Figure 4.7, a successful sample has been produced with a maximum height of 14.5 nm between conducting and non-conducting regions. Detailed scans of the sample performed by F. Richheimer of the NPL confirmed that other regions to have sub-5 nm topography [280]. The scans will be able to provide data of not only the electrochemical resolution but topographic resolution aswell, giving insight into further development with SECM probes. However, due to de-prioritisation of the SECM work at the collaborating institution, development of this sample was not pursued further.

4.1.3.1 Reflections

During the first few attempts of fabricating the sample, the interdigitated electrodes would merge into one due to a growth in the exposed area compared to the written are because of exposure by the backscattered electrons. The degree of backscattering is dependent on the substrate, resist and the properties of the beam. The exposure produced by the beam can be modelled using Monte Carlo simulations or measurements.

Proximity error correction (PEC) is used to account for the backscattering to give the desired pattern shape [281]. It takes the data gained from the Monte Carlo simulation and the PEC learns the dose profile for single pixel exposure, also known as the point spread function (PSF). It then adjusts the dose at certain points, leading to the intended geometry being patterned. An example of a failed device fabricated without PEC is shown in Figure 4.8.

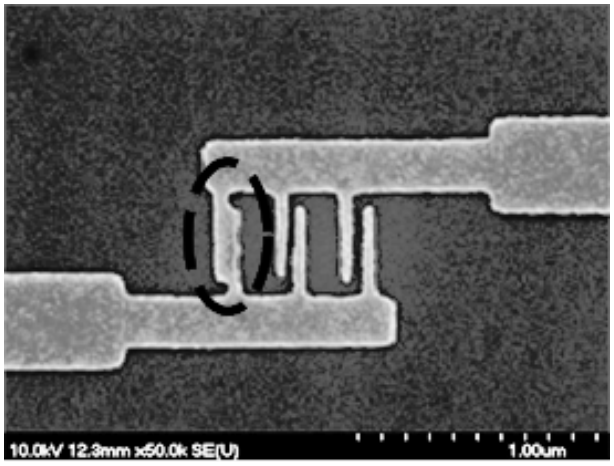

FIGURE 4.8: Image of the interdigitated electrodes merging together, it should be like Figure 4.7.

In order to generate better adhesion to the nitride and thus, a reduction in topography, an adhesive such a NiCr could be put on the top layer (on top of the gold). This is different compared to the standardised sample, with NiCr being the metal being the adhesive bottom layer of the sample.It is also critical that the curing temperature of the SU-8 remains stable during baking as to reduce stress formation as the solvent evaporates, this can lead to cracking and delamination of the SU-8. Care must be taken with manual handling of the III-V material as they are fragile and can break very easily. These samples also have a limited lifetime, when exposed to air they must be used immediately or immersed in electrolyte as to not form an oxide layer and inhibit the effectiveness of the device. Within a closed/sealed vacuum container they can be kept indefinitely after using the fabrication methodology presented.

A 33.3% total yield (1/3 samples) was successfully fabricated. The yield can be improved upon by following the careful considerations presented.

4.2 Correlation Aligned Sample

As the second part of the project was to fabricate TERS probes, a calibration sample for these probes was also required. The probes could make use of this sample by interrogating a small gap between two metal structures, giving an intense EM enhancement which should remain consistent amongst all probes. These gaps are made to resemble plasmonic gap antennae, which in theory could be fabricated onto a TERS probe (EBL alignment and dosing permitting). A method for designing dots and triangles separated by nano-scale gaps using a correlated alignment method was used. The process was carried out in three lithographic stages, one for the markers and the other two for each of the dots. By defining the dots on seperate levels, constraints induced through resist collapse are removed.

The design for the sample had 200 nm dots defined using L-edit [282]. These dots were at first manually designed as rectangles to reduce beam writing time, however, these turned out as very sharp rectangles and not dots. The maximum frequency for the new tool, EBPG5200, was also capped at 100 MHz due to the machine crashing upon writing at frequencies above this, therefore, finding the correct grid size to fit in with these parameters was critical. The final challenge was that of thermal expansion and relaxation of the gold. As a usual bake for PMMA is done at 180°C to take the resit above the glass transition temperature to make it amorphous, it can be assumed that the gold will diffuse under these conditions. This poses a problem when aiming for 1 nm gaps. Therefore, for the final lithographic level it was proposed to expose unbaked resist.

4.2.1 Design and Fabrication

In the design, it was proposed to have a geometry like a dimer structure (similar to a TERS probe design) and dots. A dimer is where two separate geometries of the same size are coupled due to the minute separation distance. The chosen diameter for the dots was set at 200 nm and 200 nm from base to tip on the triangles. As the EM enhancement for the gap plasmon between the two metallic structures decreases rapidly with growing separation due to the dipole field decay factor $(1/d)^{12}$ [283], where d is the separation distance, it is imperative to have a small gap size between patterns.

Although small circular dots are easy to write using single pixel exposure at each period of the beam step size (BSS) for sizes less than 100 nm in diameter, dots larger than this are more troublesome. Due to the Gaussian nature of the electron beam's spot, by drawing a 200 nm circle you will end up with a feature larger than this.

The other issue is the writing time. The two main delays on writing dots are the stage and shape delays. Taking into account movement and settling time for each shape, and as we want a small gap increment (1 nm) between dots, the VRU would have to be 1. This significantly increases writing time compared to writing a big rectangle with a large VRU at high beam current, however it would give the accurate shape placement required.

4.2.1.1 Alignment

In order to achieve a gap size of $\approx$1 nm, smaller than the minimum size using a single exposure due to mechanical collapse of the resist, each half of the dimer is fabricated seperately, since resist collapse places no limits on the position of a structure. The alignment between levels has to be of order gap size i.e. $\geq$1 nm. Therefore, the alignment technique is critical and have been employed [244], [284].

For the correlation markers, Penrose patterns are fabricated to be used within each cell. Penrose patterns are infinite aperiodic tilings of the 2D plane comprised of 2 shapes. The translational aperiodicity gives the Penrose tiling an advantage [285] when used for markers as each local area is unique within the complete pattern. The full geometries of the tile are triangular and rhombic which are incoherent with the Cartesian pixel addressing of the exposure tool because of the 5-fold rotational symmetry. The benefit of this is that a small change in the sampling position causes a large change in the detected pattern at any value offset, without significant variations in sensitivity with position as would be obtained using an alignment pattern based on a rectangular sampling grid. The pattern is also only roughly 50% full of shapes with similar size, leading to a large number of potential edges for the tool to detect [285].

Polygonal markers are still designed within this substrate for global alignment, however, these are more likely to get edge defects such as flagging, rough edges and rat bites [244]. The global polygonal markers are used alongside the Penrose markers in the correlation process as the correlation process can only cope with a maximum initial error of 2 μm. These markers give a good initial point for the alignment process. When fabricated correctly, the Penrose marker will not be hindered by edge defects as there are vastly more edges for detection [244]. Penrose tiles have been used to get an alignment accuracy of

0.63 nm and as such, are perfect for this application [268]. An image of a Penrose marker is shown in Figure 4.9.

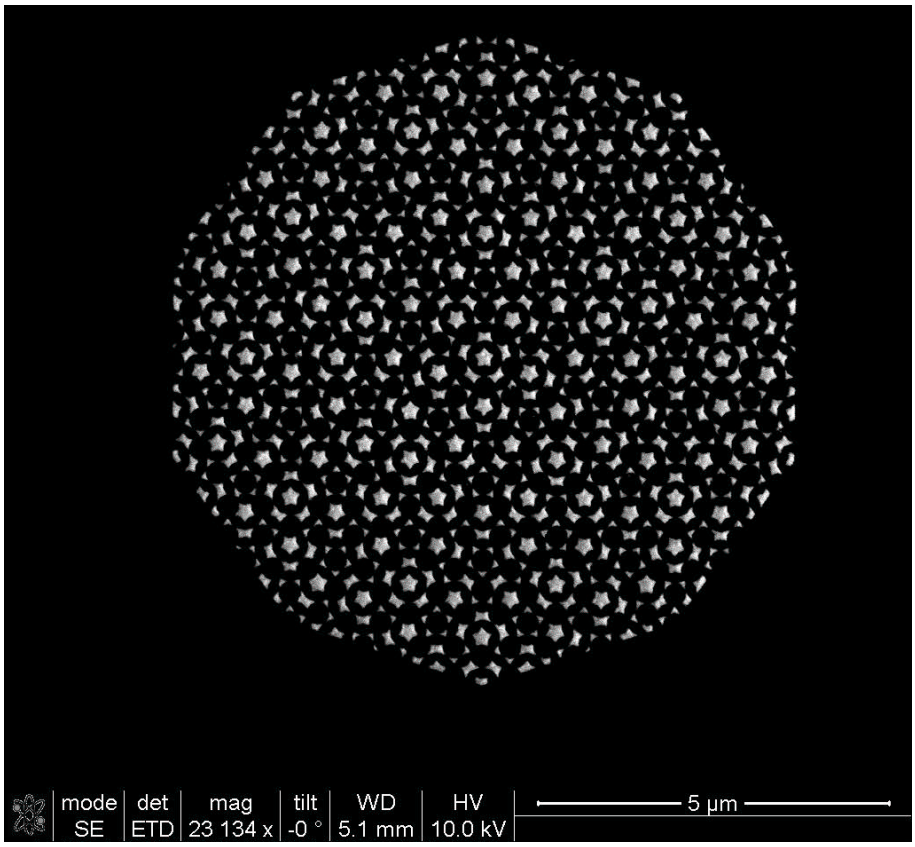

FIGURE 4.9: SEM image of a Penrose marker used for the correlation search.

The next alignment technique corrects for any misalignment from marker searches or any drift within an e-beam tool that is of the order of a few nanometres. The technique is useful when a sparse array of gaps between patterns is required. A notable publication by Steinmann et al. used the technique to produce 1.3 ± 0.7 nm gap spacing between electrodes [286]. The same technique has been employed for these patterns, whereby the two sets of feature's alignment varies systematically over an array so that adjacent features differ in alignment by 1 nm. This is simply done by differing the period of one of the features by 1 nm in x and y in Vernier. An image of the technique is shown in Figure 4.10.

4.2.1.2 Fracturing

As the requirements for placement are extreme, great care is needed in defininig ow the structures are exposed. BEAMER allows the user to "Follow Geometry", meaning that it

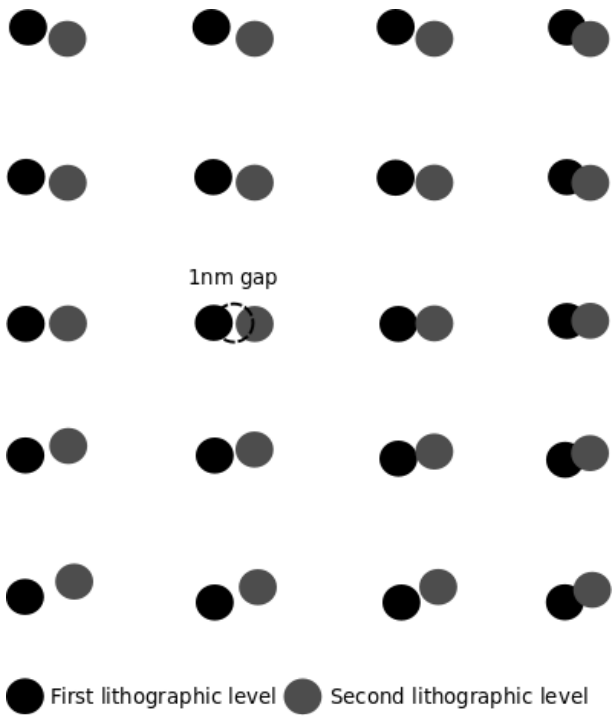

FIGURE 4.10: Schematic drawing of the dots arrayed out with the alignment technique employed.

will write one pattern at a time opposed to multiple at the same time. If the dots and Penrose patterns are written one at a time there will be less error due to drifting of the e-beam during the exposure of a complete field of a structure.

4.2.1.3 Fabrication

The steps used to fabricate the global and Penrose markers on the sample is outlined in the Table 4.2 below. The Penrose markers took a dose of 800 μC/cm^2, VRU of 4 and 1nA beam to write. The global cross and square markers took a dose of 800 μC/cm^2, VRU of 32 and 64nA beam to write.

The next stage was to fabricate the dots and triangles within the boundary of 4 Penrose markers and the use of the alignment markers. The first layer of dots was arrayed out with a period of 10 μm with a VRU of 1, dose of 1250 μC/cm^2 and a beam size of 1nA. The first layer of triangles was also arrayed out with a period of 10 μm, but with a VRU of 2, dose of 1150 μC/cm^2 and a beam size of 1nA. The 10 μm separation distance is a nice optical separation so that each dot pair can be interrogated without crosstalk in a conventional optical microscope. The process from Table 4.2 stays the same for this development, starting from step 2. However, the thickness of metal changes from 5 nm of

Process flow for the TERS calibration sample	
Step number	Stage details
1	A 400 μm SSP silicon wafer with 315 nm of silicon nitride on top was cleaved with a diamond scribe into 20x20 mm^2 pieces. The samples are then cleaned with acetone, methanol, IPA (all within an ultrasonic bath) and an RO water rinse, respectively for 5 minutes each
2	All resist (AR-P 632.09), with a molecular weight of 50 kDa, is spun on the front side at 4000 rpm for 60 seconds to give a thickness of 200 nm.
3	Sample is baked at 180 °C for 10 minutes.
4	All resist (AR-P 679.01), with a molecular weight of 950 kDa, is spun on the front side at 4000 rpm for 60 seconds to give a thickness of 30 nm. The total thickness is now 230 nm.
5	Sample is baked at 180 °C for 10 minutes.
6	Sample is exposed with the EBPG to give the marker layer pattern.
7	Sample is developed in a 23 °C 2.5:1 MIBK:IPA solution for 30 seconds before an IPA rinse and nitrogen gun dry.
8	Sample is oxygen barrel ashed at 80W for 30 seconds.
9	5 nm of NiCr and 75 nm of Au is evaporated onto the substrate before being soaked in a 50 °C acetone solution for 2 hours.
10	The remaining resist is then removed using fresh acetone, finishing off with an IPA rinse and nitrogen gun dry.

TABLE 4.2: Table detailing the process flow for the fabrication of the TERS calibration sample's markers.

NiCr to 1nm of NiCr. The reasoning behind this is to limit the interference from the NiCr as it is known to dampen the plasmon, which should be negligible at 1 nm, but to have just enough as to act as an adhesive between the gold and substrate. SEM images of the fabricated patterns are shown in Figure 4.11.

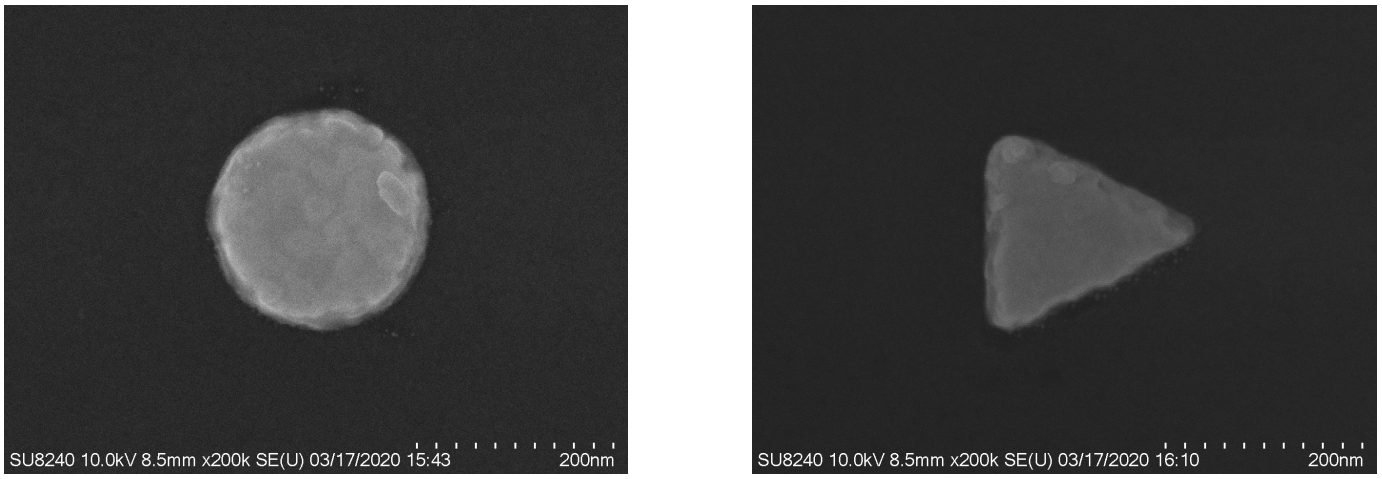

FIGURE 4.11: The image on the left shows an SEM image of a dot fabricated with the EBPG. The image on the right is an SEM image of a triangle fabricated with the EBPG.

The last stage, and the most crucial, was to recreate the same triangles and dots but array them out with a period of 10.001 μm. The problem with this stage however is the resist bake. At 180 °C, the previous layers features are susceptible to thermal activated diffusion and recrystallisation which can shrink the features by a few nanometres. This poses a problem, as even a few nanometres reduction in the feature size could result in the 1 nm gap size between structures becoming several. Therefore, a dose test was conducted to see if it was possible to do high resolution lithography with unbaked resist.

Following the exact same stages as the second layer, however not baking the resist, the first dose test sample was written on again. Writing on the previous dose test sample would also allow the further inspection of the previous layers dots and triangles. Multiple SEM images of the dose test was taken, however, only the best will be reported on here. The images are shown in Figure 4.12.

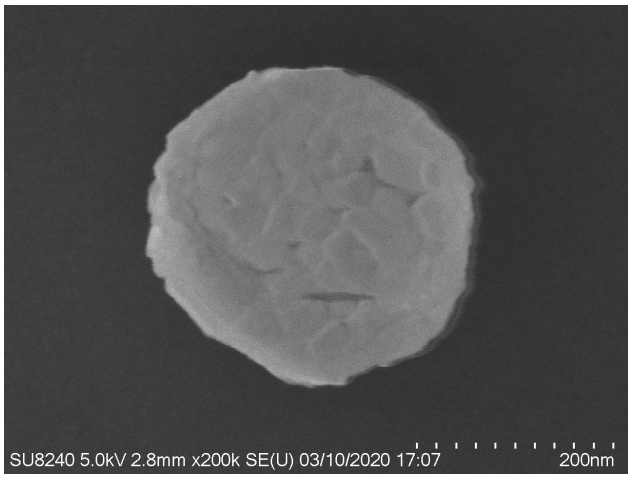

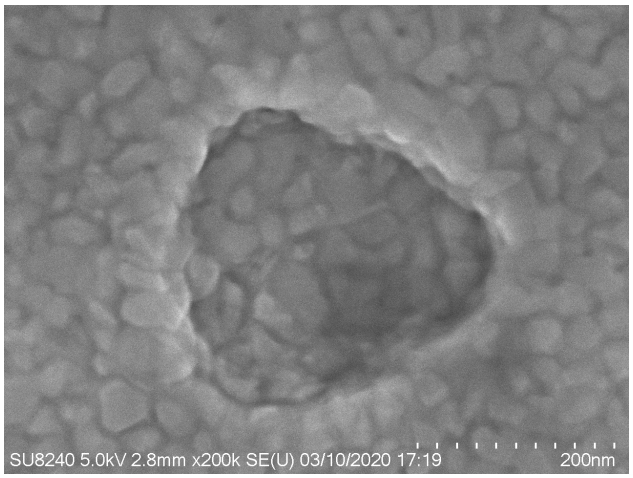

FIGURE 4.12: The image on the left shows an SEM image of a dot fabricated with the EBPG on unbaked resist. The image on the right is an SEM image of a triangle fabricated with the EBPG on unbaked resist.

Surprisingly, the dot had turned out circular in geometry and with more time developing the process, the pattern could potentially work with an unbaked resist. The triangles however, did not turn out well. The image depicted above was the only one showing any sign of a triangular geometry, the rest were not visible.

As the dots were the only ones to turn out, a proposal to do a long, low temperature bake was employed. Baking above the glass transition temperature of the resist (108°C) at 120°C seemed a reasonable temperature to bake at. As the solvent diffusion rate in the PMMA is related to the square root of time, a short bake will not do, therefore a 30 minute bake was proposed. The sample was prepared using the same techniques and dose as the second layer job, however, both resists spun were baked at 120°C. The results of this is shown in Figure 4.13.

As shown in Figure 4.13, the small gap between the dots can be achieved with good alignment. The next stage would be to test them, expecting a large increase in the electric field intensity. The Raman system was however lately moved from the NPL, to a system in the University of Glasgow where a transparent sample is required to test the above sample. The substrate material was therefore switched from Silicon-Silicon nitride to a 160 μm glass slide. The resist spin and cleaning requirements remained the same, however when fabricating with glass a charge conduction layer is required. In order to accommodate this, after the resist spin but before exposure, 20 nm Al was deposited onto the sample. After exposure this Al layer is then removed using a MF319 solution for 30s, when the sample is then therefore subjected to development and metal deposition as normal.

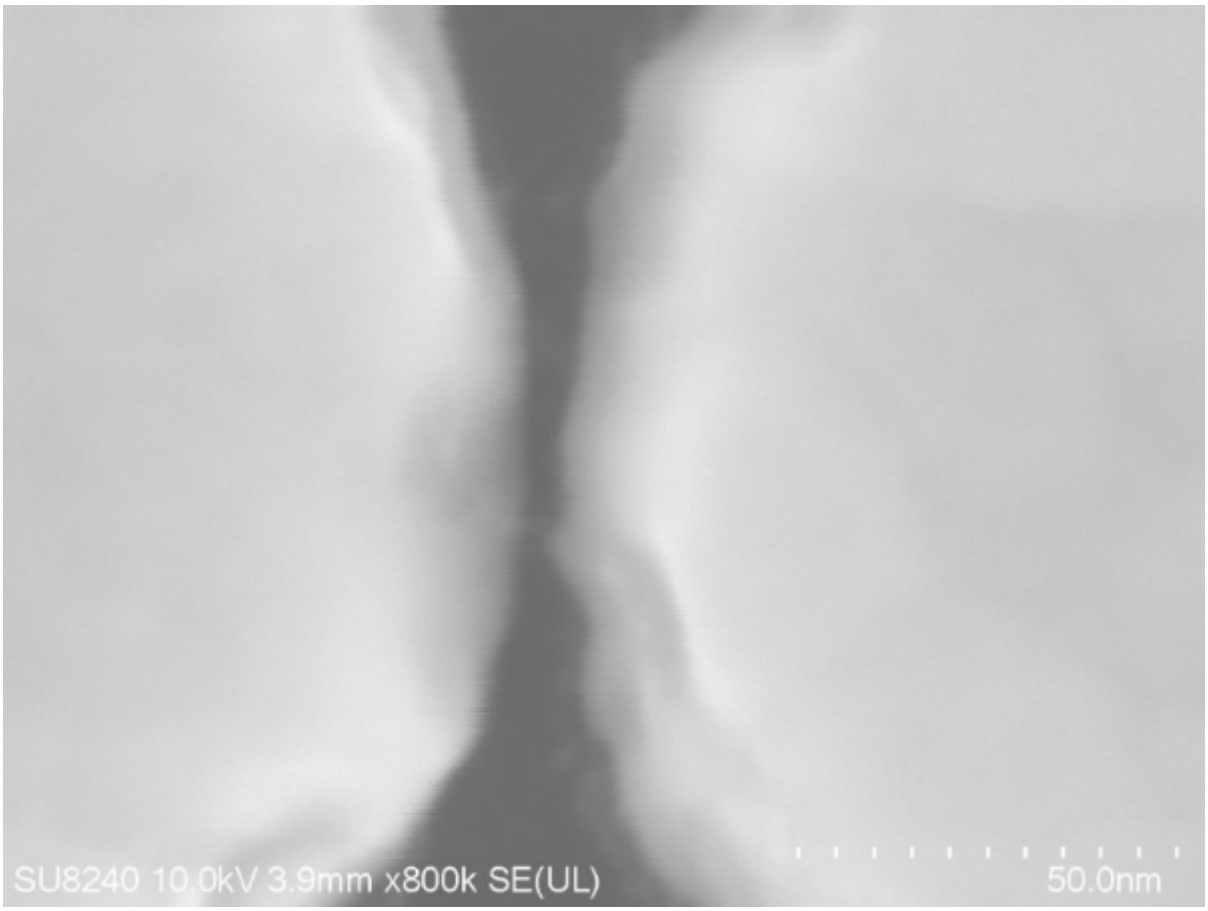

FIGURE 4.13: SEM image of a dot pair separated by 3 nm. Smaller gaps were obtained but imaging them in the SEM was challenging

4.3 TERS Flat Probe

After the designs of the TERS probes were chosen, it was decided that having the sensor on a flat sample would give some preliminary results on reflectance and an idea on the enhancement that would come from the device. The setup of the AFM at the NPL takes a while to assemble and align and the other spectrometer-microscope available is a top-down illumination tool. The manipulation of the setup for the probes is time consuming, hence it was felt to be useful to use these flat samples to provide data before the finished probes were tested.

4.3.1 Flat Probe Fabrication

As the flat probes were to resemble what kind of enhancement is seen from an actual probe, the design parameters were to be kept similar to that of the probes themselves.

The grating period and waveguide opening angle followed the same geometries of the probes, alongside every other dimension. Glass substrates with the same sensor design, including material stack (no silicon or silicon nitride) were fabricated too, these could be used within the TERS experiments. The process of designing the flat probes is shown in Table 4.3 below.

Process flow for the flat probe sample	
Step number	Stage details
1	A 400 μm SSP silicon wafer with 400 nm of silicon nitride on top was cleaved with a diamond scribe into 15x15 mm^2 pieces. The samples are then cleaned with acetone, methanol, IPA (all within an ultrasonic bath) and an RO water rinse, respectively for 5 minutes each
2	All resist (AR-P 632.09), with a molecular weight of 50k Da, is spun on the front side at 4000 rpm for 60 seconds to give a thickness of 200 nm.
3	Sample is baked on a hotplate at 180 °C for 3 minutes.
4	All resist (AR-P 679.01), with a molecular weight of 950k Da, is spun on the front side at 4000 rpm for 60 seconds to give a thickness of 30 nm. The total thickness is now 230 nm.
5	Sample is baked on a hotplate at 180 °C for 3 minutes.
6	Sample is exposed with the EBPG in the shape of the sensor design pattern.
7	Sample is developed in a 23 °C 2.5:1 MIBK:IPA solution for 30 seconds before an IPA rinse and nitrogen gun dry.
8	Sample is oxygen barrel ashed at 80W for 30 seconds.
9	1 nm of NiCr and 70 nm of Au is evaporated onto the substrate before being soaked in a 50 °C acetone solution for a minimum 2 hours.
10	The remaining resist is then removed using fresh acetone, finishing off with an IPA rinse and nitrogen gun dry.

TABLE 4.3: Table detailing the process flow for the fabrication of the TERS flat sample.

Due to the sample being flat and not up a pyramid, which a probe would be, the clearance dose is reduced by 30%. The dose is reduced because the areal exposure on the slope is reduced. The clearance dose of the resist for the design was 1400 μC/cm^2, with a beam step size of 2 and a beam current of 2 nA. Each sensor design was arrayed out in 300 μm^2 squares, large enough for the scan range of the AFM and the reflectance spectrometer's microscope's field of view. The period of each sensor was kept at 3 μm, keeping the plasmon interference with each sensor to a minimum whilst not allowing the dominant signal to be returned be that of the silicon. Gold squares and antennae with the coupler filled in were fabricated as references for the reflectance measurements, maintaining the 300 μm^2 array size. Images of one antenna archetype following the fabrication are depicted in Figure 4.14 below.

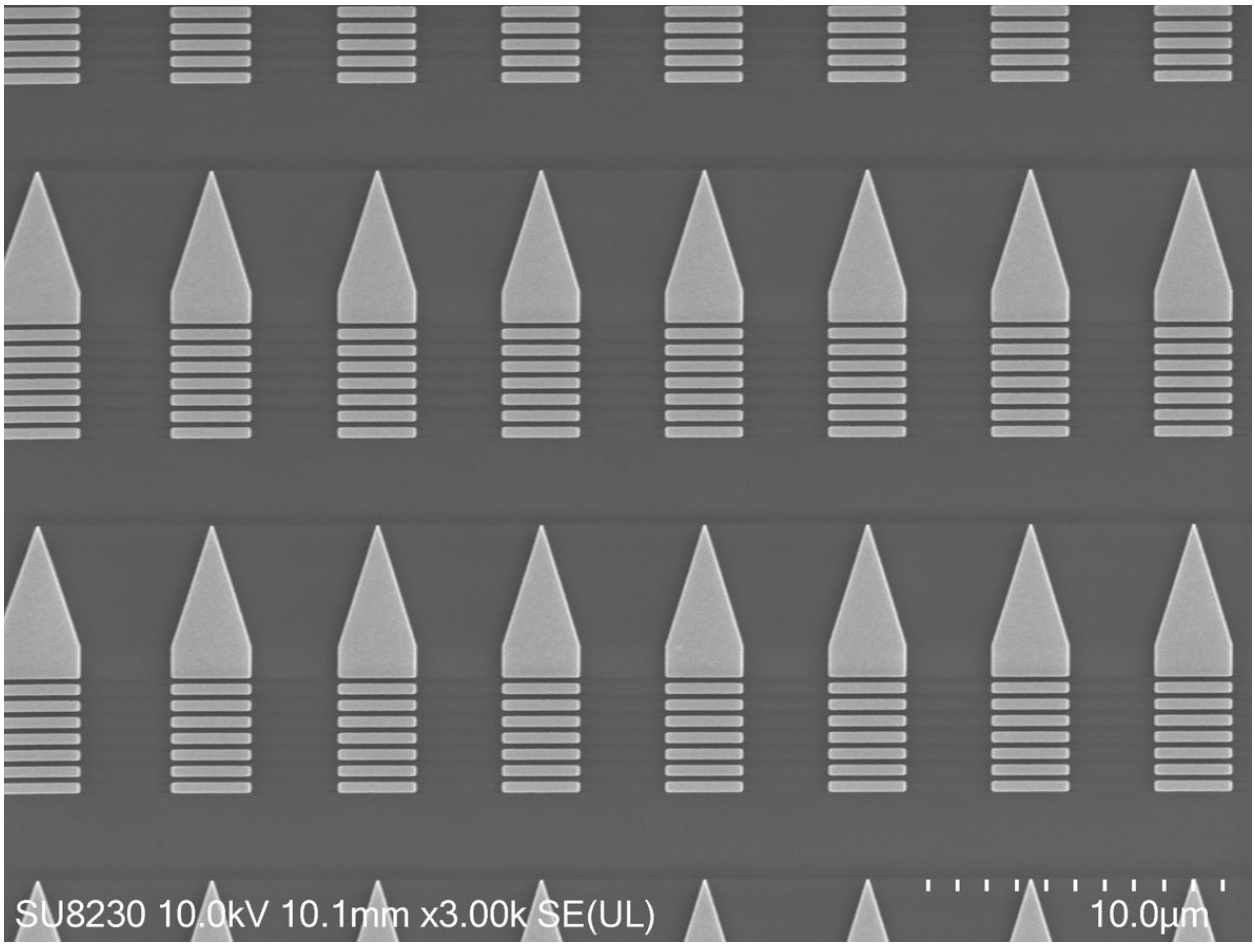

FIGURE 4.14: SEM image of the 25 ° opening angle, 350 nm period antenna.

4.3.1.1 Summary

The planar probe substrates with and without the grating component were successfully fabricated without any yield loss. The substrates will be interrogated using linear spectroscopy. The linear spectroscopy results of these structures shown in Figure 4.14 are contained within Section 5.3.

5 Experiments

5.1 TERS experimental setup (NPL)

The first tests whilst using the probes were conducted whilst at the NPL. The NPL house a TERS setup which is built to give quantitative measurements of a TERS enhancement [287]–[289]. Thus makes it the perfect place to measure a potential enhancement out of the probes.

5.1.1 Spectrometer

As with all TERS set-ups, the spectrometer is one of the most important parts. With the Raman signal being so small and close to the wavelength of the pump, how well a spectrometer operates is based on how it blocks out the signal of the pump from the Raman signal. The NPL use a Horiba Labram Evolution HR 800 spectrometer, which uses an edge filter specific to each wavelength. This filter removes the Rayleigh scattering component and measures the Raman Stokes shift from around 100 cm^{-1} [83]. The spectral gratings installed on the system were 150, 300, 600 and 1800 lines/mm.

5.1.2 Optical Alignment NPL

As this setup was configured by the NPL, the optical alignment from the probes and spectrometer excitation to detection required extensive manual adjustment and operator expertise. All alignment and measurements taken were performed by S. Wood, with me working with him to configure the system to take the measurements I wanted to make. The whole alignment procedure of the side illumination excitation follows the path of the collimated beam before finally arriving at the long working distance objective, around 30 degrees from the sample plane, for collection/excitation. To ensure the beam follows the correct path, 2 mirrors are put in place. These mirrors act as a periscope, redirecting the

optical path, and are mechanically tilted and rotated to ensure that the beam is collinear and centred on the objective's optical axis. This setup can be viewed in Figure 5.1.

To ensure the beam is properly centred, 2 optical irises are put in the beams path, replacing that of the far field objective. The optical irises are mounted with a custom-made part for the NPL, where they a fixed centrally to ensure it is where the objective should be. The irises are separated with one close to the sample and one further back, whereby a small change in the angle detects poor collinearity. The irises start in a fully open position and are slowly closed, adjustment of the mirrors is made to ensure the beam is still centred and the maximum amount of light is transmitted onto a laser detector card as the opening shrinks.

Further fine tuning of the reflected beam/incoming beam was also previously done by S. Wood where a mirror is placed where the objective lens/detector card would be. An Iris is placed in the centre of the laser path coming out from the spectrometer, where if it's in the centre, the collimated beam will reach the new mirror. The periscope mirrors are then adjusted slightly as to have the reflected beam pass into the spectrometer along the same path as the excitation beam. If the angle is offset, the beam will diverge and not reach the spectrometer. This fine tuning is depicted in Figure 5.2. With the spectrometer running under continuous acquisition, the peak intensity of the Rayleigh scattering should be at a maximum if correctly aligned. Further adjustments of the mirror should be made until the maximum is achieved. The same is done with the silicon reference sample, making sure the peak Raman signal is maximised. This last stage however has its downfall as it relies on the sample properties remaining constant from a previous known perfect alignment. For a further breakdown of the alignment from start to finish, see F. Richeimer thesis [83].

5.1.2.1 SPM setup

With the TERS probes successfully fabricated it was time to test them to see if we get an enhancement, and if so, what magnitude. The first SPM kit to be used was housed at the NPL, a custom built AFM (Combiscope 1000, AIST-NT) with optically aligned optics. It houses a 3-axis piezoelectric scanner, allowing for better control on the scans and easier alignment. The laser for the AFM itself had a larger wavelength, 1300 nm, as to not interfere with the other optical coupling introduced by the spectrometer.

During the experimental stage the 100x (0.7 NA) magnification objective was preferred, however during the beam alignment a reduced magnification was used in order

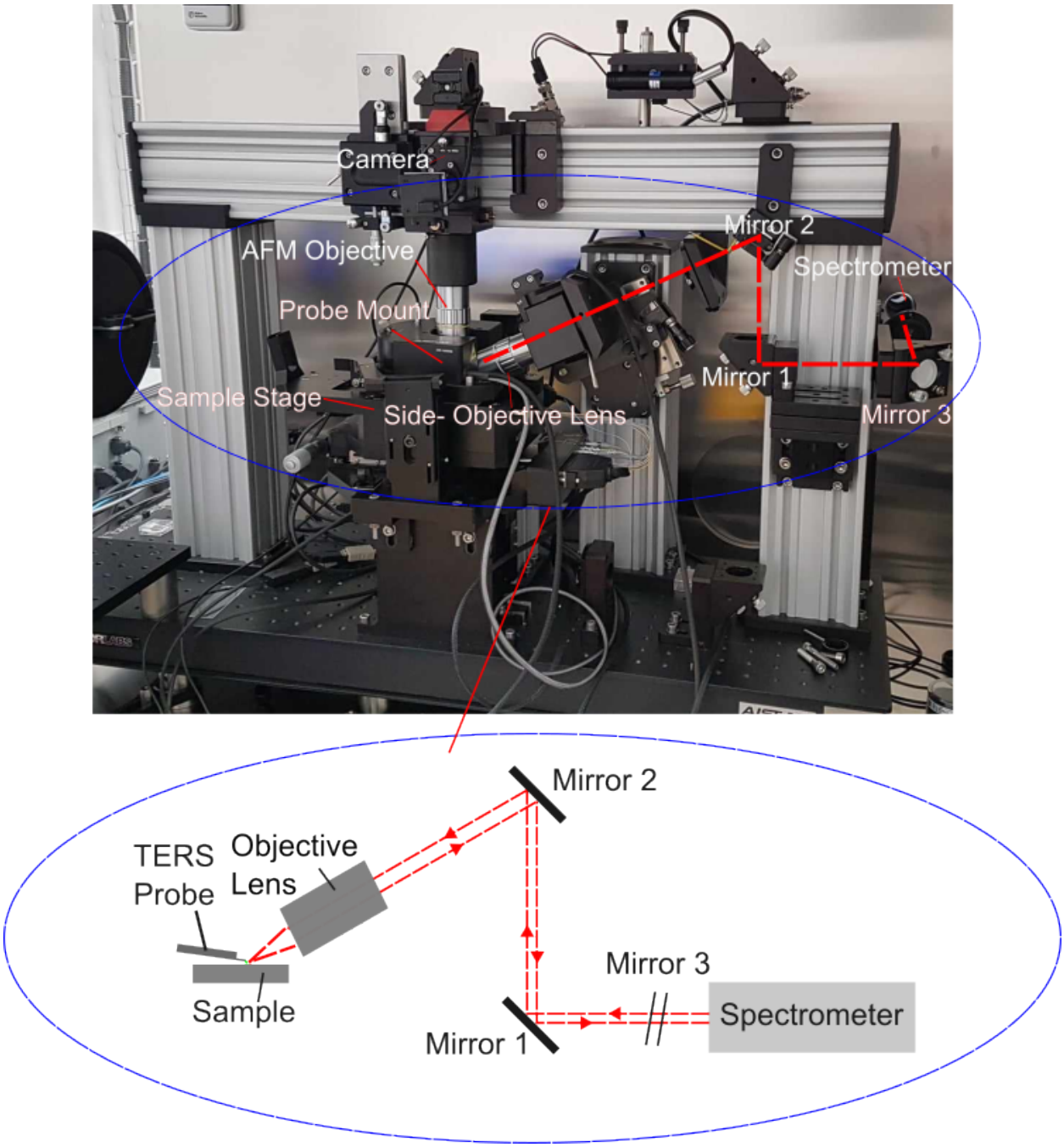

FIGURE 5.1: The top image shows an annotated photograph diagram of the optical setup for the NPL. The bottom image shows a schematic diagram of the periscope setup and how light travels to the sample.

to gain a wider field of view. The coupling angle for the laser path was roughly 30^o and beam was redirected with the use of mirrors.

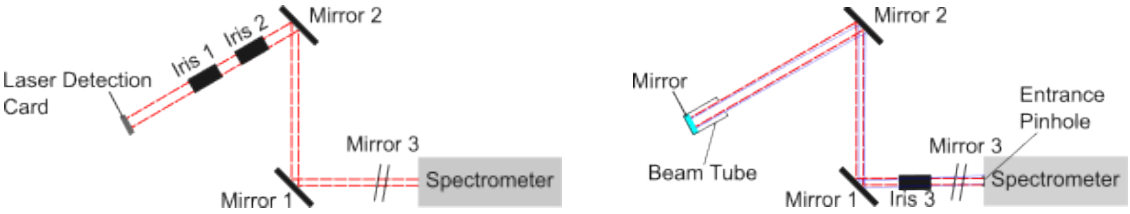

FIGURE 5.2: Fine alignment of the NPL setup. The image on the left shows the two optical irises in place to ensure the beam is centred. These Iris replace where the objective lens goes. The image on the right shows a third iris being added to ensure the beam is centred on the way back from the beam path, ensure it is centred going back into the spectrometer.

5.2 NPL Results

The first comparative results of examining a probe were undertaken by F. Richeimer. This test was to use an already fabricated SThM probe, which has the same dimension and angles, representative of any TERS probes and mount it within this TERS setup. A Raman map was taken of the tip apex and of the silicon sample. An Image of the results taken by the NPL and sent via email to myself is shown in Figure 5.3.

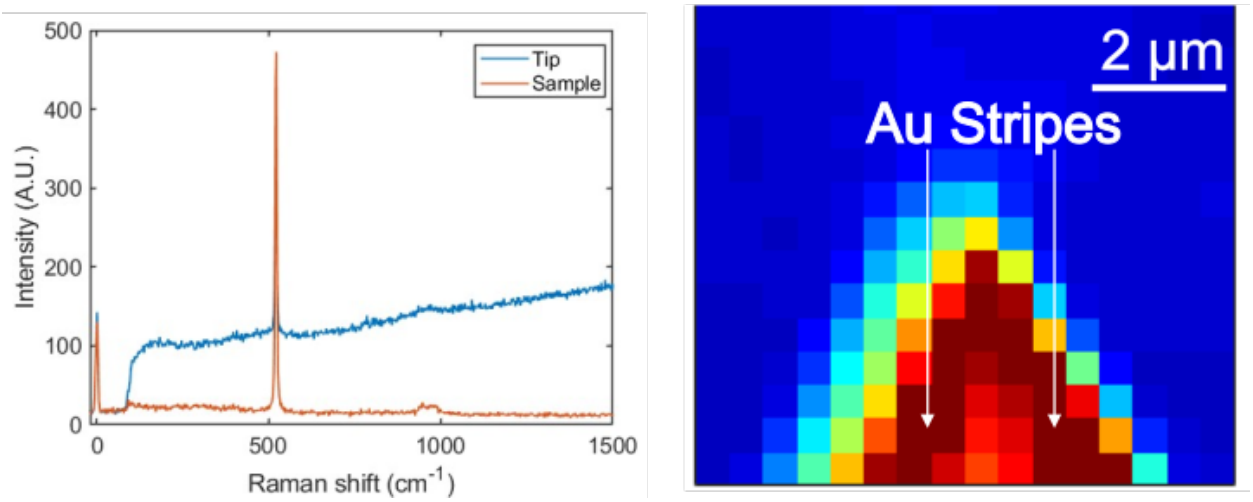

FIGURE 5.3: Image on the left shows the Raman Spectrometry data of a mounted SThM probe, just above a Silicon sample. The image on the right shows the PL intensity, with the darker shade (red) giving a lager fluorescence.

These results indicate that the Raman Spectrometer is working as should be, we start to see a strong Si peak at 520 cm^{-1}, in orange, which is expected. But the image on the right also shows a strong background fluorescence of the gold, indicated by the white arrows. This doesn't give much insight into it's TERS capabilities as fluorescence and

Raman are differing phenomena. It does however show us that the gold is absorbing photons and emitting them at a higher wavelength within this setup. So, if a gold tip was brought into contact, it will be capable of absorption, but surface plasmon resonance still must occur to generate Raman scattering. This experiment however does prove that we can image a tip of the same geometry in the NPL setup, retrieve a spectroscopic signal off it and scan with it. To make them functional as SPP probes, a metallic grating of a relevant period will allow the k vector of the light and k of a plasmon polariton to match allowing for propagation. Achieving the current excitation angle of this grating proved challenging due to the reduced freedom with the "periscope" mirrors in this setup shown in Figure 5.1 and 5.2.

Although the diffraction angles of the gratings were determined based on the information provided by the NPL, modification of the system to accommodate the required incidence angle was not permitted, due to the technically capable person leaving and the desire of others in NPL to leave the system in a fixed state to support its work on calibration. Knowing this, some probes were taken and tested to see if we could generate a plasmon within this setup. The results are shown in Figure 5.5.

The Si substrate, with statistically and correlation aligned gold dots sample was used during experimentation. A Raman active molecule (Raman Reporter) adhering to the metal would be required to see an enhanced Raman signal off this sample, as gold is not Raman active. A lack of availability of any Raman active molecules within the facility meant the experimentation had to be done without one, but the silicon substrate provides a good Si background signal.

Within the AFM measurements, the normal force and lateral force relate to the mechanical deflection of the probe's cantilever. When the spectrometer laser is directed onto the tip, the laser is typically visible within these signals as a crosstalk, these signals can be used to determine if the laser is in the correct position.

The first point is to find the resonance frequency of the probe to ensure it has a peak and can perform in tapping mode, which it has. This is shown in Figure 5.4. Of the various resonances observed, the large resonance at 220kHz was used due to its large peak and tapping mode was found to operate at this frequency.

After alignment the laser was then positioned onto the cantilever as shown in Figure 5.5, before performing Raman maps of the tips when out of contact, then re-aligning when close to contact.

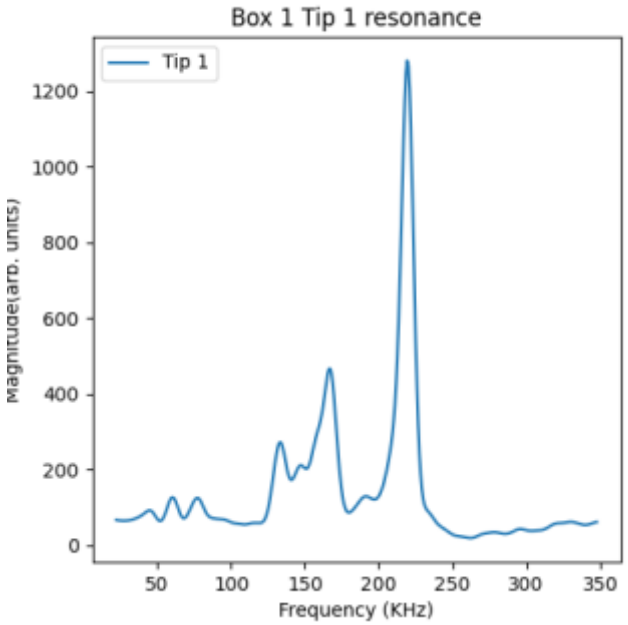

FIGURE 5.4: Frequency vs vibration magnitude plot of the TERS probe's cantilever.

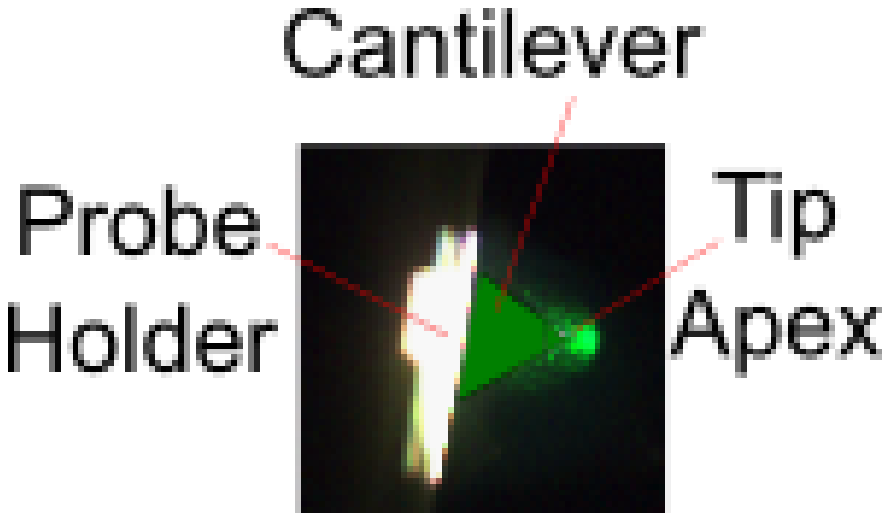

FIGURE 5.5: Camera image of the green laser on the TERS probe cantilever. A sketch of the TERS probe has been overlaid to make the image clearer.

As can be seen from the normal and lateral force images (Figure 5.6) and the video image (Figure 5.5), we do in fact have the laser location right for scanning or achieving a TERS signal. The laser is visible within these areas. With the Raman map indicates a slight fluorescence at the top left, this is interestingly an area where a metal "flag" is. This metal is not attached to the cantilever, but rather the metal already existing on the substrate. There are no features, apart from the flag, that show there is a plasmonic signal.

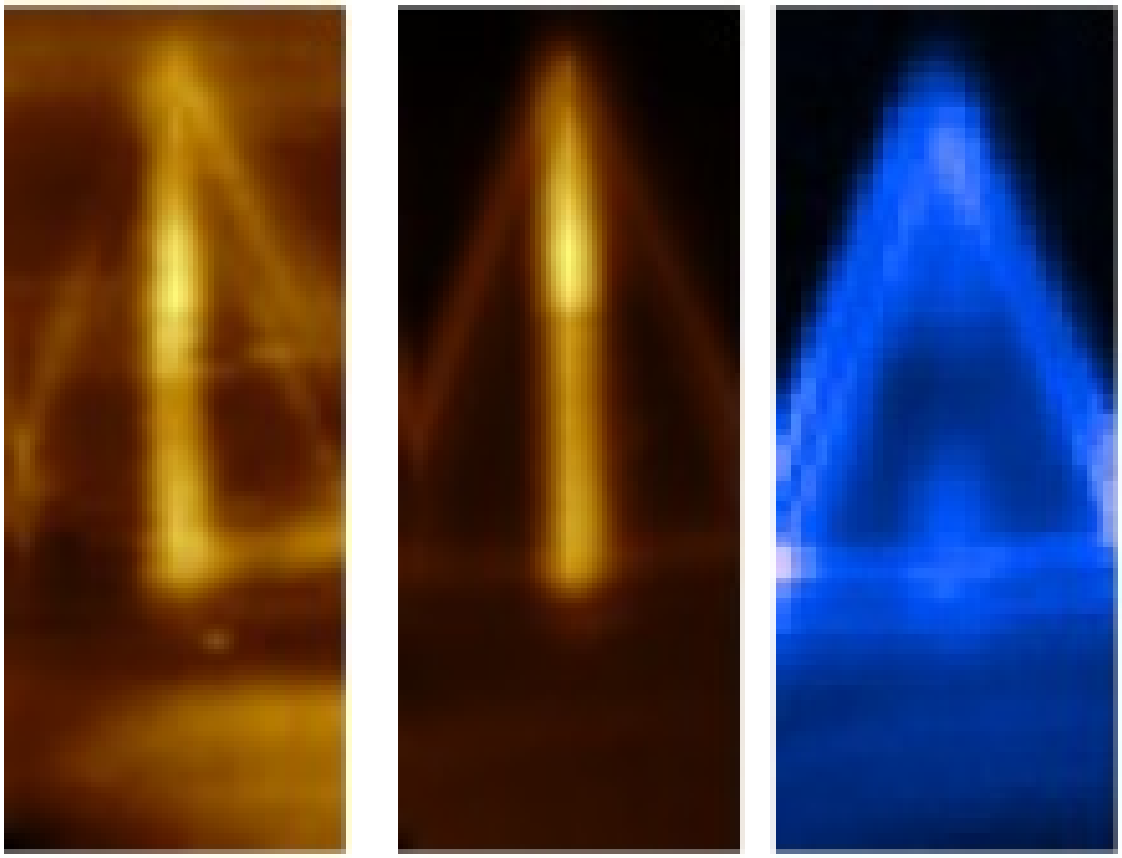

FIGURE 5.6: Left image shows the lateral force signal and middle is the normal force signal, indicating we are in the correct position. The laser is turned on and is visible on this region. The image on the right shows the results of a Raman spectrum map of this area.

To investigate whether the background fluorescence from the gold was masking evidence of plasmonically generated fluorescence, the grating density was changed from 600 gr/mm to 300 gr/mm, reducing the dispersion to give a lower spectral resolution but a larger spectral range, providing a larger "search" area. The tip was also changed, to see if the tip was an issue. Using the same 532 nm laser, approaching the tip to the sample the areas are examined.

The lateral and normal force images do resolve the grating and the tip of the Au structure. There is still no plasmonic signal however except from the metallic flag.This is all to be expected as we cannot couple from the angles set up with the NPL system. A red laser (633 nm) was attempted on probes, however this still made no difference.

Following these results, it was concluded that the NPL tool was inadequate to investigate the operation of the TERS probes. Freedom to move mirrors, change angles and have more time available on a tool were required. The flexibility of doing this was not

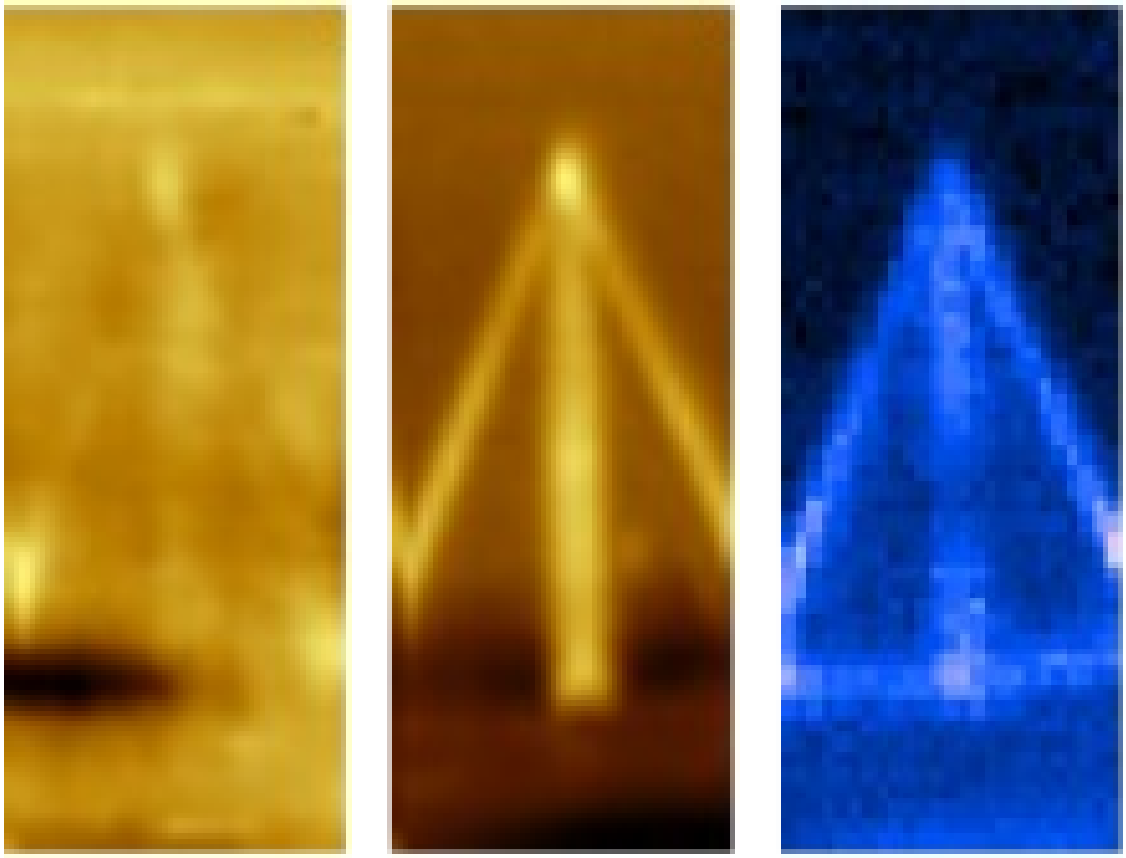

FIGURE 5.7: Left image shows the lateral force signal and middle is the normal force signal. We can see the illumination of the grating area. The image on the right shows the results of a Raman spectrum map of this area.

feasible with the available setup, with modification of the system to accommodate the required incidence angle not permitted. It was therefore decided to abandon this setup as we could not do any more, and attempt to continue the work with a new setup at the University of Glasgow, where more flexibility was offered.

5.2.1 Linear Spectrocopy

After undertaking TERS experiments at the NPL, the analysis indicated no significant fluorescence from a direct illumination from the laser sources apart from areas of metal flags. This raised the question of whether the gold behaved optically as expected and testing of this was required. As plasmon generation relies on the absorption of light into metal (in this case gold), one way to test gold's absorption is through linear spectroscopy. These tests would determine if the gold were absorbing similarly to samples used in

published papers, with an outlook of absorbing close to 633 nm which is needed with the laser used for TERS.

5.2.1.1 Polarisation Microscope

The microscope used for these experiments had an unpolarised broadband light source (50 W Tungsten halogen lamp) which was passed through a collimating lens. The propogating light was then vertically polarised with a Glan-Thompson calcite polariser, where it was then diverted by a 50:50 beamsplitter. The beam then passed through a 10x objective lens with a 0.3NA, where a reasonable FOV can be achieved. A 50x objective lens was available, however as the tool is widely used, then 10x remains in place with a seperate microscope used for the higher magnification experiments. The reflected light then passed back through the beamsplitter, another polariser and then another 50:50 beamplsitter. One path was sent to a camera, whereby images of the sample surface can be seen and microscope alignment can be checked. The focus can be manipulated with the z stage micrometer, and tilt and rotation done with seperate micrometers to ensure the reflected beam is normal to the sample surface. The other path was then sent to a spectrometer. An image of the setup is shown in Figure 5.8.

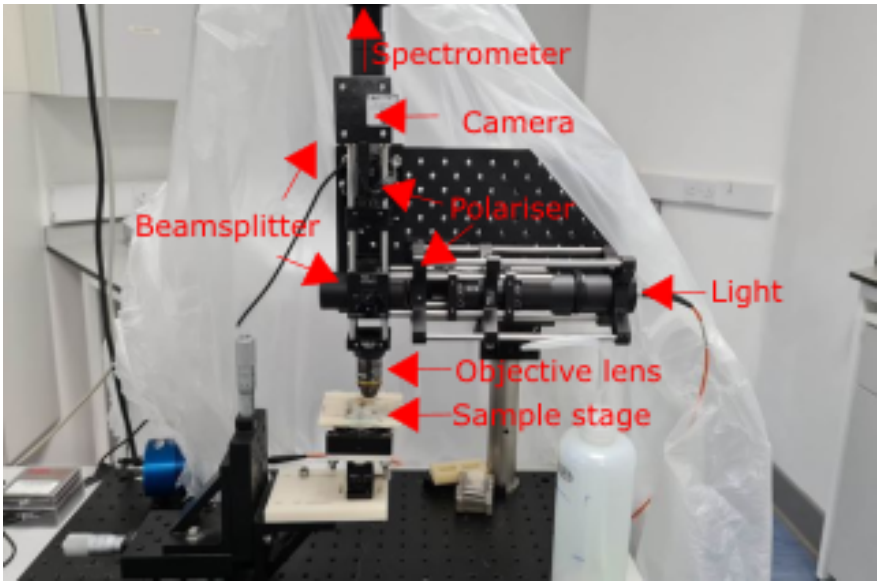

FIGURE 5.8: An annotated diagram showing the setup of the polarisation microscope.

5.2.1.2 Reflectance Spectroscopy

Using the polarisation microscope setup, reflectance spectroscopy can be performed. As the antennae are pointed in one direction, keeping the polarisation plane in line with the tip apex. An image showing the polarisation plane in relation to the antenna is shown in Figure 5.9.

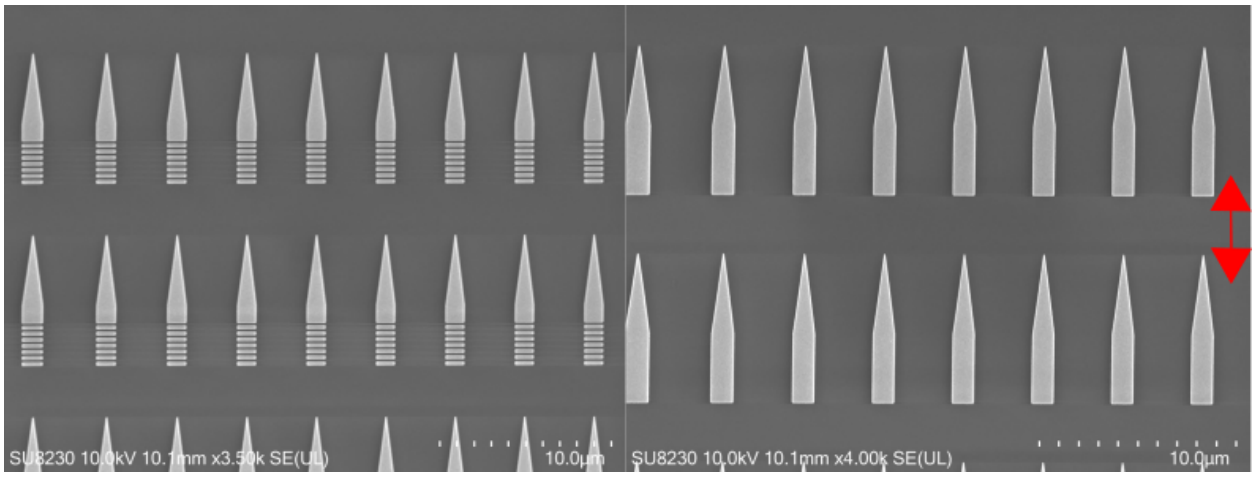

FIGURE 5.9: SEM image of antenna design with (A) and without (B) the grating coupler. The direction of polarisation where the measurements are conducted is shown in red.

The measurements are taken off the array of the antennae discussed in section 4.3, with the structures without the waveguide, gold square and the backing substrate used as background measurements. The relative reflectance of the sample can be understood with the following relation:

$$RelativeReflectance = \frac{I_{antennae}}{I_{Background}} \tag{5.1}$$

As the feature size is on the microscale and much larger than the wavelength of visible light, this means the interaction between the conduction electrons of the gold and incident light no longer support the resonant condition needed for LSPR. Plasmon generation would have to be supported via a propagating mode, such as using the grating and matching the momentum and energy of the incoming light wave vector. The nature of the machines setup during experimentation meant that we couldn't change the incident angle, meaning it is will not match the momentum and energy required to induce a propagating plasmonic response.

The first measurement of this experiment was to check the polarisation, taking a measurement with the polarisation following the antenna apex and the other 90deg relative to it. A shift in the peak intensity wavelength should be visible with the path of polarisation. Keeping the polarisation in-plane, testing was performed on the planar probe samples. A flat gold square was patterned as a reference; however, a gold square is highly reflective and not close to the true representative dimensions of the probe's antenna. Using the dielectric as a reference was not a close representation either, however it provided a reference on what is being absorbed by the metal vs. what was being absorbed by the silicon/silicon nitride. The planar SPR waveguides (without the grating) would provide a good reference for the grating devices, being of similar dimensions and made of the same material with surrounding dielectric, and were used as such.

The measurements were taken of the structures with a period of 250, 350, 450 and 550 nm. The first row had a cone opening angle of 15°, with a second-row angle of 25 and third 35°.

5.3 Linear Spectroscopy Results

Each geometric pattern was imaged 2 times and comparisons of the data set was performed to see if there were any significant errors. The first geometric profiles to be examined consisted of a NiCr adhesive layer with 70 nm of gold on top of a silicon nitride topped silicon substrate. These are to mimic the foundation of the probe's tips. These are then compared against a similar period structure but without a grating to form a comparison. The results of this is in Table 5.1.

Examining the data we can see a trend of the resonance frequency falling at around 600 nm, which is close to the optical excitation of the red laser. This is to be expected as the reflected resonance of gold is around this point [290], this is due to the metal's electrons oscillating over a larger area and hence lower frequency. Due to the size of the features and the fact the excitation laser is normal to the surface, any local plasmons or SPP's will not be excited, and this is seen from the tabulated data. Some of the raw data plots of the structures relative to the patterns without a grating are shown in Figure 5.10

This plot also shows that there is a lack of plasmonic activity as the dip in reflectance is over a broad wavelength with a low intensity reduction, where as a surface plasmon response has a sharp dip [291]. Only 7 - 12 % of the light is being absorbed by the gold features with the grating relative to that of the solid body. This will also include instances

Opening angle (deg)	Period (nm)	Average Peak Wavelength (nm)	Average Relative Reflectance
15	350	609.01	0.90
15	450	634.31	0.87
15	550	578.66	0.90
25	250	586.89	0.86
25	350	598.30	0.86
25	450	600.06	0.94
25	550	641.68	0.96
35	250	640.91	0.90
35	350	598.40	0.86
35	450	642.18	0.85
35	550	591.40	0.90

TABLE 5.1: Table of the varied coupling angle device's reflectance, relative to the similar devices without a grating

Opening angle (deg)	Period (nm)	Average Peak Wavelength (nm)	Average Relative Reflectance
15	350	617.90	1.17
15	450	595.99	1.20
15	550	618.66	1.21
25	250	602.27	1.24
25	350	602.49	1.26
25	450	598.70	1.32
25	550	612.69	1.34
35	250	616.30	1.33
35	350	617.90	1.31
35	450	612.01	1.39
35	550	619.38	1.42

TABLE 5.2: Table of the varied coupling angle device's reflectance, relative to the surrounding silicon nitride capped silicon substrate.

where the incident light will be scattered off the grating and not collected from the spectrometer. The 450 nm period with the 35 degree opening differs (has a positive peak) due to the relative pattern not being on the sample due to spacing issues. This means it was taken relative to the next available feature, for 450 nm this was the 350 nm period's relative pattern. The other positive dipped plot (550 nm 35 degree opening) was found to be this way as well, however this measurement was retaken to see if the dip remained the same, which it did not. The experiment was repeated again which agreed with the other retaken measurement, indicating it was a measurement error. The main indication is that the wavelength does not properly scale with the period of the grating, however we can

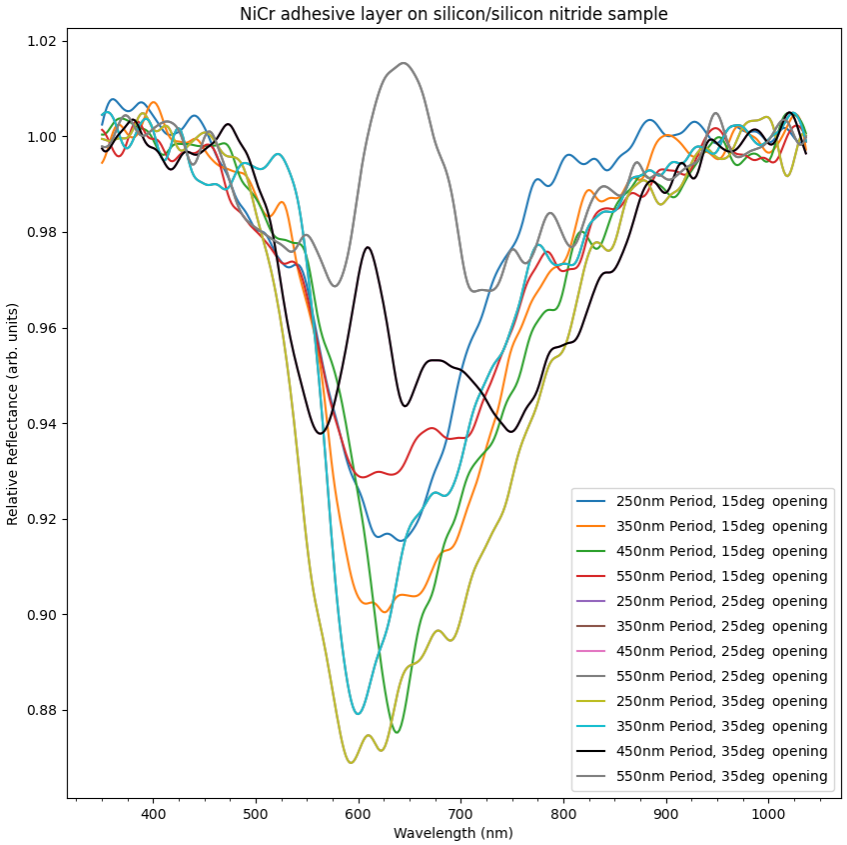

FIGURE 5.10: Plot of the relative reflectance spectra of various period and cone angled patterns relative to the patterns without a grating

see a larger wavelength for a wider cone angle due to more gold being there.

Taking this data forward, we can conclude that optically the gold is in fact absorbing within the bandwidth of the laser used at the University of Glasgow. In continuing this research, it would require an angled laser to couple and then generate and propagate a SPP, or some roughness of the tip to generate a LSPR.

5.4 TERS Setup (University of Glasgow)

5.4.1 Optical Alignment

As the equipment at the University of Glasgow is commercial, and not made in house, alignment of the system is less complex than the NPL system. To begin experimenting with probes, the optics need to be aligned to visualise what is happening within the system. As with any TERS setup, the first part of the procedure was to set up the AFM, ensuring that the probes could withstand contact and not fracture with the misaligned etched slit in the cantilever. The probes were clamped with a retention clip on a sapphire pedestal within the AFM head, ensuring the tip is over the edge and facing the user. An image of the holder is shown in Figure 5.11. The AFM head must be positioned 2mm or more from the sample to ensure that the tip does not crash into the sample whilst loading.

The laser is then positioned onto the cantilever, where a camera shows a live feed of the optical path to the cantilever. The microscope used a conventional quadrant photodiode force detection system and was operated in tapping mode with a maximum scan size of 100x100 μm^2.

The sample surface is imaged with an optical viewing system with a rough resolution of 3 μm and 4.5 mm field of view. With the device array total size of 300 μm this should be enough to resolve the area of the device placement, but not any individual nanostructures (200 nm or below). It utilises an optical microscope with a CCD camera attached to the output, with a manual coarse and fine focus. A lamp feeds light through a fibre optic cable to the base of the microscope, where it in turn illuminates the area beneath the objective lens. As the lamp is broadband light, the lamp must be turned off during the Raman scans otherwise the spectrometer CCD detector becomes over-saturated and prevents reliable Raman intensity measurements over the broadband wavelength. The microscope beam path is focused onto the sample surface like a periscope, with the beam path positioned directly onto an auxiliary mirror. This mirror redirects the path towards the viewing mirror attached to the AFM head which in turn show the top side of the probe, with the sample area beneath and surrounding it. As it is a periscope setup, this made the coarse positional viewing of the sample difficult, as if any of the mirrors were rotated slightly out of place, you would potentially see none of the sample. This means that a more noticeable region, like a sample edge or large metallic feature, has to be placed directly below the focal path of the objective lens and try to achieve a coarse focus whilst adjusting the mirror

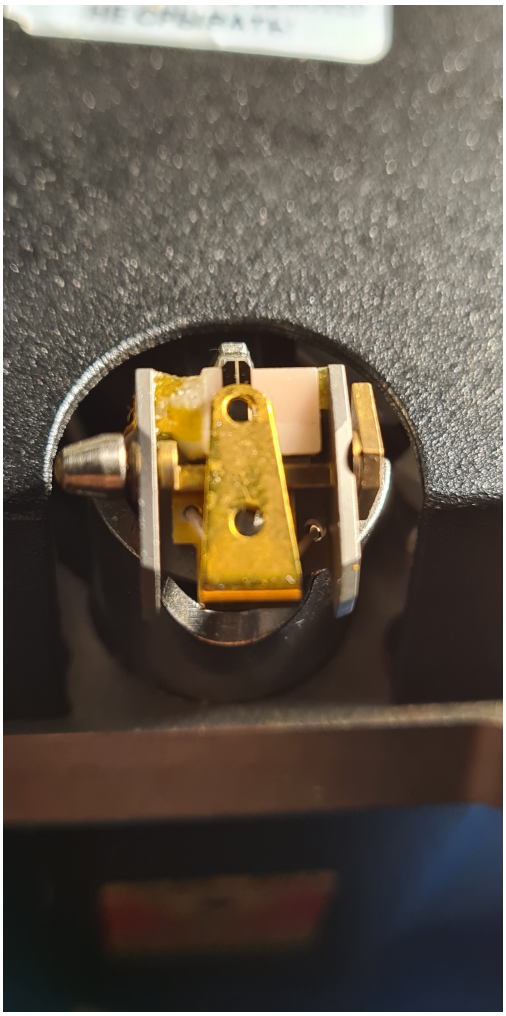

FIGURE 5.11: Image of an AFM probe mounted onto the AFM head. The probe tip is facing the reader (out of the page).

position to generate a focused image of the sample surface. A schematic diagram of this setup is shown in Figure 5.12.

5.4.2 Spectrometer alignment

Raman spectra were recorded using a NT-MDT NTEGRA Raman microscope [292] with a 633 nm laser excitation (35mW power) with varying accumulation times. The laser is a HeNe, with a Gaussian TEM00 mode. The laser was coupled into a fibre; however, the stray light is filtered within the laser casing. The laser signal is further filtered within the spectrometer system as the beam splitters and reflectors are dichroic. Excitation and collection of Raman scattered light was done using a x20 objective with an estimated spot size of 790 nm, where it is magnified to appear on a 100 μm aperture for spatial filtering.

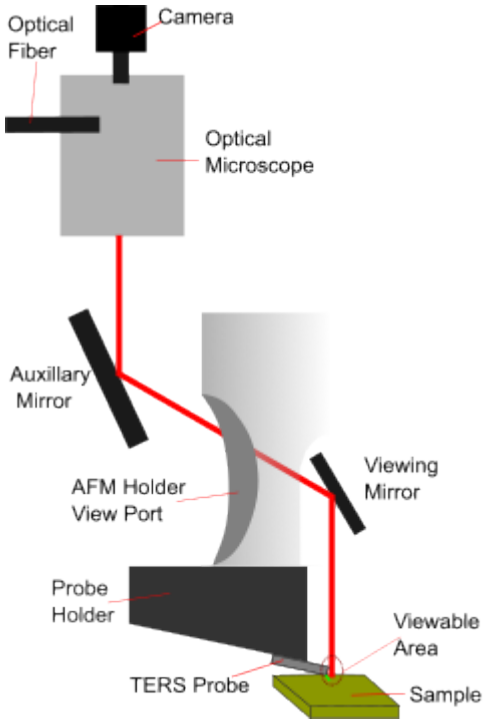

FIGURE 5.12: Schematic diagram of the optical viewing system of the AFM setup.

During the Raman measurements, maximum transmittance of the ND filter was applied as a reduction in the light means a lower Raman intensity. A reduction in transmittance was applied whilst aligning the laser so alignment of the laser to the features was easier. The pinhole diameter was set as 100 μm, this filters out the analysis volume so that the Raman scatter is only obtained from the focal plane. A reduction in the pinhole provides better axial resolution as it blocks out the out of focus scatter, however the Raman scatter intensity at the detector is too low and would take significantly longer to achieve an accurate spectrum. The diffraction grating was set as 600 lines/mm, with a larger density causing a larger spread over the CCD and hence increase spectral resolution. As the expected peaks for the materials were expected over a large spectral range, a larger density is not efficient. The selected density provides a trade-off in the spectral resolution, having it at a moderate level, whilst maintaining a moderate spectral range (1855cm^{-1} for 600 lines/mm grating). To check the polarization of the laser, the polariser input on the spectrometer was changed to allow for the differing polarisers installed in the system to change the spectra of a 400 nm thick silicon nitride coated silicon substrate. After checking polariser 1-6, there was no change to the spectrum and the light was therefore found to be unpolarised. This means only the TM component will couple and excite SPR, reducing the efficiency and enhancement of the probes as the TE light cannot match the

phase matching condition for excitation of SPR at the metal-dielectric interface [293]. The resolution can be calculated by examining a sharp silicon peak at 520cm^{-1}, taken with this spectrometer in Figure 5.24.

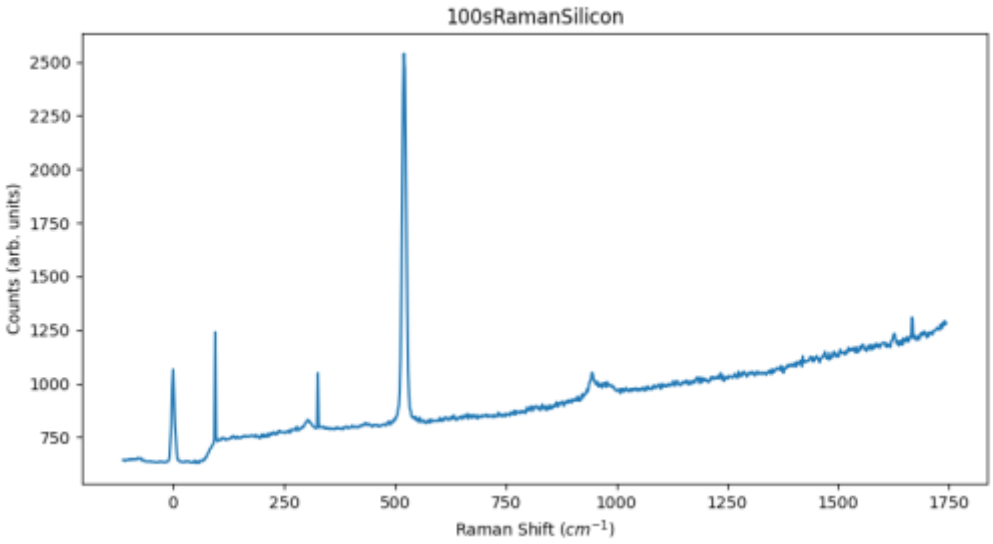

FIGURE 5.13: Raman plot of a silicon sample with a large peak at 520 cm^{-1} due to centring the laser paths. This plot cannot be post-processed to remove any cosmic rays.

The Si peak has a minimum intensity of 837, with a maximum of 2539 cnts. Subtracting the values we get a value for the total height of the peak (making 837 the origin) = 1702, this is the maximum. Taking half the value we get a value of the FWHM is 851. Adding 851 onto the spectrum minimum, a value of 1688 cnts is that spectrums FWHM value. The wavenumber value either side of this intensity is interpolated = 526 – 515, giving a spectral resolution of roughly 11cm^{-1}.

The spectrometer setup makes use of a photomultiplier tube (PMT). The PMT is very fast and sensitive, but it is a single channel detector used to measure the reflected light and produce a scatter diagram. This makes no spectroscopy measurements. As a photon strikes the PMT's photocathode, it dislodges an electron. The electric field within the PMT causes the electron to accelerate towards a dynode, where the collision releases several new electrons which are accelerated into another dynode [294]. This process continues through the dynode chain until it finally reaches the anode. The initial photocathode current I_c at the end stage has been amplified to $I_c E^n$ [295], where E is the secondary electron emission coefficient and n is the number of dynodes. The quantum efficiency of the photocathode typically does not exceed 40%. The typical electron gain of the electron multiplier is 10^6, where the current can be measured directly. The PMT does have a lower

quantum efficiency compared to that of a CCD detector, but if a photon does generate an electron, it will be detected. As the optical setup is scanning, the PMT is very useful in determining the positioning of the laser in an efficient manner.

A linear process called photon counting can be used to generate a better signal/noise ratio (SNR) of the current signal and discriminate what is a true representation of a Raman signal or noise. The PMT used will generate one current pulse per electron. If these pulses come faster than the response time it is not possible to detect single photons. The SNR of this process is also shot noise limited where the current pulse rate is proportional with intensity.

In this case the PMT is used to collect a fast image of the Rayleigh scattering, where a larger signal is present for an in-focus laser on a metallic surface. The actual Raman spectrum was recorded whilst using an Andor Charge Coupled Device (CCD) camera, cooled to -60°C. Then the Raman Scattered light is dispersed out of the grating, it is put onto the long axis of the CCD. Each element of the CCD will detect light in differing cm^{-1} points, with the first at the low edge of the spectrum and the last the highest [294]. To improve the SNR, collection of the spectrum can be restricted to a region where there is a large spectral signal. An annotated photograph of the spectrometer setup used for the Raman measurements at Glasgow is shown in Figure 5.14.

Figure 5.14 gives an oversight of the laser path through the spectrometer, with the laser beam starting at an input unit, going through 2 mirrors (not shown in the image) and coming out the top. The beam path starts by going through the adjustable neutral density filter and then to the beam expander, where it is automated and gives control of the beam diameter and collimation. The beam path then passes through 2 mirrors before being directed onto the edge filter. The filter then reflects the laser and passes it onto the measurement head lens and then onto the sample. The reflection of the laser from the sample is recorded with 2 mechanisms. The first way is through the laser optical setup, where a confocal image of the sample from the laser is recorded. This occurs by the reflected light coming back the way, reflected from the sample and through the measuring head, reflected from the edge filter and into a mirror. Only 3% of the total light passes through the next mirror and into the reflection unit, where a lens focuses the beam through the pinhole and into the PMT to produce a scatter image. The next mechanism is the spectral optics, where a confocal image of the sample is taken by the light of secondary radiation. Raman light is emitted from the sample and then collimated by the measuring head, before passing through a glass prism and then bandpass filter. The light is then focused and directed onto the adjustable pinhole at the monochromator entrance,

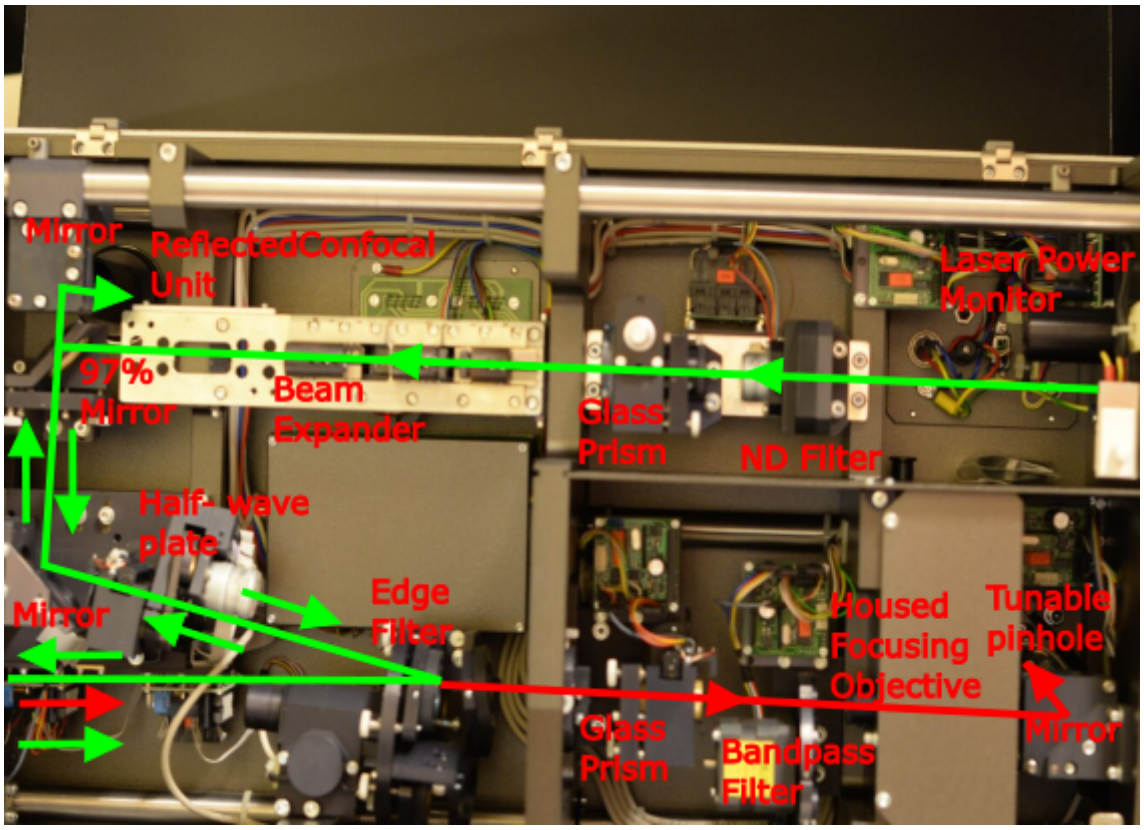

FIGURE 5.14: An annotated photograph of the spectrometer setup at the University of Glasgow.

where diffraction gratings separate the light into spectral components, which is then read by the CCD camera.

5.4.3 Raman Measurement Setup

From the previous NPL measurements and initial experiments on the new setup, obtaining an enhanced Raman spectra from a plasmonic mode was put to one side. Determining if the setup produced a reliable Raman signal of a known quantity was the first step. The first sample to be interrogated was a 380 μm thick silicon piece coated with 400 nm of silicon nitride. As the sample is not transparent, the focus of the laser would be on the bottom side of the sample (side closest to the objective). The sample z-stage was adjusted, through manual (coarse focus) and motorized (fine focus) control, until the PMT signal was at a maximum, indicating the maximum number of photons are getting reflected into the detector.

As the silicon base is crystalline, a high intensity peak is expected at a Raman shift of 520cm^{-1}. This is due to silicon only having one first order Raman active phonon, with the peak at the long wavelength transverse optical phonon mode. This mode is the result of the lattice vibrations within the silicon crystal displacing perpendicularly to the lights path [296].

The first few measurements were taken at an accumulation time of 1s, where the signal to noise ratio is low, which was just enough to determine if the objective was centred in the laser path. The x and y position of the objective is controlled via motors and was adjusted from a position which was completely out of the laser path into the laser path, then back out of the laser path in the other direction. The x and y positional values were noted as a function of intensity until such a time the 520cm^{-1} silicon peak was at its maximum, indicating the laser path is centred.

The low stress silicon nitride layer has a peak at 520cm^{-1}, which is the first-order transverse optical phonon mode of the Si-Si bonds within the crystalline silicon lattice [297]. The material vibrational mode has absorbed energy and moved to a higher energy state, with the low energy and longer wavelengths indicating Stokes scattering. The intense 520 cm^{-1} peak from this vibrational mode makes the silicon containing substrate a great calibration for the Raman measurements.

5.5 Raman on Gold dots

As the statistically and correlated aligned sample was still with the NPL and made on a silicon substrate, new dot samples were fabricated. These fabricated gold dots are understood to be an electric dipole. When the frequency of the propagating light matches that of the eigen vibrations of the dipole, the resonance can create an increase in the local near field. This is known as a localised surface plasmon resonance (LSPR) [225].

When a plasmon is excited by light, the electrons within the metal start to oscillate with an increase in potential energy of the dipole's electric field. The absorption spectra peaks become maximised when the energy of the oscillating electrons become large. The positioning of the peaks (wavelength) are determined by the geometry of the metal, the type of metal and its properties and dielectric constant of the surrounding substrate [225]. A diagram of this is shown in Figure 5.15.

As the size gradually decreases, the intensity of the LSPR response and half-width change increases, the frequency remains in a similar position [298]. It is known that the

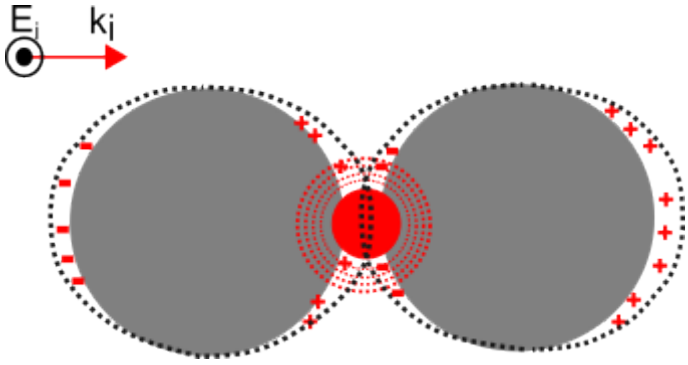

FIGURE 5.15: Schematic diagram showing a localised dipole surface plasmon.

electric field is weakly enhanced at the centre of the particles with an enormous increase towards the edges. This is due to edge and skin effects from electron conduction, brought on by the optical frequency [299].

Taking inspiration from a paper by Rahaman et al., 50 nm thick Au nanocylinders were created [299] with a 1 nm NiCr layer to induce LSPR. The starting substrate was a 160 μm thick borosilicate glass slide with an average refractive index of 1.51 at 633 nm [300], which was then coated with bi-layer PMMA and exposed with a 2nA electron beam. The VRU of this exposure was 4 with a 1200 $\mu C/cm^2$ clearing dose. The dots had varying diameters of 200, 100, 50 and 25 nm. The gaps between the dots were prescribed to range, but the substrate ended up having varying diameter dots with a consistent 250 nm spacing, with the consistency of the period being the most important thing. A SEM image of the 200 nm dots with the consistent spacing shown in Figure 5.16. The larger spacing meant faster write times due to a reduction in the infill in the sample area, so processing was quicker, and there was no interference from any proximity of the electron beam, which would hinder the clean geometry of the devices. This also left a large enough gap that the microfabricated tips could resolve with AFM as those have a radius of less than 100 nm. These are arrayed out in 300x300 μm blocks, which is easy enough for the AFM camera to visualise and then scan over when the maximum scan range is 100 μm.

To test testing if the dots were patterned correctly, the sample had 20 nm Al evaporated onto them to act as a charge conduction layer before being examined with a SEM. Another sample with the same exposure did not have Al coated so there was no residue remaining, allowing for any further processing.

As can be seen in the images (Figures 5.16 - 5.17) the dot features have turned out with the expected feature size, with the edge having a $\approx 20^\circ$ due to the mask hole shrinking as gold builds up on the resist. In the 50 nm dots image (Figure 5.17), edge effect contrast

can be seen due to the electrons being emitted more at the edges of the dots compared to that of a flat region, where the incident electrons scatter into the sample. This provides an additional contribution to the secondary electron signal making it brighter than the flat region. The proximity effect was prominent whilst writing the 25 nm diameter dots (Figure 5.18) features of a gap less than 250 nm and therefore saw features merging, these would not be useful because the measurements trying to be taken assumed a uniform pattern of identical dots. In terms of TERS this means it wouldn't matter which site we were at, the measurements taken would be identical and the dependence of the TERS enhancement vs dot diameter could be monitored, without further near-field interactions such as gap plasmons taking effect. Regardless of the dot diameter, a TERS response could still be seen and used to validate the probes. Having a set period also plays well for SERS, as the spot size is larger than an individual dot, the influence of the SERS response again can be tuned with the period and not due to defects on the sample. This means that when comparing a TERS vs SERS enhancement, the resulting spectral intensity is entirely dependent on the enhancement method and not sample structural dependence. A proximity effect correction could not currently be placed on the e-beam exposure as it had not been set up to run on the tool yet, with the features fabricated still good enough for testing.

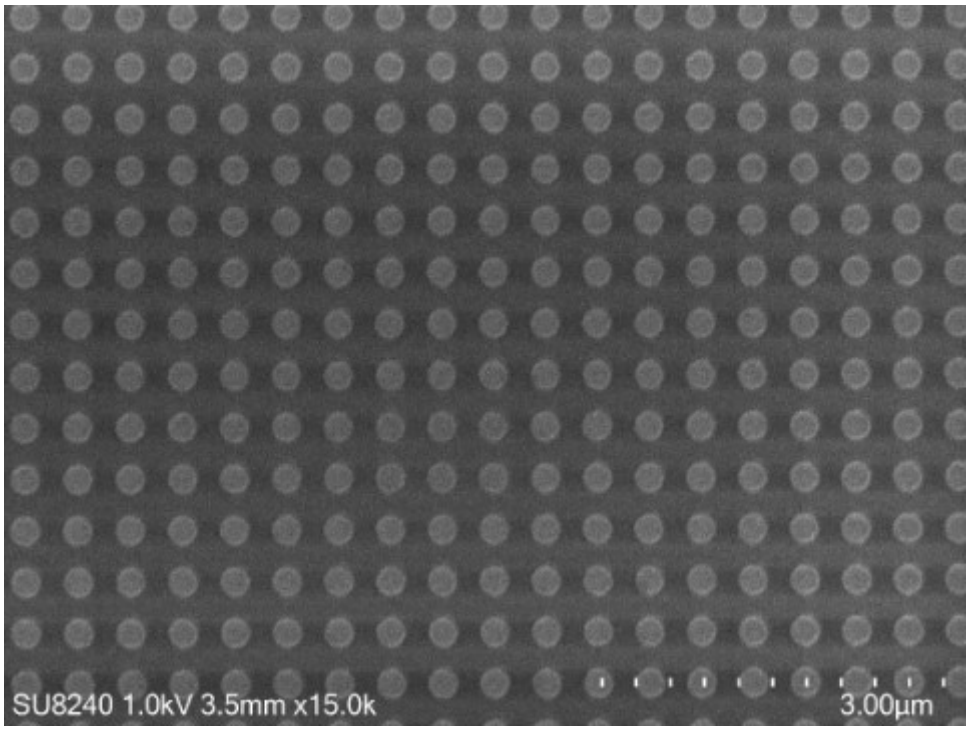

FIGURE 5.16: SEM image of the 200 nm gold dots with a 250 nm gap between them.

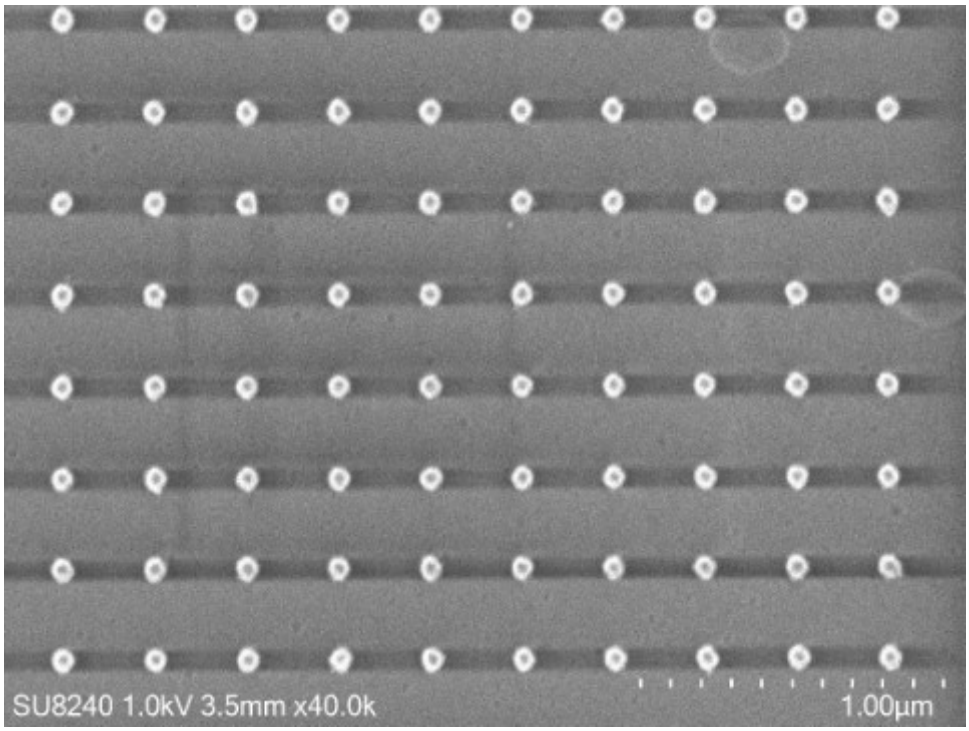

FIGURE 5.17: SEM image of the 50 nm gold dots with a 250 nm gap between them.

As the gold dots themselves are not Raman active, a material is needed to coat the gold dots to provide a measurable Raman response to the field enhancement. To do this, the sample was immersed in a 3 mM methanol solution of 95% biphenyl-4,4'-dithiol (BPDT) (Sigma-Aldrich) for 24 hours to form a self assembled monolayer. This BPDT binds onto the dots (nano-cylinders), and acts as a Raman reporter of the near field intensities. Raman spectra were recorded using a NT-MDT NTEGRA Raman microscope with a 633 nm laser excitation with varying accumulation times.

The Raman shift values corresponding to the vibration of the BPDT are taken from M. Kartau's thesis [195]. Where the BPDT spectroscopic data retrieved from M. Kartau's thesis was taken on the same tool, with the same bottle of BPDT and same excitation source. The corresponding values and assignments are shown in Table 5.3.

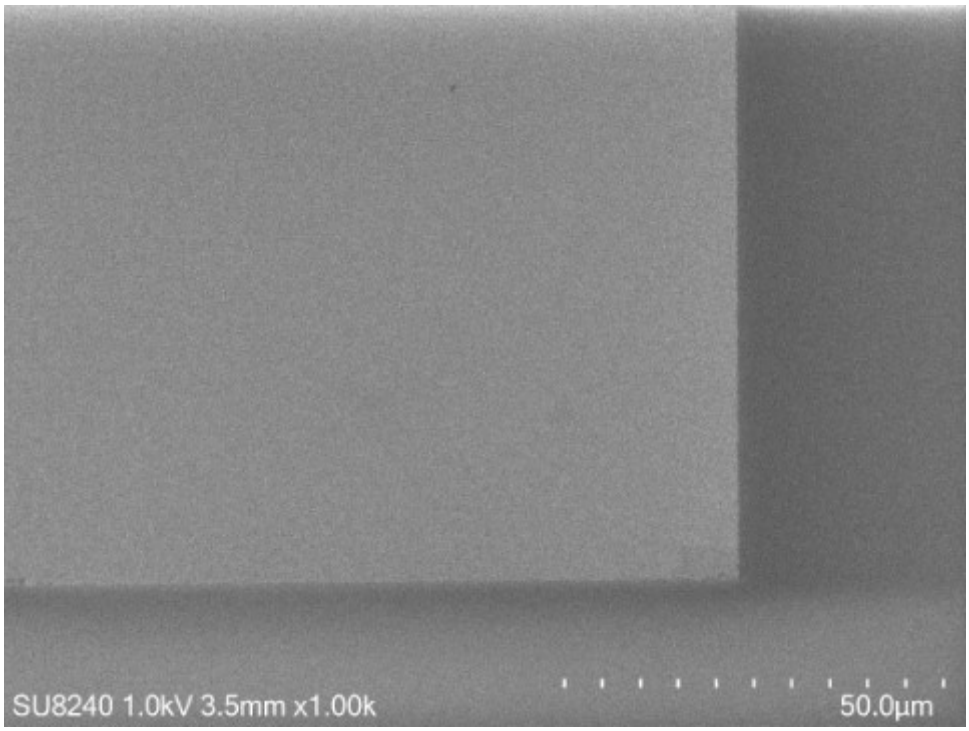

FIGURE 5.18: SEM image of the 25 nm diameter dot area. The image shows that as there is no proximity correction, the dots have merged into one, forcing an area of individual dots to turn into a large rectange.

Peak (cm^{-1})	**Assignment**
411	C-S v_{asym}
542	C-S v_{sym}
703	Out-of-plane skeletal
774	Ring deformation
830	C-H Out-of-plane
1015	Ring Deformation
1084	C_{ring}-S in-plane
1200	12 C–H in-plane
1285	Inter-ring C-C stretching
1474	C-C stretching
1589	C-C stretching

TABLE 5.3: SERS peak positions and relative assignments. Data taken from M. Kartau's thesis [195].

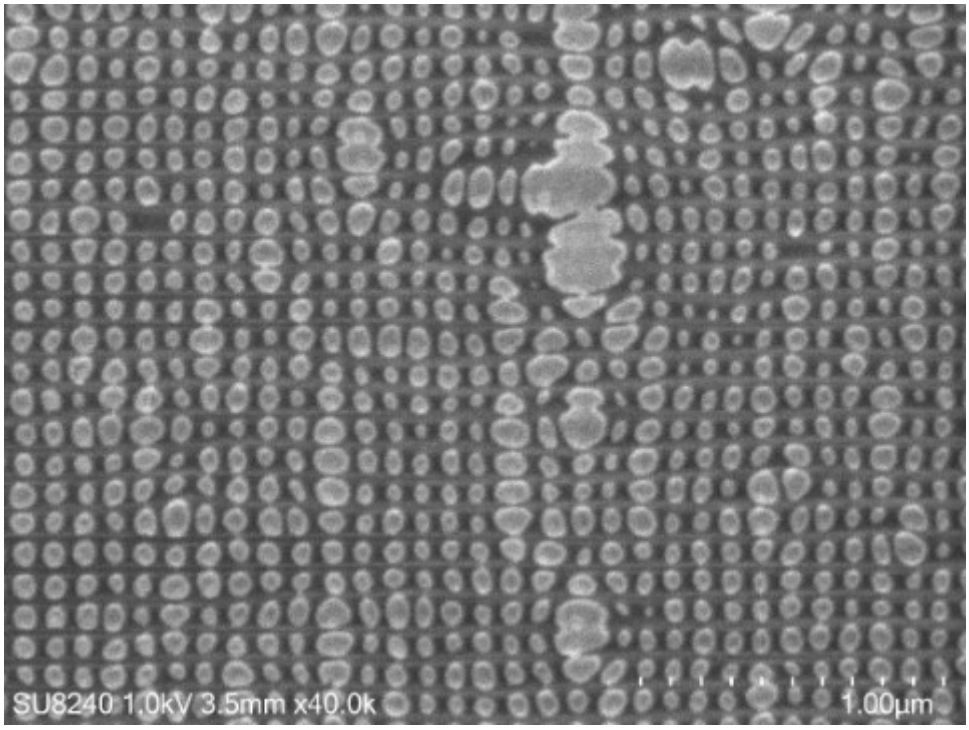

FIGURE 5.19: SEM image of a failed 50 nm diameter dot area. Proximity correction was also not applied in this area resulting in an overexposure of features where they have begun to merge and increase from the prescribed diameter.

5.6 Raman Results

5.6.1 Spectroscopic Processing

All processing of the raw spectra was done with a Python package named RamanSPy [301].

As the Raman spectrometer used has a CCD detector, spikes caused by cosmic rays can appear on the spectra. Upon analysis of the data, these spikes can hinder the detection of smaller Raman modes and skew the plotted axes due to their large, positive, narrow bandwidth peaks. An example spectrum with cosmic rays and no post processing removal is shown in Figure 5.20.

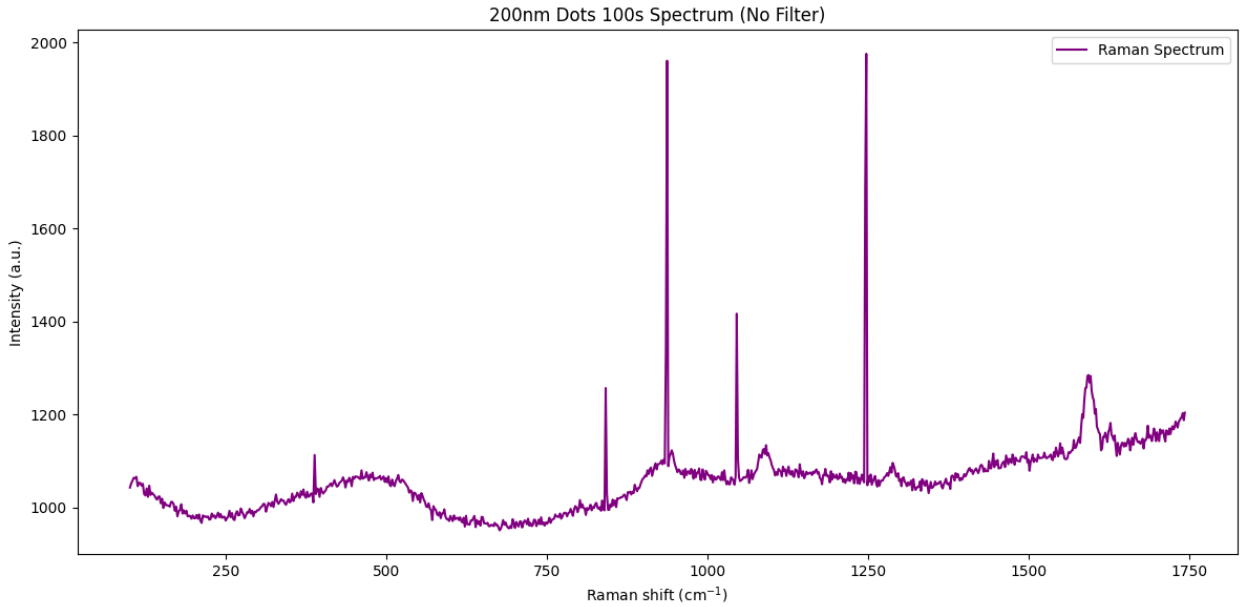

FIGURE 5.20: Raman plot of 200 nm diameter dots coated with BPDT. This is a Raman plot without the removal of any cosmic Rays.

A cosmic ray removal filter was selected to run within the package and utilises a Whitaker Hayes algorithm to carry out modified z-score filtering [302]. It utilises the use of z-scores, which is a determination of how far the next iterations value is from the average of median absolute deviation. The code extrapolates the spectral information from a .txt file, calculates the median and median absolute deviation Raman intensity, and uses the difference between consecutive, equally spaced, spectrum points to calculate a z-score, in this case a kernel size of 3. A threshold is then set in place to indicate whether a value is within range or is a cosmic ray, this value was set as default (8). For the threshold to detect the cosmic rays, an absolute z-score value is calculated. For the elimination of

the cosmic rays, the intensity values are interpolated at each detected wavenumber by calculating the mean of the surrounding values. The cosmic rays are then removed and smoothed off by applying a moving average filter. An example of the cosmic ray removal applied to the same data in Figure 5.20 is shown within Figure 5.21.

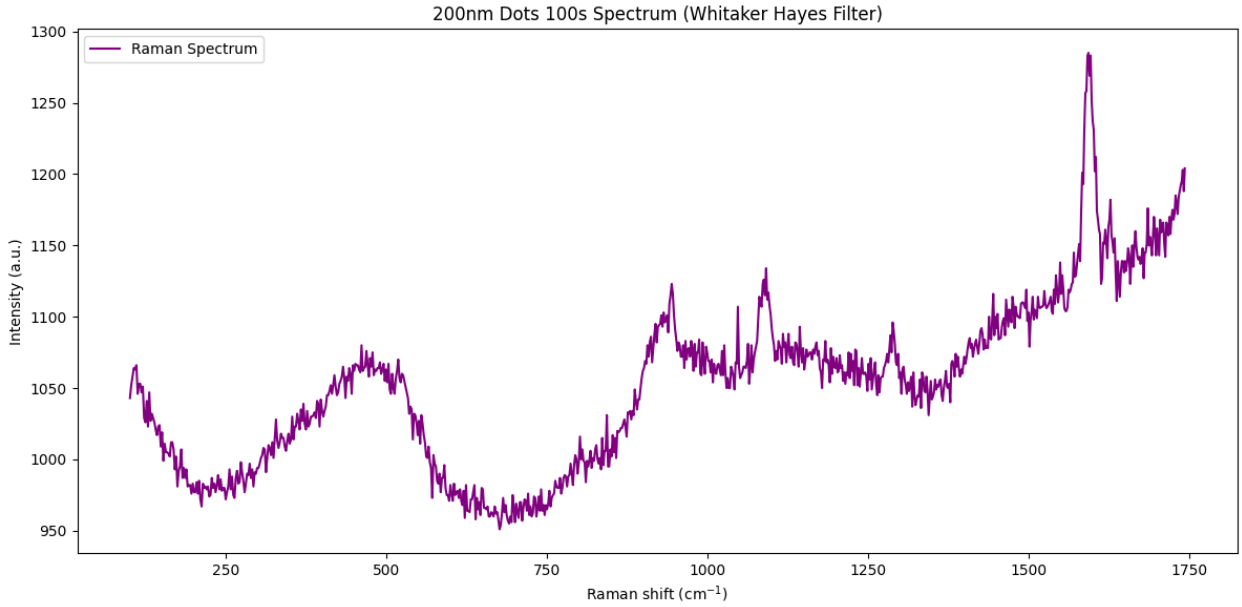

FIGURE 5.21: Raman plot of 200 nm diameter dots coated with BPDT with the cosmic ray filter applied.

Each SERS and TERS spectra are also baseline corrected using an adaptive smoothness penalised least squares (asPLS) method [303]. This method adaptively determines the smoothness of the baseline, taking the difference between the original signal and the fitted baseline signal, using an iterative process rather than applying a fixed global smoothing parameter. The Rayleigh scatter was also removed from the spectra as this doesn't contain any information on the Raman of the substrate. It is important to note, all the parameters were kept the same within the processing of all the spectra (all processed the same way, with the same parameters). Using the same data in Figure 5.20, the outcome of the basline correction and cosmic ray removal can be seen in Figure 5.22.

Each acquisition for the SERS and TERS spectra was then further intensity normalised, before the processing of the data, to compensate for measurement time. This ensures that the spectral intensity is proportional to the signal rate rather than the total counts over the acquisition.

A copy of the algorithm used to modify the images is in the appendix (B).

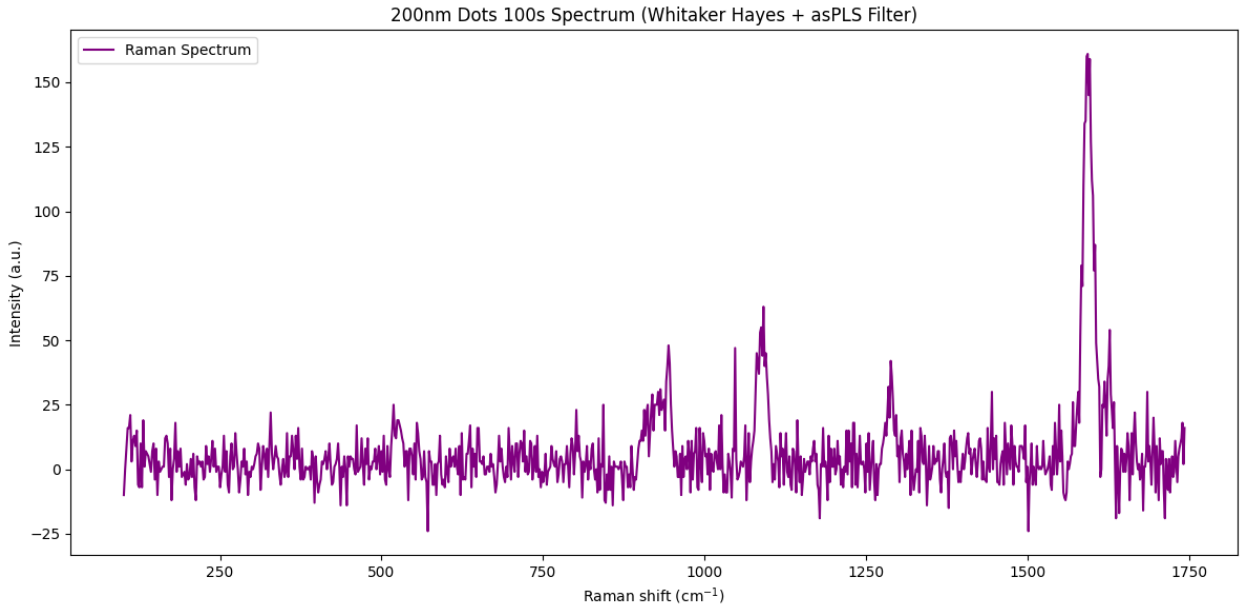

FIGURE 5.22: Raman plot of 200 nm diameter dots coated with BPDT, with the cosmic ray removal filter and asPLS correction applied.

5.7 AFM Results

The first experiment was to perform AFM measurements using the microfabricated TERS probes as this is a necessary part of performing TERS microscopy. Utilising a scan rate of 0.5Hz, a TERS probe was scanned over the 200 nm dot area with the resulting image shown in Figure 5.23.

The results from the AFM scan show that although the cantilevers are mechanically imperfect (see Figure3.10 in chapter 3.3.3), AFM is still possible with these probes. The 200 nm dots are well resolved, but also show the difference in thickness of the evaporated metal surface. The vertical gaps between dots are smaller than the horizontal ones, reflecting the asymmetry of the tip but the image is convincingly free of double tip artefacts. This is highlighted by the fact that the grain structure at the top of each dot is different. Due to the cut out on the probe and general scanning, the probe is prone to twisting which can also distort the resolved features, but also not visible within this image as well.

As we know the TERS probes are capable of topographic resolution, testing to ensure that they can enhance a Raman signal is the next step. To achieve this, the first experiment was to make sure the spectrometer is producing reliable Raman Spectroscopy results of standardised samples. The first excitation was just an un-patterned 380 μm silicon sample with 400 nm of silicon nitride on it.

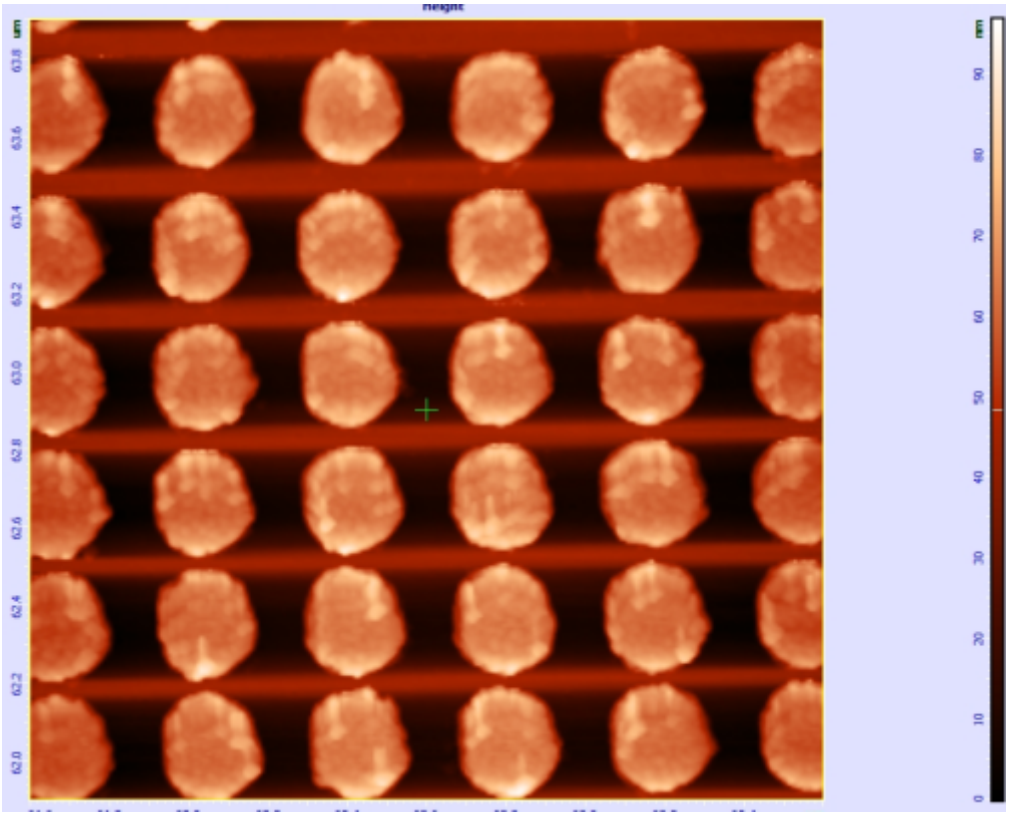

FIGURE 5.23: AFM scan of the 200 nm dot features with a fabricated SPP TERS probe.

This substrate was chosen as it was readily available and silicon nitride is known to be transparent within the visible regime [304], [305]. This means the excitation sources laser will pass through with little absorption due to the materials low extinction coefficient (k$< 10^{-4}$) [306]. The silicon substrate is highly absorbing within the visible regime. Geist et al. measured the extinction coefficient of a 13 μm thick silicon film as 0.01564 and the absorption coefficient as 3105 cm^{-1}, at a wavelength of 633 nm [307]. The penetration depth is calculated as the reciprocal of the absorption coefficient, where the intensity drops to 1/e of what it initially was [308]. This means that the 633 nm laser for use in the Raman experiments would essentially pass through the silicon nitride and will be exponentially attenuated by the silicon, with a characteristic penetration depth of approximately $1/3105\ cm^{-1}$ = 3.22 μm. Although there is little absorption of the silicon nitride, it can still scatter light due to vibrational modes within the material. However, the large peaks of the Si will still be clearly visible for aligning the system and that is the purpose of the substrate.

The integrating time for the scan is 100 s, which has shown to give a good SNR, however, can incur more cosmic rays. Fine adjustments of the laser path were made,

moving the x and y objective using the motors until the Raman peak was at a maximum (2500 units). This system does need re-aligning at the start of the day and after moving to a different site, this is due to small changes in topography of a sample surface at different sites and needing to adjust the spectrometer laser so that it is in focus on the sample surface and giving the largest PMT voltage. A Raman spectrum of the silicon sample with a centred beam is shown in Figure 5.24.

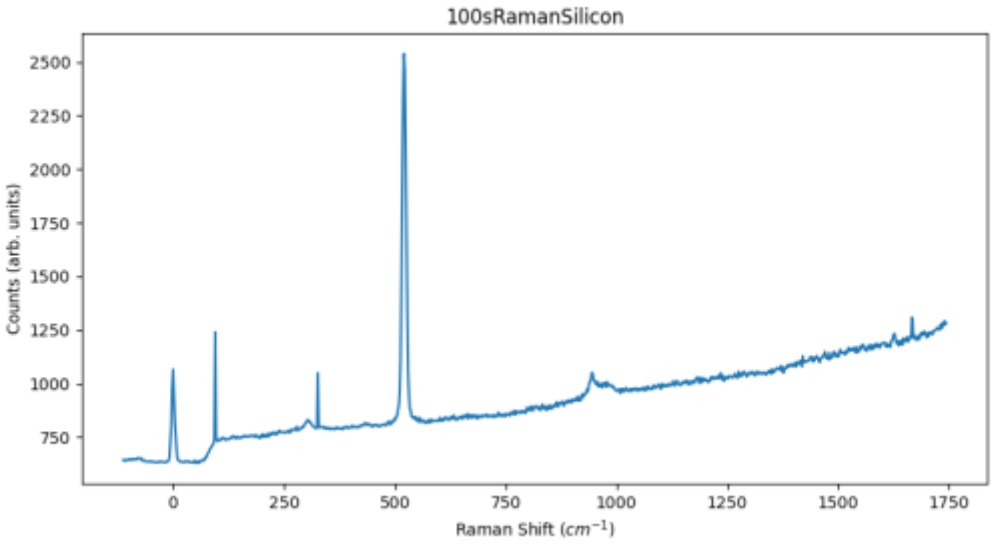

FIGURE 5.24: Raw Raman plot of a silicon sample with a large peak at 520 cm^{-1} due to centring the laser paths.

Figure 5.24 shows a weak peak at 300 cm^{-1}, this is a second-order Raman feature arising from acoustic phonons in silicon [309]. The 520 cm^{-1} is the the first-order transverse optical phonon mode of the Si-Si bonds within the crystalline silicon lattice. The 950 cm^{-1} is indicative of a asymmetric stretching mode [310].

As the light was therefore centred and able to pick up a spectrum, the glass slide with the gold cylinders and BPDT was loaded onto the sample stage. With the AFM head in place, the mirror attached to it allowed the confocal microscope to have a live image of the sample surface, if the illumination intensity was high. The laser spot was monitored, and sample moved until the required region was illuminated. The focus of the laser was then monitored with the PMT signal, a low PMT signal indicated we were not in focus with the top side (where the cylinders are) of the sample. The Z of the sample stage was moved until the PMT signal was at a maximum, with further fine tuning done within the software. A Raman scan (moving the sample) was then performed, taking Raman spectra with an acquisition time of 10 s per site with a step size of 150 nm. If the PMT is in focus,

then the scan would resolve the gold dots. The spectrum of this Raman map is shown in Figure 5.25.

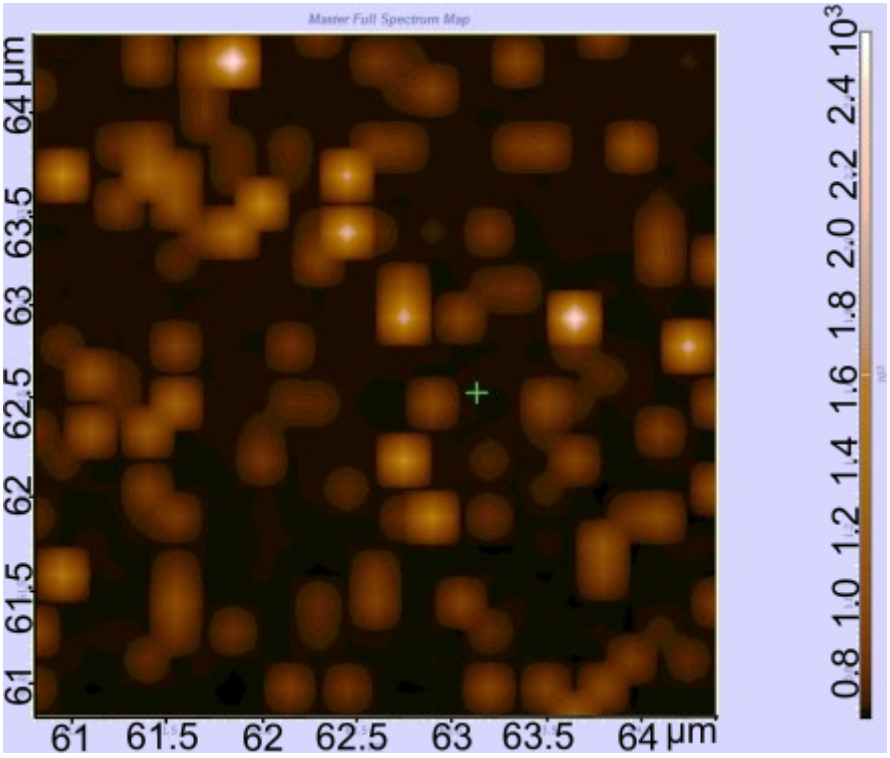

FIGURE 5.25: Master Raman plot of the PMT signal. It indicates small glowing dots.

The Raman software interpolated between measurements to give a high resolved impression, this means that any cosmic rays gave a massive value and obscures the smaller resolved dot values. The image was reprocessed and does show random dots of around 100 nm but on a defined 250 nm grid, which indicates it is registering the dots, but it also has very bright areas of cosmic rays. This means that a 150 nm step size for the PMT scan has under-sampled a 250 nm grid, leading to a random brightness of the original image as it interpolates between measurements. The 10 s integration time during the scan is also very small, which is enough time to also pick up some cosmic rays. A Raman acquisition of the sample dots covered with BPDT was the better option. To further on with SERS, a 100 s integration time single acquisition of the 200 nm dots is shown in Figure 5.26 below:

Examining Figure 5.26 we can see multiple peaks in the spectra pertaining to the BPDT. The prominent peaks shown at 1084, 1285 and 1592 cm^{-1} are indicative of a vibration of the BPDT. The intensity is influenced by the coupling of the molecule's aromatic

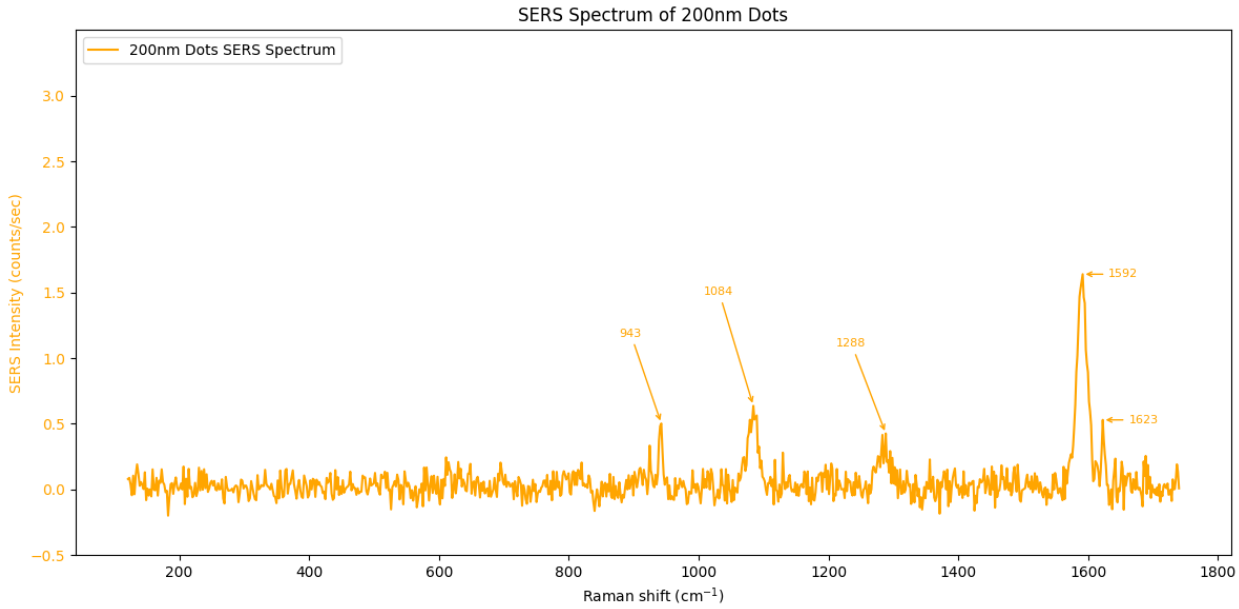

FIGURE 5.26: SERS plot of the 200 nm dots coated with BPDT with 100 s integration time.

-electron system of phenyl rings, coupled with its chemical bond with sulfur to the metal surface [311]. The band at 1084 cm^{-1} is assigned to an in-plane aromatic ring vibration with a significant contribution from the C-S stretching mode. The band at 1285 cm^{-1} is assigned to the C-C bonds connecting the two phenyl rings stretching. The final band at 1592 cm^{-1} corresponds to the aromatic C-C stretching mode within the phenyl rings [311].

The 412 cm^{-1} band is assigned to the C-S ν_{asym} mode, meaning the C-S bonds of the di-thiol molecule stretch and contract in opposition to each other. The C-S (ν_{sym}) stretch is assigned to the 545 cm^{-1} band, where the C-S bonds stretch and contract at the same time and in the same direction [195].

Following this demonstration of SERS the function of the TERS probes was investigated. The first stage of after scanning with the tip was to scan the PMT to look for any indication that the tip was there.

Looking at the PMT scan in Figure 5.27 we can start to see regions where a drop in the PMT voltage is visible, this is the region that would indicate that a TERS probe or metal is there. Because of the limited objectives available, a 20x was the best magnification possible at this stage. The laser was focused on this area and looking at through the top objective camera we could visibly see the laser on top of the probe (Figure 5.28).

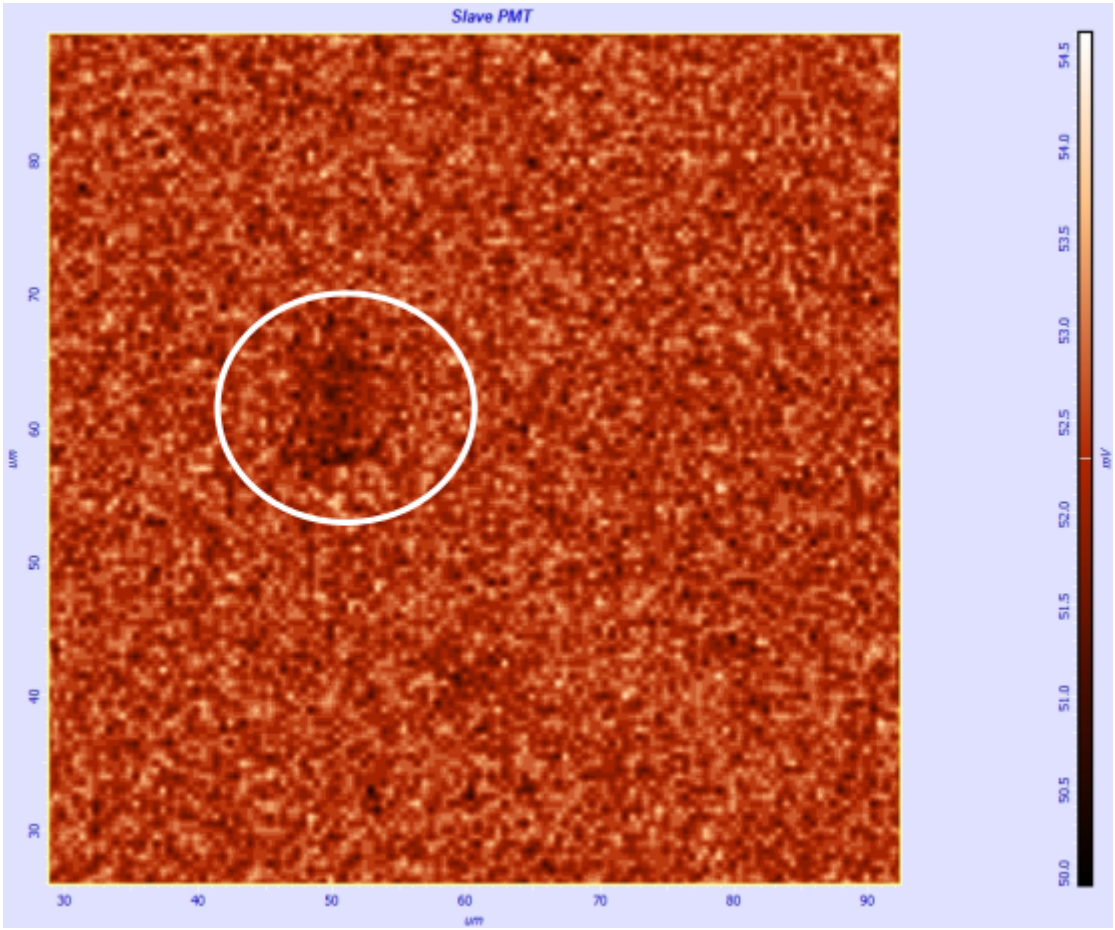

FIGURE 5.27: PMT scan of the region where the SPP TERS tip would be. Scan is also above 100 nm dots with a 500 nm PMT step size

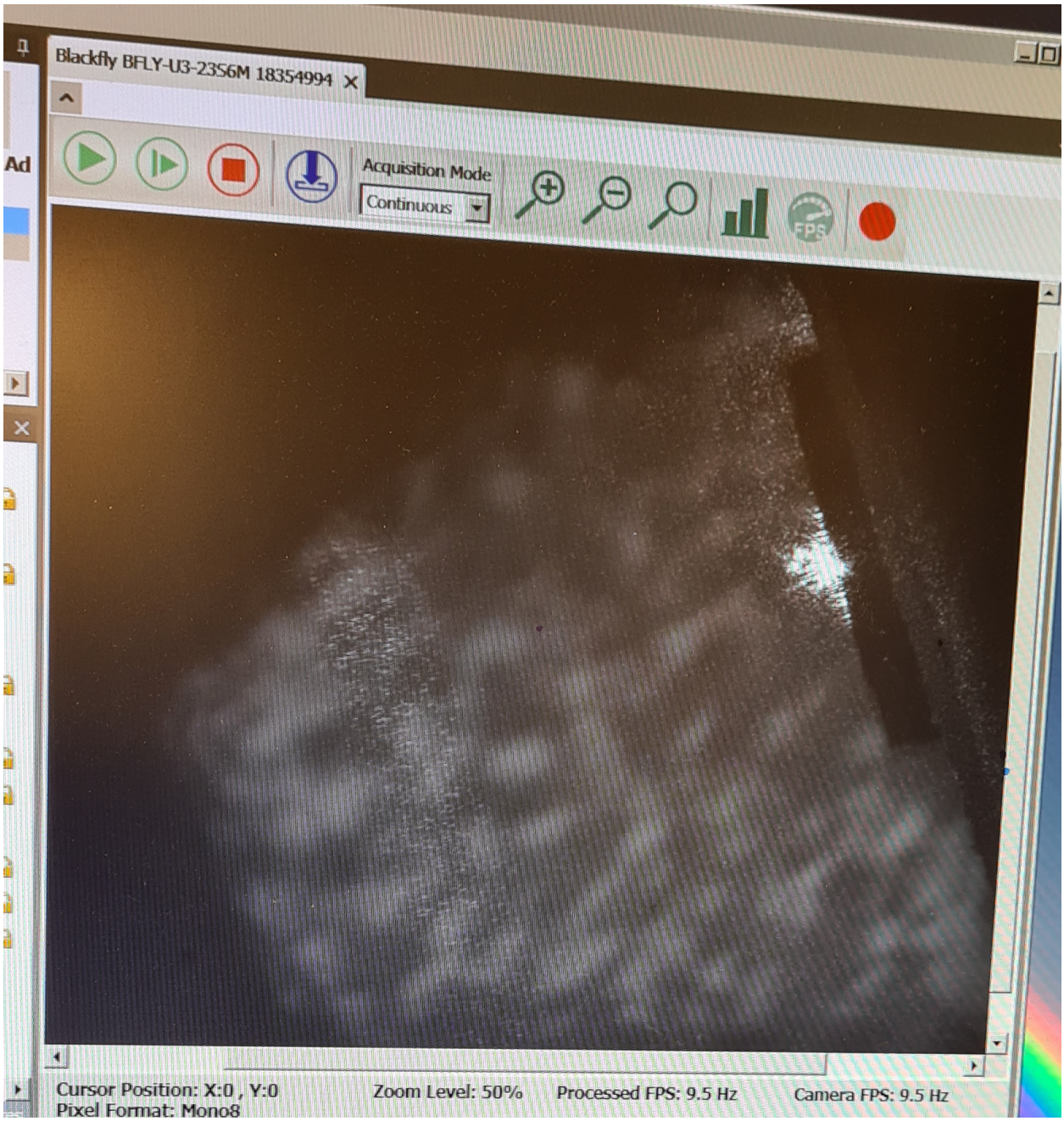

FIGURE 5.28: Camera picture of the video feed on the spectrum screen. It shows the laser of the spectrometer and probe aligned onto the tip.

A SERS of the area was then taken, so as to have a baseline of the Raman (Figure 5.29 SERS of the area was then taken, so as to have a baseline of the Raman, before bringing the tip into contact.

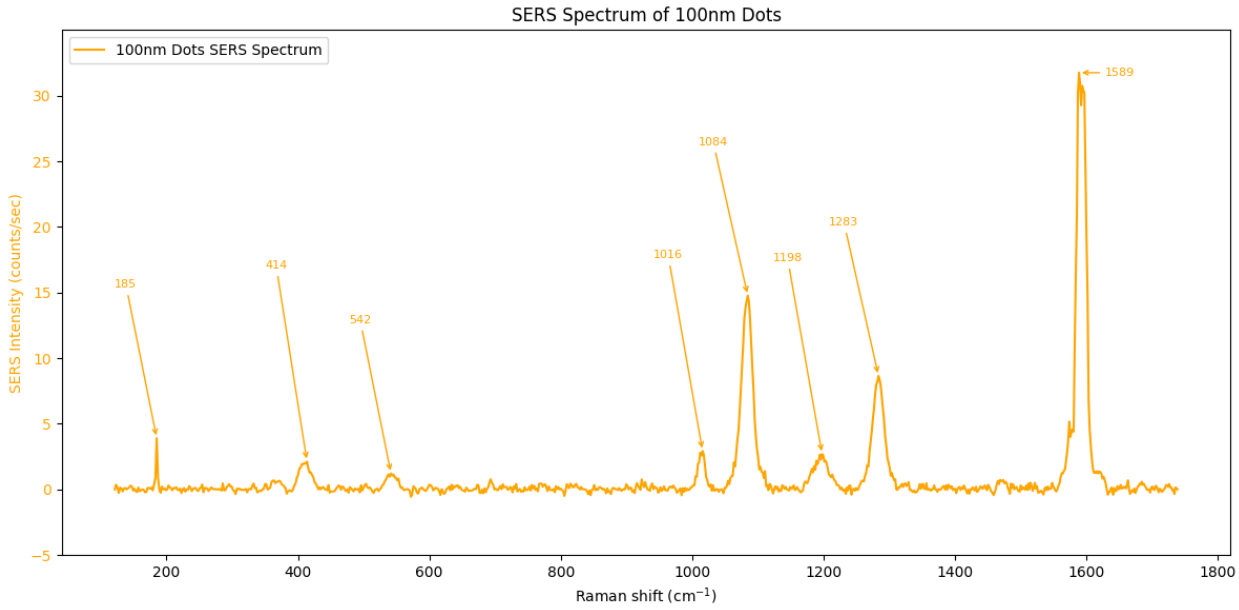

FIGURE 5.29: SERS spectra of 100 nm dot sample coated with BPDT. The integration time is 100 s.

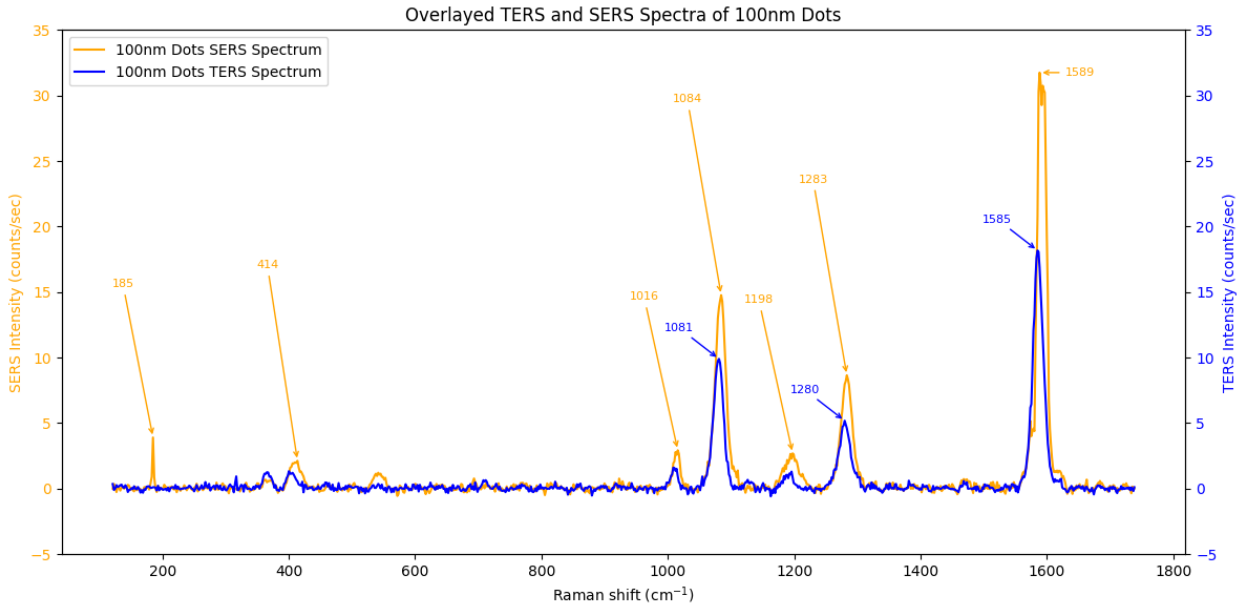

FIGURE 5.30: Raman spectra of the TERS tip in contact, with the SERS spectrum of the 100 nm diameter dots overlayed. The integration time is 100 s.

Examining Figure 5.30, it is clear to see the peaks from the SERS scan is more enhanced (x1.5 at 1589 cm^{-1}) than the TERS scan. It is however picking up very similar

modes seen with the SERS scan, albeit with a reduction in intensity, meaning the chemical identity and molecular environment of the BPDT are unchanged. From this data it can be concluded that both techniques are probing the same species and environment, however, there are no observable chemical or physical perturbations due to the tips proximity. The reduction in intensity means that from engaging with the tip has provided no tip-induced electromagnetic enhancements with the bottom illumination setup.

Multiple tips were attempted with even differing sites to get a direct illumination enhancement off the SPP TERS probes as can be seen in Figure 5.31 and 5.32.

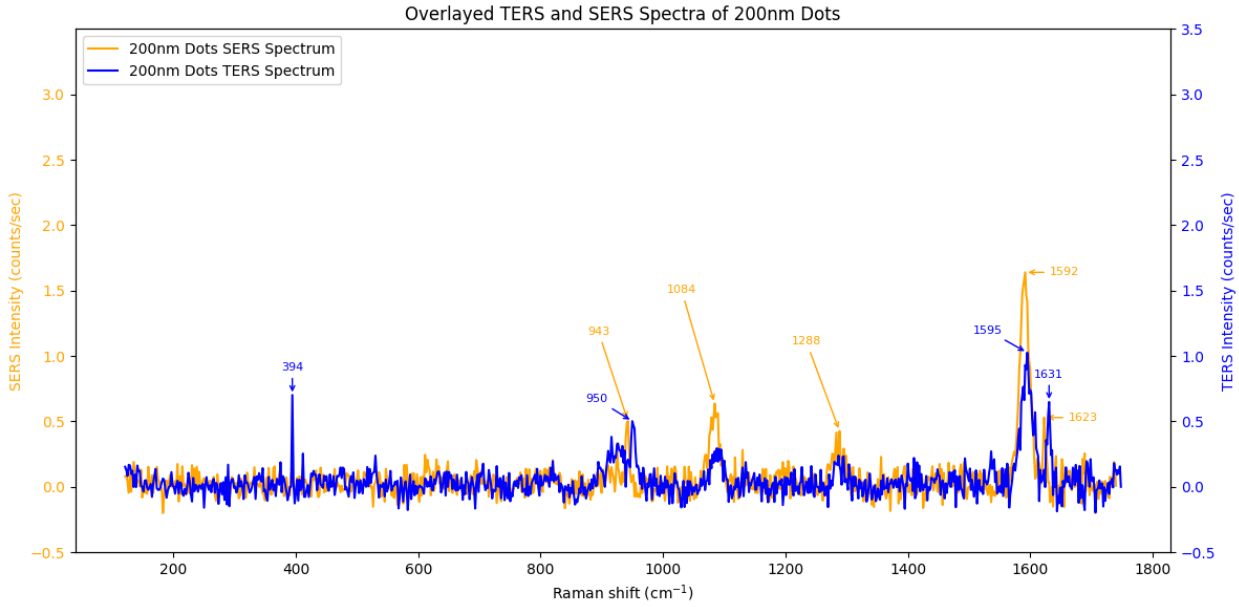

FIGURE 5.31: Raman spectra of the TERS tip in contact, with the SERS spectrum of the 200 nm diameter dots overlayed. The integration time is 100 s.

A change from a red laser to blue was even attempted (Figure 5.33), but due to the plasmon resonance of gold being further from the wavelength of blue light, the background noise is very prominent.

As can be seen by Figures 5.31, 5.32 and 5.33, we cannot retrieve a TERS enhancement of the gold dots with these probes, no matter the site, nor laser wavelength. However, the 100 nm dots do show a band at 1198 cm^{-1}, which is C-H in-plane assignment [195]. It also shows a band at 1010 cm^{-1}, which is assigned to aromatic ring deformation [195] (bending and stretching) of the bi-phenyl rings. As this cannot be seen with the BPDT coated 200 nm and 50 nm dots, it confirms the enhancement and appearance of bands vary with nanoparticle size and helps dictate SERS visibility for some vibrational modes.

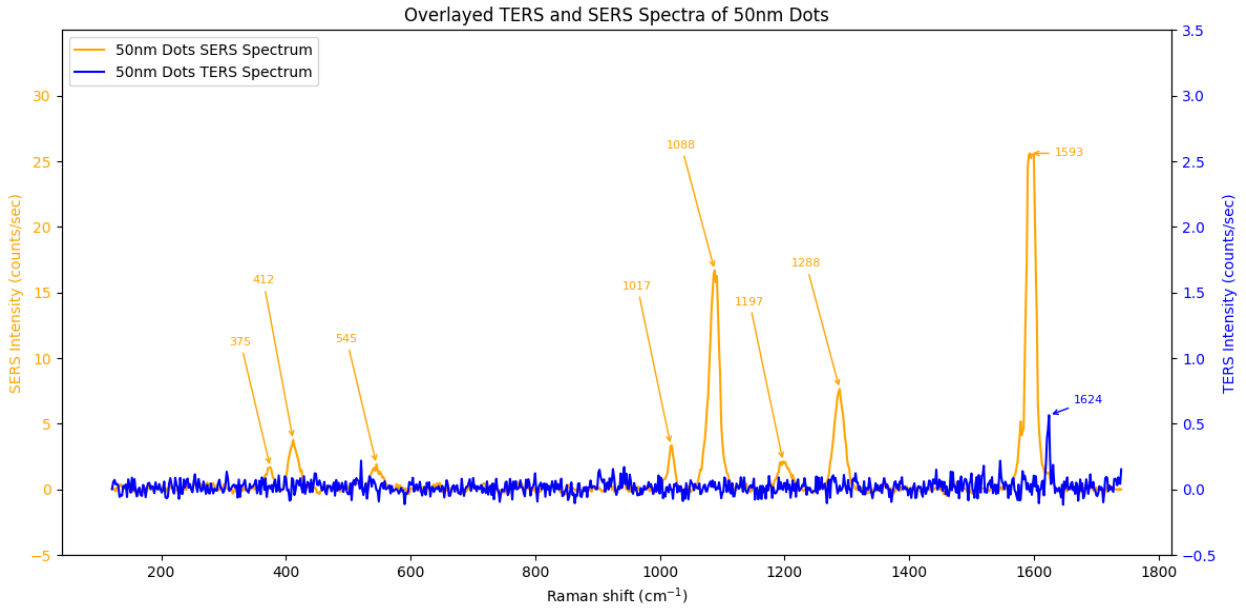

FIGURE 5.32: Raman spectra of the TERS tip in contact, with the SERS spectrum of the 50 nm diameter dots overlayed. The integration time is 100 s.

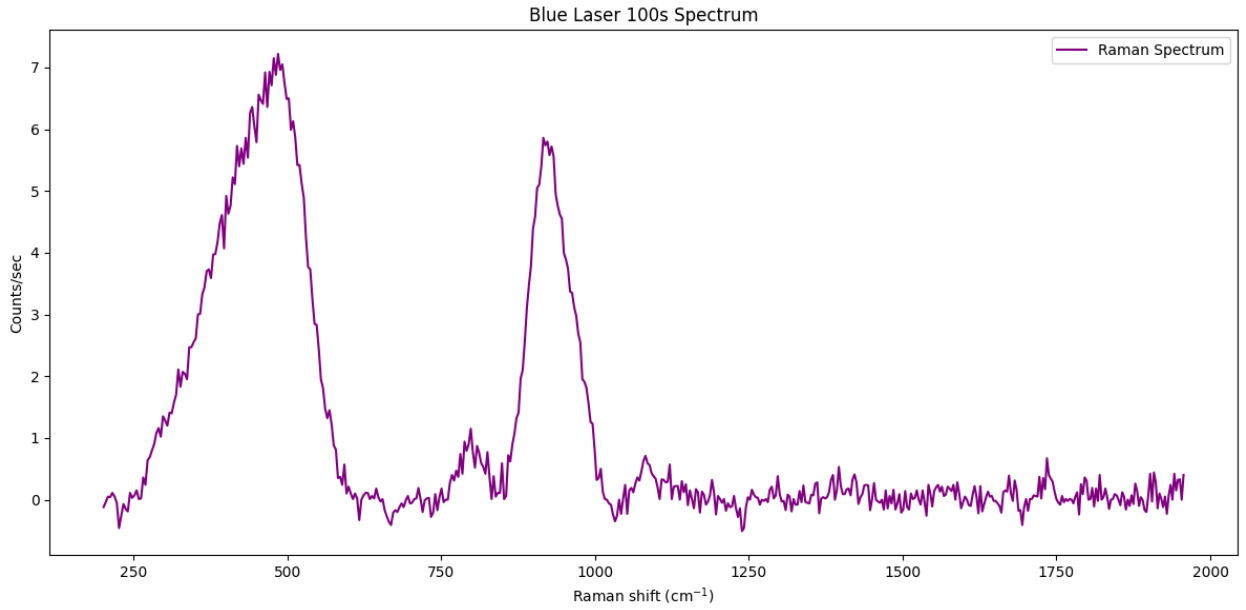

FIGURE 5.33: New tip in contact with BPDT coated 100 nm diameter dots with a 473 nm laser. Integration time is 100 s.

The results with the 633 nm laser suggests the gold structure supports plasmonic enhancement at this wavelength, allowing for more resolved Raman peaks. At 473 nm (Figure 5.33), the gold is off-resonance and provides a weak electromagnetic enhancement, resulting in higher background fluorescence and spectral broadening. It does not

align with what is shown whilst using the 633 nm laser, where the results align with literature [195], [311]. It was concluded the 473 nm is not useful for this specific application as it is not able to generate reliable Raman spectra of the sample and will not enhance the signal, using the probes, as it is off-resonance.

The groove density is sitting at 600 gr/mm, reducing the groove to 150 gr/mm gives a broader spectrum. This attempt increased the spectral range but decreases the resolution. With TERS the 600gr/mm grating should be more than enough to resolve a TERS signal where a SERS signal is apparent, the probes are however just quenching any Raman signal. Further testing of whether the probes can couple through the SPP grating is not possible due to the probe mount and the spectrometer exciting and collecting through a bottom illumination mode. Experiments were therefore performed to try and determine the root cause of this behaviour and if possible, to determine whether any operating mode would allow these probes to perform TERS.

5.8 Troubleshooting

As the fabricated TERS probes were not retrieving an enhanced Raman signal, even though the tips were directly illuminated onto the apex, further research into the root cause was undertaken. One analysis of the problem was to perform EDX on the probes and see if the deposited metal was gold. A tip which wasn't scanned and deemed in worse condition under visual inspection was used for this analysis. This tip was from the exact same wafer the scanned tips were from and therefore the metal stack would be consistent. It just wouldn't be used for scanning due to a break in the metal, which would cause any plasmons to leak at the break. Images of the tip with a varying contrast per different examined material is shown in Figure 5.34.

The EDX analysis has concluded that the sensor material is Au, with a silicon nitride cantilever. The spectrum also picks up an Al signal, this is from the holder the probe is clamped to when under analysis. The next step was to set up a probe for TERS with a differing tip geometry. This would rule out that the shape is preventing the enhancement of the electric field or generating plasmons. The NiCr adhesion layer was removed from these probes as it is known to quench a Raman signal [312].

To do this, RFESPW Si probes were taken out of a wafer. Using an evaporator, the tips of the probes were coated in 42 nm of gold, this should give a tip radius of 50 nm. This radius was based off of research by Yang [293], whereby a Si tip coated with Au

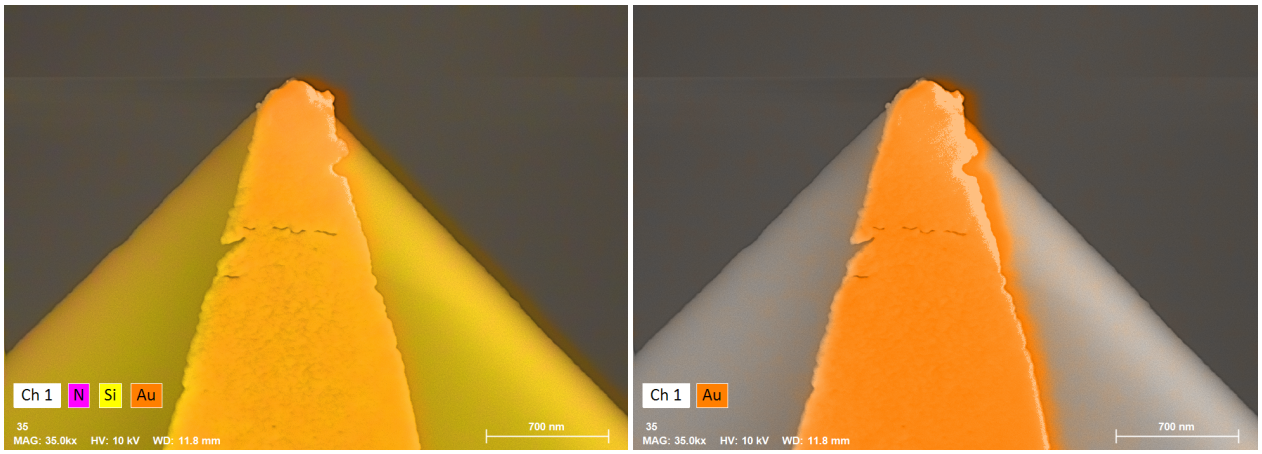

FIGURE 5.34: Both pictures show SEM images with EDX analysis of a micro-fabricated TERS tip. The image on the left has the Si, N, and Au channels on it, where it indicates the tip material is Silicon nitride with a gold sensor. The image on the right just shows the isolated Au channel, indicating that the tips are made from gold.

having a radius of 5 nm gives a large electric field enhancement due to the lightning rod effect but starts to decrease until 15 nm, whilst testing on a gold substrate. The radius of the commercial probes is not guaranteed to be 8 nm, with a max radius of 12 nm, and with a 10% overshoot/undershoot of metal evaporation, the chances of achieving below 15 nm (2 nm evaporation) and having it adhere are very slim. The next highest electric field enhancement (at around 200) from his paper with a red laser is 50 nm, whereby a drop in the enhancement isn't seen until 100 nm radius or the thickness of the Au is larger than 80 nm. These results also line up with Meng et. al. [274] where he saw the strongest enhancement (4000) of a gold coated silicon substrate with a Si tip, boasting a resonant frequency of 616 nm whilst having a radius of 50 nm. This is however just short of his ideal gold thickness of 50-100 nm. Meng et. al., however, noticed a strong enhancement at 30 nm Au thickness and proved that with an increasing thickness of gold (up to 100 nm), TERS can be achieved due to the dipole-dipole coupling effect between the tip and substrate. An image of the probe before coating and an image of the gold coated RFESPW probe are shown in Figure 5.35 and 5.36.

In using these coated probes, the apex is small enough to allow for high aspect ratio features to be interrogated, and within range of Yang's research [293] to generate a greater electric field enhancement. There is also no adhesion layer, this means there is no sticky layer to dampen any potential enhancement, providing a solid experimental basis into whether we can get a TERS enhancement through this setup.

Furthering on from this, the probes were put into the TERS setup and ready to do an

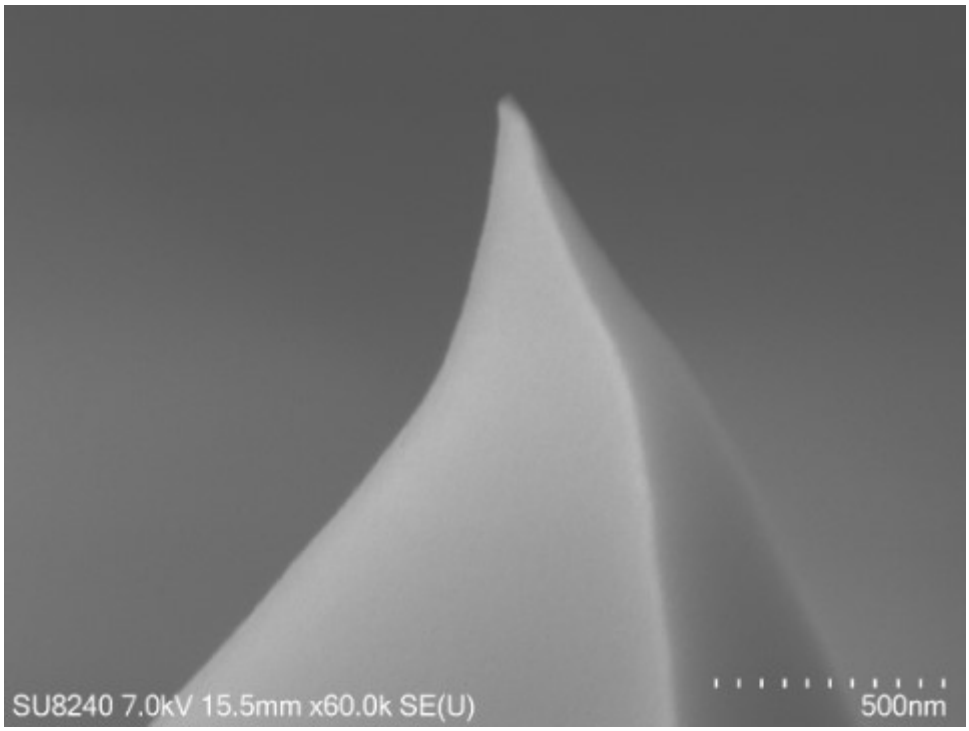

FIGURE 5.35: SEM image of the RFESPW probe.

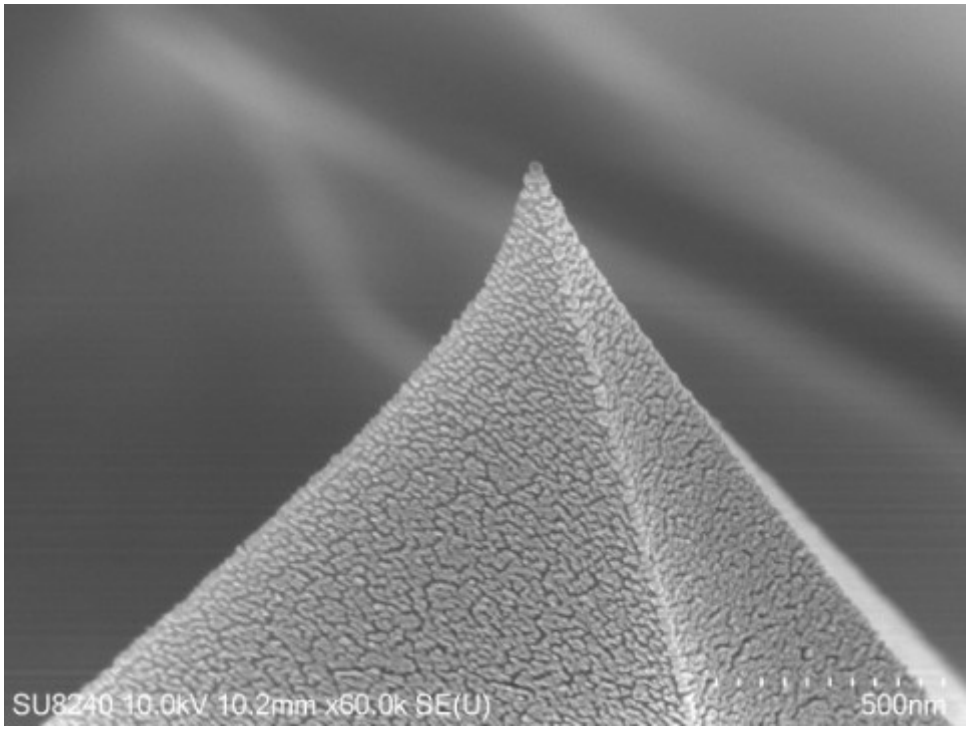

FIGURE 5.36: SEM image of the RFESPW probe after being coated with 42 nm of Au.

AFM scan. The 200 nm diameter dots were scanned at 0.5Hz to give the resulting image in Figure 5.37.

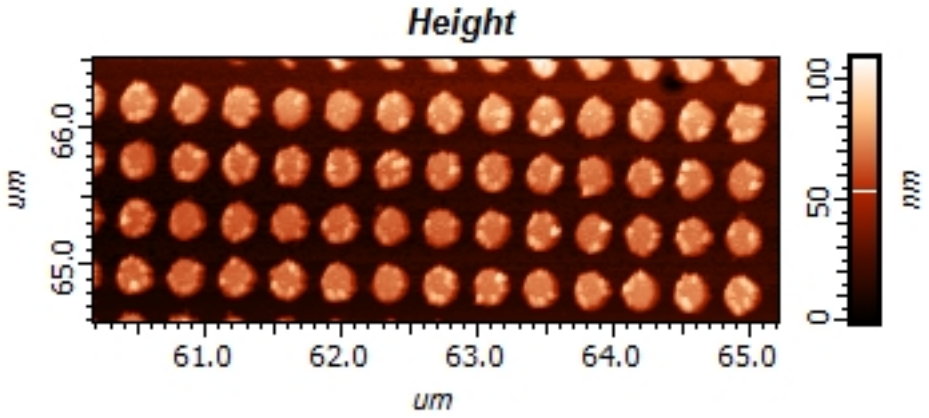

FIGURE 5.37: AFM scan of the BPDT coated 200 nm diameter dots with a 0.5Hz scan rate.

Looking at Figure 5.37 we can see that the RFESPW probes can still resolve the gold features well, even whilst coated with gold. Comparing to Figure 5.23 earlier we can see that the topography on top of the dots would be a result of the evaporation. The rough surface does provide a good location for the BPDT to bind too.

As the probes can perform AFM, more experimentation on determining if an enhanced Raman signal was conducted. The tip was engaged into contact with the BPDT coated 100 nm dots, and a Raman spectrum taken with a 100 s integration time. Another spectrum was run straight after without touching any of the controls to find out if there is any drift within the system. The results of these are overlayed in Figure 5.38.

As can be seen from Figure 5.38 and comparing it to the previous SERS of the 100 nm dots (Figure 5.29), the lower wavenumber Raman modes are there, however it is not enhanced. At the 1588 cm^{-1} band, it is almost half as weak. As the integration time is 100 s in Figure 5.38, it is entirely plausible that the tip is drifting whilst the scan is being undertaken. Not to an extent whereby no enhancement will be detected but enough that the integration picks up the less intense values and adds this to the final value as the laser misaligns.

Comparing Figure 5.30 to this, which was the SERS of the 100 nm dots vs the attempted TERS, the most pronounced difference in peaks is the silicon signal. This indicates the tip could've been damaged, exposing more of the Si, or that the spectral data is not consistent due to a potential drift or spectrometer problem. To find out more, the

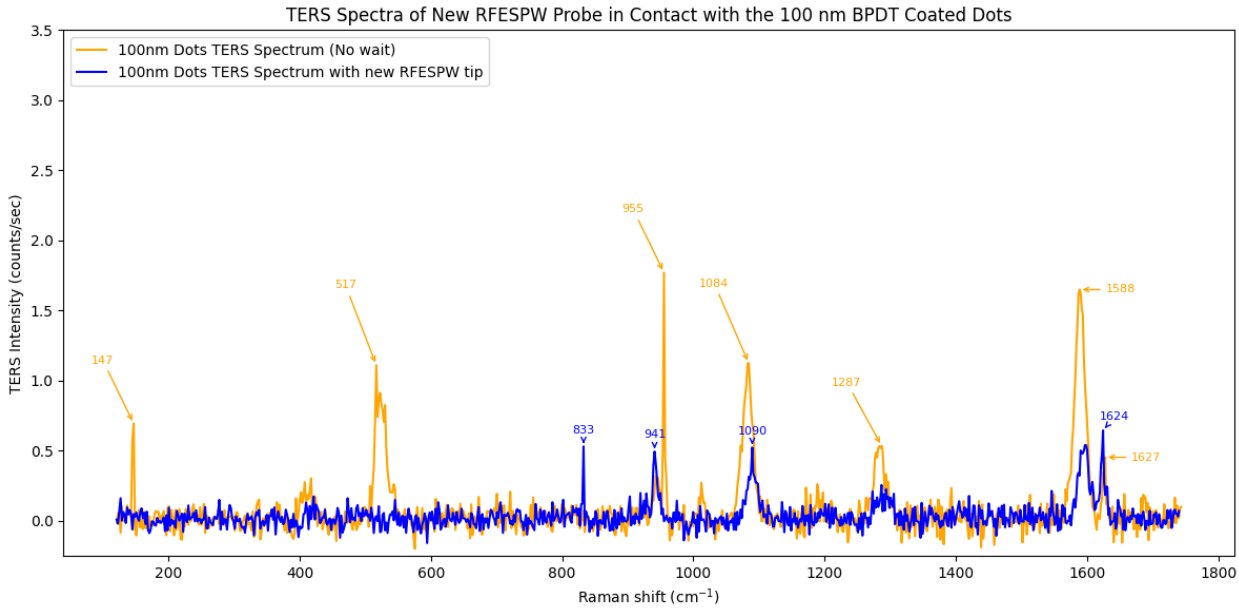

FIGURE 5.38: Overlayed Raman scan of the RFESPW tip in contact with the BPDT coated 100 nm dots with the other scan acquired straight after. Integration time was 100 s.

equipment was kept as is with the tip in contact and left untouched for an hour to evaluate any drift in the system. The results of this are shown in Figure 5.39.

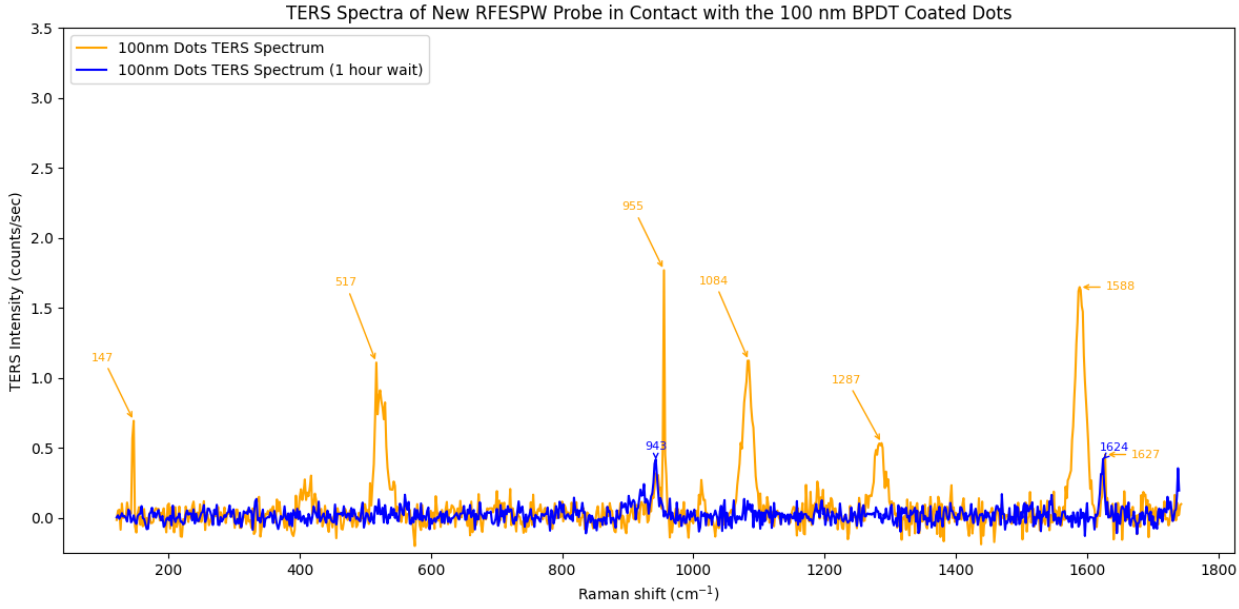

FIGURE 5.39: Spectrum of the same site as taken in 5.38, overlayed with the Raman spectrum taken 1 hour after without touching the controls.

Comparing Figure 5.38 with 5.39 we can see how the spectral map is now missing

Raman modes without even touching the equipment. This indicates that the laser is drifting as well as is the tip. This could even indicate slight drift between the 100 s integration time; however, this is necessary to develop a good SNR.

Another tip was loaded and landed onto the substrate to determine if the pressure threshold was too high to detect contact, and then to see if we could get an enhanced signal with these even if the tip was damaged. The results of this are shown in Figure 5.40.

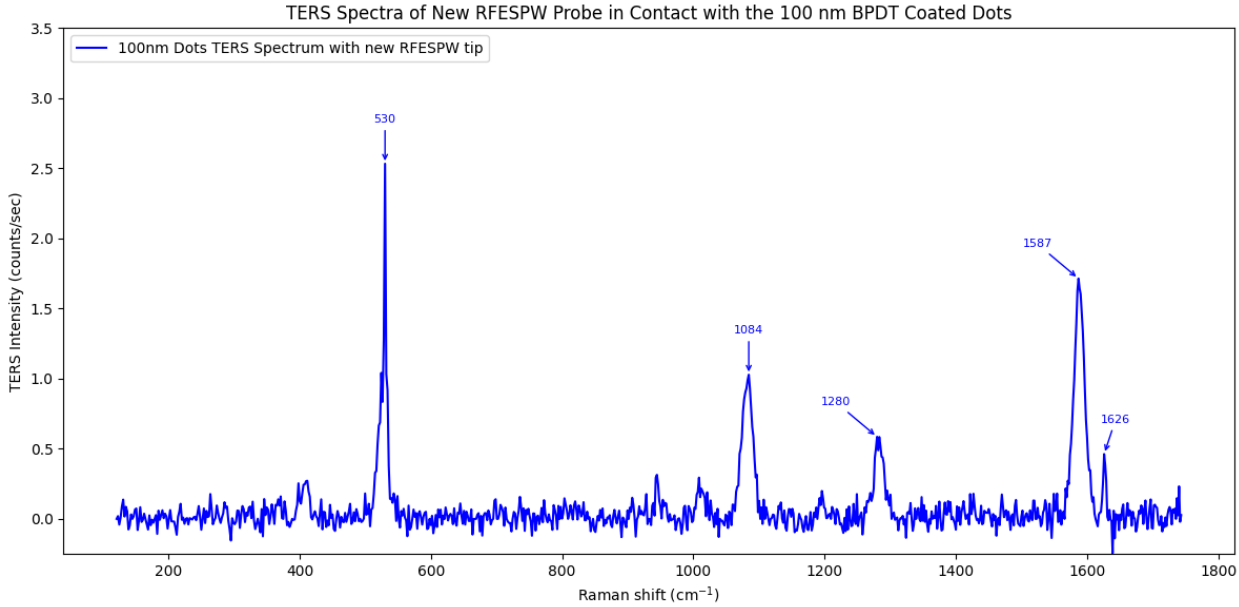

FIGURE 5.40: Spectrum with a new gold coated RFESPW tip in contact with the 100 nm dots. The integration time is 100 s.

As can be seen in Figure 5.40, another strong silicon peak is shown, indicating we are on the tip. However, as the Raman signal is one of the strongest modes, the landing pressure of the probe could be damaging the tip. The pressure could not be reduced any further as the NTEGRA wouldn't register a lower pressure as a deflection, then it could not scan. A SEM investigation of the tips was performed to see how badly damaged the probes are after landing. These are shown in Figure 5.41 and 5.42.

As can be seen in Figures 5.41 and 5.42 the probes have been severely damaged through landing and scanning. This has led to the removal of the gold apex of the probe, revealing the Si underneath which explains why there is a large Si peak. It means that the probes can't perform TERS as is due to tip damage.

One of the microfabricated TERS probes from this project were also interrogated with a SEM to see the damage on them after use within the Glasgow setup.

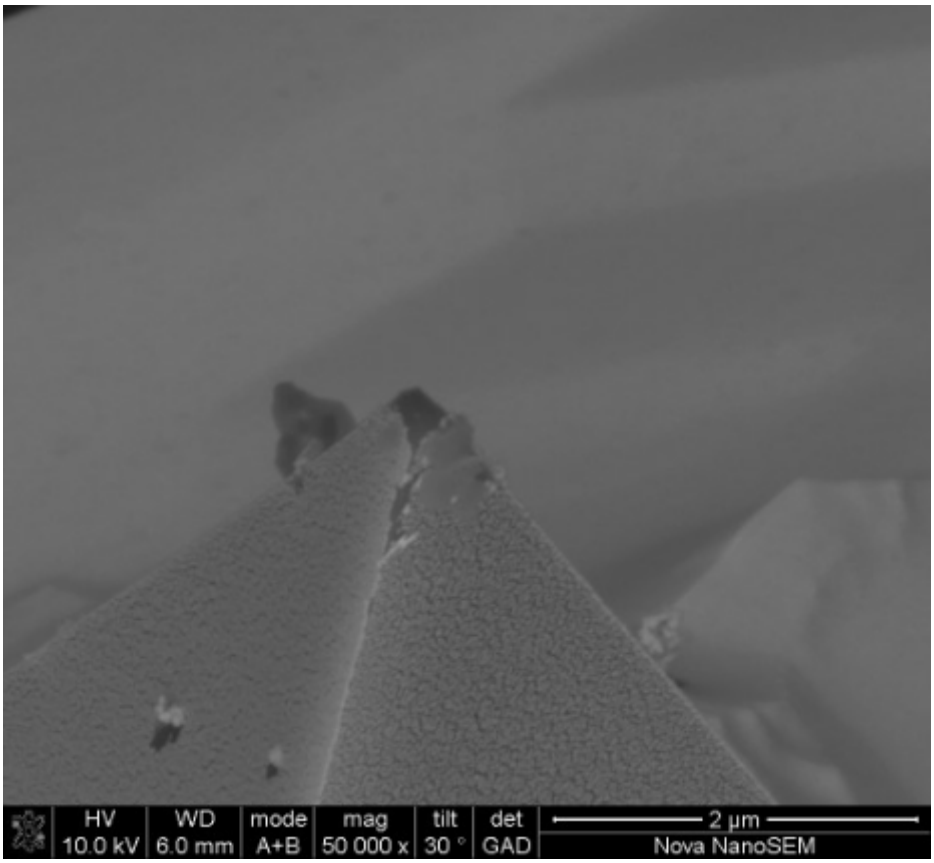

FIGURE 5.41: SEM image of a gold coated RFESPW probes after scanning.

As can be seen in Figure 5.43 and 5.44 the TERS probes have been able to withstand the scanning and contact of the experiments. Figure 5.43 gives a better contrast of the area as it uses backscattered electrons, and some rough bumps along the end of the antenna can be seen. This would become leakage points for the SPP and would dampen any enhancement received at the end due to a less than optimal propagation mode on the surface. It is not known if this bump arose from the silicon nitride beneath the surface of the gold, which would also dampen any mode contained between the gold and dielectric as well. Figures 5.43 and 5.44 do indicate that there is still metal at the end of the probe and protruding, which means that it theoretically should be able to produce an enhancement through direct illumination of the apex as the tip has no visible signs of damage. The experiment using the referenced paper as a guideline had the tips damaged upon contact, it is feasible that the damage caused lead to a loss of enhancement at the apex.

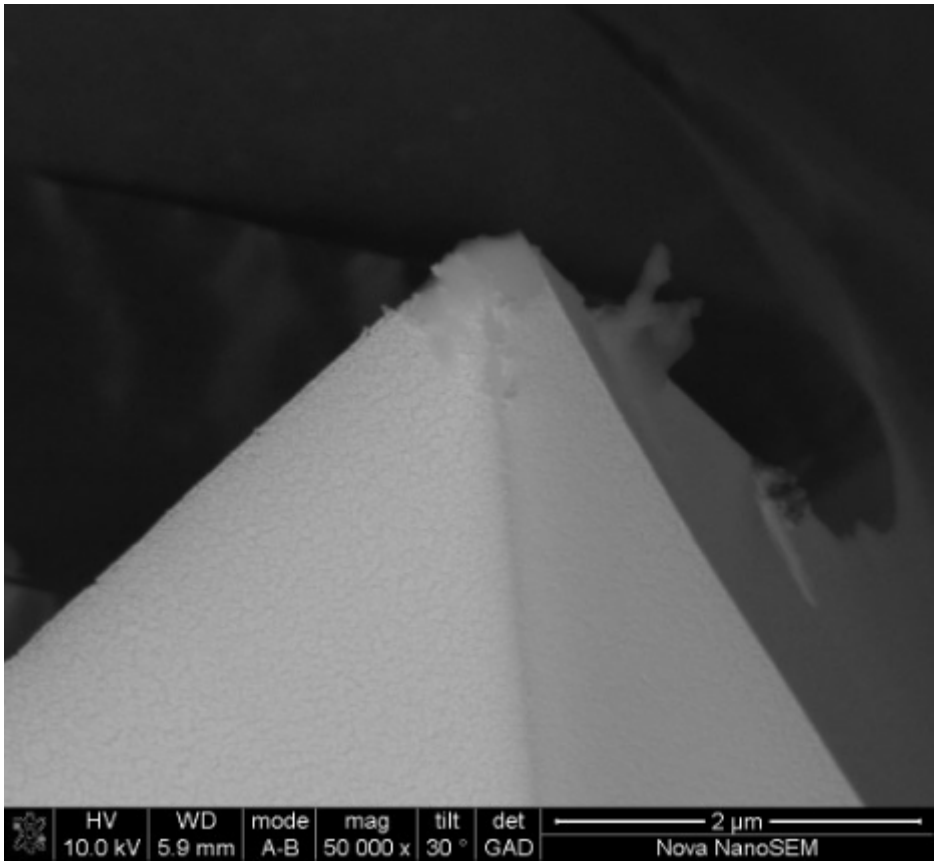

FIGURE 5.42: SEM image of a gold coated RFESPW probes after landing.

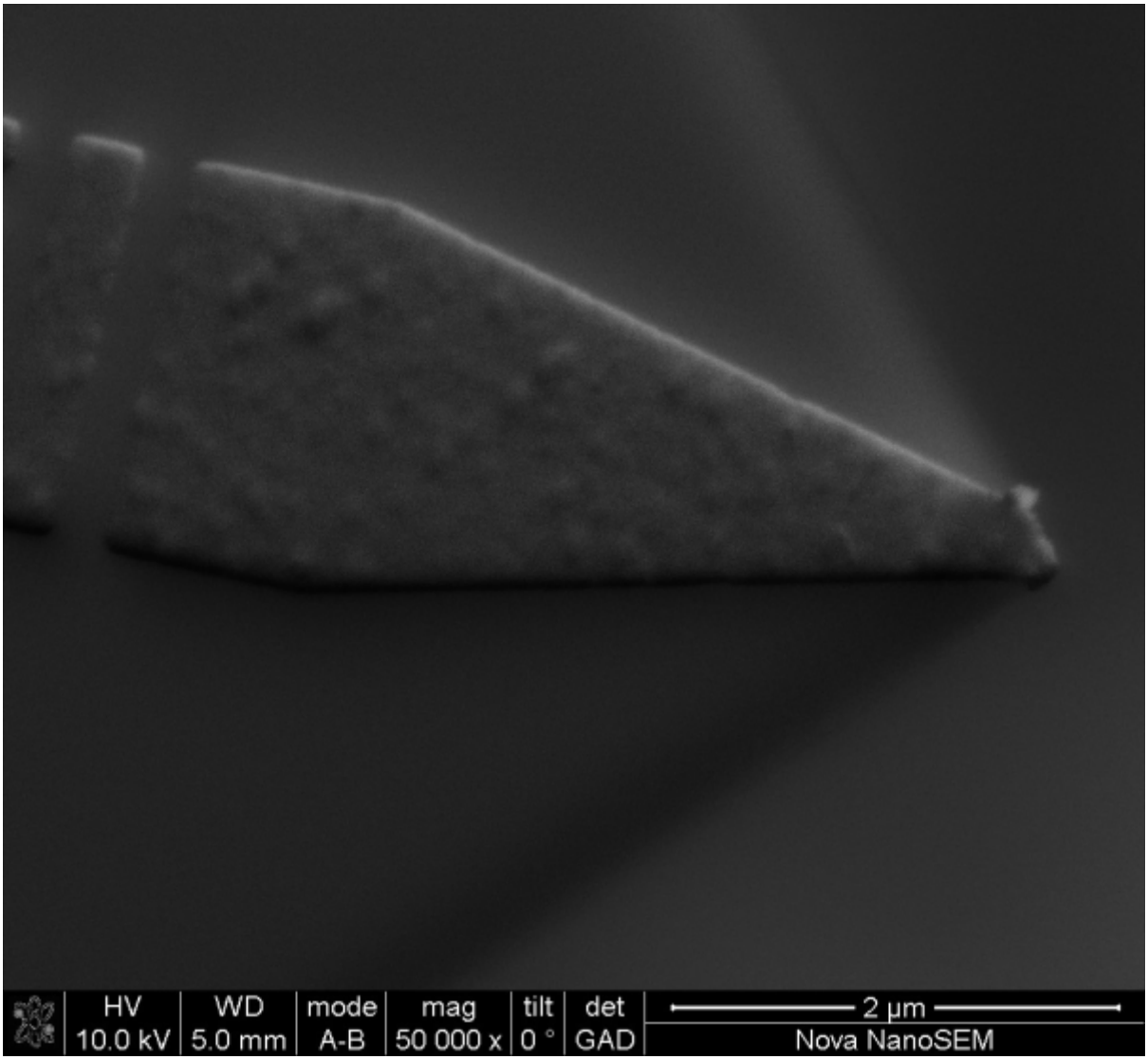

FIGURE 5.43: SEM, with the gaseous analytical detector, image of the microfabricated TERS probe (350 nm period 25 degrees opening angle) after performing Raman Spectroscopy.

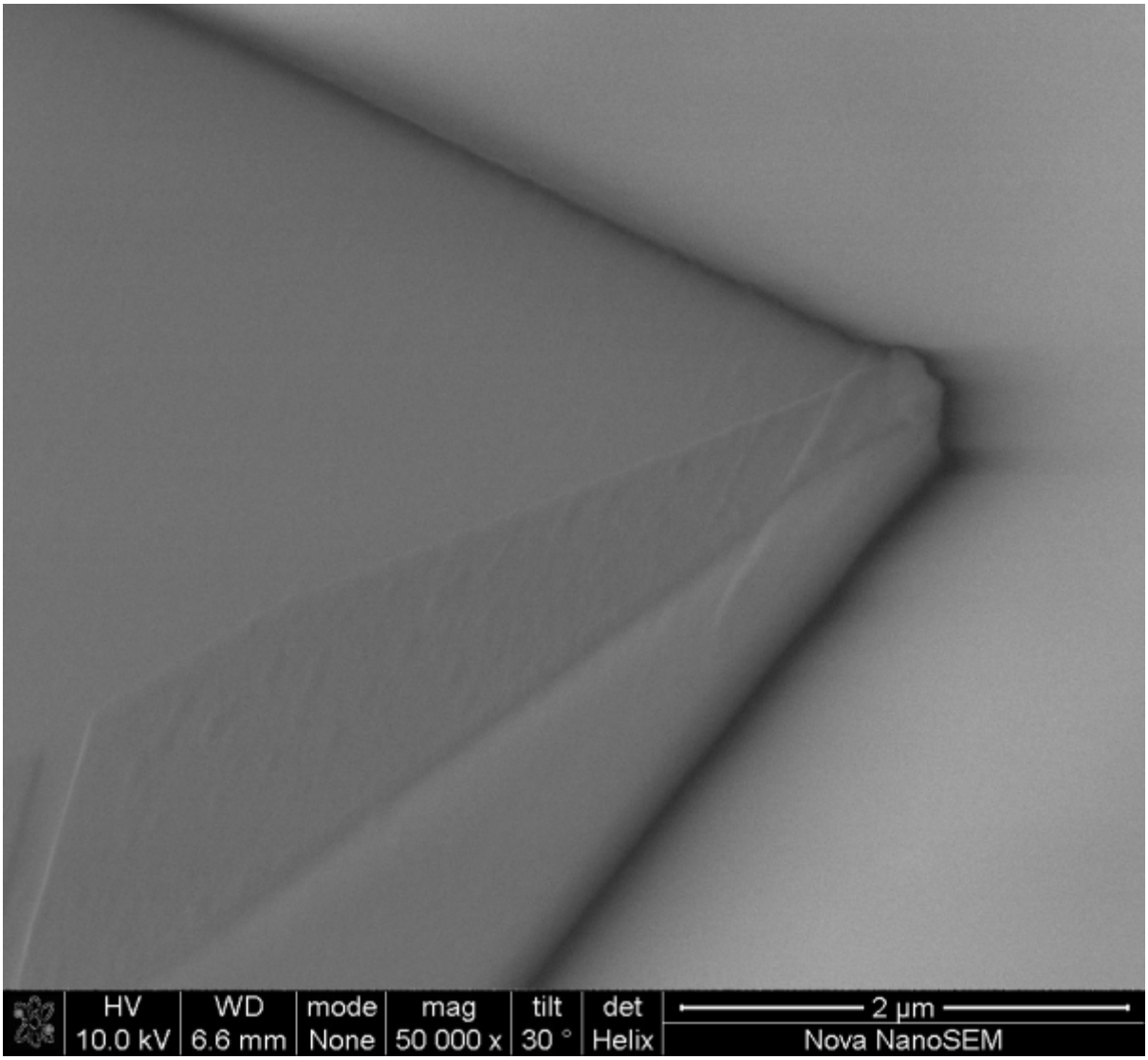

FIGURE 5.44: SEM image, with the helix detector, of the microfabricated TERS probe (350 nm period 25 degrees opening angle) after performing Raman Spectroscopy

5.9 Conclusion of Experiments

Through experimental observations it was found that the microfabricated TERS probes do not have any visible plasmonic activity. The testing throughout this work concluded that the fabricated TERS probes don't enhance a Raman signal through direct illumination. The initial intention was to use them so that they could be remotely excited via the grating but the angle of the incident lasers on both Glasgow and the NPL's system wouldn't allow for that. To test the theory, a side illumination, bottom illumination, spectrometer, and laser changes have been performed.

At the NPL there was a slight fluorescent enhancement, however this was found to be a metallic flag. The microfabricated TERS probes chosen showed no sign of any plasmonic fluorescence with both a green and red laser, with grating changes and laser intensity changes. To check that the gold was in fact absorbing and behaving as expected optically, linear spectroscopy was performed. These results concluded that the metal was fine. EDX was also conducted on the metal which determined it was gold.

At Glasgow, the bottom illumination setup gave excitation from another angle. We could start to identify Si peaks on the probes, however comparing with the SERS spectrum of the same area, the probes were quenching the signal. A change of probe to that of literature were performed, which also omitted a signal damping adhesion layer, however damage to the tips upon landing broke the metal off the tip and could no longer keep in contact with the samples. Any signal that was taken did not show any sign of enhancement, much like that of the microfabricated probes. Modifying the laser wavelength, changing the grating density, and making sure everything was aligned at every stage did not make a difference to the enhancement.

5.10 Epilogue

Looking at the probe archetype designed, and the results which show no plasmonic activity, a look into the behaviour of the dielectric guided mode was undertaken. In this design, a wave in the nitride couples into a plasmon in the sensor end because the wave is propagating at a matched k-vector in the nitride and in the plasmon, just like a prism coupler. The grating scatters the free space light into the nitride at an angle large enough to give TIR, but small enough to match the plasmon k-vector. This happens at an angle of 27.407°, this is depicted in Figure 5.45.

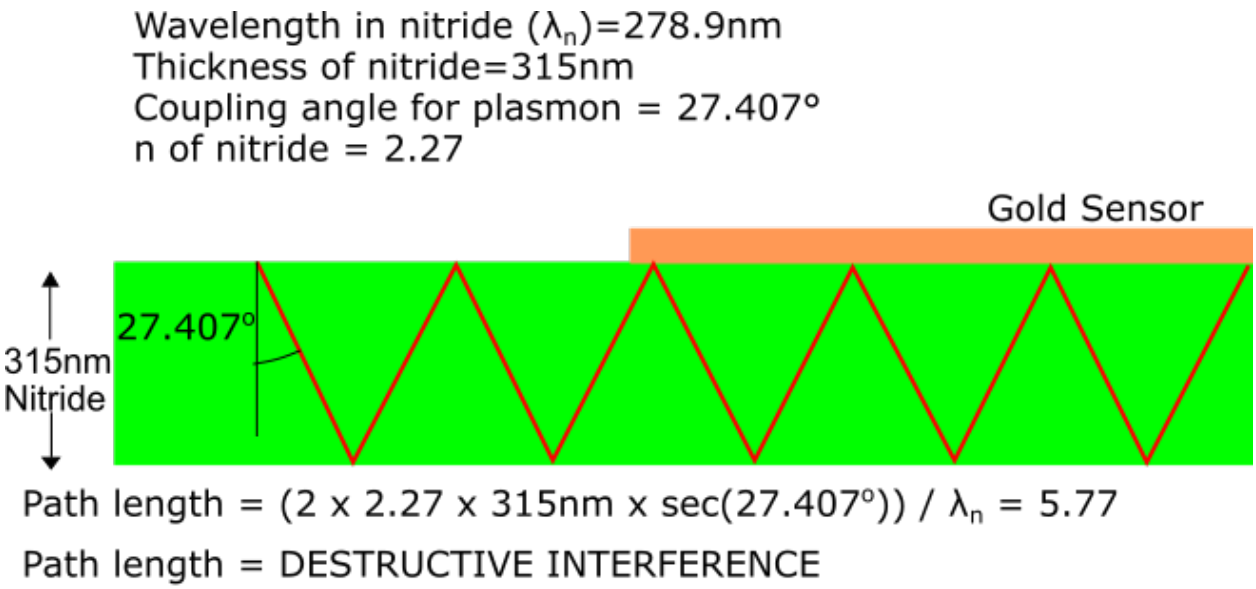

FIGURE 5.45: Diagram depicting the TIR path of the light within the nitride with the TERS gold sensor apex at the top. The optical path length equation and result indicates that the path shows destructive interference within the nitride

As the wave propagates along the slab waveguide, it bounces back and forth as it goes along. There is then interference between the waves going from top to bottom of the nitride, to the bottom up. Only when the path length within this back and forth round trip is a whole number of wavelengths can the wave propagate. As can be seen from Figure 5.45, this does not happen for the probes as fabricated and the interference is destructive (partial constructive). Anything that is not constructive gets supressed at every reflection and acts as a filter. Propagation at other wavelengths can occur at the resonant angle for plasmons. This in turn means we need a specific thickness of nitride for light at a particular wavelength to hit the gold to couple into a plasmon and if not, the light will leave the waveguide and never couple into a plasmon.

From the original design choice, we would need a nitride thickness of 327.22 or 272.69 nm (nearest values) to reach a whole number and not achieve destructive interference. With the current LPCVD nitride deposition the uniformity and control over deposition thickness is not great (3.12% uniformity and 21% less than specified) with a mean value of 315 nm, instead of 400 nm.

Without the changing nitride thickness, the existing probes could still work. However, the wavelength of the excitation light would need to be tuned to match the mode of the dielectric waveguide, then illuminate at the angle which gets the grating to match the plasmon *k*-vector and provide total internal reflection in the nitride. This means that

the normal fixed wavelength edge or notch filters within the spectrometer will no longer serve their purpose as we change the excitation wavelength, so either a triple axis spectrometer for improved rejection of the pump will have to be used or one would need to replace the notch filter with one at a custom wavelength. A tunable laser would also be required. Tunable lasers are esoteric and even if it all functions, when the probes run out, the microscope is possibly derelict. Since the uniformity of the deposited nitride is poor, despite the fabrication of a whole wafer of probes, few probes will work out of a batch at any specific wavelength.

There is also the possibility of making this a single mode by using a thinner cantilever. To calculate this we take the normalised frequency (v-number) as less than 2.405 for a single mode [313]. The equation for the v number is [314] :

$$V = \frac{2\pi d}{\lambda}\sqrt{{n_{core}}^2 - {n_{cladding}}^2} \tag{5.2}$$

Where the excitation wavelength is 633 nm, d is the thickness of the silicon nitride layer, n_{core} is the refractive index of the core (nitride) and $n_{cladding}$ is the refractive index of the surrounding air. Rearranging to solve for d being less than 2.405 [313]:

$$\begin{aligned} d &< \frac{(633 * 2.405)}{(2\pi) * \sqrt{(2.27^2 - 1^2)}} \\ &< 118.7nm \end{aligned} \tag{5.3}$$

Therefore, for a single mode operation within a planar silicon nitride waveguide at 633 nm would require the dielectric to be approximately 118.7 nm thick. This will however make the probes less stiff, meaning it is more susceptible to thermal and environmental vibrations and the ability to detect small forces and displacements is compromised making it hard to scan. This method also relies on a fluorine based isotropic dry etch of the probes to etch the material down to this thickness or rely on some part of the wafer achieving this thickness during deposition, using the lack of uniformity to an advantage. This will then affect the yield as all other thicknesses are redundant and it becomes hard to tell which thickness is which. The dry etch approach will also undercut the gold, which is a good thing as it provides better access of the metal towards the substrate surface. An easy way to tell if the thickness is correct would be to SEM the tip and measure the thickness using the in-built measurement tool. This is also reliant on the SEM's distance measurement being calibrated correctly and free of charging, as this can affect where the user perceives where the dielectric starts and ends. Another downside is the handling of the fragile probes may be an issue as the tips are prone to breaking.

The thinner nitride on the probes would also decrease the tip radius, leading to a higher spatial resolution probe and better electric field enhancement at the end, but more prone to breakage throughout. An alternative would be to fabricate very thick cantilevers, so that the modes are closely spaced in wavelength and the waveguide behaves more like a bulk glass prism. For a multimode waveguide with modes space at half degree angles around the plasmon angle the waveguide would need to be of order 27 μm thick, which is impractical.

A grating could also be fabricated in the gold so that coupling can be done directly into the metal. This would resemble something like Ropers et. al made [234], where local field enhancements of 10 were seen with a excitation source centre wavelength of 800 nm. The issue with this is the range of a SPP is about 20 μm in gold at 633 nm [315], so it then becomes optically harder to discriminate between pump light and scattered light and gives a smaller target for the laser to illuminated, but much more likely to be reliable.

Thermal oxidation growth of silicon dioxide would seem a better alternative, allowing for highly reproducible thickness and reproducible optical properties. The downside of this is it is an inherently high stress material, making it prone to crumpling, however fabricated probes using silicon dioxide with a very high yield have been made at the University of Glasgow before by Zhang et.al. [258], [316]. Care has to be taken when growing the dielectric as the oxidation rate of different crystallographic directions is different, so testing of the growth is needed, however this means we can get precise control of the thickness from the oxygen diffusing through the oxide to get to the silicon. Since diffusion slows down (time $\propto$ thickness^2), once you get to a certain thickness the diffusion slows down to make it very reproducible. At the temperatures for thermal oxidation ($900^{\circ}C$), oxygen will also get rid of contamination.

6 Summary and Outlook

6.1 Introduction

Tip enhanced Raman Spectroscopy continues to be a leader in high resolution, high sensitivity measurement tools in realising phonon spectra. As plasmonic technology develops into discovering new ways of enhancing the electric field at the end of a noble metals, the actual probe development for TERS has been left behind. Much to the large enhancement achieved with commercial and in-house made silver probes, the manner in which they are made (sputter coating/evaporating singularly or a few at a time) leaves a lot to be desired with reproducibility issues between probes. The selection of silver also means that the probes must be used almost immediately as it begins to form a sulphide layer over time, preventing any large enhancements as it grows. Although batch fabrication is possible and proven, control over the antenna dimensioning is left to wet etch techniques, which aren't stable.

Within the AFM group, scanning probe technology has been continually advanced into a commercial, reliable process flow where using this as a base line, provided a great starting point for the batch fabrication of these probes. This thesis has presented the ability to batch fabricate TERS probes, whilst having precise control over the sensor dimensions using e-beam.

The following sections in this chapter will summarise the conclusions from each part of this work, whilst having an outlook on the future work required to develop this technology further.

6.2 Calibration Samples

The topography free substrate has provided a method of taking a SECM measurement whilst removing any tip-related artefacts. It proves to be an excellent substrate in determining a tip's sensor sensitivity without being influenced by topography. The substrate

pattern consisted of decreasing separation interdigitated electrodes, however as it was a direct write EBL technique, this pattern could be modified to suit the user's needs/sample archetype. The resulting AFM scans of this sample had sub-12nm topography and even less than 5nm in regions whilst under interrogation. The issue with this sample is the lifetime to use, it must be used within a quick timeframe as to prevent/minimise any oxygen growth or particle growth which could inhibit the redox reaction it will undergo when in use. Nitride adhesion was also an issue. Future work to improve this sample could see an adhesion layer, like NiCr, being evaporated onto the gold to adhere to the nitride. This sample can be progressed, especially for future use on SThM or SECM probes to make the reliability much better through improving adhesion and temperature control of the SU-8 bakes. This sample was however not used for TERS as to bind a Raman active molecule onto the gold requires some surface roughness to initiate the binding. The main purpose of this sample is in the reduction of topography.

Further on from this, a new sample for TERS was devised and put into production. These samples utilised correlated alignment, whilst using EBL to generate cylinders and triangles onto a Si substrate. The alignment technique makes use of the fact that the alignment of the EBPG is never perfect, nor repeatable (as no marker is the exact same), so if the patterns are arrayed out like a vernier, one can compensate for the variable alignment. The generated substrate has some features with less than 3nm separation between them, which would mean a large electric field can be generated between the pairs and would be a fantastic sample for TERS. However, it becomes more challenging to distinguish features below this distance, as it is near the resolution limit of a SEM. STEM could be a viable option in examining features below this separation distance, however this would require a much smaller sample size (about $5mm^2$, which is also thin (<50nm), which then becomes an issue of it not being good enough for TERS due to potential damage from the tip and the required manual handling of the sample.

As there were no Raman Active molecules available at the NPL, nor a standardised or microfabricated TERS tip, these samples could not be tested. For future work, actually coating these samples with a Raman active solution would be imperative to be useful as a TERS substrate. The separation gap could be plotted against enhanced Raman in an experiment, which could then be used as a calibration for future TERS probes. This sample could also not be used in Glasgow as it was Si based and the setup uses bottom illumination, meaning the light doesn't sufficiently propagate through the back of the sample to the gold top surface. To compensate for larger variances the sample had $\pm$ 45nm variation in prescribed positioning, this could be reduced to $\pm$ 20nm as the variation was within 20nm, meaning that less surface area would be wasted. Due to the large surface

area it also made it very difficult to spot where the smaller separation dimers were. To enhance the viability of making this sample standardised, the ± 20nm prescribed separation plus a SEM investigation would be required. The analysis would reveal the positioning of the smaller separated features, they would then be noted and then using e-beam, a box/arrow or any identification feature could be written onto the sample to highlight this region. This would make it much easier to locate before performing any separation/enhancement plots.

6.3 Wafer Fabrication

The main goal of this project was to batch fabricate TERS probes, whilst using EBL to define the sensor and control the differing dimensions. This has been achieved. By microscope inspection all of the tips survived the wet etch, along with the probe chip, meaning a high reliability process of fabricating probes was developed. Although the process was built off of an existing process, issues such as the large reflow of the resist, and the "mow the grass" stage causing the tips to perforate the coated resist were combatted to make the process even more robust. It still remains to be seen if float coated resist is as reliable as resist coating a wafer should be, however work is underway by others to remove this technique and replace it with a more conventional alternative.

6.4 TERS

6.4.1 Silicon Dioxide Probes

If utilising a thermal oxidation growth of silicon dioxide, it is imperative that the thickness of oxide will allow for constructive interference and the angles still allow for SPR. In order to determine the interference mode the refractive index of the material must be known. The refractive index of silicon dioxide is 1.457 [317] for a 633nm laser, as it is oxide we can assume this is reproducible (unlike nitride where the stoichiometry is defined by the growth conditions). Using the equations defined in section 3.2.1, the critical angle for oxide and angle of incidence for SPR match can be calculated.

$$\theta_{(Crit)} = sin^{-1}(\frac{1}{n_{oxide}}) = 43.34^{\circ} \tag{6.1}$$

$$\theta_{inc} = sin^{-1}(\frac{\lambda_{oxide}}{\frac{2\pi}{\beta}}) = 45.79^{\circ} \tag{6.2}$$

The thickness of the oxide has to be expressed in terms of angular tolerance for the plasmon. Using data given by Daniyal et. al. [318], which shows plasmon admittance at a 2° range for a 50nm gold film excited by a 633nm laser, the phase of the guided modes can be calculated. The first step of this is to get the average thickness of oxide across the wafer, to do this, the data from the nitride deposition at Chalmers was used to give an idea of uniformity. This data is expressed in Table 6.1.

Measured thickness (nm)	Average Thickness (nm)
337.6	-
331.7	334.65
325.8	328.75
320	322.9
314.1	317.05
308.2	311.15
302.3	305.25

TABLE 6.1: Table of measured silicon nitride thickness values and average values.

As stated earlier, there is a range of admittance which means that for every average thickness, there is a max, min and average value of this angle. These angles are tabulated below:

Angle Min (°) / Rad	Angle Average (°) / Rad	Angle Max (°) / Rad
44.79 / 0.78	45.79 / 0.80	46.79 / 0.81

TABLE 6.2: Table of plasmon admittance angles with values of $\theta_{inc} \pm 1^{\circ}$

For ease whilst using the formula to determine the phase of the guided modes, the sec of the angles $(\frac{1}{\cos\theta_{inc}})$ are then tabulated:

sec Angle Min (Rad)	sec Angle Average (Rad)	sec Angle Max (Rad)
1.41	1.43	1.46

TABLE 6.3: Table of $sec\theta_{inc}$ values of the thickness value limits.

The path length and phase of the oxide values can then be calculated using the following relation:

$$OPL = 2 * n * d * sec(\theta_{inc}) \tag{6.3}$$

Using this data, the excitation wavelength needed at the required thickness for a path difference of 2 wavelengths between the interfering waves (N=2) can be calculated. The relation for doing so is as follows:

$$\lambda_{inc} = \frac{OPL}{N} \tag{6.4}$$

The results of using these relations at the various thickness is tabulated below:

Average Thickness (nm)	OPL min (nm)	OPL ave (nm)	OPL max (nm)
334.65	1373.96	1398.40	1424.16
328.75	1349.74	1373.75	1399.05
322.9	1325.72	1349.30	1374.16
317.05	1301.70	1324.85	1349.26
311.15	1277.48	1300.20	1324.15
305.25	1253.26	1275.55	1299.05

TABLE 6.4: Table of path length with the corresponding average thickness values.

This data can then be used to calculate the corresponding wavelength which will give constructive interference (N=2), within the acceptance angle range of SPR ($\theta_{inc} \pm 1^{\circ}$), for the thickness variations across a wafer.

Average Thickness (nm)	λ_{min} (nm)	λ_{ave} (nm)	λ_{max} (nm)
334.65	686.98	699.20	712.08
328.75	674.87	686.87	699.53
322.9	662.86	674.65	687.08
317.05	650.85	662.43	674.63
311.15	638.74	650.10	662.07
305.25	626.63	637.77	649.52

TABLE 6.5: Table of incident wavelength required for light to guide within the oxide with it's corresponding average thickness values.

As can be seen from Table 6.5, even with oxide, at these thicknesses we do not attain constructive interference anywhere across a wafer. This means that a change to the thickness is needed to achieve it. If a uniform dry etch is performed, or the growth is reduced by 20nm and the uniformity is kept the same, the same calculations can be performed until a match is found. This is shown in Table 6.6.

Average Thickness (nm)	λ_{min} (nm)	λ_{ave} (nm)	λ_{max} (nm)
314.65	645.93	657.41	669.52
308.75	633.81	645.09	656.97
302.9	621.80	632.86	644.52
297.05	609.80	620.64	632.07
291.15	597.68	608.31	619.52
285.25	585.57	595.99	606.97

TABLE 6.6: Table of incident wavelength required for light to guide within the oxide with it's corresponding average thickness values after a perfectly uniform 20nm etch.

Examining Table 6.6, it can be seen that we are at exactly the red laser wavelength (632.8nm) for 302.9nm. No other values are within the range, so it is assumed that the thickness variation to excite at 633nm with constructive interference is less than the difference between the nearest average thickness values (308.75 - 302.9 = 5.85nm). Now if the plasmon admittance is decreased to $\pm 0.5^{\circ}$ and say the tolerance between thickness values is 2nm with a 10nm range, the following values are found:

Average Thickness (nm)	λ_{min} (nm)	λ_{ave} (nm)	λ_{max} (nm)
298.9	618.98	624.51	630.18
300.9	623.12	628.68	634.40
302.9	627.26	632.86	638.62
304.9	631.40	637.04	642.83
306.9	635.54	641.22	647.05
308.9	639.69	645.40	651.27

TABLE 6.7: Table of incident wavelength required for light to guide within the oxide, where the angle of a SPR match tolerance is 45.79 $\pm 0.5^{\circ}$.

Looking at Table 6.7, a 302.9nm thickness of silicon dioxide is perfect as the average wavelength is 632.8nm. The thickness of 300.9nm still works with a HeNe as it is at the maximum end but could be even slightly thinner.The 304.9nm thickness also works as the minimum wavelength is just a bit less than 632.8. This gives an average range of 4nm thickness tolerance to a 45.79 $\pm 0.5^{\circ}$ plasmon admittance, which means the thickness of the oxide has to be uniform to 1.64 % whilst the average stays as 302.9nm.

Now to calculate the excitation angle from air into the silicon dioxide so that a 45.79 $\pm 0.5^{\circ}$ plasmon admittance can be achieved.

This means that for a 302.9nm thickness silicon dioxide probe wafer, with 1.64 % uniformity, can produce a plasmon at the tip apex, when the plasmon admittance is 45.79

Grating Period (nm)	$\sin(\theta_{int})$	θ_{ext} (deg)	Angle to Vertical Z-axis
250	-1.02	-	-
350	-0.52	-49.79	106.30
450	-0.25	-21.22	77.73
550	-0.07	-6.1	62.61
650	0.05	4.06	52.45

TABLE 6.8: Table of the Coupling Angles with respect to period for a silicon dioxide TERS probe with m=1

Grating Period (nm)	$\sin(\theta_{int})$	θ_{ext} (deg)	Angle to Vertical Z-axis
250	1.02	-	-
350	0.52	49.79	6.72
450	0.25	21.22	35.29
550	0.07	6.1	50.41
650	-0.05	-4.06	60.57

TABLE 6.9: Table of the Coupling Angles with respect to period for a silicon dioxide TERS probe with m=-1

$\pm 0.5^{\circ}$, when excited at the angles given in Table 6.8 and 6.9 under the "Angle to Vertical Z-axis" column.

The same can be done for a thicker deposition for oxide, where 132nm more oxide is grown on the wafer. For a 3rd order mode, plasmon admittance of 45.79 $\pm 0.5^{\circ}$ and 2nm tolerance, the wavelength that will allow constructive interference with respect to thickness is calculated:

Average Thickness (nm)	λ_{min} (nm)	λ_{ave} (nm)	λ_{max} (nm)
450.9	622.50	628.06	633.76
452.9	625.26	630.84	636.58
454.9	628.02	633.63	639.39
456.9	630.78	636.42	642.20
458.9	633.54	639.20	645.01
460.9	636.30	641.99	647.82

TABLE 6.10: Table of incident wavelength required for light to guide within oxide, where the angle of a SPR match tolerance is 45.79 $\pm 0.5^{\circ}$.

From Table 6.10, it can be seen that for a thicker oxide and a higher mode there is a larger increase in the thickness values which match the wavelength with constructive interference. The 450.9nm thickness has a maximum wavelength value of 633.76nm, and

it also matches 456.9nm within the thinner end of the specification. This gives a thickness range of 6nm, so a thicker oxide will also increase the chances of phase matching even if there is a slightly lower uniformity (more tolerance).

6.4.2 Silicon Nitride Probes

After discovery that the silicon nitride TERS probes would have destructive interference, some calculations can be done to determine the thickness the silicon nitride has to be to have constructive interference. This is a least cost method, whereby probes that are on the wafer this now can still be utilised.

Using the data given by the Chalmers on the deposition of the current nitride, average thickness values are taken. These values are displayed in Table 6.1 in the previous section. If the incident angle for plasmons is 27.4°, with a tolerance of $\pm 1^{\circ}$, then the wavelength range for the thickness variation of the nitride to allow for constructive interference are shown in Table 6.11.

Average Thickness (nm)	λ_{min} (nm)	λ_{ave} (nm)	λ_{max} (nm)
334.65	562.56	567.57	572.84
328.75	552.64	557.56	562.74
322.9	542.81	547.64	552.72
317.05	532.98	537.72	542.71
311.15	523.06	527.71	532.61
305.25	513.14	517.70	522.51

TABLE 6.11: Table of incident wavelength required for light to guide within the current nitride probes, where the angle of a SPR match tolerance is 45.79 $\pm 0.5^{\circ}$.

The average wavelengths vary from 568 to 517nm across the wafer. If the 322.9nm thickness is examined, it means for the full range of wavelengths for exciting a plasmon, at one thickness slot it will fail for the next thickness slot. This data however does provide an interesting point, if the thickness of nitride on a probe was between 311.15-317.05nm, then it could potentially be excited by a green laser (532nm at the NPL). This could explain why there was a sign of fluorescence on the StHM probe when tested in the NPL setup, the thickness matched the wavelength for constructive interference. It was capable of exciting a plasmon in Pd, which means the enhancement of gold should be greater as it has a lower damping of plasmons, just there was no phase match.

Etching and using a lower order mode (2) can cause the scatter to get worse, however a match at 633nm can be achieved. The results of the calculations where a uniform 74nm etch was carried out and the SPR match tolerance is still 45.79 $\pm 0.5^{\circ}$ are calculated in Table 6.12.

Average Thickness (nm)	λ_{min} (nm)	λ_{ave} (nm)	λ_{max} (nm)
260.65	657.25	663.09	669.25
254.75	642.37	648.08	654.10
248.9	627.61	633.20	639.08
243.05	612.87	618.32	624.06
237.15	597.99	603.31	608.91
231.25	583.11	5588.30	593.76

TABLE 6.12: Table of incident wavelength required for light to guide within the current nitride probes after a 74nm uniform etch, where the angle of a SPR match tolerance is $27.4 \pm 0.5^{\circ}$.

By reducing the thickness we get mode matching at one thickness (248.9nm) but not at any of the others. The etching is really critical in being able to get constructive interference. Comparing this with oxide, because it has a lower refractive index, the oxide has more room for a thickness variation (6nm). It is important to note that the phase shift upon reflections was neglected in the calculations for both oxide and nitride, hence the values for thickness are not the exact ones to be used in a device. However, the calculations are used to determine how practical the fabrication of the TERS probes would be by giving the correct constraints on the variation of film thickness.

6.5 Implementation

As stated earlier, the nitride can be dry etched to remove material. The silicon dioxide would have to be grown by thermal oxidation techniques. Data available from the wet oxidation furnace at the JWNC in Figure 6.1 shown below:

Thermal oxidation seems the better choice for the probes in the future, especially since the control over thickness and uniformity is much better. With a very thick layer the dielectric will become largely multimode, then it may not matter about the uniformity as there will always be a matched mode. If the decided route was to use a wet oxidation technique and 4.88μm is the desired thickness, then the data from the JWNC suggests it can generate thicknesses of around 4.8μm with 0.95% uniformity, which is a lot better

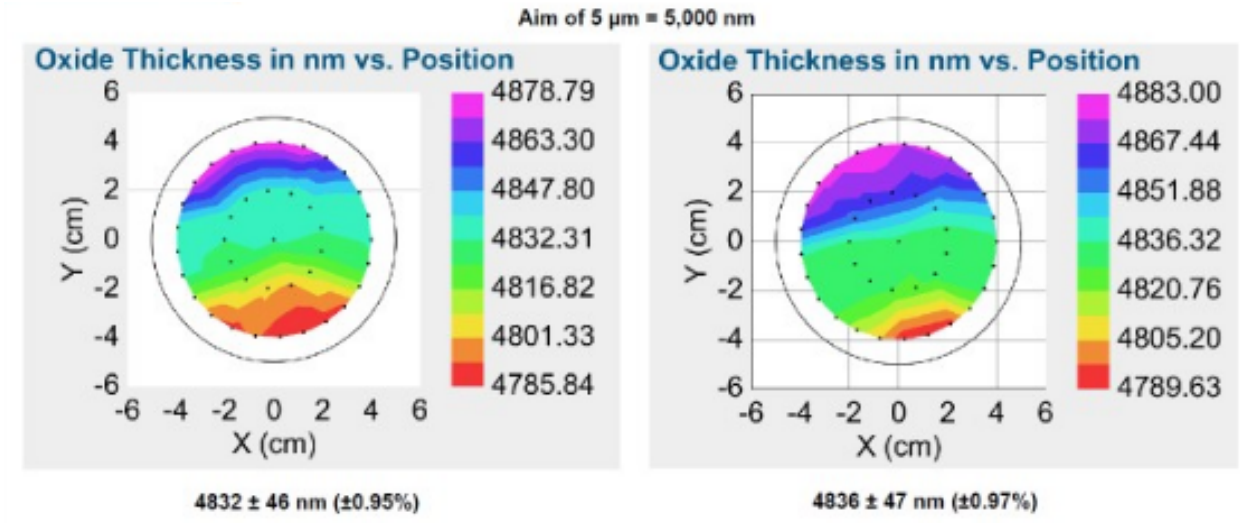

FIGURE 6.1: Results of wet oxidation growth of silicon dioxide with a target growth of 5μm. The image comes from an email conversation with D.Paul and J.Weaver[319].

than the current PECVD process. The number of guided modes can be calculated using the following relations:

$$V = \frac{2\pi d}{\lambda}\sqrt{n_1^2 - n_2^2} = 14.33 \tag{6.5}$$

Where the cladding is air $n_1 = 1$, λ is 633nm, d is the dielectric thickness and the refractive index of oxide $n_2 = 1.45$. The maximum number of modes that can propagate in a slab waveguide is calculated with the V number, the modes which will propagate within a symmetric slab waveguide can be determined with the following:

$$m < \frac{14.33}{\pi} + 1 = 5.56 \tag{6.6}$$

Which means there are 5 guided mode orders at 633nm, the fundamental m=0 and m=1,2,3 and 4. Each mode order has a TE and TM mode, but only TM couples to plasmons, so there are 5 available modes.

Dry oxidation is another method of oxide growth, this is usually much more reliable but very slow. The results from the JWNC dry oxidation growth of dioxide is depicted in the Figure 6.2 and 6.3 below:

The results from a dry oxidation run indicate that the thickness uniformity is much lower than the current silicon nitride LPCVD growth and the proposed wet oxidation

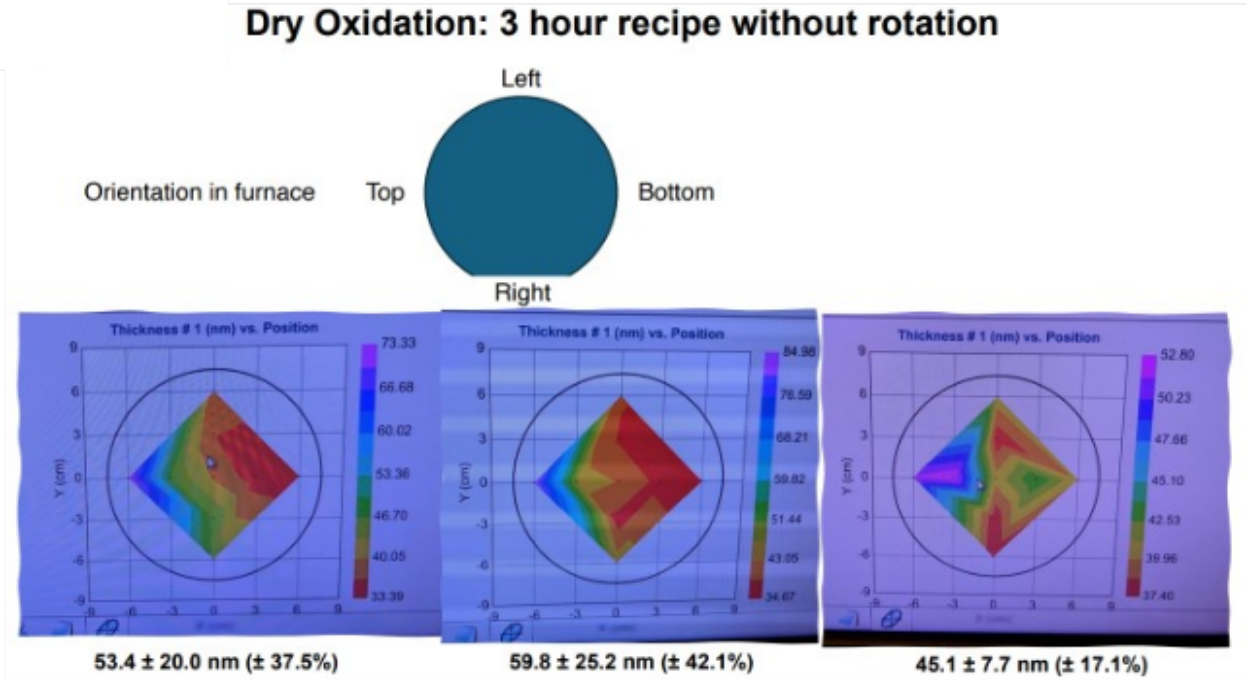

FIGURE 6.2: Results of dry oxidation growth of silicon dioxide within the JWNC. The image comes from an email conversation with D.Paul and J.Weaver[319].

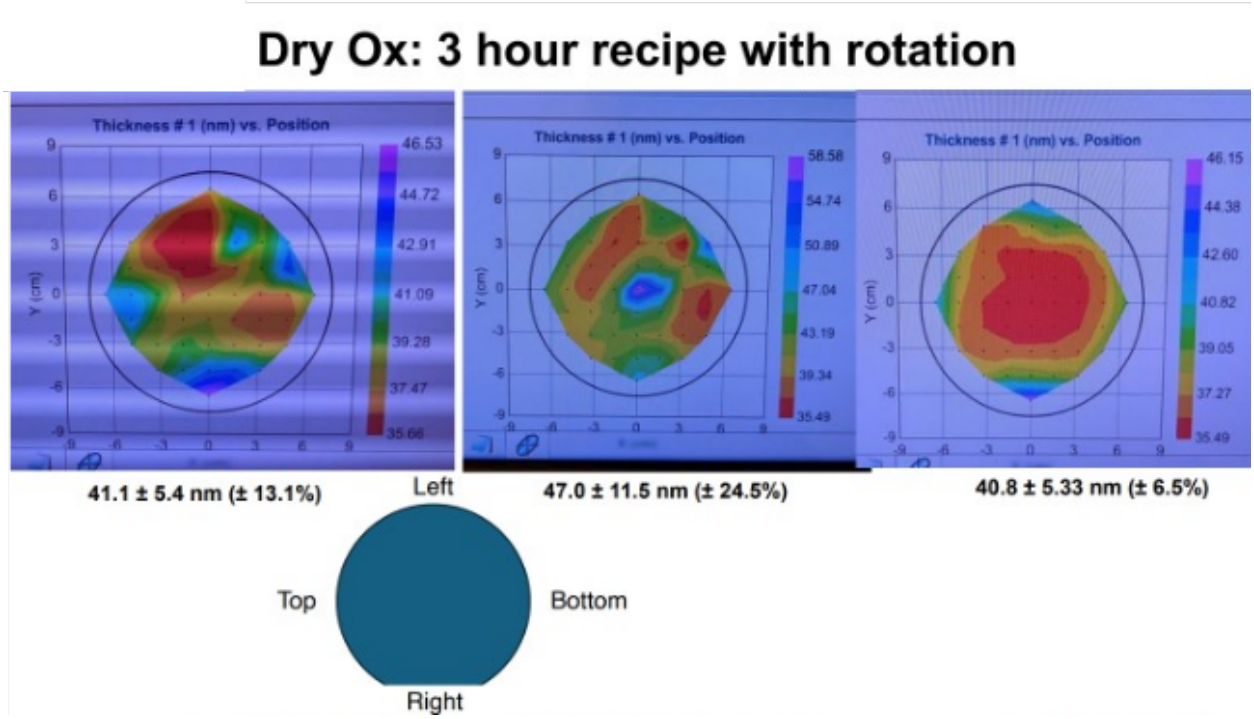

FIGURE 6.3: Results of dry oxidation growth of silicon dioxide within the JWNC. The image comes from an email conversation with D.Paul and J.Weaver[319].

growth. The minimum thickness variation of this process is 6.5%, however it is optimised for 5nm thick oxide and not larger growths and not used very often. The wet oxidation process is more heavily used for thicker layers and more than likely has less contamination.

Reproducibility of the oxide growth (wet) will have to be investigated. Thermal gradients within the tube can also cause the thicknesses to be non-uniform [320], so placement (horizontal or vertical) of wafers will have to be investigated so that a conformal growth can be achieved. As discussed earlier we can oxide within a 5.85nm range of 302.9nm, however measuring this would be a challenge, especially as the oxide will be on a pyramid slope. One possible way of measuring at the end would be to take a side profile SEM image of the probes after release etch. Assuming the calibration of the scale is exact on the system, an evaluation of the nitride thickness can be determined, whereby the Helix detector could be used to reduce charging.

Another method would be to have pyramidal witness wafers (during the first deposition), these would have in-house grown PECVD nitride and oxide to start (reduction of cost compared to external deposition), go through the same process with the same spec limits and have oxide deposited at the same time as the other wafers. These are essentially sacrificial, so they could be scribed and cleaved to reveal a side profile of oxide on pyramid. However the oxide could delaminate due to cleave damage. The same would have to be done for a trim etch, so this would bring the total to 2 wafers. One for initial measurements, second after trim etch.

Ellipsometry spectroscopy is another technique which could be used to measure the dielectric on the pyramid, appropriate optical models would have to be employed to account for the slope on the pyramid[321]. However trial and error on film thickness measurements would have to be employed so that the model would be suitable for live wafers i.e. ensure it is accurate.

AFM could also be used as a measurement tool. After the cantilever dry etch and chrome etch, the step height of the tip apex onto the pyramid could be measured to give an estimate of film thickness around the probe. A trim etch could be employed after this stage.

TMAH does also etch silicon dioxide, it is found that a wet growth of oxide etches faster than dry and the etch rate is higher for lower concentrations[322]. The exact etch rate of the TMAH and IPA solution at 80° would have to be evaluated on test material so this could be accounted for in the growth.

Fabricating a slit coupler or a grating would be more reliable as the fabrication would start to rely on lithographic definition as opposed to growth and etching of dielectric layers. As the growth starts to get large to make the probes multimodal, the topographic spatial resolution of the tip could achieve would decrease (have more material). But as stated earlier, the range of a SPP in gold is limited (20μm in gold at 633nm [315]), so it then becomes optically harder to discriminate between pump light and scattered light and gives a smaller target for the laser to illuminate.

A Appendix

A.1 Previous probes

A.1.1 Introduction

Although this body of work is based on TERS. The first half of the project considered SECM probe fabrication as the main process to improve on, and improving on the functionalised probe process[323]. The issue with SECM was mainly pinholes in the dielectric, this provides an area for the analyte to seep in and attach to the gold, which is not necessarily at the apex of the probe. A lot of work was done on finding a suitable replacement of the dielectric. This work is detailed below.

A.1.2 Scanning Electrochemical Microscopy

Scanning electrochemical microscopy (SECM) is an electroanalytical scanning probe technique used to measure the electrochemical behaviour of liquid/liquid[142], liquid/gas and liquid/solid interfaces. When the sensor is combined with AFM, simultaneous imaging of a substrate's topography and surface reactivity can be mapped. During an SECM scan, current flows through an ultramicroelectrode (UME) fabricated onto the probe's apex. The UME is fabricated to a nm or μm scale and in various geometries such as a disk, ring or sphere. The probe's tip is placed in close proximity to a conductive, semiconductive or insulating substrate which is immersed in a solution. The tip and substrate are part of a four-electrode electrochemical cell, with a bipotentiostat to control the potential and current at both the tip and the substrate. Spatially resolved electrochemical signals are retrieved by measuring the current at the SECM probe's tip, resolved as a function of tip position. The SECM signal is analysed based on diffusion-limited current phenomena[143]. After the scan, the information is compiled to make images of surface reactivity, chemical kinetics and topography. A schematic diagram of a SECM system is shown in Figure A.1.

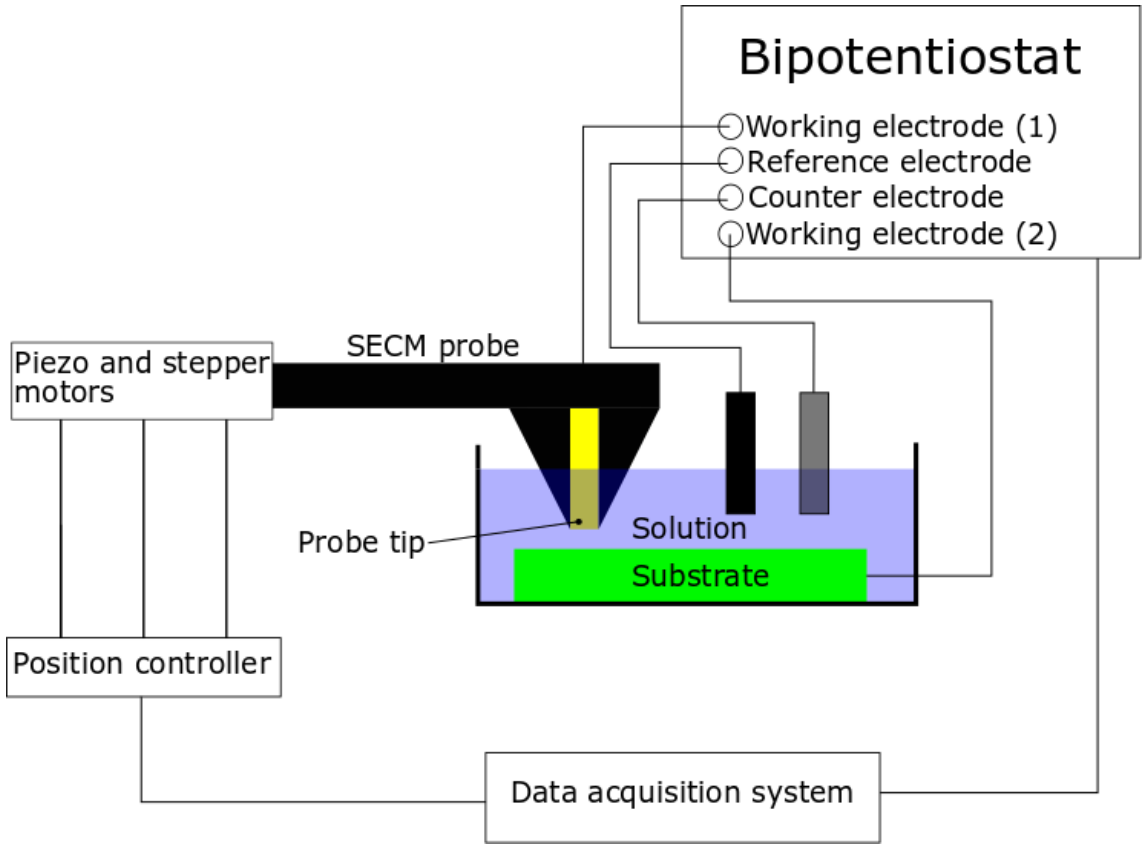

FIGURE A.1: Schematic diagram of an SECM system.

Since the introduction of SECM, a large amount of research has been undertaken into improving the modes of operation for the system, especially for nm scale measurements. The four main modes that are used and developed for different applications include feedback, generation/collection (G/C), shielding and potentiometric.

In potentiometric mode, the potential of the probe must be calculated at an open circuit. The tip behaves as a passive probe, whereby the activity of the reactant species is reflected on its potential. The probe is unable to produce or generate species and as such, is limited with its chemical detection range. One such method is to coat the tip with a PH sensitive layer. Within a potentiometric mode experiment, the PH of the layer changes to suggest a reaction is taking place. The system allows for either the current or potential to be measured as a function of position[324].

Feedback mode is the most frequently seen, whereby the tip current is the only thing monitored. Feedback mode was first demonstrated in 1989 primarily by Bard and Kwak's work[325], [326]. In a bulk solution, the oxidised species is reduced at the tip to generate a steady-state current. When the tip is in close proximity to a conductive substrate, immersed in solution, the reduced species then oxidises onto the conductor's surface. This

regenerative cycle produces an increase in the tip's current and is known as positive feedback. An image of this regenerative cycle is shown in Figure A.2. In contrast, when an insulator is examined, the oxidised species cannot regenerate and diffusion at the electrode is blocked. This cycle causes a reduction of the tip current and is known as negative feedback. Feedback mode has also been used to map topography and electrochemical activity within porous membranes[327]. The tip is in contact with the membrane, with no amperometric signal until it enters the solution filled pore. Upon entering the pore a signal is seen due to the diffusion-controlled oxidation of the solution, displacing the solution and extending the region of electrochemical activity. Feedback mode has also been successfully used to study heterogeneous catalysis[327].

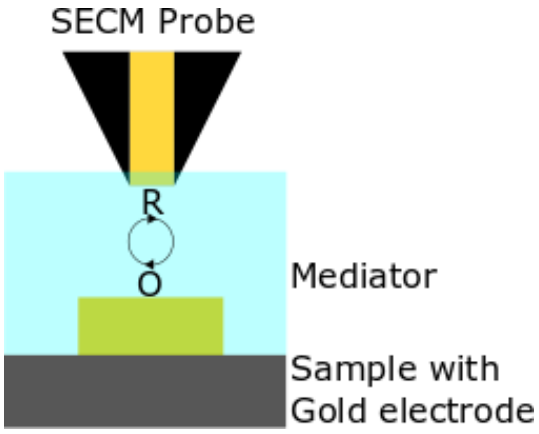

FIGURE A.2: A schematic diagram of a redox cycle within an SECM experiment.

If the species can't be easily generated at the tip and the product can't be easily monitored, the shielding method is used. The same reaction occurs at the tip and the substrate, so the tip current is decreased i.e. the tip becomes shielded and competes with the substrate for the same reactant. This phenomena is called hindered diffusion. The reactant is studied by how well the substrate competes with the tip for consumption[328]. Hindered diffusion can also be used to map topography in this mode

In generation/collection (G/C) mode both the tip and substrates current is monitored, with either one being a generator or collector. In tip generation/substrate collection (TG/SC) mode, the tip is used to generate a reactant that is detected at a substrate electrode. The potential is held at the tip whereby the reaction occurs, the substrate will be held at a different potential where the product of the tip's reaction will react and be "collected". This mode is commonly used in determining homogenous chemical reaction rates[329]. The opposite mode, where the tip is the collector (SG/TC), is commonly seen in studies of reactions at a samples surface[329].

In SECM experiments the probe is out of contact, relieving the constraints for it to be as hard as commercial AFM probes. Its resonant properties are also unimportant as it will not operate in tapping mode and in solution. The attention then turns to the electrical performance, complete insulation coverage and most importantly, the sensor geometry.

A.1.3 Insulators

One of the most important aspects of an SECM probe is its insulator. The insulator coats the working electrode to limit the area of a redox reaction. This allows for the acquisition of a potential without galvanic contact to the body of the remaining electrode, improving electrode life and defining the spatial resolution of the microscope. As the insulator is such a key component to the system, care must be taken to ensure complete coverage of the probe (except the very tip and bond pads) with no pinholes. Pinholes are topographic defects within the insulator which allow electrochemical reactions to occur at this region, which is remote from the tip, therefore producing inaccurate results.An example of a pinhole formation is shown in Figure A.3. In this figure, the insulator can't fully cover a particle on top of a substrate and a void is left in-between the substrate and deposited material. As there isn't complete coverage and a gap is left, the pinhole forms a parasitic electrode at some distance from the tip.

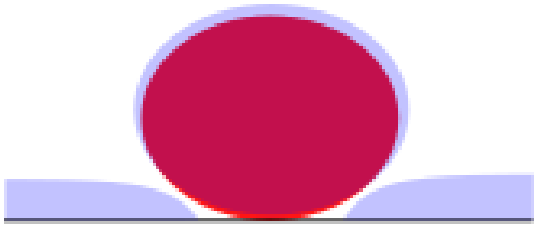

FIGURE A.3: Schematic diagram showing the formation of a pinhole. The particle is shown in red and insulator shown in blue. A void between the particle and deposited insulator is illustrated, this is known as a pinhole.

As discussed earlier, the fabrication methods to produce SPM probes are well established; however, the probes are not normally coated with an insulator. Experimental results and literature concerning the poor adhesion of an insulator onto metal shows this to be a major hurdle, with the formation of pinholes also playing its part[330]. As the probes go through over 30 fabrication stages until insulator deposition and the number of wafers are limited, it is too costly to test insulator adhesion at the final steps. As a result, these tests on small samples are described in the next section, where the cluster ICP-CVD deposition of silicon nitride proved to be the best at adhering to metal.

A.2 Planar Probe

A.2.1 Processing

As the insulation tests were conducted on geometric shapes similar to that of a probe, and the micromachined wafers are too valuable for testing on, it was proposed that small samples undergo the same fabrication stages, without the pyramids. These fabrication stages will also provide a means of getting used to the processing required before upscaling.

As the global and cell markers are fabricated in the early stages of the micromachined wafers, i.e. before the external LPCVD silicon nitride deposition, new markers would have to be made for the planar test samples. The markers consisted of nine 750μm crosses and seventy-two 30μm^2 boxes made from 5nm titanium (Ti) and 70nm of gold (Au).Titanium was chosen as the adhesive layer as there is a chrome etch later on in the process, which would etch away the NiCr. Gold is chosen as the top layer for it's high atomic number, useful for marker contrast in backscattered electron detection. The markers were placed outside the probe's chip to avoid interference with the pattern and unintentional marker search exposure. The planar probe processing is intended, as far as possible, to follow the process steps on the micromachined wafers.

A.2.2 Fabrication

In order to fabricate the test samples, a 400μm SSP silicon wafer with 300nm of silicon nitride was cleaved into 20x20mm pieces using a diamond scribe. These samples were the foundation for the subsequent dose tests and final lithographic stages. Each sample was solvent cleaned for five minutes each using acetone, methanol, IPA and RO water consecutively.

From previous insulation tests[331] it was found that a NiCr-Au/Pt stack with ICP-CVD silicon nitride, from the ICP380 tool within the JWNC, yielded the most promising results. Henceforth, these were put into action during the planar probe tests.

Due to the triangular geometry of the cantilever, it is hard to modify sensor geometry from previously made probes by Dobson et. al.[332]. The reason for this difficulty is the cantilever tapers to a point, making the final exposed area triangular in shape (see FigureA.4). Within Dobson's work, the success rate of fabrication for the probes is around 80% and produced stable topographical and electrochemical images. Although the success rate is high and the probes are batch fabricated, the insulator-metal adhesion problem

was not tackled in this work and poses a problem for wafer reproducibility. In addition to the poor adhesion, the method used to connect the probe to the system used various layer of conductive paint and nail varnish, a limited exploitation of the technology. Tackling this, the sensor's metal, dielectric material and thickness are available to modify to increase the success rate, without making changes to the cantilever shape.

From previous work on the insulator release tests, it was found that platinum produced better adhesion to the subsequent insulation layer and was therefore used. Platinum and gold are excellent conductors when used as electrochemical electrodes, however, gold did not adhere well to the silicon nitride insulator.

For deposition of the insulator, the ICP380 tool was used. 80nm of silicon nitride was deposited on top of all the sample +/- 5nm. The problem with exposure during the next phase, where a gap is made in the insulator at the very tip and bond pads so current can flow, is that PMMA etches roughly 2.5 times faster than the silicon nitride. To overcome this, the resist layer is made as thick as possible, given the need for high resolution, but care taken to ensure the exposed regions are fully developed. The tip resistor and etched region jobs did however employ Elvacite. The last two lithography levels of the sensor design and electrochemical aperture in the insulator was float coated despite the fact that the test probes are planar. It was important to test the fabrication using the same resist stack as that used to fabricate the final devices, giving an idea on tip resolution and experience on the fabrication techniques. The process followed is shown in Table A.1.

An image of the sensor and probe body post lift-off is shown in Figure A.4.

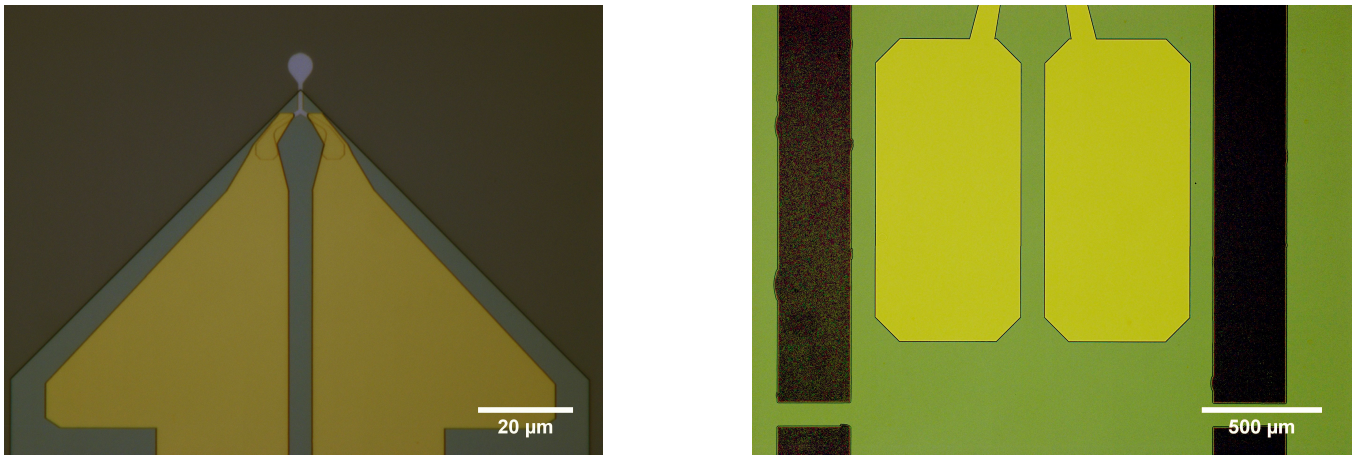

FIGURE A.4: The image on the left shows an image of the platinum tip with its gold connecting wires. The right hand image shows bond pads and start of the connecting wires for the probe.

As can be seen from Figure A.4, all areas for deposition were successfully fabricated with high resolution. The balloon shape at the end of the probe on the left hand image was intended to enhance the lift-off process as it hangs over an etched end. This does not pose a problem for experimentation as only the area exposed post deposition will be electrically active.

It should be noted that the bars surrounding the probe body were deliberate and due to photolithography and etching. These silicon-silicon nitride bars become very fragile during the release etch, and as such, make cleaving out the probe's from the wafer much easier.

A.2.3 Results and Discussion

The results of the dry etch are shown in the microscope image's in Figure A.6 below. It can be clearly seen in the image that an etch was successful with a visible cut but also a clean gold surface on the pads. For confirmation, a Dektak scan was undertaken whereby it confirmed a 80nm difference between the pads and the region surrounding. There are regions with a slightly larger difference, however this can be put down to contamination. For further confirmation of this value, an AFM scan could be undertaken. The results in Figure A.5 suggests that the insulator remained intact and the etchant did not get through the PMMA.

The most crucial part is that the insulator remained on the probe body post wet-etch, which it did. The next step for these tests was to fabricate the probes with the ICP 380 silicon nitride and NiCr-Au/Pt stack and to see if there was any improvement to the fabricated yield and to test their electrochemical response. The flat probes could also be tested to see if they are behaving as expected electrochemically, however the topographic spatial resolution is limited as they don't have protruding tips and they would have to be scribed and cleaved out of the substrate (to test them individually). This part of the project did not progress any further as the collaborators were more invested in the fabrication of TERS probes.

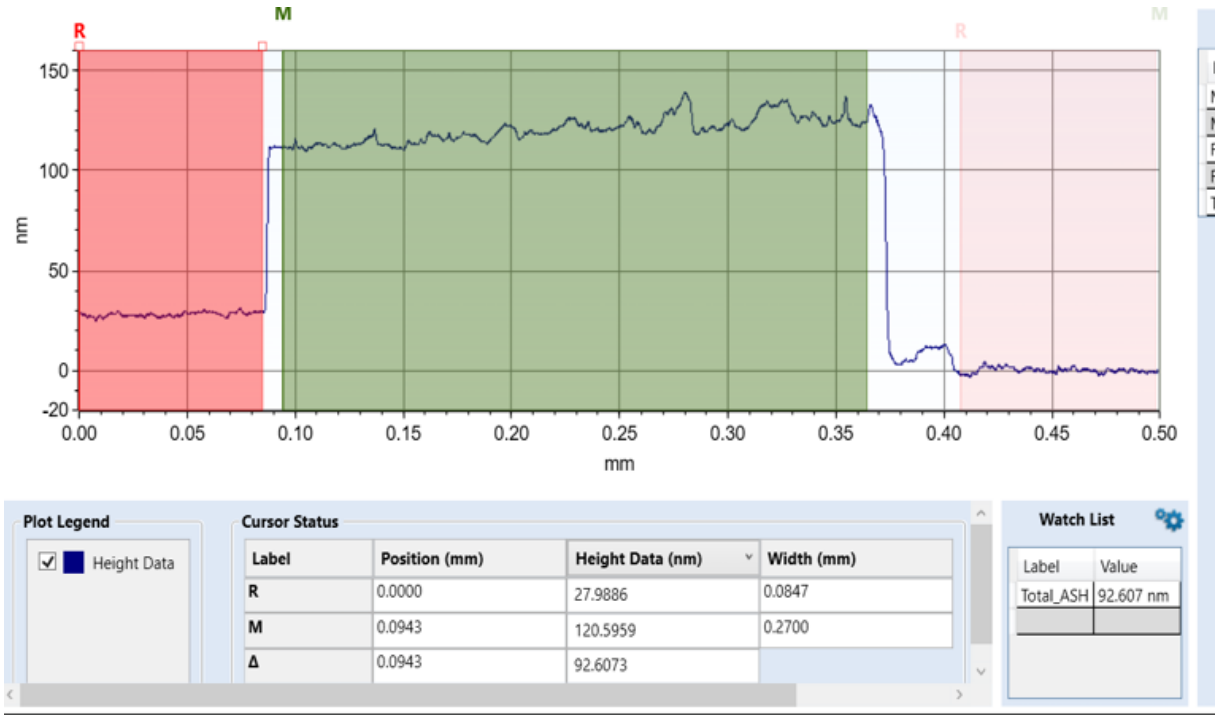

FIGURE A.5: A Dektak scan of the bond pads to connecting wires. It clearly shows that there is a difference in height between the etched pads and insulated wires.

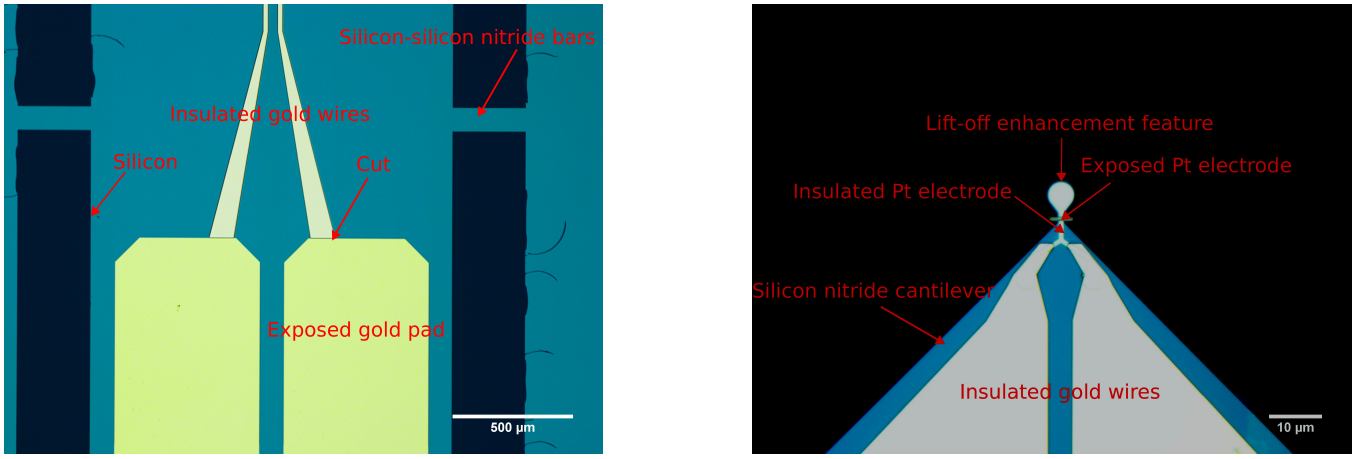

FIGURE A.6: The image on the left shows an image of the bond pads with connecting wires, the cut between them shows the nitride etch. The right hand image shows the probes cantilever and sensor post-dry etch.

Process flow for the sensor fabrication	
Step number	Stage details
1	A 400μm SSP previously processed silicon sample, with 300nm silicon nitride on top is cleaned with acetone, methanol,IPA (all within an ultrasonic bath) and an RO water rinse, respectively for 5 minutes each.
2	Sample is oxygen barrel ashed at 100W for 5 minutes.
3	8% 2010 PMMA with a molecular weight of 84kDa is spun at 2500rpm.
4	Sample is baked at 180°C for 15 minutes.
5	4% 2041 PMMA with a molecular weight of 410MDa is spun at 2500rpm for 30 seconds.
6	Sample is baked at 180°C for 15 minutes.
7	1.5% 2041 PMMA with a molecular weight of 410MDa is float coated onto the sample.
8	Sample is baked at 180°C for 15 minutes. Step 7 and 8 is repeated once more after this.
9	The sample is exposed with the VB6 to produce the designed sensor geometry.
10	Sample is developed in a 23°C 1:1 MIBK:IPA solution for 30 seconds before an IPA rinse and nitrogen gun dry.
11	The sample is then oxygen barrel ashed at 80W for 30 seconds.
12	The sample then has 8nm of NiCr and 40nm of Pt evaporated onto it, before being soaked in a 50°C acetone solution for 2 hours.
13	The remaining resist is then removed using fresh acetone, finishing off with an IPA rinse and nitrogen gun dry.
14	The sample is oxygen barrel ashed at 100W for 5 minutes.
15	The front face of the sample has 80nm of silicon nitride deposited on it with the ICP380.
16	Steps 1-6 are repeated.
17	1.5% 2041 PMMA with a molecular weight of 410MDa is float coated onto the sample.
18	Sample is baked at 180°C for 15 minutes. Step 14 and 15 is repeated two more times after this.
19	The sample is exposed with the VB6 to produce the designed tip etch and bond pad areas.
20	Sample is developed in a 23°C 1:1 MIBK:IPA solution for 30 seconds before an IPA rinse and nitrogen gun dry.
21	The sample is then oxygen barrel ashed at 80W for 30 seconds.
22	The sample is dry etched within the RIE 80+. The process required C2F6 as the etchant gas, flowing at 20sccm with a pressure of 23mT, with the tool operating at a power of 200W for 3.5 minutes at 22 °C.
23	The sample is then cleaned with acetone, methanol,IPA (all within an ultrasonic bath) and an RO water rinse, respectively for 5 minutes each.
24	The sample is then oxygen barrel ashed for 10 minutes at 150W.
25	The sample is then wet etched in a 80°C solution comprising of 1.4L of TMAH and 350mL of IPA for 2.5 hours. The sample is then neutralised in RO water before being dried from methanol with a nitrogen gun.
26	The sample is then cleaved into individual probes.

TABLE A.1: Table detailing the process flow for the fabrication of the sensors on the planar probe.

B Appendix

B.1 Raman Cosmic Ray Detection and Spectra Processing Script

```
import pandas as pd
import numpy as np
from scipy.signal import find_peaks
import matplotlib.pyplot as plt

# File paths and acquisition times
ters_path = " #insertname.txt"
sers_path = " #insertname.txt"
acq_time_ters = 100
acq_time_sers = 100

import ramanspy as rp

def load_and_process(path, acq_time):
df = pd.read_csv(path, delimiter=";", skiprows=3, header=None)
x = df.iloc[:, 0].values
y = df.iloc[:, 1].values
y_counts_sec = y / acq_time
spectrum = rp.Spectrum(y_counts_sec, x)
pipeline = rp.preprocessing.Pipeline([
rp.preprocessing.misc.Cropper(region=(120, None)),
rp.preprocessing.despike.WhitakerHayes(),
rp.preprocessing.baseline.ASPLS(),
])
```

```
return pipeline.apply(spectrum)

# Process both spectra
processed_ters = load_and_process(ters_path, acq_time_ters)
processed_sers = load_and_process(sers_path, acq_time_sers)

# Extract data for plotting and peak finding
ters_x, ters_y = processed_ters.spectral_axis, processed_ters.spectral_data
sers_x, sers_y = processed_sers.spectral_axis, processed_sers.spectral_data

# Find peaks
ters_peaks, _ = find_peaks(ters_y, height=0.2, prominence=0.5, distance=10)
sers_peaks, _ = find_peaks(sers_y, height=0.2, prominence=0.5, distance=10)

# --- Plot as a single y-axis ---
fig, ax = plt.subplots(figsize=(12, 6))

# Plot both spectra
ax.plot(sers_x, sers_y, label=" #insertname", color='orange')
ax.plot(ters_x, ters_y, label=" #insertname", color='blue')

ax.set_ylim(-0.25, 3.5)
ax.set_ylabel("TERS Intensity (counts/sec)")
ax.set_xlabel("Raman shift (cm$^{-1}$)")
ax.set_title("TERS Spectra #insertname")

# Peak annotation parameters
line_height_sers = (max(sers_y) - min(sers_y)) * 0.03
line_height_ters = (max(ters_y) - min(ters_y)) * 0.05
tolerance = 3
# SERS annotation: 1589 horizontal, others up/left
for i, peak in enumerate(sers_peaks):
x_peak = sers_x[peak]
y_peak = sers_y[peak]

# Special case: 1589 horizontal annotation
if abs(x_peak - 1589) <= tolerance:
```

```
ax.annotate(
f"{x_peak:.0f}",
xy=(x_peak, y_peak),
xytext=(x_peak + 40, y_peak),
textcoords='data',
arrowprops=dict(arrowstyle="->", color='orange', lw=1),
ha='left', va='center', color='orange', fontsize=8,
rotation=0
)
continue

# Special case: 1627 (text to right)
    if abs(x_peak - 1627) <= tolerance:
ax.annotate(
f"{x_peak:.0f}",
xy=(x_peak, y_peak),
xytext=(x_peak + 40, y_peak),
textcoords='data',
arrowprops=dict(arrowstyle="->", color='orange', lw=1),
ha='left', va='center', color='orange', fontsize=8,
rotation=0
)
continue

# Default annotation for other peaks: slightly up and left or right with offsets
y_offset = line_height_sers * (7 if i % 2 == 0 else 9)
ax.annotate(
f"{x_peak:.0f}",
xy=(x_peak, y_peak),
xytext=(x_peak - 30, y_peak + y_offset),
textcoords='data',
arrowprops=dict(arrowstyle="->", color='orange', lw=1),
ha='right',
va='bottom',
color='orange',
fontsize=8,
rotation=0
```

```
)

# TERS annotation: 1048 up, 1079/1280/1585 northwest, 1623 up/right, others up
for i, peak in enumerate(ters_peaks):
x_peak = ters_x[peak]
y_peak = ters_y[peak]
if abs(x_peak - 1048) <= tolerance:
ax.annotate(
f"{x_peak:.0f}",
xy=(x_peak, y_peak),
xytext=(x_peak, y_peak + line_height_ters * 2),
textcoords='data',
arrowprops=dict(arrowstyle="->", color='blue', lw=1),
ha='center', va='bottom', color='blue', fontsize=8,
rotation=0
)
continue
elif any(abs(x_peak - t) <= tolerance for t in [950, 1079, 1280, 1585]):
ax.annotate(
f"{x_peak:.0f}",
xy=(x_peak, y_peak),
xytext=(x_peak - 40, y_peak + line_height_ters * 1.5),
textcoords='data',
arrowprops=dict(arrowstyle="->", color='blue', lw=1),
ha='right', va='bottom', color='blue', fontsize=8,
rotation=0
        )
continue
elif any(abs(x_peak - t) <= tolerance for t in [1623]):
ax.annotate(
f"{x_peak:.0f}",
xy=(x_peak, y_peak),
xytext=(x_peak + 40, y_peak + line_height_ters * 1.5),
textcoords='data',
arrowprops=dict(arrowstyle="->", color='blue', lw=1),
ha='right', va='bottom', color='blue', fontsize=8,
rotation=0
```

```
)
continue
ax.annotate(
f"{x_peak:.0f}",
xy=(x_peak, y_peak),
xytext=(x_peak, y_peak + line_height_ters * 2),
textcoords='data',
arrowprops=dict(arrowstyle="->", color='blue', lw=1),
ha='center', va='bottom', color='blue', fontsize=8
)

ax.legend(loc='upper left')
plt.tight_layout()
plt.show()
```

Bibliography

[1] H. Gest, "The discovery of microorganisms by Robert Hooke and Antoni van Leeuwenhoek, Fellows of The Royal Society", *Notes and Records of the Royal Society of London*, vol. 58, no. 2, pp. 187–201, 2004, ISSN: 0035-9149. DOI: 10.1098/rsnr.2004.0055.

[2] G. A. Kausche, E. Pfankuch, and H. Ruska, "Die Sichtbarmachung von pflanzlichem Virus im Ubermikroskop", *Die Naturwissenschaften*, vol. 27, no. 18, pp. 292–299, 1939, ISSN: 0028-1042. DOI: 10.1007/BF01493353.

[3] C. S. Goldsmith and S. E. Miller, "Modern Uses of Electron Microscopy for Detection of Viruses", *Clinical Microbiology Reviews*, vol. 22, no. 4, pp. 552–563, 2009, ISSN: 0893-8512. DOI: 10.1128/CMR.00027-09.

[4] S. C. Gopinath, S. Ramanathan, M. N. Mohd Yasin, M. I. Shapiai Razak, Z. H. Ismail, S. Salleh, Z. Sauli, M. Malarvili, and S. Subramaniam, "Failure analysis on silicon semiconductor device materials: optical and high-resolution microscopic assessments", *Journal of Materials Research and Technology*, vol. 21, pp. 3451–3461, 2022, ISSN: 22387854. DOI: 10.1016/j.jmrt.2022.10.116.

[5] S. Dey and N. Mehta, "Automobile pollution control using catalysis", *Resources, Environment and Sustainability*, vol. 2, p. 100 006, 2020, ISSN: 26669161. DOI: 10.1016/j.resenv.2020.100006.

[6] F. Maurer, J. Jelic, J. Wang, A. Gänzler, P. Dolcet, C. Wöll, Y. Wang, F. Studt, M. Casapu, and J.-D. Grunwaldt, "Tracking the formation, fate and consequence for catalytic activity of Pt single sites on CeO2", *Nature Catalysis*, vol. 3, no. 10, pp. 824–833, 2020, ISSN: 2520-1158. DOI: 10.1038/s41929-020-00508-7.

[7] N. M. Bouvier and P. Palese, "The biology of influenza viruses", *Vaccine*, vol. 26, pp. D49–D53, 2008, ISSN: 0264410X. DOI: 10.1016/j.vaccine.2008.07.039.

[8] T. Nakane, A. Kotecha, A. Sente, G. McMullan, S. Masiulis, P. M. G. E. Brown, I. T. Grigoras, L. Malinauskaite, T. Malinauskas, J. Miehling, T. Uchański, L. Yu, D. Karia, E. V. Pechnikova, E. de Jong, J. Keizer, M. Bischoff, J. McCormack, P. Tiemeijer, S. W. Hardwick, D. Y. Chirgadze, G. Murshudov, A. R. Aricescu, and

S. H. W. Scheres, "Single-particle cryo-EM at atomic resolution", *Nature*, vol. 587, no. 7832, pp. 152–156, 2020, ISSN: 0028-0836. DOI: 10.1038/s41586-020-2829-0.

[9] M. Saur, M. J. Hartshorn, J. Dong, J. Reeks, G. Bunkoczi, H. Jhoti, and P. A. Williams, "Fragment-based drug discovery using cryo-EM", *Drug Discovery Today*, vol. 25, no. 3, pp. 485–490, 2020, ISSN: 13596446. DOI: 10.1016/j.drudis.2019.12.006.

[10] L. Maveyraud and L. Mourey, "Protein X-ray Crystallography and Drug Discovery.", *Molecules (Basel, Switzerland)*, vol. 25, no. 5, 2020, ISSN: 1420-3049. DOI: 10.3390/molecules25051030.

[11] A. McPherson and J. A. Gavira, "Introduction to protein crystallization", *Acta Crystallographica Section F Structural Biology Communications*, vol. 70, no. 1, pp. 2–20, 2014, ISSN: 2053-230X. DOI: 10.1107/S2053230X13033141.

[12] P. Roingeard, "Viral detection by electron microscopy: past, present and future", *Biology of the Cell*, vol. 100, no. 8, pp. 491–501, 2008, ISSN: 0248-4900. DOI: 10.1042/BC20070173.

[13] Y. Maeda, T. Shibahara, Y. Wada, K. Kadota, T. Kanno, I. Uchida, and S. Hatama, "An outbreak of teat papillomatosis in cattle caused by bovine papilloma virus (BPV) type 6 and unclassified BPVs", *Veterinary Microbiology*, vol. 121, no. 3-4, pp. 242–248, 2007, ISSN: 03781135. DOI: 10.1016/j.vetmic.2006.12.015.

[14] K. D. Reed, J. W. Melski, M. B. Graham, R. L. Regnery, M. J. Sotir, M. V. Wegner, J. J. Kazmierczak, E. J. Stratman, Y. Li, J. A. Fairley, G. R. Swain, V. A. Olson, E. K. Sargent, S. C. Kehl, M. A. Frace, R. Kline, S. L. Foldy, J. P. Davis, and I. K. Damon, "The Detection of Monkeypox in Humans in the Western Hemisphere", *New England Journal of Medicine*, vol. 350, no. 4, pp. 342–350, 2004, ISSN: 0028-4793. DOI: 10.1056/NEJMoa032299.

[15] A. Hartschuh, "Tip-Enhanced Near-Field Optical Microscopy", *Angewandte Chemie International Edition*, vol. 47, no. 43, pp. 8178–8191, 2008, ISSN: 14337851. DOI: 10.1002/anie.200801605.

[16] J. L. Meyzonnette, J. Mangin, and M. Cathelinaud, "Refractive Index of Optical Materials", in *Springer Handbooks*, 2019. DOI: 10.1007/978-3-319-93728-1_29.

[17] A. Maznev and O. Wright, "Upholding the diffraction limit in the focusing of light and sound", *Wave Motion*, vol. 68, pp. 182–189, 2017, ISSN: 01652125. DOI: 10.1016/j.wavemoti.2016.09.012. arXiv: 1602.07958.

[18] J. Zhang, H. Zhang, J. Wu, and J. Zhang, "Fuel Cell Degradation and Failure Analysis", in *Pem Fuel Cell Testing and Diagnosis*, Elsevier, 2013, ch. 11, pp. 283–335, ISBN: 978-0-444-53688-4. DOI: 10.1016/B978-0-444-53688-4.00011-5.

[19] X. Chen, B. Zheng, and H. Liu, "Optical and digital microscopic imaging techniques and applications in pathology", *Analytical Cellular Pathology*, vol. 34, no. 1-2, pp. 5–18, 2011, ISSN: 22107177. DOI: 10.3233/ACP-2011-0006.

[20] T. Mappes, N. Jahr, A. Csaki, N. Vogler, J. Popp, and W. Fritzsche, "The Invention of Immersion Ultramicroscopy in 1912-The Birth of Nanotechnology?", *Angewandte Chemie International Edition*, vol. 51, no. 45, pp. 11 208–11 212, 2012, ISSN: 14337851. DOI: 10.1002/anie.201204688.

[21] L. Schermelleh, A. Ferrand, T. Huser, C. Eggeling, M. Sauer, O. Biehlmaier, and G. P. C. Drummen, "Super-resolution microscopy demystified", *Nature Cell Biology*, vol. 21, no. 1, pp. 72–84, 2019, ISSN: 1465-7392. DOI: 10.1038/s41556-018-0251-8.

[22] E. Betzig, S. W. Hell, and W. E. Moerner, "THE NOBEL PRIZE IN CHEMISTRY 2014 : How the optical microscope became a nanoscope", THE ROYAL SWEDISH ACADEMY OF SCIENCES, Tech. Rep., 2014. [Online]. Available: https://www.nobelprize.org/uploads/2018/06/popular-chemistryprize2014.pdf.

[23] V. Magidson and A. Khodjakov, "Circumventing Photodamage in Live-Cell Microscopy", in, 2013, pp. 545–560. DOI: 10.1016/B978-0-12-407761-4.00023-3.

[24] M. Lelek, M. T. Gyparaki, G. Beliu, F. Schueder, J. Griffié, S. Manley, R. Jungmann, M. Sauer, M. Lakadamyali, and C. Zimmer, "Single-molecule localization microscopy", *Nature Reviews Methods Primers*, vol. 1, no. 1, p. 39, 2021, ISSN: 2662-8449. DOI: 10.1038/s43586-021-00038-x.

[25] J. Xu, H. Ma, and Y. Liu, "Stochastic Optical Reconstruction Microscopy (STORM)", *Current Protocols in Cytometry*, vol. 81, no. 1, 2017, ISSN: 1934-9297. DOI: 10.1002/cpcy.23.

[26] D. Lin, L. A. Gagnon, M. D. Howard, A. R. Halpern, and J. C. Vaughan, "Extended-Depth 3D Super-Resolution Imaging Using Probe-Refresh STORM", *Biophysical Journal*, vol. 114, no. 8, pp. 1980–1987, 2018, ISSN: 00063495. DOI: 10.1016/j.bpj.2018.03.023.

[27] B. Egger and S. G. Sprecher, "Super-Resolution STED and STORM/PALM Microscopy for Brain Imaging", in *Advanced Optical Methods for Brain Imaging*, vol 5, Springer Singapore, 2019, ch. 12, pp. 245–258, ISBN: 978-981-10-9020-2. DOI: 10.1007/978-981-10-9020-2_12. [Online]. Available: http://link.springer.com/10.1007/978-981-10-9020-2{_}12.

[28] H. Blom and J. Widengren, "STED microscopy—towards broadened use and scope of applications", *Current Opinion in Chemical Biology*, vol. 20, pp. 127–133, 2014, ISSN: 13675931. DOI: 10.1016/j.cbpa.2014.06.004.

[29] G. Vicidomini, P. Bianchini, and A. Diaspro, "STED super-resolved microscopy", *Nature Methods*, vol. 15, no. 3, pp. 173–182, 2018, ISSN: 1548-7091. DOI: 10.1038/nmeth.4593.

[30] F. Göttfert, C. A. Wurm, V. Mueller, S. Berning, V. C. Cordes, A. Honigmann, and S. W. Hell, "Coaligned Dual-Channel STED Nanoscopy and Molecular Diffusion Analysis at 20 nm Resolution", *Biophysical Journal*, vol. 105, no. 1, pp. L01–L03, 2013, ISSN: 00063495. DOI: 10.1016/j.bpj.2013.05.029.

[31] N. Kilian, A. Goryaynov, M. D. Lessard, G. Hooker, D. Toomre, J. E. Rothman, and J. Bewersdorf, "Assessing photodamage in live-cell STED microscopy", *Nature Methods*, vol. 15, no. 10, pp. 755–756, 2018, ISSN: 1548-7091. DOI: 10.1038/s41592-018-0145-5.

[32] C. Osseforth, J. R. Moffitt, L. Schermelleh, and J. Michaelis, "Simultaneous dual-color 3D STED microscopy", *Optics Express*, vol. 22, no. 6, p. 7028, 2014, ISSN: 1094-4087. DOI: 10.1364/OE.22.007028.

[33] S. J. Sahl and S. W. Hell, "High-Resolution 3D Light Microscopy with STED and RESOLFT", in *High Resolution Imaging in Microscopy and Ophthalmology*, Cham: Springer International Publishing, 2019, pp. 3–32. DOI: 10.1007/978-3-030-16638-0_1.

[34] G. Vicidomini, P. Bianchini, and A. Diaspro, "STED super-resolved microscopy", *Nature Methods*, vol. 15, no. 3, pp. 173–182, 2018, ISSN: 1548-7091. DOI: 10.1038/nmeth.4593. [Online]. Available: https://www.nature.com/articles/nmeth.4593.

[35] G. Huszka and M. A. Gijs, "Super-resolution optical imaging: A comparison", *Micro and Nano Engineering*, vol. 2, pp. 7–28, 2019, ISSN: 25900072. DOI: 10.1016/j.mne.2018.11.005.

[36] J. M. Guerra, "Photon tunneling microscopy", *Applied Optics*, vol. 29, no. 26, p. 3741, 1990, ISSN: 0003-6935. DOI: 10.1364/AO.29.003741.

[37] R. P., "Photon tunnelling microscopy", *Nature*, vol. 348, no. 6298, pp. 196–196, 1990, ISSN: 0028-0836. DOI: 10.1038/348196a0.

[38] G. L. Dyer, "Photon tunnelling microscopy: new instruments from old theory", *Materials & Design*, vol. 14, no. 2, pp. 123–125, 1993, ISSN: 02613069. DOI: 10.1016/0261-3069(93)90005-G.

[39] I. Snigireva and A. Snigireva, "MICROSCOPY TECHNIQUES | X-Ray Microscopy", in *Encyclopedia of Analytical Science*, Elsevier, 2005, pp. 151–158. DOI: 10.1016/B0-12-369397-7/00729-9.

[40] K. Fukazawa, "Ultraviolet Microscopy", in, 1992, pp. 110–121. DOI: 10.1007/978-3-642-74065-7_8.

[41] K. Akhtar, S. A. Khan, S. B. Khan, and A. M. Asiri, "Scanning Electron Microscopy: Principle and Applications in Nanomaterials Characterization", in *Handbook of Materials Characterization*, Cham: Springer International Publishing, 2018, pp. 113–145. DOI: 10.1007/978-3-319-92955-2_4.

[42] A. Ul-Hamid, "Introduction", in *A Beginners' Guide to Scanning Electron Microscopy*, Cham: Springer International Publishing, 2018, pp. 1–14. DOI: 10.1007/978-3-319-98482-7_1.

[43] R. Leary and R. Brydson, "Chromatic Aberration Correction", in, 2011, pp. 73–130. DOI: 10.1016/B978-0-12-385861-0.00003-8.

[44] R. Shiloh, R. Remez, P.-H. Lu, L. Jin, Y. Lereah, A. H. Tavabi, R. E. Dunin-Borkowski, and A. Arie, "Spherical aberration correction in a scanning transmission electron microscope using a sculpted thin film", *Ultramicroscopy*, vol. 189, pp. 46–53, 2018, ISSN: 03043991. DOI: 10.1016/j.ultramic.2018.03.016.

[45] P. Moran and B. Coats, "Biological Sample Preparation for SEM Imaging of Porcine Retina", *Microscopy Today*, vol. 20, no. 2, pp. 28–31, 2012, ISSN: 1551-9295. DOI: 10.1017/S1551929511001374.

[46] A. Ul-Hamid, "Contrast Formation in the SEM", in *A Beginners' Guide to Scanning Electron Microscopy*, Cham: Springer International Publishing, 2018, pp. 77–128. DOI: 10.1007/978-3-319-98482-7_3.

[47] Y Hashimoto, S Takeuchi, T Sunaoshi, and Y Yamazawa, "Voltage Contrast Imaging with Energy-Controlled Signal in an FE-SEM.", *Microscopy and Microanalysis*, vol. 24, no. S1, pp. 662–663, 2018. DOI: 10.1017/S143192761800380X.

[48] P. C. Hackley, R. J. McAleer, A. M. Jubb, B. J. Valentine, and J. E. Birdwell, "Cathodoluminescence differentiates sedimentary organic matter types", *Scientific Reports*, vol. 14, no. 1, p. 5969, 2024. DOI: 10.1038/s41598-024-53168-z.

[49] J. Chen and T. Sekiguchi, "Electron-Beam-Induced Current", in *Compendium of Surface and Interface Analysis*, Singapore: Springer Singapore, 2018, pp. 149–154. DOI: 10.1007/978-981-10-6156-1_26.

[50] S. Zaefferer and N.-N. Elhami, "Theory and application of electron channelling contrast imaging under controlled diffraction conditions", *Acta Materialia*, vol. 75, pp. 20–50, 2014. DOI: 10.1016/j.actamat.2014.04.018.

[51] H. Tsurusawa, N. Nakanishi, K. Kawano, Y. Chen, M. Dutka, B. Van Leer, and T. Mizoguchi, "Robotic fabrication of high-quality lamellae for aberration-corrected transmission electron microscopy", *Scientific Reports*, vol. 11, no. 1, p. 21 599, 2021, ISSN: 2045-2322. DOI: 10.1038/s41598-021-00595-x.

[52] C. Kisielowski, B. Freitag, M. Bischoff, H. van Lin, S. Lazar, G. Knippels, P. Tiemeijer, M. van der Stam, S. von Harrach, M. Stekelenburg, M. Haider, S. Uhlemann,

H. Müller, P. Hartel, B. Kabius, D. Miller, I. Petrov, E. Olson, T. Donchev, E. Kenik, A. Lupini, J. Bentley, S. Pennycook, I. Anderson, A. Minor, A. Schmid, T. Duden, V. Radmilovic, Q. Ramasse, M. Watanabe, R. Erni, E. Stach, P. Denes, and U. Dahmen, "Detection of Single Atoms and Buried Defects in Three Dimensions by Aberration-Corrected Electron Microscope with 0.5-Å Information Limit", *Microscopy and Microanalysis*, vol. 14, no. 5, pp. 469–477, 2008, ISSN: 1431-9276. DOI: 10.1017/S1431927608080902.

[53] J. Verbeeck, S. Hens, P. Potapov, and D. Schryvers, "Electron Energy Loss Spectrometry", in *Encyclopedia of Analytical Science*, Elsevier, 2005, pp. 324–331. DOI: 10.1016/B0-12-369397-7/00605-1.

[54] M. A. Aronova and R. D. Leapman, "Elemental Mapping by Electron Energy Loss Spectroscopy in Biology", in, 2013, pp. 209–226. DOI: 10.1007/978-1-62703-137-0_13.

[55] G. P. Holmes-Hampton, W.-H. Tong, and T. A. Rouault, "Biochemical and Biophysical Methods for Studying Mitochondrial Iron Metabolism", in, 2014, pp. 275–307. DOI: 10.1016/B978-0-12-801415-8.00015-1.

[56] H. Hirai, "Electron Energy-Loss Spectroscopy and its Applications to Characterization of Carbon Materials", in *Carbon Alloys*, Elsevier, 2003, pp. 239–256. DOI: 10.1016/B978-008044163-4/50015-2.

[57] J. A. Hachtel, A. R. Lupini, and J. C. Idrobo, "Exploring the capabilities of monochromated electron energy loss spectroscopy in the infrared regime", *Scientific Reports*, vol. 8, no. 1, p. 5637, 2018, ISSN: 2045-2322. DOI: 10.1038/s41598-018-23805-5.

[58] A. Shah, Q. Ramasse, J. Wen, A. Bhattacharya, and J. Zuo, "Practical spatial resolution of electron energy loss spectroscopy in aberration corrected scanning transmission electron microscopy", *Micron*, vol. 42, no. 6, pp. 539–546, 2011, ISSN: 09684328. DOI: 10.1016/j.micron.2010.12.008.

[59] L. Meitner, "Über den Zusammenhang zwischen β- und γ-Strahlen", *Zeitschrift fur Physik*, vol. 9, no. 1, pp. 145–152, 1922, ISSN: 1434-6001. DOI: 10.1007/BF01326963.

[60] P. Auger, "Sur l'effet photoélectrique composé", *Journal de Physique et le Radium*, vol. 6, no. 6, pp. 205–208, 1925, ISSN: 0368-3842. DOI: 10.1051/jphysrad:0192500606020500.

[61] W Mehlhorn, "70 years of Auger spectroscopy, a historical perspective", *Journal of Electron Spectroscopy and Related Phenomena*, vol. 93, no. 1-3, pp. 1–15, 1998, ISSN: 03682048. DOI: 10.1016/S0368-2048(98)00153-4.

[62] K. Oura, M. Katayama, A. V. Zotov, V. G. Lifshits, and A. A. Saranin, "Surface Analysis II. Electron Spectroscopy Methods", in, 2003, pp. 77–108. DOI: 10.1007/978-3-662-05179-5_5.

[63] S. R. Bare and G. Somorjai, "Surface Chemistry", in *Encyclopedia of Physical Science and Technology*, Elsevier, 2003, pp. 373–421. DOI: 10.1016/B0-12-227410-5/00757-2.

[64] T. Schuelke, "Auger Electron Spectroscopy (AES)", in *Encyclopedia of Tribology*, Boston, MA: Springer US, 2013, pp. 149–154. DOI: 10.1007/978-0-387-92897-5_1224.

[65] E. Martinez, P. Yadav, M. Bouttemy, O. Renault, Ł. Borowik, F. Bertin, A. Etcheberry, and A. Chabli, "Scanning Auger microscopy for high lateral and depth elemental sensitivity", *Journal of Electron Spectroscopy and Related Phenomena*, vol. 191, pp. 86–91, 2013, ISSN: 03682048. DOI: 10.1016/j.elspec.2013.11.008.

[66] A. Erbe, S. Nayak, Y.-H. Chen, F. Niu, M. Pander, S. Tecklenburg, and C. Toparli, "How to Probe Structure, Kinetics, and Dynamics at Complex Interfaces In Situ and Operando by Optical Spectroscopy", in *Encyclopedia of Interfacial Chemistry*, Elsevier, 2018, pp. 199–219. DOI: 10.1016/B978-0-12-409547-2.14061-2.

[67] M. Yoshikawa, "Photoluminescence (PL) Spectroscopy", in *Advanced Optical Spectroscopy Techniques for Semiconductors*, Cham: Springer International Publishing, 2023, pp. 27–32. DOI: 10.1007/978-3-031-19722-2_3.

[68] J. Smith, "Characterisation of single defects in diamond in the development of quantum devices", in *Quantum Information Processing with Diamond*, Elsevier, 2014, pp. 68–97. DOI: 10.1533/9780857096685.1.68.

[69] R. W. Welker, "Size Analysis and Identification of Particles", in *Developments in Surface Contamination and Cleaning*, Elsevier, 2012, pp. 179–213. DOI: 10.1016/B978-1-4377-7883-0.00004-3.

[70] S. Roy, B. Chamberlin, and A. J. Matzger, "Polymorph Discrimination Using Low Wavenumber Raman Spectroscopy", *Organic Process Research & Development*, vol. 17, no. 7, pp. 976–980, 2013, ISSN: 1083-6160. DOI: 10.1021/op400102e.

[71] D. Liu and P. E. J. Flewitt, "Raman measurements of stress in films and coatings", in *Spectroscopic Properties of Inorganic and Organometallic Compounds*, 2014, ch. 5, pp. 141–177, ISBN: 9781849739191. DOI: 10.1039/9781782621485-00141.

[72] U. A. Jayasooriya and R. D. Jenkins, "Introduction to Raman Spectroscopy", in *An Introduction to Laser Spectroscopy*, Boston, MA: Springer US, 2002, ch. 3, pp. 77–104. DOI: 10.1007/978-1-4615-0727-7_3.

[73] C. J. Sheppard, "Scanning optical microscopy", in *Advances in Imaging and Electron Physics*, vol. 213, 2020, pp. 227–325. DOI: 10.1016/bs.aiep.2019.11.001.

[74] T. Wilson, D. K. Hamilton, P. J. Shadbolt, and B. Dodd, "Scanning optical microscope as new metallographic tool", *Metal Science*, vol. 14, no. 4, pp. 144–146, 1980, ISSN: 0306-3453. DOI: 10.1179/msc.1980.14.4.144.

[75] M. Minsky, "Memoir on inventing the confocal scanning microscope", *Scanning*, vol. 10, no. 4, pp. 128–138, 1988, ISSN: 0161-0457. DOI: 10.1002/sca.4950100403. [Online]. Available: https://onlinelibrary.wiley.com/doi/10.1002/sca.4950100403.

[76] J. B. Pawley, "Fundamental Limits in Confocal Microscopy", in *Handbook Of Biological Confocal Microscopy*, Boston, MA: Springer US, 2006, pp. 20–42. DOI: 10.1007/978-0-387-45524-2_2.

[77] G. W. Stachowiak, A. W. Batchelor, and G. B. Stachowiak, "Characterization of Test Specimens", in, 2004, pp. 115–150. DOI: 10.1016/S0167-8922(04)80022-1.

[78] A. D. Elliott, "Confocal Microscopy: Principles and Modern Practices", *Current Protocols in Cytometry*, vol. 92, no. 1, 2020. DOI: 10.1002/cpcy.68.

[79] C. Fouquet, J.-F. Gilles, N. Heck, M. Dos Santos, R. Schwartzmann, V. Cannaya, M.-P. Morel, R. S. Davidson, A. Trembleau, and S. Bolte, "Improving Axial Resolution in Confocal Microscopy with New High Refractive Index Mounting Media", *PLOS ONE*, vol. 10, no. 3, e0121096–e0121096, 2015. DOI: 10.1371/journal.pone.0121096.

[80] D Axelrod, D. E. Koppel, J Schlessinger, E Elson, and W. W. Webb, "Mobility measurement by analysis of fluorescence photobleaching recovery kinetics", *Biophysical Journal*, vol. 16, no. 9, pp. 1055–1069, 1976. DOI: 10.1016/S0006-3495(76)85755-4.

[81] M. B. M. Meddens, S. de Keijzer, and A. Cambi, "High Spatiotemporal Bioimaging Techniques to Study the Plasma Membrane Nanoscale Organization", in *Fluorescence Microscopy*, Elsevier, 2014, pp. 49–63. DOI: 10.1016/B978-0-12-409513-7.00004-X.

[82] R Hard, J Hipp, M. A. Tangrea, and J. E. Tomaszewski, "Applications of Image Science in Pathology and Cell Biology", in *Pathobiology of Human Disease*, Elsevier, 2014, pp. 3723–3759. DOI: 10.1016/B978-0-12-386456-7.07203-8.

[83] Filipe Richheimer, "Electrical and tip-enhanced optical scanning probe microscopy for the functional characterisation of emerging electronic materials", PhD thesis, University of Surrey, 2021. DOI: 10.15126/thesis.900269.

[84] H. Yu, "Scanning acoustic microscopy for material evaluation", *Applied Microscopy*, vol. 50, no. 1, p. 25, 2020, ISSN: 2287-4445. DOI: 10.1186/s42649-020-00045-4.

[85] B. Misof, P. Roschger, and P. Fratzl, "3.26 Imaging Mineralized Tissues in Vertebrates", in *Comprehensive Biomaterials II*, Elsevier, 2017, pp. 549–578. DOI: 10.1016/B978-0-12-803581-8.09827-1.

[86] R. Kohli, "Developments in Imaging and Analysis Techniques for Micro- and Nanosize Particles and Surface Features", in *Developments in Surface Contamination and*

Cleaning, Elsevier, 2012, pp. 215–306. DOI: 10.1016/B978-1-4377-7883-0.00005-5.

[87] W. Arnold, "NDT Techniques: Acoustic Microscopy and Holography", in *Encyclopedia of Materials: Science and Technology*, Elsevier, 2001, pp. 6004–6006. DOI: 10.1016/B0-08-043152-6/01054-8.

[88] N. Smith, "Science with Soft X Rays", *Physics Today*, vol. 54, no. 1, pp. 29–34, 2001, ISSN: 0031-9228. DOI: 10.1063/1.1349609.

[89] X Zhou and G. Thompson, "Electron and Photon Based Spatially Resolved Techniques", in *Reference Module in Materials Science and Materials Engineering*, Elsevier, 2017. DOI: 10.1016/B978-0-12-803581-8.10140-7.

[90] K. Li, S. Ali, M. Wojcik, V. De Andrade, X. Huang, H. Yan, Y. S. Chu, E. Nazaretski, A. Pattammattel, and C. Jacobsen, "Tunable hard x-ray nanofocusing with Fresnel zone plates fabricated using deep etching", *Optica*, vol. 7, no. 5, p. 410, 2020, ISSN: 2334-2536. DOI: 10.1364/OPTICA.387445.

[91] J. C. Andrews, F. Meirer, Y. Liu, Z. Mester, and P. Pianetta, "Transmission X-ray microscopy for full-field nano imaging of biomaterials", *Microscopy Research and Technique*, vol. 74, no. 7, pp. 671–681, 2011, ISSN: 1059-910X. DOI: 10.1002/jemt.20907.

[92] R. Young, J. Ward, and F. Scire, "The topografiner: An instrument for measuring surface microtopography", *Review of Scientific Instruments*, vol. 43, no. 7, pp. 999–1011, 1972, ISSN: 00346748. DOI: 10.1063/1.1685846.

[93] H. Adachi, A. Suzuki, T. Onodera, K. Suzuki, and K. Mukasa, "Stable operation of topografiner in the atmosphere by use of charge injection current in an insulating liquid", *Sensors and Actuators A: Physical*, vol. 23, no. 1-3, pp. 954–957, 1990, ISSN: 09244247. DOI: 10.1016/0924-4247(90)87067-S.

[94] D. Zanin, M. Erbudak, L. De Pietro, H. Cabrera, A. Redmann, A. Fognini, T. Michlmayr, Y. Acremann, D. Pescia, and U. Ramsperger, "The topografiner with energy analysis", in *2013 26th International Vacuum Nanoelectronics Conference (IVNC)*, IEEE, 2013, pp. 1–2, ISBN: 978-1-4673-5993-1. DOI: 10.1109/IVNC.2013.6624755.

[95] R. Smallman and A. Ngan, "Characterization and Analysis", in *Modern Physical Metallurgy*, Elsevier, 2014, pp. 159–250. DOI: 10.1016/B978-0-08-098204-5.00005-5.

[96] M. Nasrollahzadeh, M. Atarod, M. Sajjadi, S. M. Sajadi, and Z. Issaabadi, "Plant-Mediated Green Synthesis of Nanostructures: Mechanisms, Characterization, and Applications", in, 2019, pp. 199–322. DOI: 10.1016/B978-0-12-813586-0.00006-7.

[97] A. Mayeen, L. K. Shaji, A. K. Nair, and N. Kalarikkal, "Morphological Characterization of Nanomaterials", in *Characterization of Nanomaterials*, Elsevier, 2018, pp. 335–364. DOI: 10.1016/B978-0-08-101973-3.00012-2.

[98] P. K. Hansma and J. Tersoff, "Scanning tunneling microscopy", *Journal of Applied Physics*, vol. 61, no. 2, R1–R24, 1987, ISSN: 0021-8979. DOI: 10.1063/1.338189.

[99] E. W. Muller, "The dependence of field electron emission on exit work.", *Z. Physik*, vol. 102, no. 11-12, pp. 734–761, 1936, ISSN: 1434-6001. DOI: 10.1007/BF01338540.

[100] H. Yanagisawa, M. Bohn, F. Goschin, A. P. Seitsonen, and M. F. Kling, "Field emission microscope for a single fullerene molecule", *Scientific Reports*, vol. 12, no. 1, p. 2714, 2022, ISSN: 2045-2322. DOI: 10.1038/s41598-022-06670-1.

[101] E. W. Muller, "Das Feldionenmikroskop", *Zeitschrift fur Physik*, vol. 131, no. 1, pp. 136–142, 1951, ISSN: 1434-6001. DOI: 10.1007/BF01329651.

[102] E. W. Müller and K. Bahadur, "Field Ionization of Gases at a Metal Surface and the Resolution of the Field Ion Microscope", *Physical Review*, vol. 102, no. 3, pp. 624–631, 1956, ISSN: 0031-899X. DOI: 10.1103/PhysRev.102.624.

[103] M. Dagan, B. Gault, G. D. W. Smith, P. A. J. Bagot, and M. P. Moody, "Automated Atom-By-Atom Three-Dimensional (3D) Reconstruction of Field Ion Microscopy Data", *Microscopy and Microanalysis*, vol. 23, no. 2, pp. 255–268, 2017, ISSN: 1431-9276. DOI: 10.1017/S1431927617000277.

[104] E. W. Müller, J. A. Panitz, and S. B. McLane, "The Atom-Probe Field Ion Microscope", *Review of Scientific Instruments*, vol. 39, no. 1, pp. 83–86, 1968, ISSN: 0034-6748. DOI: 10.1063/1.1683116.

[105] B. Gault, M. P. Moody, J. M. Cairney, and S. P. Ringer, "Specimen Preparation", in *Atom Probe Microscopy. Springer Series in Materials Science*, vol. 160, 2012, pp. 71–110. DOI: 10.1007/978-1-4614-3436-8_4.

[106] L. Zhao, A. Normand, J. Houard, I. Blum, F. Delaroche, O. Latry, B. Ravelo, and F. Vurpillot, "Optimizing Atom Probe Analysis with Synchronous Laser Pulsing and Voltage Pulsing", *Microscopy and Microanalysis*, vol. 23, no. 2, pp. 221–226, 2017, ISSN: 1431-9276. DOI: 10.1017/S1431927616012666.

[107] W. Peng, H. Wang, H. Lu, L. Yin, Y. Wang, B. Grandidier, D. Yang, and X. Pi, "Recent Progress on the Scanning Tunneling Microscopy and Spectroscopy Study of Semiconductor Heterojunctions", *Small*, vol. 17, no. 50, 2021. DOI: 10.1002/smll.202100655.

[108] T. Ekino, T. Takasaki, R. Ribeiro, T. Muranaka, and J. Akimitsu, "Scanning tunnelling microscopy and spectroscopy of MgB2", *Journal of Physics: Conference Series*, vol. 61, pp. 278–282, 2007. DOI: 10.1088/1742-6596/61/1/056.

[109] C. Fleischmann, K. Paredis, D. Melkonyan, and W. Vandervorst, "Revealing the 3-dimensional shape of atom probe tips by atomic force microscopy", *Ultramicroscopy*, vol. 194, pp. 221–226, 2018, ISSN: 03043991. DOI: 10.1016/j.ultramic.2018.08.010.

[110] B. W. Krakauer and D. N. Seidman, "Systematic procedures for atom-probe field-ion microscopy studies of grain boundary segregation", *Review of Scientific Instruments*, vol. 63, no. 9, pp. 4071–4079, 1992, ISSN: 0034-6748. DOI: 10.1063/1.1143214.

[111] M. K. Miller and R. G. Forbes, "The Art of Specimen Preparation", in *Atom-Probe Tomography*, Boston, MA: Springer US, 2014, pp. 189–228. DOI: 10.1007/978-1-4899-7430-3_4.

[112] D. Melkonyan, C. Fleischmann, A. Veloso, A. Franquet, J. Bogdanowicz, R. Morris, and W. Vandervorst, "Wet-chemical etching of atom probe tips for artefact free analyses of nanoscaled semiconductor structures", *Ultramicroscopy*, vol. 186, pp. 1–8, 2018, ISSN: 03043991. DOI: 10.1016/j.ultramic.2017.12.009.

[113] J. S. Lee, R. T. Hill, A. Chilkoti, and W. L. Murphy, "Surface Patterning", in *Biomaterials Science*, Elsevier, 2020, pp. 553–573. DOI: 10.1016/B978-0-12-816137-1.00037-4.

[114] A. C. Fischer, M. Mäntysalo, and F. Niklaus, "Inkjet printing, laser-based micromachining, and micro–3D printing technologies for MEMS", in *Handbook of Silicon Based MEMS Materials and Technologies*, Elsevier, 2020, pp. 531–545. DOI: 10.1016/B978-0-12-817786-0.00021-9.

[115] S. Nasrazadani and S. Hassani, "Modern analytical techniques in failure analysis of aerospace, chemical, and oil and gas industries", in *Handbook of Materials Failure Analysis with Case Studies from the Oil and Gas Industry*, Elsevier, 2016, pp. 39–54. DOI: 10.1016/B978-0-08-100117-2.00010-8.

[116] M. K. Miller, K. F. Russell, K. Thompson, R. Alvis, and D. J. Larson, "Review of Atom Probe FIB-Based Specimen Preparation Methods", *Microscopy and Microanalysis*, vol. 13, no. 6, pp. 428–436, 2007, ISSN: 1431-9276. DOI: 10.1017/S1431927607070845.

[117] D. Larson, D. Foord, A. Petford-Long, H Liew, M. Blamire, A Cerezo, and G. Smith, "Field-ion specimen preparation using focused ion-beam milling", *Ultramicroscopy*, vol. 79, no. 1-4, pp. 287–293, 1999, ISSN: 03043991. DOI: 10.1016/S0304-3991(99)00055-8.

[118] M. Miller, C. Liu, J. Wright, W. Tang, and K. Hildal, "APT characterization of some iron-based bulk metallic glasses", *Intermetallics*, vol. 14, no. 8-9, pp. 1019–1026, 2006, ISSN: 09669795. DOI: 10.1016/j.intermet.2006.01.040.

[119] D. Larson, D. Foord, A. Petford-Long, T. Anthony, I. Rozdilsky, A Cerezo, and G. Smith, "Focused ion-beam milling for field-ion specimen preparation:" *Ultramicroscopy*, vol. 75, no. 3, pp. 147–159, 1998, ISSN: 03043991. DOI: 10.1016/S0304-3991(98)00058-8.

[120] D. E. Perea, J. E. Allen, S. J. May, B. W. Wessels, D. N. Seidman, and L. J. Lauhon, "Three-Dimensional Nanoscale Composition Mapping of Semiconductor Nanowires", *Nano Letters*, vol. 6, no. 2, pp. 181–185, 2006, ISSN: 1530-6984. DOI: 10.1021/nl051602p.

[121] G. Binnig and C. F. Quate, "Atomic Force Microscope", *Physical Review Letters*, vol. 56, no. 9, pp. 930–933, 1986, ISSN: 0031-9007. DOI: 10.1103/PhysRevLett.56.930.

[122] L. Gross, F. Mohn, N. Moll, P. Liljeroth, and G. Meyer, "The Chemical Structure of a Molecule Resolved by Atomic Force Microscopy", *Science*, vol. 325, no. 5944, pp. 1110–1114, 2009, ISSN: 0036-8075. DOI: 10.1126/science.1176210.

[123] D. Rugar and P. Hansma, "Atomic force microscopy", *Physics Today*, vol. 43, no. 10, pp. 23–30, 1990. DOI: 10.1063/1.881238.

[124] N. P. D'Costa and J. H. Hoh, "Calibration of optical lever sensitivity for atomic force microscopy", *Review of Scientific Instruments*, vol. 66, no. 10, pp. 5096–5097, 1995, ISSN: 00346748. DOI: 10.1063/1.1146135.

[125] M. J. Higgins, R. Proksch, J. E. Sader, M. Polcik, S. Mc Endoo, J. P. Cleveland, and S. P. Jarvis, "Noninvasive determination of optical lever sensitivity in atomic force microscopy", *Review of Scientific Instruments*, vol. 77, no. 1, pp. 1–5, 2006, ISSN: 00346748. DOI: 10.1063/1.2162455.

[126] H. Xie, J. Vitard, S. Haliyo, and S. Régnier, "Optical lever calibration in atomic force microscope with a mechanical lever", *Review of Scientific Instruments*, vol. 79, no. 9, 2008, ISSN: 00346748. DOI: 10.1063/1.2976108.

[127] M. Boudaoud, Y. Haddab, Y. Le Gorrec, and P. Lutz, "Study of thermal and acoustic noise interferences in low stiffness atomic force microscope cantilevers and characterization of their dynamic properties", *Review of Scientific Instruments*, vol. 83, no. 1, 2012, ISSN: 00346748. DOI: 10.1063/1.3673637.

[128] U. Rabe and W. Arnold, "Atomic force microscopy at MHz frequencies", *Annalen der Physik*, vol. 506, no. 7-8, p. 589, 1994, ISSN: 15213889. DOI: 10.1002/andp.19945060704.

[129] A. F. Guedes, F. A. Carvalho, I. Malho, N. Lousada, L. Sargento, and N. C. Santos, "Atomic force microscopy as a tool to evaluate the risk of cardiovascular diseases in patients", *Nature Nanotechnology*, vol. 11, no. 8, pp. 687–692, 2016, ISSN: 1748-3387. DOI: 10.1038/nnano.2016.52.

[130] P. C. Braga, D. Ricci, D. Ricci, and P. C. Braga, "Recognizing and Avoiding Artifacts in AFM Imaging", *Methods in molecular biology*, vol. 242, pp. 25–38, 2003. DOI: 10.1385/1-59259-647-9:25.

[131] V. B Zhong, Q.; Inniss, D.; Kjoller, K.; Elings, "Fractured polymer/silica fiber surface studied by tapping mode atomic force microscopy", *Surface Science Letters*, vol. 290, no. 1, pp. 688–692. 1993. DOI: 10.1016/0167-2584(93)90906-Y.

[132] F. J. Giessibl and S. Morita, "Non-contact AFM", *Journal of Physics: Condensed Matter*, vol. 24, no. 8, p. 080 301, 2012, ISSN: 0953-8984. DOI: 10.1088/0953-8984/24/8/080301.

[133] A. J. Weymouth, "Non-contact lateral force microscopy", *Journal of Physics: Condensed Matter*, vol. 29, no. 32, 2017, ISSN: 0953-8984. DOI: 10.1088/1361-648X/aa7984.

[134] L. Wang, B. Gautier, A. Sabac, and G. Bremond, "Investigation of tip-depletion-induced fail in scanning capacitance microscopy for the determination of carrier type", *Ultramicroscopy*, vol. 174, pp. 46–49, 2017, ISSN: 03043991. DOI: 10.1016/j.ultramic.2016.12.016.

[135] R. Biberger, G. Benstetter, T. Schweinboeck, P. Breitschopf, and H. Goebel, "Intermittent-contact scanning capacitance microscopy versus contact mode SCM applied to 2D dopant profiling", *Microelectronics Reliability*, vol. 48, no. 8-9, pp. 1339–1342, 2008, ISSN: 00262714. DOI: 10.1016/j.microrel.2008.06.013.

[136] R. Coq Germanicus, F. Lallemand, D. Chateigner, W. Jouha, N. Moultif, O. Latry, A. Fouchet, H. Murray, C. Bunel, and U. Lüders, "Dopant activity for highly in-situ doped polycrystalline silicon: hall, XRD, scanning capacitance microscopy (SCM) and scanning spreading resistance microscopy (SSRM)", *Nano Express*, vol. 2, no. 1, p. 010 037, 2021, ISSN: 2632-959X. DOI: 10.1088/2632-959X/abed3e.

[137] L. Wang, S. Guillemin, J. Chauveau, V. Sallet, F. Jomard, R. Brenier, V. Consonni, and G. Brémond, "Characterization of carrier concentration in ZnO nanowires by scanning capacitance microscopy", *physica status solidi c*, vol. 13, no. 7-9, pp. 576–580, 2016, ISSN: 1862-6351. DOI: 10.1002/pssc.201510268.

[138] A. Erickson, L. Sadwick, G. Neubauer, J. Kopanski, D. Adderton, and M. Rogers, "Quantitative scanning capacitance microscopy analysis of two-dimensional dopant concentrations at nanoscale dimensions", *Journal of Electronic Materials*, vol. 25, no. 2, pp. 301–304, 1996, ISSN: 0361-5235. DOI: 10.1007/BF02666260.

[139] C. Frisbie, "Scanning Probe Microscopy", in *Encyclopedia of Physical Science and Technology*, Elsevier, 2003, pp. 469–484. DOI: 10.1016/B0-12-227410-5/00675-X.

[140] G. Wielgoszewski and T. Gotszalk, "Scanning Thermal Microscopy (SThM): How to Map Temperature and Thermal Properties at the Nanoscale", in *Advances in*

Imaging and Electron Physics, P. W. Hawkes, Ed., vol. 190, Elsevier, 2015, ch. 4, pp. 177–221, ISBN: 9780128023808. DOI: 10.1016/bs.aiep.2015.03.011.

[141] R. Lambert, "Design, Fabrication and Characterisation of Thermally Optimised Novel SThM Probes", PhD thesis, University of Glasgow, 2019, p. 29.

[142] S. Amemiya, Z. Ding, J. Zhou, and A. J. Bard, "Studies of charge transfer at liquid | liquid interfaces and bilayer lipid membranes by scanning electrochemical microscopy", *Journal of Electroanalytical Chemistry*, vol. 483, no. 1, pp. 7–17, 2000, ISSN: 00220728. DOI: 10.1016/S0022-0728(00)00021-8.

[143] G. Wittstock, M. Burchardt, S. E. Pust, Y. Shen, and C. Zhao, "Scanning electrochemical microscopy for direct imaging of reaction rates", *Angewandte Chemie - International Edition*, vol. 46, no. 10, pp. 1584–1617, 2007, ISSN: 14337851. DOI: 10.1002/anie.200602750.

[144] H. Chen, A. Baitenov, Y. Li, E. Vasileva, S. Popov, I. Sychugov, M. Yan, and L. Berglund, "Thickness Dependence of Optical Transmittance of Transparent Wood: Chemical Modification Effects", *ACS Applied Materials & Interfaces*, vol. 11, no. 38, pp. 35 451–35 457, 2019, ISSN: 1944-8244. DOI: 10.1021/acsami.9b11816.

[145] P. S. Miedema, "Raman Spectroscopy with X-Rays", in *Raman Spectroscopy and Applications*, InTech, 2017. DOI: 10.5772/65427.

[146] B. J. Jones, "Microscopy in Forensic Sciences", in, 2019, pp. 1507–1524. DOI: 10.1007/978-3-030-00069-1_32.

[147] M. R. Joya, C. E. Paris, and J Barba-Ortega, "Non-lineal equations for the Raman spectroscopy analysis", *Journal of Physics: Conference Series*, vol. 490, 2014, ISSN: 1742-6596. DOI: 10.1088/1742-6596/490/1/012058.

[148] T. Runka, M. Kozielski, M. Drozdowski, and L. Szczepańska, "Raman scattering study of the ferroelectric phase transition in GPI and DGPI single crystals", *Ferroelectrics*, vol. 239, no. 1, pp. 125–131, 2000, ISSN: 0015-0193. DOI: 10.1080/00150190008213314.

[149] G. Barbillon, "Plasmonics and its Applications", *Materials*, vol. 12, no. 9, p. 1502, 2019, ISSN: 1996-1944. DOI: 10.3390/ma12091502.

[150] M. Mansuripur and A. R. Zakharian, "Maxwell's macroscopic equations, the energy-momentum postulates, and the Lorentz law of force", *Physical Review E*, vol. 79, no. 2, p. 026 608, 2009, ISSN: 1539-3755. DOI: 10.1103/PhysRevE.79.026608.

[151] X. Wei, H. Shi, Q. Deng, X. Dong, C. Liu, Y. Lu, and C. Du, "Artificial metal with effective plasma frequency in near-infrared region", *Optics Express*, vol. 18, no. 4, p. 3370, 2010, ISSN: 1094-4087. DOI: 10.1364/OE.18.003370.

[152] W. Chen and R. A. Marcus, "The Drude-Smith Equation and Related Equations for the Frequency-Dependent Electrical Conductivity of Materials: Insight from

a Memory Function Formalism", *ChemPhysChem*, vol. 22, no. 16, pp. 1667–1674, 2021, ISSN: 1439-4235. DOI: 10.1002/cphc.202100299.

[153] I. Langmuir, "The Constitution and Fundamental Properties of Solids and Liquids. Part I. Solids.", *Journal of the American Chemical Society*, vol. 38, no. 11, pp. 2221–2295, 1916, ISSN: 0002-7863. DOI: 10.1021/ja02268a002.

[154] L. Tonks and I. Langmuir, "Oscillations in Ionized Gases", *Physical Review*, vol. 33, no. 2, pp. 195–210, 1929, ISSN: 0031-899X. DOI: 10.1103/PhysRev.33.195.

[155] E. L. Albuquerque and M. G. Cottam, "Basic Properties of Excitations in Solids", in *Polaritons in Periodic and Quasiperiodic Structures*, Elsevier, 2004, pp. 1–23. DOI: 10.1016/B978-044451627-5/50001-8.

[156] S. G. C., "The Image Field Effect: How Important Is It?", in *Surface Enhanced Raman Scattering*, R. K. Chang and T. E. Furtak, Eds., Boston, MA: Springer US, 1982, ch. 2, p. 44, ISBN: 978-1-4615-9259-4. DOI: 10.1007/978-1-4615-9257-0.

[157] N. D. Israelsen, C. Hanson, and E. Vargis, "Nanoparticle Properties and Synthesis Effects on Surface-Enhanced Raman Scattering Enhancement Factor: An Introduction", *The Scientific World Journal*, vol. 2015, pp. 1–12, 2015, ISSN: 2356-6140. DOI: 10.1155/2015/124582.

[158] D. Costa, M. S. Rodrigues, E. Alves, N. P. Barradas, J. Borges, and F. Vaz, "Tuning the Refractive Index Sensitivity of LSPR Transducers Based on Nanocomposite Thin Films Composed of Noble Metal Nanoparticles Dispersed in TiO2", *Materials*, vol. 16, no. 23, p. 7355, 2023, ISSN: 1996-1944. DOI: 10.3390/ma16237355. [Online]. Available: https://www.mdpi.com/1996-1944/16/23/7355.

[159] M. Keil, A. E. Wetzel, K. Wu, E. Khomtchenko, J. Urbankova, A. Boisen, T. Rindzevicius, A.-I. Bunea, and R. J. Taboryski, "Large plasmonic color metasurfaces fabricated by super resolution deep UV lithography", *Nanoscale Advances*, vol. 3, no. 8, pp. 2236–2244, 2021, ISSN: 2516-0230. DOI: 10.1039/D0NA00934B. [Online]. Available: https://xlink.rsc.org/?DOI=D0NA00934B.

[160] F. A. A. Nugroho, D. Świtlik, A. Armanious, P. O'Reilly, I. Darmadi, S. Nilsson, V. P. Zhdanov, F. Höök, T. J. Antosiewicz, and C. Langhammer, "Time-Resolved Thickness and Shape-Change Quantification using a Dual-Band Nanoplasmonic Ruler with Sub-Nanometer Resolution", *ACS Nano*, vol. 16, no. 10, pp. 15 814–15 826, 2022, ISSN: 1936-0851. DOI: 10.1021/acsnano.2c04948. [Online]. Available: https://pubs.acs.org/doi/10.1021/acsnano.2c04948.

[161] M. D'Acunto, F. Fuso, R. Micheletto, M. Naruse, F. Tantussi, and M. Allegrini, "Near-field surface plasmon field enhancement induced by rippled surfaces", *Beilstein Journal of Nanotechnology*, vol. 8, pp. 956–967, 2017, ISSN: 2190-4286. DOI: 10.3762/bjnano.8.97.

[162] S. A. Maier, "Localized Surface Plasmons", in *Plasmonics: Fundamentals and Applications*, New York, NY: Springer US, 2007, pp. 65–88. DOI: 10.1007/0-387-37825-1_5.

[163] S. Peng, J. M. McMahon, G. C. Schatz, S. K. Gray, and Y. Sun, "Reversing the size-dependence of surface plasmon resonances", *Proceedings of the National Academy of Sciences*, vol. 107, no. 33, pp. 14 530–14 534, 2010. DOI: 10.1073/pnas.1007524107.

[164] F. Y. Alzoubi, A. A. Ahmad, I. A. Aljarrah, A. B. Migdadi, and Q. M. Al-Bataineh, "Localize surface plasmon resonance of silver nanoparticles using Mie theory", *Journal of Materials Science: Materials in Electronics*, vol. 34, no. 32, p. 2128, 2023. DOI: 10.1007/s10854-023-11304-x.

[165] G. Janith, H. Herath, N. Hendeniya, D. Attygalle, D. Amarasinghe, V. Logeeshan, P. Wickramasinghe, and Y. Wijayasinghe, "Advances in surface plasmon resonance biosensors for medical diagnostics: An overview of recent developments and techniques", *Journal of Pharmaceutical and Biomedical Analysis Open*, vol. 2, p. 100 019, 2023, ISSN: 2949771X. DOI: 10.1016/j.jpbao.2023.100019.

[166] I. I. Smolyaninov and A. V. Zayats, "Super-resolution microscopy using surface plasmon polaritons", in *Nanophotonics with Surface Plasmons*, Elsevier, 2007, pp. 63–107. DOI: 10.1016/B978-044452838-4/50004-7.

[167] R. H. Ritchie, "Plasma Losses by Fast Electrons in Thin Films", *Physical Review*, vol. 106, no. 5, pp. 874–881, 1957, ISSN: 0031-899X. DOI: 10.1103/PhysRev.106.874.

[168] Y. Kalachyova, D. Mares, O. Lyutakov, M. Kostejn, L. Lapcak, and V. Švorčík, "Surface Plasmon Polaritons on Silver Gratings for Optimal SERS Response", *The Journal of Physical Chemistry C*, vol. 119, no. 17, pp. 9506–9512, 2015, ISSN: 1932-7447. DOI: 10.1021/acs.jpcc.5b01793.

[169] X. X. Han, R. S. Rodriguez, C. L. Haynes, Y. Ozaki, and B. Zhao, "Surface-enhanced Raman spectroscopy", *Nature Reviews Methods Primers*, vol. 1, no. 1, p. 87, 2022, ISSN: 2662-8449. DOI: 10.1038/s43586-021-00083-6.

[170] J. Duan, H. Guo, S. Dong, T. Cai, W. Luo, Z. Liang, Q. He, L. Zhou, and S. Sun, "High-efficiency chirality-modulated spoof surface plasmon meta-coupler", *Scientific Reports*, vol. 7, no. 1, p. 1354, 2017, ISSN: 2045-2322. DOI: 10.1038/s41598-017-01664-w.

[171] L. Li, "Experimental Basics of Surface Plasmon Polaritons", in *Manipulation of Near Field Propagation and Far Field Radiation of Surface Plasmon Polariton.* 2017, pp. 7–32, ISBN: 978-981-10-4662-9. DOI: 10.1007/978-981-10-4663-6_2.

[172] M. Aftab, M. S. Mansha, T. Iqbal, and M. Farooq, "Surface Plasmon Excitation: Theory, Configurations, and Applications", *Plasmonics*, 2023, ISSN: 1557-1955. DOI: 10.1007/s11468-023-02095-2.

[173] F. Ding, Y. Yang, R. A. Deshpande, and S. I. Bozhevolnyi, "A review of gap-surface plasmon metasurfaces: fundamentals and applications", *Nanophotonics*, vol. 7, no. 6, pp. 1129–1156, 2018, ISSN: 2192-8614. DOI: 10.1515/nanoph-2017-0125.

[174] S. I. Bozhevolnyi and J. Jung, "Scaling for gap plasmon based waveguides", *Optics Express*, vol. 16, no. 4, p. 2676, 2008, ISSN: 1094-4087. DOI: 10.1364/OE.16.002676.

[175] S. Boroviks, Z.-H. Lin, V. A. Zenin, M. Ziegler, A. Dellith, P. A. D. Gonçalves, C. Wolff, S. I. Bozhevolnyi, J.-S. Huang, and N. A. Mortensen, "Extremely confined gap plasmon modes: when nonlocality matters", *Nature Communications*, vol. 13, no. 1, p. 3105, 2022, ISSN: 2041-1723. DOI: 10.1038/s41467-022-30737-2.

[176] L. Zhang, X. Wang, H. Chen, C. Liu, and S. Deng, "A planar plasmonic nano-gap and its array for enhancing light-matter interactions at the nanoscale", *Nanoscale*, vol. 14, no. 34, pp. 12 257–12 264, 2022, ISSN: 2040-3364. DOI: 10.1039/D2NR01282K.

[177] M. Yang, M. S. Mattei, C. R. Cherqui, X. Chen, R. P. Van Duyne, and G. C. Schatz, "Tip-Enhanced Raman Excitation Spectroscopy (TERES): Direct Spectral Characterization of the Gap-Mode Plasmon", *Nano Letters*, vol. 19, no. 10, pp. 7309–7316, 2019, ISSN: 1530-6984. DOI: 10.1021/acs.nanolett.9b02925.

[178] S. Raza, N. Stenger, A. Pors, T. Holmgaard, S. Kadkhodazadeh, J. B. Wagner, K. Pedersen, M. Wubs, S. I. Bozhevolnyi, and N. A. Mortensen, "Extremely confined gap surface-plasmon modes excited by electrons", *Nature Communications*, vol. 5, no. 1, p. 4125, 2014, ISSN: 2041-1723. DOI: 10.1038/ncomms5125.

[179] D. Tosi, M. Sypabekova, A. Bekmurzayeva, C. Molardi, and K. Dukenbayev, "Principles of fiber optic sensors", in *Optical Fiber Biosensors*, Elsevier, 2022, pp. 19–78. DOI: 10.1016/B978-0-12-819467-6.00016-0.

[180] O. Lozan, "Surface Plasmons and Hot Electrons Imaging with Femtosecond Pump-Probe Thermoreflectance", PhD thesis, L'UNIVERSITÉ DE BORDEAUX, 2015. [Online]. Available: https://theses.hal.science/tel-01295431.

[181] M. W. Vogel, "Optimization of plasmon nano-focusing in tapered metal rods", *Journal of Nanophotonics*, vol. 2, no. 1, p. 021 852, 2008, ISSN: 1934-2608. DOI: 10.1117/1.3046689.

[182] A. Taguchi, N. Hayazawa, K. Furusawa, H. Ishitobi, and S. Kawata, "Deep-UV tip-enhanced Raman scattering", *Journal of Raman Spectroscopy*, vol. 40, no. 9, pp. 1324–1330, 2009, ISSN: 03770486. DOI: 10.1002/jrs.2287.

[183] M.-H. Chiu, J.-H. Li, and T. Nagao, "Optical Properties of Au-Based and Pt-Based Alloys for Infrared Device Applications: A Combined First Principle and Electromagnetic Simulation Study", *Micromachines*, vol. 10, no. 1, p. 73, 2019. DOI: 10.3390/mi10010073.

[184] M. A. Ordal, L. L. Long, R. J. Bell, S. E. Bell, R. R. Bell, R. W. Alexander, and C. A. Ward, "Optical properties of the metals Al, Co, Cu, Au, Fe, Pb, Ni, Pd, Pt, Ag, Ti, and W in the infrared and far infrared", *Applied Optics*, vol. 22, no. 7, p. 1099, 1983. DOI: 10.1364/AO.22.001099.

[185] M. O. Sallam, G. A. E. Vandenbosch, G. Gielen, and E. A. Soliman, "Integral equations formulation of plasmonic transmission lines", *Optics Express*, vol. 22, no. 19, p. 22 388, 2014, ISSN: 1094-4087. DOI: 10.1364/OE.22.022388.

[186] A. P. Hibbins, "GRATING COUPLING OF SURFACE PLASMON POLARITONS AT VISIBLE AND MICROWAVE FREQUENCIES Submitted by", PhD thesis, University of Exeter, 1999. [Online]. Available: https://books.google.co.uk/books?id=zzS3GwAACAAJ.

[187] A. Hessel and A. A. Oliner, "A New Theory of Wood's Anomalies on Optical Gratings", *Applied Optics*, vol. 4, no. 10, p. 1275, 1965, ISSN: 0003-6935. DOI: 10.1364/AO.4.001275.

[188] U Fano, "The Theory of Anomalous Diffraction Gratings and of Quasi-Stationary Waves on Metallic Surfaces (Sommerfeld's Waves)", *J. Opt. Soc. Am.*, vol. 31, no. 3, pp. 213–222, 1941. DOI: 10.1364/JOSA.31.000213. [Online]. Available: https://opg.optica.org/abstract.cfm?URI=josa-31-3-213.

[189] S. M. A. Uddin, S. S. Chowdhury, and E. Kabir, "Numerical Analysis of a Highly Sensitive Surface Plasmon Resonance Sensor for SARS-CoV-2 Detection", *Plasmonics*, vol. 16, no. 6, pp. 2025–2037, 2021, ISSN: 1557-1955. DOI: 10.1007/s11468-021-01455-0.

[190] C. E. Nilsson, S Abbas, M Bennemo, A Larsson, M. D. Hämäläinen, and Å Frostell-Karlsson, "A novel assay for influenza virus quantification using surface plasmon resonance", *Vaccine*, vol. 28, no. 3, pp. 759–766, 2010, ISSN: 0264410X. DOI: 10.1016/j.vaccine.2009.10.070.

[191] N. Shukla, P. Chetri, R. Boruah, A. Gogoi, and G. A. Ahmed, "Surface Plasmon Resonance Biosensors Based on Kretschmann Configuration: Basic Instrumentation and Applications", in, 2022, pp. 191–222. DOI: 10.1007/978-3-030-99491-4_6. [Online]. Available: https://link.springer.com/10.1007/978-3-030-99491-4{_}6.

[192] G. Janith, H. Herath, N. Hendeniya, D. Attygalle, D. Amarasinghe, V. Logeeshan, P. Wickramasinghe, and Y. Wijayasinghe, "Advances in surface plasmon resonance biosensors for medical diagnostics: An overview of recent developments and techniques", *Journal of Pharmaceutical and Biomedical Analysis Open*, vol. 2, p. 100 019, 2023, ISSN: 2949771X. DOI: 10.1016/j.jpbao.2023.100019.

[193] S. Berweger, "Plasmonic Antennas for Optical Nanocrystallography and Femtosecond Spatio-Temporal Control", PhD thesis, University of Washington, Seattle, 2011.

[194] H. Raether, "Surface plasmons on smooth surfaces", in, 1988, pp. 4–39. DOI: 10.1007/BFb0048319.

[195] M. Kartau, A. Skvortsova, V. Tabouillot, S. K. Chaubey, P. Bainova, R. Kumar, V. Burtsev, V. Svorcik, N. Gadegaard, S. W. Im, M. Urbanova, O. Lyutakov, M. Kadodwala, and A. S. Karimullah, "Chiral Metafilms and Surface Enhanced Raman Scattering for Enantiomeric Discrimination of Helicoid Nanoparticles", *Advanced Optical Materials*, vol. 11, no. 9, 2023, ISSN: 2195-1071. DOI: 10.1002/adom.202202991.

[196] S. T. Koev, A. Agrawal, H. J. Lezec, and V. A. Aksyuk, "An Efficient Large-Area Grating Coupler for Surface Plasmon Polaritons", *Plasmonics*, vol. 7, no. 2, pp. 269–277, 2012, ISSN: 1557-1955. DOI: 10.1007/s11468-011-9303-7.

[197] R. L. Olmon, B. Slovick, T. W. Johnson, D. Shelton, S.-H. Oh, G. D. Boreman, and M. B. Raschke, "Optical dielectric function of gold", *Physical Review B*, vol. 86, no. 23, p. 235 147, 2012, ISSN: 1098-0121. DOI: 10.1103/PhysRevB.86.235147.

[198] P Lalanne, J. P. Hugonin, and J. C. Rodier, "Theory of Surface Plasmon Generation at Nanoslit Apertures", *Physical Review Letters*, vol. 95, no. 26, p. 263 902, 2005, ISSN: 0031-9007. DOI: 10.1103/PhysRevLett.95.263902.

[199] R. Mehfuz, F. A. Chowdhury, and K. J. Chau, "Imaging slit-coupled surface plasmon polaritons using conventional optical microscopy", *Optics Express*, vol. 20, no. 10, p. 10 526, 2012, ISSN: 1094-4087. DOI: 10.1364/OE.20.010526.

[200] S. Berweger, J. M. Atkin, R. L. Olmon, and M. B. Raschke, "Adiabatic Tip-Plasmon Focusing for Nano-Raman Spectroscopy", *The Journal of Physical Chemistry Letters*, vol. 1, no. 24, pp. 3427–3432, 2010, ISSN: 1948-7185. DOI: 10.1021/jz101289z.

[201] J. Renger, S. Grafström, and L. M. Eng, "Direct excitation of surface plasmon polaritons in nanopatterned metal surfaces and thin films", *Physical Review B*, vol. 76, no. 4, p. 45 431, 2007, ISSN: 1098-0121. DOI: 10.1103/PhysRevB.76.045431.

[202] D. K. Gramotnev and M. W. Vogel, "Ultimate capabilities of sharp metal tips for plasmon nanofocusing, near-field trapping and sensing", *Physics Letters A*, vol. 375, no. 39, pp. 3464–3468, 2011, ISSN: 03759601. DOI: 10.1016/j.physleta.2011.07.053.

[203] J. J. Burke, G. I. Stegeman, and T. Tamir, "Surface-polariton-like waves guided by thin, lossy metal films", *Physical Review B*, vol. 33, no. 8, pp. 5186–5201, 1986, ISSN: 0163-1829. DOI: 10.1103/PhysRevB.33.5186.

[204] O. Lozan, R. Sundararaman, B. Ea-Kim, J.-M. Rampnoux, P. Narang, S. Dilhaire, and P. Lalanne, "Increased rise time of electron temperature during adiabatic plasmon focusing", *Nature Communications*, vol. 8, no. 1, p. 1656, 2017, ISSN: 2041-1723.

DOI: 10.1038/s41467-017-01802-y. [Online]. Available: https://www.nature.com/articles/s41467-017-01802-y.

[205] E. Verhagen, A. Polman, and L. K. Kuipers, "Nanofocusing in laterally tapered plasmonic waveguides", *Optics Express*, vol. 16, no. 1, p. 45, 2008, ISSN: 1094-4087. DOI: 10.1364/OE.16.000045.

[206] M. I. Stockman, "Nanofocusing of Optical Energy in Tapered Plasmonic Waveguides", *Physical Review Letters*, vol. 93, no. 13, p. 137 404, 2004, ISSN: 0031-9007. DOI: 10.1103/PhysRevLett.93.137404.

[207] S. Wijesuriya, K. Burugapalli, R. Mackay, G. Ajaezi, and W. Balachandran, "Chemically Roughened Solid Silver: A Simple, Robust and Broadband SERS Substrate", *Sensors*, vol. 16, no. 10, p. 1742, 2016, ISSN: 1424-8220. DOI: 10.3390/s16101742.

[208] C.-H. Lai, G.-A. Wang, T.-K. Ling, T.-J. Wang, P.-k. Chiu, Y.-F. Chou Chau, C.-C. Huang, and H.-P. Chiang, "Near infrared surface-enhanced Raman scattering based on star-shaped gold/silver nanoparticles and hyperbolic metamaterial", *Scientific Reports*, vol. 7, no. 1, p. 5446, 2017, ISSN: 2045-2322. DOI: 10.1038/s41598-017-05939-0.

[209] G. W. Auner, S. K. Koya, C. Huang, B. Broadbent, M. Trexler, Z. Auner, A. Elias, K. C. Mehne, and M. A. Brusatori, "Applications of Raman spectroscopy in cancer diagnosis", *Cancer and Metastasis Reviews*, vol. 37, no. 4, pp. 691–717, 2018, ISSN: 0167-7659. DOI: 10.1007/s10555-018-9770-9.

[210] Q. Zou, S. Mo, X. Pei, Y. Wang, T. Xue, M. Mayilamu, and G. Qin, "Fabrication of novel biological substrate based on photolithographic process for surface enhanced Raman spectroscopy", *AIP Advances*, vol. 8, no. 8, 2018, ISSN: 21583226. DOI: 10.1063/1.5039600.

[211] S. Olaf, "Planar Interfaces", in *The Physics of Thin Film Optical Spectra*, 2nd ed., Springer International Publishing, 2016, p. 86, ISBN: 978-3-319-21602-7. DOI: 10.1007/978-3-319-21602-7.

[212] E. V. Stenson, J. Horn-Stanja, M. R. Stoneking, and T. S. Pedersen, "Debye length and plasma skin depth: two length scales of interest in the creation and diagnosis of laboratory pair plasmas", *Journal of Plasma Physics*, vol. 83, no. 1, 2017, ISSN: 0022-3778. DOI: 10.1017/S0022377817000022.

[213] F. Logiurato, "Relativistic Derivations of de Broglie and Planck-Einstein Equations", *Journal of Modern Physics*, vol. 05, no. 01, pp. 1–7, 2014, ISSN: 2153-1196. DOI: 10.4236/jmp.2014.51001. arXiv: 1208.0119.

[214] F. Shao and R. Zenobi, "Tip-enhanced Raman spectroscopy: principles, practice, and applications to nanospectroscopic imaging of 2D materials", *Analytical and*

Bioanalytical Chemistry, vol. 411, no. 1, pp. 37–61, 2019, ISSN: 1618-2642. DOI: 10.1007/s00216-018-1392-0.

[215] A. B. Zrimsek, N. Chiang, M. Mattei, S. Zaleski, M. O. McAnally, C. T. Chapman, A.-I. Henry, G. C. Schatz, and R. P. Van Duyne, "Single-Molecule Chemistry with Surface- and Tip-Enhanced Raman Spectroscopy", *Chemical Reviews*, vol. 117, no. 11, pp. 7583–7613, 2017, ISSN: 0009-2665. DOI: 10.1021/acs.chemrev.6b00552.

[216] N. Kumar, S. Mignuzzi, W. Su, and D. Roy, "Tip-enhanced Raman spectroscopy: principles and applications", *EPJ Techniques and Instrumentation*, vol. 2, no. 1, p. 9, 2015, ISSN: 2195-7045. DOI: 10.1140/epjti/s40485-015-0019-5.

[217] Y. Seo and W. Jhe, "Atomic force microscopy and spectroscopy", *Reports on Progress in Physics*, vol. 71, no. 1, 2008, ISSN: 0034-4885. DOI: 10.1088/0034-4885/71/1/016101.

[218] E. Sheremet, L. Kim, D. Stepanichsheva, V. Kolchuzhin, A. Milekhin, D. Zahn, and R. Rodriguez, "Localized surface curvature artifacts in tip-enhanced nanospectroscopy imaging", *Ultramicroscopy*, vol. 206, 2019, ISSN: 03043991. DOI: 10.1016/j.ultramic.2019.112811.

[219] E. J. Ayars, H. D. Hallen, and C. L. Jahncke, "Electric Field Gradient Effects in Raman Spectroscopy", *Physical Review Letters*, vol. 85, no. 19, pp. 4180–4183, 2000, ISSN: 0031-9007. DOI: 10.1103/PhysRevLett.85.4180.

[220] D. Langley, R. A. Coutu Jr., L. A. Starman, and S. Rogers, "Optical metamaterials for photonics applications", S. Rogers, D. P. Casasent, J. J. Dolne, T. J. Karr, and V. L. Gamiz, Eds., 2009, 74680H. DOI: 10.1117/12.828509.

[221] K.-S. Lee and M. A. El-Sayed, "Gold and Silver Nanoparticles in Sensing and Imaging: Sensitivity of Plasmon Response to Size, Shape, and Metal Composition", *The Journal of Physical Chemistry B*, vol. 110, no. 39, pp. 19 220–19 225, 2006, ISSN: 1520-6106. DOI: 10.1021/jp062536y.

[222] Pilot, Signorini, Durante, Orian, Bhamidipati, and Fabris, "A Review on Surface-Enhanced Raman Scattering", *Biosensors*, vol. 9, no. 2, p. 57, 2019, ISSN: 2079-6374. DOI: 10.3390/bios9020057.

[223] C. Zhang, C. Min, L. Li, Y. Zhang, S. Wei, X. Wang, and X. Yuan, "Effect of the focused gap-plasmon mode on tip-enhanced Raman excitation and scattering", *Optics Express*, vol. 31, no. 3, p. 4216, 2023, ISSN: 1094-4087. DOI: 10.1364/OE.481152.

[224] F. Pashaee, R. Hou, P. Gobbo, M. S. Workentin, and F. Lagugné-Labarthet, "Tip-Enhanced Raman Spectroscopy of Self-Assembled Thiolated Monolayers on Flat Gold Nanoplates Using Gaussian-Transverse and Radially Polarized Excitations",

The Journal of Physical Chemistry C, vol. 117, no. 30, pp. 15 639–15 646, 2013, ISSN: 1932-7447. DOI: 10.1021/jp403157v.

[225] I. A. Milekhin, A. G. Milekhin, and D. R. T. Zahn, "Surface- and Tip-Enhanced Raman Scattering by CdSe Nanocrystals on Plasmonic Substrates", *Nanomaterials*, vol. 12, no. 13, p. 2197, 2022, ISSN: 2079-4991. DOI: 10.3390/nano12132197.

[226] K. S. Youngworth and T. G Brown, "Focusing of high numerical aperture cylindrical-vector beams", *Optics Express*, vol. 7, no. 2, p. 77, 2000, ISSN: 1094-4087. DOI: 10.1364/OE.7.000077.

[227] Z. D. Schultz, J. M. Marr, and H. Wang, "Tip enhanced Raman scattering: plasmonic enhancements for nanoscale chemical analysis", *Nanophotonics*, vol. 3, no. 1-2, pp. 91–104, 2014, ISSN: 2192-8614. DOI: 10.1515/nanoph-2013-0040.

[228] A. Taguchi, J. Yu, P. Verma, and S. Kawata, "Optical antennas with multiple plasmonic nanoparticles for tip-enhanced Raman microscopy", *Nanoscale*, vol. 7, no. 41, pp. 17 424–17 433, 2015, ISSN: 2040-3364. DOI: 10.1039/C5NR05022G.

[229] H. Ditlbacher, A. Hohenau, D. Wagner, U. Kreibig, M. Rogers, F. Hofer, F. R. Aussenegg, and J. R. Krenn, "Silver Nanowires as Surface Plasmon Resonators", *Physical Review Letters*, vol. 95, no. 25, 2005, ISSN: 0031-9007. DOI: 10.1103/PhysRevLett.95.257403.

[230] M. Futamata, Y. Maruyama, and M. Ishikawa, "Local Electric Field and Scattering Cross Section of Ag Nanoparticles under Surface Plasmon Resonance by Finite Difference Time Domain Method", *The Journal of Physical Chemistry B*, vol. 107, no. 31, pp. 7607–7617, 2003, ISSN: 1520-6106. DOI: 10.1021/jp022399e.

[231] B.-S. Yeo, W. Zhang, C. Vannier, and R. Zenobi, "Enhancement of Raman Signals with Silver-Coated Tips", *Applied Spectroscopy*, vol. 60, no. 10, pp. 1142–1147, 2006, ISSN: 0003-7028. DOI: 10.1366/000370206778664662.

[232] W. Bao, M. Melli, N. Caselli, F. Riboli, D. S. Wiersma, M. Staffaroni, H. Choo, D. F. Ogletree, S. Aloni, J. Bokor, S. Cabrini, F. Intonti, M. B. Salmeron, E. Yablonovitch, P. J. Schuck, and A. Weber-Bargioni, "Mapping Local Charge Recombination Heterogeneity by Multidimensional Nanospectroscopic Imaging", *Science*, vol. 338, no. 6112, pp. 1317–1321, 2012, ISSN: 0036-8075. DOI: 10.1126/science.1227977.

[233] W. Bao, N. J. Borys, C. Ko, J. Suh, W. Fan, A. Thron, Y. Zhang, A. Buyanin, J. Zhang, S. Cabrini, P. D. Ashby, A. Weber-Bargioni, S. Tongay, S. Aloni, D. F. Ogletree, J. Wu, M. B. Salmeron, and P. J. Schuck, "Visualizing nanoscale excitonic relaxation properties of disordered edges and grain boundaries in monolayer molybdenum disulfide", *Nature Communications*, vol. 6, no. 1, 2015, ISSN: 2041-1723. DOI: 10.1038/ncomms8993.

[234] C. Ropers, C. C. Neacsu, T. Elsaesser, M. Albrecht, M. B. Raschke, and C. Lienau, "Grating-Coupling of Surface Plasmons onto Metallic Tips: A Nanoconfined Light Source", *Nano Letters*, vol. 7, no. 9, pp. 2784–2788, 2007, ISSN: 1530-6984. DOI: 10.1021/nl071340m.

[235] W. Bao, M. Staffaroni, J. Bokor, M. B. Salmeron, E. Yablonovitch, S. Cabrini, A. Weber-Bargioni, and P. J. Schuck, "Plasmonic near-field probes: a comparison of the campanile geometry with other sharp tips", *Optics Express*, vol. 21, no. 7, p. 8166, 2013, ISSN: 1094-4087. DOI: 10.1364/OE.21.008166.

[236] K. Zhang, Y. Bao, M. Cao, S.-i. Taniguchi, M. Watanabe, T. Kambayashi, T. Okamoto, M. Haraguchi, X. Wang, K. Kobayashi, H. Yamada, B. Ren, and T. Tachizaki, "Low-Background Tip-Enhanced Raman Spectroscopy Enabled by a Plasmon Thin-Film Waveguide Probe", *Analytical Chemistry*, vol. 93, no. 21, pp. 7699–7706, 2021. DOI: 10.1021/acs.analchem.1c00806.

[237] T. Itoh, M. Procházka, Z.-C. Dong, W. Ji, Y. S. Yamamoto, Y. Zhang, and Y. Ozaki, "Toward a New Era of SERS and TERS at the Nanometer Scale: From Fundamentals to Innovative Applications", *Chemical Reviews*, vol. 123, no. 4, pp. 1552–1634, 2023, ISSN: 0009-2665. DOI: 10.1021/acs.chemrev.2c00316. [Online]. Available: https://pubs.acs.org/doi/10.1021/acs.chemrev.2c00316.

[238] J. Langer, D. Jimenez de Aberasturi, J. Aizpurua, R. A. Alvarez-Puebla, B. Auguié, J. J. Baumberg, G. C. Bazan, S. E. J. Bell, A. Boisen, A. G. Brolo, J. Choo, D. Cialla-May, V. Deckert, L. Fabris, K. Faulds, F. J. García de Abajo, R. Goodacre, D. Graham, A. J. Haes, C. L. Haynes, C. Huck, T. Itoh, M. Käll, J. Kneipp, N. A. Kotov, H. Kuang, E. C. Le Ru, H. K. Lee, J.-F. Li, X. Y. Ling, S. A. Maier, T. Mayerhöfer, M. Moskovits, K. Murakoshi, J.-M. Nam, S. Nie, Y. Ozaki, I. Pastoriza-Santos, J. Perez-Juste, J. Popp, A. Pucci, S. Reich, B. Ren, G. C. Schatz, T. Shegai, S. Schlücker, L.-L. Tay, K. G. Thomas, Z.-Q. Tian, R. P. Van Duyne, T. Vo-Dinh, Y. Wang, K. A. Willets, C. Xu, H. Xu, Y. Xu, Y. S. Yamamoto, B. Zhao, and L. M. Liz-Marzán, "Present and Future of Surface-Enhanced Raman Scattering", *ACS Nano*, vol. 14, no. 1, pp. 28–117, 2020, ISSN: 1936-0851. DOI: 10.1021/acsnano.9b04224. [Online]. Available: https://pubs.acs.org/doi/10.1021/acsnano.9b04224.

[239] T. Deckert-Gaudig, A. Taguchi, S. Kawata, and V. Deckert, "Tip-enhanced Raman spectroscopy – from early developments to recent advances", *Chemical Society Reviews*, vol. 46, no. 13, pp. 4077–4110, 2017, ISSN: 0306-0012. DOI: 10.1039/C7CS00209B. [Online]. Available: https://xlink.rsc.org/?DOI=C7CS00209B.

[240] Z. Zhang, S. Sheng, R. Wang, and M. Sun, "Tip-Enhanced Raman Spectroscopy", *Analytical Chemistry*, vol. 88, no. 19, pp. 9328–9346, 2016, ISSN: 0003-2700. DOI: 10.

1021/acs.analchem.6b02093. [Online]. Available: https://pubs.acs.org/doi/10.1021/acs.analchem.6b02093.

[241] I. Maouli, A. Taguchi, Y. Saito, S. Kawata, and P. Verma, "Optical antennas for tunable enhancement in tip-enhanced Raman spectroscopy imaging", *Applied Physics Express*, vol. 8, no. 3, p. 032 401, 2015, ISSN: 1882-0778. DOI: 10.7567/APEX.8.032401. [Online]. Available: https://iopscience.iop.org/article/10.7567/APEX.8.032401.

[242] "Thin Film Processes", in *Hybrid Microcircuit Technology Handbook*, J. J. Licari and L. R. Enlow, Eds., 2nd, Elsevier, 1998, ch. 3, pp. 63–103, ISBN: 978-0-8155-1423-7. DOI: 10.1016/B978-081551423-7.50005-5. [Online]. Available: https://linkinghub.elsevier.com/retrieve/pii/B9780815514237500055.

[243] I. Lalovic and A. Kroyan, *Illumination spectrum affects lithographic imaging*, 2001. [Online]. Available: https://www.laserfocusworld.com/optics/article/16556779/illumination-spectrum-affects-lithographic-imaging (visited on 01/16/2023).

[244] K. E. Docherty, "Improvements to the alignment process in electron-beam lithography", PhD thesis, 2009.

[245] S. Thoms, D. S. Macintyre, K. E. Docherty, and J. M. Weaver, "Alignment verification for electron beam lithography", *Microelectronic Engineering*, vol. 123, pp. 9–12, 2014, ISSN: 01679317. DOI: 10.1016/j.mee.2014.02.005.

[246] L. M. Li, "An algorithm for computing exact least-trimmed squares estimate of simple linear regression with constraints", *Computational Statistics & Data Analysis*, vol. 48, no. 4, pp. 717–734, 2005, ISSN: 01679473. DOI: 10.1016/j.csda.2004.04.003.

[247] D. E. Davis, "Registration Mark Detection for Electron-Beam Lithography—EL1 System", *IBM Journal of Research and Development*, vol. 24, no. 5, pp. 545–553, 1980, ISSN: 0018-8646. DOI: 10.1147/rd.245.0545.

[248] K. Docherty, K. Lister, J. Romijn, and J. Weaver, "High robustness of correlation-based alignment with Penrose patterns to marker damage in electron beam lithography", *Microelectronic Engineering*, vol. 86, no. 4-6, pp. 532–534, 2009, ISSN: 01679317. DOI: 10.1016/j.mee.2008.11.037.

[249] D. M. Holburn, G. A. C. Jones, and H. Ahmed, "A pattern recognition technique using sequences of marks for registration in electron beam lithography", *Journal of Vacuum Science and Technology*, vol. 19, no. 4, pp. 1229–1233, 1981, ISSN: 0022-5355. DOI: 10.1116/1.571250.

[250] I. Buyanova, A. Henry, B. Monemar, J. Lindström, and G. Oehrlein, "Photoluminescence characterization of SF6–O2 plasma etching of silicon", in *C,H,N and O*

in Si and Characterization and Simulation of Materials and Processes, Elsevier, 1996, pp. 100–103. DOI: 10.1016/B978-0-444-82413-4.50027-5.

[251] N.-T. Nguyen, "Fabrication technologies", in *Micromixers*, Elsevier, 2012, pp. 113–161. DOI: 10.1016/B978-1-4377-3520-8.00004-8.

[252] S. Tinck, E. C. Neyts, and A. Bogaerts, "Fluorine–Silicon Surface Reactions during Cryogenic and Near Room Temperature Etching", *The Journal of Physical Chemistry C*, vol. 118, no. 51, pp. 30 315–30 324, 2014, ISSN: 1932-7447. DOI: 10.1021/jp5108872.

[253] S. K. Lamichhane and M. R. Lamsal, "Etching of Crystalline Silicon in Thermal Environment", *Himalayan Physics*, vol. 2, pp. 38–42, 2011, ISSN: 2542-2545. DOI: 10.3126/hj.v2i2.5209.

[254] A. Midha, "Batch-fabrication of novel nanoprobes for SPM. PhD thesis", PhD thesis, University of Glasgow, 1999, pp. 369–382.

[255] H. Seidel, L. Csepregi, A. Heuberger, and H. Baumgärtel, "Anisotropic Etching of Crystalline Silicon in Alkaline Solutions: I . Orientation Dependence and Behavior of Passivation Layers", *Journal of The Electrochemical Society*, vol. 137, no. 11, pp. 3612–3626, 1990, ISSN: 0013-4651. DOI: 10.1149/1.2086277.

[256] Y. Bar-Cohen, "High Temperature Materials and Mechanisms", in *High Temperature Materials and Mechanisms*, Y. Bar-Cohen, Ed., CRC Press, 2014, ch. 7, p. 206, ISBN: 9780429099847. DOI: 10.1201/b16545.

[257] N. Fujitsuka, K. Hamaguchi, and H. Funabashi, "Aluminum Protected Silicon Anisotropic Etching Technique Using TMAH with an Oxidizing Agent and Dissolved Si", *R&D Review of Toyota*, vol. 39, no. 2, pp. 34–40, 2004.

[258] Y. Zhang, K. Docherty, and J. Weaver, "Batch fabrication of cantilever array aperture probes for scanning near-field optical microscopy", *Microelectronic Engineering*, vol. 87, no. 5-8, pp. 1229–1232, 2010, ISSN: 01679317. DOI: 10.1016/j.mee.2009.11.140.

[259] M. J. Kim and R. W. Carpenter, "Composition and structure of native oxide on silicon by high resolution analytical electron microscopy", *Journal of Materials Research*, vol. 5, no. 2, pp. 347–351, 1990. DOI: 10.1557/JMR.1990.0347.

[260] D. Burt, P. Dobson, L. Donaldson, and J. Weaver, "A simple method for high yield fabrication of sharp silicon tips", *Microelectronic Engineering*, vol. 85, no. 3, pp. 625–630, 2008, ISSN: 01679317. DOI: 10.1016/j.mee.2007.11.010.

[261] T. Monteiro, P. Kastytis, L. Gonçalves, G. Minas, and S. Cardoso, "Dynamic Wet Etching of Silicon through Isopropanol Alcohol Evaporation", *Micromachines*, vol. 6, no. 10, pp. 1534–1545, 2015, ISSN: 2072-666X. DOI: 10.3390/mi6101437.

[262] H. Zhou, B. K. Chong, P. Stopford, G. Mills, A. Midha, L. Donaldson, and J. M. R. Weaver, "Lithographically defined nano and micro sensors using "float coating" of resist and electron beam lithography", *Journal of Vacuum Science & Technology B: Microelectronics and Nanometer Structures*, vol. 18, no. 6, p. 3594, 2000, ISSN: 0734211X. DOI: 10.1116/1.1321271.

[263] B. Sun, P. Zhang, T. Zhang, S. Shangguan, S. Wu, and X. Ma, "Single step electron-beam lithography archiving lift-off for T-gate in high electron mobility transistor fabrication", *Microelectronic Engineering*, vol. 229, p. 111 337, 2020, ISSN: 01679317. DOI: 10.1016/j.mee.2020.111337.

[264] M. M. Hossain and M. A. Talukder, "Graphene surface plasmon sensor for ultra-low-level SARS-CoV-2 detection", *PLOS ONE*, vol. 18, no. 4, R. Thotagamuge, Ed., e0284812, 2023, ISSN: 1932-6203. DOI: 10.1371/journal.pone.0284812.

[265] R. Verkhovskii, A. Kozlova, V. Atkin, R. Kamyshinsky, T. Shulgina, and O. Nechaeva, "Physical properties and cytotoxicity of silver nanoparticles under different polymeric stabilizers", *Heliyon*, vol. 5, no. 3, e01305, 2019, ISSN: 24058440. DOI: 10.1016/j.heliyon.2019.e01305.

[266] T. W. Huh, G. Han, W. J. Ban, and H. S. Ahn, "Efficient fabrication of gold tips by electrochemical etching for tip-enhanced Raman spectroscopy", *International Journal of Precision Engineering and Manufacturing*, 2017, ISSN: 20054602. DOI: 10.1007/s12541-017-0028-1.

[267] M. Martina, M. Fleischer, and C. Burkhardt, "Template stripping and bonding of smooth probes with nanoscale features for tip-enhanced Raman spectroscopy", *Microelectronic Engineering*, vol. 171, pp. 31–36, 2017, ISSN: 01679317. DOI: 10.1016/j.mee.2017.01.033. [Online]. Available: https://linkinghub.elsevier.com/retrieve/pii/S0167931717300424.

[268] K. Docherty, S. Thoms, P. Dobson, and J. Weaver, "Improvements to the alignment process in a commercial vector scan electron beam lithography tool", *Microelectronic Engineering*, vol. 85, no. 5-6, pp. 761–763, 2008, ISSN: 01679317. DOI: 10.1016/j.mee.2008.01.081.

[269] T. Umakoshi, M. Tanaka, Y. Saito, and P. Verma, "White nanolight source for optical nanoimaging", *Science Advances*, 2020, ISSN: 23752548. DOI: 10.1126/sciadv.aba4179.

[270] C. S. Gardner and G. Papen, "Optical Communications", in *Reference Data for Engineers*, W. M. Middleton and M. E. Van Valkenburg, Eds., 9th ed., Elsevier, 2002, ch. 22, pp. 22–1–22–28, ISBN: 9780750672917. DOI: doi.org/10.1016/B978-075067291-7/50024-8..

[271] C. Palmer, "The Properties of Diffraction Gratings", in *Diffraction Grating Handbook (eighth edition)*, 8th ed., Newport Corporation (MKS Instruments), 2020.

[272] K. F. Domke and B. Pettinger, *Comment on "Scanning-probe Raman spectroscopy with single-molecule sensitivity"*, 2007. DOI: 10.1103/PhysRevB.75.236401.

[273] Y. Shwan, B. Ghafoor, and G. Hamasalih, "Optimization of Surface Plasmon Resonance (SPR) for Gold/Air Interface by using Kretschmann Configuration", *Engineering and Technology Journal*, vol. 40, no. 10, pp. 1–7, 2022, ISSN: 2412-0758. DOI: 10.30684/etj.2022.132902.1151. [Online]. Available: https://etj.uotechnology.edu.iq/article{_}175706.html.

[274] L. Meng, T. Huang, X. Wang, S. Chen, Z. Yang, and B. Ren, "Gold-coated AFM tips for tip-enhanced Raman spectroscopy: theoretical calculation and experimental demonstration", *Optics Express*, vol. 23, no. 11, p. 13 804, 2015, ISSN: 1094-4087. DOI: 10.1364/OE.23.013804.

[275] R. Wang, J. Li, J. Rigor, N. Large, P. Z. El-Khoury, A. Y. Rogachev, and D. Kurouski, "Direct Experimental Evidence of Hot Carrier-Driven Chemical Processes in Tip-Enhanced Raman Spectroscopy (TERS)", *The Journal of Physical Chemistry C*, vol. 124, no. 3, pp. 2238–2244, 2020, ISSN: 1932-7447. DOI: 10.1021/acs.jpcc.9b12002. [Online]. Available: https://pubs.acs.org/doi/10.1021/acs.jpcc.9b12002.

[276] J.-W. Lee, Z. Feng, R. L. Engelstad, and E. G. Lovell, "Modeling thermal reflow of resist contact hole arrays", in *23rd Annual BACUS Symposium on Photomask Technology*, 2003. DOI: 10.1117/12.517886.

[277] E. Meyer, H. J. Hug, and R. Bennewitz, "Artifacts in SPM", in *Advanced Texts in Physics*, 2004, ch. 6, pp. 153–171, ISBN: 978-3-662-09801-1. DOI: 10.1007/978-3-662-09801-1_6.

[278] Liming Ren and Baoqin Chen, "Proximity effect in electron beam lithography", in *Proceedings. 7th International Conference on Solid-State and Integrated Circuits Technology, 2004.*, IEEE, 2004, 579–582 vol.1, ISBN: 0-7803-8511-X. DOI: 10.1109/ICSICT.2004.1435073.

[279] Y. Ge, Y. Zhang, J. M. R. Weaver, H. Zhou, and P. S. Dobson, "Topography-free sample for thermal spatial response measurement of scanning thermal microscopy", *Journal of Vacuum Science & Technology B, Nanotechnology and Microelectronics: Materials, Processing, Measurement, and Phenomena*, vol. 33, no. 6, 06FA03, 2015, ISSN: 2166-2746. DOI: 10.1116/1.4933172.

[280] F. Richheimer, *Personal Communication, Feb 2020*.

[281] E. Seo, B. K. Choi, and O. Kim, "Determination of proximity effect parameters and the shape bias parameter in electron beam lithography", *Microelectronic Engineering*, vol. 53, no. 1-4, pp. 305–308, 2000, ISSN: 01679317. DOI: 10.1016/S0167-9317(00)00320-8.

[282] Mentor, *Tanner AMS and MEMS Flows*. [Online]. Available: https://www.mentor.com/tannereda/l-edit (visited on 04/25/2020).

[283] X. Liu, S. Lebedkin, H. Besser, W. Pfleging, S. Prinz, M. Wissmann, P. M. Schwab, I. Nazarenko, M. Guttmann, M. M. Kappes, and U. Lemmer, "Fundamentals", in *Organic Semiconductor Lasers and Tailored Nanostructures for Raman Spectroscopy*, 1, vol. 9, KIT Scientific Publishing, 2015, ch. 2, p. 59. DOI: 10.1021/nn506589a.

[284] P. Steinmann and J. M. Weaver, "Nanometer-scale gaps between metallic electrodes fabricated using a statistical alignment technique", *Applied Physics Letters*, 2005, ISSN: 00036951. DOI: 10.1063/1.1862342.

[285] K. E. Docherty, *Improvements to the alignment process in electron-beam lithography*. University of Glasgow, 2010, p. 69.

[286] P. Steinmann and J. M. R. Weaver, "Nanometer-scale gaps between metallic electrodes fabricated using a statistical alignment technique", *Applied Physics Letters*, vol. 86, no. 6, p. 063 104, 2005, ISSN: 0003-6951. DOI: 10.1063/1.1862342.

[287] N. Kumar, B. M. Weckhuysen, A. J. Wain, and A. J. Pollard, "Nanoscale chemical imaging using tip-enhanced Raman spectroscopy", *Nature Protocols*, vol. 14, no. 4, pp. 1169–1193, 2019, ISSN: 1754-2189. DOI: 10.1038/s41596-019-0132-z.

[288] S. Wood, F. Richheimer, T. Vincent, V. Tong, A. Catanzaro, Y. Cao, O. Kazakova, and F. Araujo de Castro, "Curvature-enhanced localised emission from dark states in wrinkled monolayer WSe ₂ at room temperature", *Science and Technology of Advanced Materials*, vol. 24, no. 1, 2023, ISSN: 1468-6996. DOI: 10.1080/14686996.2023.2278443.

[289] F. Richheimer, T. Vincent, A. Catanzaro, N. J. Huáng, M. A. Baker, R. A. Dorey, C. E. Giusca, F. A. Castro, O. Kazakova, and S. Wood, "Probing Nanoscale Schottky Barrier Characteristics at WSe ₂ /Graphene Heterostructures via Electrostatic Doping", *Advanced Electronic Materials*, vol. 8, no. 9, 2022, ISSN: 2199-160X. DOI: 10.1002/aelm.202200196.

[290] N. Kakenov, O. Balci, S. Balci, and C. Kocabas, "Probing molecular interactions on carbon nanotube surfaces using surface plasmon resonance sensors", *Applied Physics Letters*, vol. 101, no. 22, 2012, ISSN: 0003-6951. DOI: 10.1063/1.4768927.

[291] W. M. Mukhtar, P. S. Menon, S Shaari, M. Z. A. Malek, and A. M. Abdullah, "Angle Shifting in Surface Plasmon Resonance: Experimental and Theoretical Verification", *Journal of Physics: Conference Series*, vol. 431, p. 012 028, 2013, ISSN: 1742-6588. DOI: 10.1088/1742-6596/431/1/012028.

[292] NT-MDT, *NTEGRA SPECTRA*. [Online]. Available: https://ntmdt.nl/home/products/ntegra-spectra/ (visited on 03/06/2024).

[293] Z. Yang, J. Aizpurua, and H. Xu, "Electromagnetic field enhancement in TERS configurations", *Journal of Raman Spectroscopy*, vol. 40, no. 10, pp. 1343–1348, 2009, ISSN: 0377-0486. DOI: 10.1002/jrs.2429.

[294] M. Pelletier and C. Pelletier, "Raman Spectroscopy | Instrumentation", in *Encyclopedia of Analytical Science*, P. Worsfold, A. Townshend, and C. Poole, Eds., Second Edi, Elsevier, 2005, pp. 94–104. DOI: 10.1016/B0-12-369397-7/00529-X.

[295] C. Burgess, "Optical Spectroscopy | Detection Devices", in *Encyclopedia of Analytical Science*, Elsevier, 2005, pp. 438–443. DOI: 10.1016/B0-12-369397-7/00431-3.

[296] P. G. Spizzirri, J. H. Fang, S. Rubanov, E. Gauja, and S. Prawer, "Nano-Raman spectroscopy of silicon surfaces", 2010. arXiv: 1002.2692.

[297] Z. Zhao, C. Yang, L. Wu, C. Zhang, R. Wang, and E. Ma, "Preparation and Characterization of Crystalline Silicon by Electrochemical Liquid–Liquid–Solid Crystal Growth in Ionic Liquid", *ACS Omega*, vol. 6, no. 18, pp. 11 935–11 942, 2021, ISSN: 2470-1343. DOI: 10.1021/acsomega.1c00304. [Online]. Available: https://pubs.acs.org/doi/10.1021/acsomega.1c00304.

[298] S. P. Apell, J Giraldo, and S Lundqvist, "Small metal particles: Non-local optical properties and quantum-size effects", *Phase Transitions*, vol. 24-26, no. 2, pp. 577–604, 1990, ISSN: 0141-1594. DOI: 10.1080/01411599008210245.

[299] M. Rahaman, A. G. Milekhin, A. Mukherjee, E. E. Rodyakina, A. Latyshev, V. M. Dzhagan, and D. R. T. Zahn, "The role of a plasmonic substrate on the enhancement and spatial resolution of tip-enhanced Raman scattering", *Faraday Discussions*, vol. 214, pp. 309–323, 2019, ISSN: 1359-6640. DOI: 10.1039/C8FD00142A.

[300] Filmetrics, *Refractive Index of BSG, Borosilicate Glass, Microscope Slide.* [Online]. Available: https://www.filmetrics.com/refractive-index-database/BSG/Borosilicate-Glass-Microscope-Slide (visited on 04/25/2024).

[301] D. Georgiev, S. V. Pedersen, R. Xie, Á. Fernández-Galiana, M. M. Stevens, and M. Barahona, "RamanSPy: An Open-Source Python Package for Integrative Raman Spectroscopy Data Analysis", *Analytical Chemistry*, vol. 96, no. 21, pp. 8492–8500, 2024, ISSN: 0003-2700. DOI: 10.1021/acs.analchem.4c00383. [Online]. Available: https://pubs.acs.org/doi/10.1021/acs.analchem.4c00383.

[302] D. A. Whitaker and K. Hayes, "A simple algorithm for despiking Raman spectra", *Chemometrics and Intelligent Laboratory Systems*, vol. 179, pp. 82–84, 2018, ISSN: 01697439. DOI: 10.1016/j.chemolab.2018.06.009.

[303] F. Zhang, X. Tang, A. Tong, B. Wang, J. Wang, Y. Lv, C. Tang, and J. Wang, "Baseline correction for infrared spectra using adaptive smoothness parameter penalized least squares method", *Spectroscopy Letters*, vol. 53, no. 3, pp. 222–233, 2020, ISSN: 0038-7010. DOI: 10.1080/00387010.2020.1730908. [Online]. Available: https://www.tandfonline.com/doi/full/10.1080/00387010.2020.1730908.

[304] L. Y. Beliaev, E. Shkondin, A. V. Lavrinenko, and O. Takayama, "Optical, structural and composition properties of silicon nitride films deposited by reactive radio-frequency sputtering, low pressure and plasma-enhanced chemical vapor deposition", *Thin Solid Films*, vol. 763, p. 139 568, 2022, ISSN: 00406090. DOI: 10.1016/j.tsf.2022.139568. [Online]. Available: https://linkinghub.elsevier.com/retrieve/pii/S0040609022004710.

[305] M. Blasco-Solvas, B. Fernández-Vior, J. Sabek, A. Fernández-Gávela, T. Domínguez-Bucio, F. Y. Gardes, C. Domínguez-Horna, and J. Faneca, "Silicon Nitride Building Blocks in the Visible Range of the Spectrum", *Journal of Lightwave Technology*, vol. 42, no. 17, pp. 6019–6027, 2024, ISSN: 0733-8724. DOI: 10.1109/JLT.2024.3404639. [Online]. Available: https://ieeexplore.ieee.org/document/10537987/.

[306] R. F. Wolffenbuttel, D. Winship, Y. Qin, Y. Gianchandani, D. Bilby, and J. H. Visser, "Optical properties of nitride-rich SiN and its use in CMOS-compatible near-UV Bragg filter fabrication", *Optical Materials: X*, vol. 24, p. 100 348, 2024, ISSN: 25901478. DOI: 10.1016/j.omx.2024.100348. [Online]. Available: https://linkinghub.elsevier.com/retrieve/pii/S2590147824000603.

[307] J. Geist, A. Schaefer, J. Song, Y. Wang, and E. Zalewski, "An accurate value for the absorption coefficient of silicon at 633 nm", *Journal of Research of the National Institute of Standards and Technology*, vol. 95, no. 5, p. 549, 1990, ISSN: 1044-677X. DOI: 10.6028/jres.095.043. [Online]. Available: https://nvlpubs.nist.gov/nistpubs/jres/095/jresv95n5p549{_}A1b.pdf.

[308] A. Ahamed, C. Bartolo-Perez, A. S. Mayet, S. Ghandiparsi, G. Ariño-Estrada, X. Zhou, J. Bec, S.-Y. Wang, L. Marcu, and S. Islam, "Optimizing the light penetration depth in APDs and SPADs for high gain-bandwidth and ultra-wide spectral response", in *Quantum Sensing and Nano Electronics and Photonics XVIII*, M. Razeghi, G. A. Khodaparast, and M. S. Vitiello, Eds., SPIE, 2022, p. 25, ISBN: 9781510648890. DOI: 10.1117/12.2610526. [Online]. Available: https://www.spiedigitallibrary.org/conference-proceedings-of-spie/12009/2610526/Optimizing-the-

light-penetration-depth-in-APDs-and-SPADs-for/10.1117/12.2610526.full.

[309] J. Overbeck, G. Borin Barin, C. Daniels, M. L. Perrin, L. Liang, O. Braun, R. Darawish, B. Burkhardt, T. Dumslaff, X.-Y. Wang, A. Narita, K. Müllen, V. Meunier, R. Fasel, M. Calame, and P. Ruffieux, "Optimized Substrates and Measurement Approaches for Raman Spectroscopy of Graphene Nanoribbons", *physica status solidi (b)*, vol. 256, no. 12, 2019, ISSN: 0370-1972. DOI: 10.1002/pssb.201900343. [Online]. Available: https://onlinelibrary.wiley.com/doi/10.1002/pssb.201900343.

[310] O. Debieu, R. P. Nalini, J. Cardin, X. Portier, J. Perrière, and F. Gourbilleau, "Structural and optical characterization of pure Si-rich nitride thin films", *Nanoscale Research Letters*, vol. 8, no. 1, p. 31, 2013, ISSN: 1556-276X. DOI: 10.1186/1556-276X-8-31.

[311] Y. R. Lee, M. S. Kim, and C. H. Kwon, "Surface-Enhanced Raman Scattering and DFT Study of 4,4'-Biphenyldithiol on Silver Surface", *Bulletin of the Korean Chemical Society*, vol. 34, no. 2, pp. 470–474, 2013, ISSN: 0253-2964. DOI: 10.5012/bkcs.2013.34.2.470. [Online]. Available: http://koreascience.or.kr/journal/view.jsp?kj=JCGMCS{\&}py=2013{\&}vnc=v34n2{\&}sp=470.

[312] L. Le Thi Ngoc, T. Yuan, N. Oonishi, J. van Nieuwkasteele, A. van den Berg, H. Permentier, R. Bischoff, and E. T. Carlen, "Suppression of Surface-Enhanced Raman Scattering on Gold Nanostructures by Metal Adhesion Layers", *The Journal of Physical Chemistry C*, vol. 120, no. 33, pp. 18 756–18 762, 2016, ISSN: 1932-7447. DOI: 10.1021/acs.jpcc.6b05375. [Online]. Available: https://pubs.acs.org/doi/10.1021/acs.jpcc.6b05375.

[313] I. Khan, M. Islam, and Z. H. Mahmood, "Silicon optical waveguides: state of the art", *International Journal of Electronics & Informatics*, vol. 2, 2013.

[314] C. H. Teh, D. Kumar, and S. P. Thiagarajah, "Normalized frequency for noncircular dielectric waveguides", *Microwave and Optical Technology Letters*, vol. 66, no. 4, 2024, ISSN: 0895-2477. DOI: 10.1002/mop.34136. [Online]. Available: https://onlinelibrary.wiley.com/doi/10.1002/mop.34136.

[315] K. J. Kaltenecker, E. Krauss, L. Casses, M. Geisler, B. Hecht, N. A. Mortensen, P. U. Jepsen, and N. Stenger, "Mono-crystalline gold platelets: a high-quality platform for surface plasmon polaritons", *Nanophotonics*, vol. 9, no. 2, pp. 509–522, 2020, ISSN: 2192-8614. DOI: 10.1515/nanoph-2019-0362.

[316] E. ul Haq, Z. Liu, Y. Zhang, S. A. A. Ahmad, L.-S. Wong, S. P. Armes, J. K. Hobbs, G. J. Leggett, J. Micklefield, C. J. Roberts, and J. M. R. Weaver, "Parallel Scanning Near-Field Photolithography: The Snomipede", *Nano Letters*, vol. 10, no. 11, pp. 4375–4380, 2010, ISSN: 1530-6984. DOI: 10.1021/nl1018782.

[317] I. H. Malitson, "Interspecimen Comparison of the Refractive Index of Fused Silica*,†", *Journal of the Optical Society of America*, vol. 55, no. 10, pp. 1205–1208, 1965, ISSN: 0030-3941. DOI: 10.1364/JOSA.55.001205.

[318] W. M. E. M. M. Daniyal, Y. W. Fen, J. Abdullah, A. R. Sadrolhosseini, and M. A. Mahdi, "Design and Optimization of Surface Plasmon Resonance Spectroscopy for Optical Constant Characterization and Potential Sensing Application: Theoretical and Experimental Approaches", *Photonics*, vol. 8, no. 9, p. 361, 2021, ISSN: 2304-6732. DOI: 10.3390/photonics8090361.

[319] D. Paul, *Oxidation Results From JWNC*, 2024.

[320] C.-H. Lin, "Oxidation (of Silicon)", in *Encyclopedia of Microfluidics and Nanofluidics*, Boston, MA: Springer US, 2008, pp. 1584–1584, ISBN: 978-0-387-48998-8. DOI: 10.1007/978-0-387-48998-8_1173.

[321] D. Chandler-Horowitz, "Assessment of Ultra-Thin SiO2 Film Thickness Measurement Precision by Ellipsometry", in *AIP Conference Proceedings*, AIP, 2003, pp. 326–330. DOI: 10.1063/1.1622490.

[322] J. Thong, W. Choi, and C. Chong, "TMAH etching of silicon and the interaction of etching parameters", *Sensors and Actuators A: Physical*, vol. 63, no. 3, pp. 243–249, 1997, ISSN: 09244247. DOI: 10.1016/S0924-4247(97)80511-0.

[323] P. S. Dobson, J. M. Weaver, M. N. Holder, P. R. Unwin, and J. V. Macpherson, "Characterization of batch-microfabricated scanning electrochemical-atomic force microscopy probes", *Analytical Chemistry*, vol. 77, no. 2, pp. 424–434, 2005, ISSN: 00032700. DOI: 10.1021/ac048930e.

[324] K. Tóth, G. Nagy, B. R. Horrocks, and A. J. Bard, "Investigation of silver iodide-based ion-selective membranes by scanning electrochemical microscopy", *Analytica Chimica Acta*, vol. 282, no. 2, pp. 239–246, 1993, ISSN: 00032670. DOI: 10.1016/0003-2670(93)80207-2.

[325] A. J. Bard, F.-R. F. Fan, J. Kwak, and O. Lev, "Scanning Electrochemical Microscopy. Introduction and Principles", *Analytical Chemistry*, vol. 61, no. 2, pp. 132–138, 1989, ISSN: 0003-2700. DOI: 10.1021/ac00177a011.

[326] J. Kwak and A. J. Bard, "Scanning electrochemical microscopy. Theory of the feedback mode", *Analytical Chemistry*, vol. 61, no. 11, pp. 1221–1227, 1989, ISSN: 15206882. DOI: 10.1021/ac00186a009.

[327] C. E. Jones, J. V. MacPherson, Z. H. Barber, R. E. Somekh, and P. R. Unwin, "Simultaneous topographical and amperometric imaging of surfaces in air: Towards a combined scanning force-scanning electrochemical microscope (SF-SECM)", *Electrochemistry Communications*, vol. 1, no. 2, pp. 55–60, 1999, ISSN: 13882481. DOI: 10.1016/S1388-2481(99)00004-1.

[328] S. Amemiya, A. J. Bard, F.-R. F. Fan, M. V. Mirkin, and P. R. Unwin, "Scanning Electrochemical Microscopy", *Annual Review of Analytical Chemistry*, vol. 1, no. 1, pp. 95–131, 2008, ISSN: 1936-1327. DOI: 10.1146/annurev.anchem.1.031207.112938.

[329] T. Kai, C. G. Zoski, and A. J. Bard, "Scanning electrochemical microscopy at the nanometer level", *Chemical Communications*, vol. 54, no. 16, pp. 1934–1947, 2018, ISSN: 1364548X. DOI: 10.1039/c7cc09777h.

[330] P. Kohl and S. A. Bidstrup, "Low Dielectric Constant insulators and Gold Metallization for GHz Multi-Chip Modules", Tech. Rep., 1992, pp. 11–19.

[331] D. T. Atkins, "Novel Probes for Multimodal Imaging at the Nanoscale - First year technical report", Tech. Rep., 2019.

[332] P. S. Dobson, J. M. R. Weaver, D. P. Burt, M. N. Holder, N. R. Wilson, P. R. Unwin, and J. V. Macpherson, "Electron beam lithographically-defined scanning electrochemical-atomic force microscopy probes: fabrication method and application to high resolution imaging on heterogeneously active surfaces", *Physical Chemistry Chemical Physics*, vol. 8, no. 33, pp. 3909–3914, 2006, ISSN: 1463-9076. DOI: 10.1039/b605828k.